

UNIVERSITY OF BUCHAREST
Faculty of Physics



Ph.D. THESIS

Kinetic simulations of plasma dynamics across
magnetic fields and applications to the physics
of planetary magnetospheres

Gabriel-Ioan Voitcu

Scientific Coordinator
Professor Dr. Gheorghe Dinescu

Gabriel-Ioan Voitcu, „*Kinetic simulations of plasma dynamics across magnetic fields and applications to the physics of planetary magnetospheres*”, Ph.D. Thesis, University of Bucharest, 2014.

This page intentionally left blank.

This page intentionally left blank.

Foreword

I would like to express my gratitude and appreciation to my supervisor, Professor Gheorghe Dinescu, for giving me the opportunity to perform my Ph.D. thesis under his guidance. I thank him for understanding and support.

It would not have been possible to elaborate my thesis without the continuous help and support of Dr. Marius Echim. I thank him for the enlightening guidance and invaluable instructions throughout all my research activities. I deeply appreciate all the time and effort he spent on working with me. Thank you very much!

I would like also to thank Professor Viviane Pierrard, Professor Richard Marchand and Professor Virgil Băran for accepting to be members of the Jury and carefully read and evaluate my thesis. Also, many thanks to Professor Daniela Dragoman for chairing the public defense session.

Once again, I wish to express my sincere gratitude to Professor Marchand and Professor Pierrard, this time for our fruitful collaborations regarding the simulation and modeling of space plasmas.

I also express my appreciation to Professor Joseph Lemaire for the valuable and encouraging advices related to my research. I thank him for our interesting discussions about plasma dynamics in non-uniform electromagnetic fields.

I am grateful to Professor Francisc Aaron for supporting my work through his SOPHRD European project.

My thanks go also to Ionel Stan from the Institute of Space Science and to Vincent Letocard and Olivier Rasson from the Belgian Institute for Space Aeronomy for their valuable technical support regarding the computing infrastructure at the two institutions.

I thank all the colleagues at the Institute of Space Science, but also to everyone who have supported, directly or indirectly, my work performed to accomplish this thesis during the last years.

Special thanks to my family.

*Gabriel-Ioan Voitcu
Măgurele, March 2014*

Abstract

In my Ph.D. thesis I investigate with test-kinetic and particle-in-cell simulations the interaction of three-dimensional plasma elements/clouds with transverse non-uniform magnetic fields. The plasma motion across transverse magnetic fields is a fundamental problem of plasma physics that is highly relevant for both laboratory and space plasmas. In our simulations, the plasma and electromagnetic field configurations are typical for the terrestrial magnetosphere. The numerical results obtained in the present thesis are important for understanding the physical processes responsible for the transfer of mass, momentum and energy in space plasmas.

The first objective of my thesis is to study the kinetic effects at the boundaries of a proton stream injected across a non-uniform transverse magnetic field typical for a one-dimensional tangential discontinuity, by using forward and backward test-kinetic simulations. The numerical results obtained suggest a physical mechanism that can explain the formation of energy-dispersed structures at the edges of proton beams interacting with non-uniform magnetic fields. We identified kinetic effects that lead to the formation of ring-shaped and non-gyrotropic velocity distribution functions within the energy dispersed structures.

The second objective of my thesis is to study the kinetic structure of tangential discontinuities by using one-dimensional electromagnetic particle-in-cell simulations. The numerical results obtained revealed the formation of a finite width transition region at the interface of two magnetized plasmas with different macroscopic parameters. The transition region has properties typical for a tangential discontinuity. The particle-in-cell results are in good agreement with the theoretical kinetic solutions and provide an independent validation of the hypothesis assumed by these models.

The third objective of my thesis is to study the interaction of a small Larmor radius plasma element/cloud with transverse non-uniform magnetic fields by means of three-dimensional full-electromagnetic particle-in-cell simulations. The plasma elements considered are streaming in vacuum and perpendicular to a background magnetic field typical to a tangential discontinuity. The simulation results revealed the physical mechanisms that enable the forward propagation of the cloud and the effects of non-uniform magnetic fields on the plasma dynamics. This is for the first time when the interaction of a plasma element with a magnetic field discontinuity is investigated with three-dimensional particle-in-cell simulations. We evidenced physical processes advocated previously by theoretical models and revealed in laboratory experiments.

Contents

| | |
|---|-----------|
| Introduction | 1 |
| 1 Kinetic effects at the boundaries of a proton stream injected into a transverse magnetic field: test-kinetic simulations | 7 |
| 1.1 Vlasov equation | 7 |
| 1.2 The test-kinetic simulation method | 8 |
| 1.2.1 The forward Liouville approach | 9 |
| 1.2.2 The backward Liouville approach | 10 |
| 1.3 Simulation setup | 12 |
| 1.4 Numerical results: forward Liouville approach | 14 |
| 1.4.1 Ring-shaped and non-gyrotropic VDFs observed by Cluster satellites in the terrestrial magnetosphere | 14 |
| 1.4.2 Case I: Antiparallel magnetic field and non-uniform electric field | 15 |
| 1.4.3 Case II: Parallel magnetic field and uniform electric field | 24 |
| 1.5 Comparison between forward and backward results | 27 |
| 1.6 Conclusions | 34 |
| 2 Kinetic simulations of tangential discontinuities | 37 |
| 2.1 Particle-in-cell simulation method | 37 |
| 2.2 Simulation setup | 41 |
| 2.3 Numerical results | 44 |
| 2.3.1 Evaluation of the intrinsic particle-in-cell noise | 44 |
| 2.3.2 Case A: Tangential discontinuity without velocity shear | 48 |
| 2.3.3 Case B: Tangential discontinuity with velocity shear | 50 |

| | | |
|----------|--|------------|
| 2.3.4 | Case C: Plasma slab streaming across a transverse magnetic field | 51 |
| 2.4 | Conclusions | 53 |
| 3 | Three-dimensional particle-in-cell simulations of plasma elements transported across transverse non-uniform magnetic fields | 55 |
| 3.1 | Three-dimensional particle-in-cell simulations | 55 |
| 3.2 | The simulation setup | 58 |
| 3.3 | Numerical results | 60 |
| 3.3.1 | Case I: Stationary plasma element in uniform magnetic field | 60 |
| 3.3.2 | Case II: Plasma element streaming across a uniform magnetic field | 73 |
| 3.3.3 | Case III: Low speed plasma element injected across a non-uniform transverse magnetic field – impenetrable magnetic barrier | 82 |
| 3.3.4 | Case IV: Intermediate speed plasma element injected across a non-uniform transverse magnetic field – penetration of the magnetic barrier | 90 |
| 3.3.5 | Case V: Fast speed plasma element injected across a non-uniform transverse magnetic field – penetration of the magnetic barrier | 97 |
| 3.4 | Conclusions | 99 |
| 4 | Summary and conclusions | 103 |
| | Acknowledgements | 107 |
| | References | 109 |
| | Appendix A – TRISTAN code | 117 |
| | Appendix B – Normalization in TRISTAN code | 123 |
| | List of tables | 125 |
| | List of figures | 127 |

Introduction

In my PhD thesis I use numerical simulations to study the interaction of non-diamagnetic plasmas with transverse magnetic fields typical for planetary magnetospheres. The plasma motion across transverse magnetic field is a fundamental problem of plasma physics that is highly relevant for both laboratory and space plasmas. The physical mechanisms that describe the interaction of solar wind irregularities (or blobs, or jets, or plasmoids) with the terrestrial magnetopause are not yet fully understood and still continue to represent an active research topic. The aim of this work is to analyse kinetic effects and their role on the dynamics of non-diamagnetic three-dimensional plasma elements/clouds across non-uniform magnetic fields using kinetic numerical simulations, namely test-kinetic and particle-in-cell simulations. The thesis is focused on three main objectives, each of them treated in a separate chapter of the thesis, as described below. The last chapter is dedicated to the summary and conclusions of my work.

First objective

In the first chapter of my thesis I investigate the kinetic effects observed at the boundaries of a proton cloud injected across a non-uniform magnetic field configuration typical for a tangential discontinuity. I study the physical mechanisms responsible for the formation of energy-dispersed structures with non-Maxwellian velocity distribution functions at the edges of the proton cloud. I use both forward and backward Liouville approaches of the test-kinetic simulation method to compute the velocity distribution function in different areas of the proton cloud. The formation of non-Maxwellian distribution functions, as ring-shaped or non-gyrotropic ones, is still a topic of active research in the field of magnetospheric physics, as the mechanisms responsible for their formation are not fully understood.

Experimental measurements performed on-board different spacecraft around the Earth revealed the presence of energy-dispersed ion structures inside the terrestrial magnetosphere (e.g. *Bosqued et al.*, 1986; *Zelenyi et al.*, 1990; *Keiling et al.*, 2004a, 2004b). The ion energy-latitude dispersion relations have been investigated in the ionospheric high-latitude mapping of the plasma sheet boundary layer by *Bosqued et al.* (1986) and *Zelenyi et al.* (1990). Also, multiple energy-dispersed ion structures have been emphasized in the plasma sheet boundary layer using Cluster data (*Keiling et al.*, 2004a, 2004b). The physical mechanisms that could generate this kind of structures are still actively investigated since they are not completely understood. Among them we mention the time-dependent effects resulting from the spacecraft encounter with successive ion beams that belongs to the same source (*Sauvaud and Kovrazhkin*, 2004) or the energy-dependent structure of the injection source itself (*Keiling et al.*, 2004a).

Non-Maxwellian velocity distribution functions have been frequently observed inside the terrestrial magnetosphere. For instance, ring-shaped distribution functions (Saito *et al.*, 1994) or non-gyrotropic distribution functions (Frank *et al.*, 1994; Grigorenko *et al.*, 2002; Meziane *et al.*, 2003; Wilber *et al.*, 2004) have been measured *in-situ* on-board different circumterrestrial satellites. Various mechanisms have been proposed to explain the formation of such kind of distributions. It has been suggested that non-Maxwellian velocity distribution functions are the result of non-adiabatic acceleration of ions inside a current sheet (Frank *et al.*, 1994). Meziane *et al.* (2003) and Lee *et al.* (2004) showed that non-gyrotropic distribution functions might be formed due to the remote sensing of a thin current sheet. On the other hand, the kinetic models of tangential discontinuities (Sestero, 1966; Lemaire and Burlaga, 1976; Roth *et al.*, 1996; Echim and Lemaire, 2005) are based on anisotropic velocity distribution functions that asymptotically tend towards isotropic/drifted Maxwellians.

Test-kinetic simulations provide a useful tool to investigate the charged particles dynamics in systems in which a good approximation of the actual electromagnetic fields can be obtained (Marchand, 2010). The electric and magnetic fields considered here are prescribed a priori and not computed self-consistently during the simulation. Over time, the test-kinetic method has been applied in various problems of space plasma physics. Speiser *et al.* (1981) applied the test-kinetic approach to map velocity distribution functions from the terrestrial magnetosphere into the magnetosheath. Curran *et al.* (1987) and Curran and Goertz (1989) mapped velocity distribution functions along test-particle orbits to study the plasma dynamics in an X-line magnetic topology. Also, the test-kinetic approach has been used to investigate the ion dynamics into the terrestrial magnetotail (Ashour-Abdalla *et al.*, 1994). The penetration of the magnetosphere by the solar wind ions has been studied by Richard *et al.* (1994) using the test-kinetic method with electric and magnetic field profiles obtained from a global magnetohydrodynamic simulation of the terrestrial magnetosphere. Rothwell *et al.* (1995) developed test-particle simulations in order to investigate non-adiabatic effects introduced by sharp spatial variations of the electromagnetic field. Also, Delcourt *et al.* (1994, 1995, 1996) used test-particle simulations to investigate the ion dynamics in the near-Earth plasma sheet. More recently, the test-kinetic approach has been applied by Mackay *et al.* (2008) and Marchand *et al.* (2008) to study the kinetic effects in collisionless perpendicular shocks in the vicinity of the Earth's bow shock and also to check consistency with a magnetohydrodynamic solution.

Second objective

In the second chapter of my thesis I investigate the kinetic structure of a one-dimensional tangential discontinuity, with and without velocity shear, using electromagnetic particle-in-cell simulations. I study the stability of the plasma and field profiles across the discontinuity and test the hypothesis assumed in theoretical kinetic models. Also, the problem of a plasma slab drifting across a uniform magnetic field in the presence of a background stagnant plasma is analysed and discussed.

The study of discontinuity regions and their associated current sheets plays a key role in understanding the physical processes responsible for the transfer of mass, momentum and energy in space plasmas. Measurements of the magnetic field performed by Cluster satellites in the solar wind plasma (*Horbury et al.*, 2001; *Knetter et al.*, 2003, 2004) have emphasized that the presence of tangential discontinuities is much more numerous than it was thought in the past (*Neugebauer et al.*, 1984). On the other hand, under some circumstances, the terrestrial magnetopause can be considered a tangential discontinuity (*Papamastorakis et al.*, 1984).

Tangential discontinuities may be viewed as finite-width current sheets separating two magnetized plasmas with different macroscopic properties, e.g density, temperature, bulk velocity. In such a discontinuity there is no plasma transport in the normal direction to the boundary surface. Also, the magnetic field has only tangential components and the total pressure is conserved across the transition region. Steady-state Vlasov equilibrium solutions have been found for different classes of tangential discontinuities. One-dimensional solutions at the interface of two stagnant plasmas with different macroscopic properties have been obtained by *Sestero* (1964) for a unidirectional magnetic field and by *Lemaire and Burlaga* (1976) for a sheared magnetic field. *Sestero* (1966) and *Roth* (1976) computed one-dimensional solutions for plasmas moving across unidirectional magnetic fields. *Roth et al.* (1996) obtained Vlasov equilibrium solutions for one-dimensional tangential discontinuities with both the magnetic field and plasma bulk velocity shears. *De Keyser and Roth* (1997) applied the equilibrium solutions for configurations typical for the Earth magnetopause and discussed the range of parameters for which the equilibrium was found. *Echim* (2004) has shown that steady-state one-dimensional solutions can be extended to the more general two-dimensional case. *Echim et al.* (2005) and *Echim and Lemaire* (2005) applied their kinetic model to study self-consistently the dynamics of a one-dimensional plasma slab and of a two-dimensional plasma flow across an external magnetic field and a background stagnant plasma. More recently, *Echim et al.* (2011) applied the theoretical model of *Roth et al.* (1996) to study the kinetic structure of the terrestrial and Venusian magnetopause.

The particle-in-cell method is a very powerful tool that allows the investigation of plasma physics phenomena at temporal and spatial kinetic scales (*Birdsall and Langdon*, 1991). In particle-in-cell simulations, the electrons and ions trajectories are followed in their self-consistent electric and magnetic fields computed from Maxwell's equations. Thus, in contrast to the test-kinetic method, the plasma internal contribution to the electromagnetic field is taken into account here. Starting with the 1960's, particle-in-cell simulations have been used to study various problems of both laboratory and space plasma physics. A comprehensive description of the method and its applications is given by the reference book of *Birdsall and Langdon* (1991). To our knowledge, no full-particle electromagnetic simulations have been performed to study the structure of a tangential discontinuity and directly cross-check the results with a theoretical kinetic model. Nevertheless, hybrid one-dimensional simulations have been carried out by *Cargill*

(1990) and *Cargill and Eastman (1991)*. In their code, the electrons are considered as a massless fluid and only the ions are treated as particles. These authors performed their study for parameters typical to the solar wind and the terrestrial magnetopause.

Third objective

In the third chapter of my thesis I investigate the interaction of a localized three-dimensional plasma cloud/element with a transverse uniform/non-uniform magnetic field by means of full-electromagnetic particle-in-cell simulations. The plasma element considered here is streaming into vacuum and perpendicular to a background magnetic field. The simulations reveal the physical mechanisms that enable the forward propagation of the cloud and the effects of non-uniform magnetic fields on the plasma dynamics. The results obtained are compared with theoretical models.

In-situ experimental measurements performed on-board different spacecraft revealed the presence of magnetospheric ions inside the terrestrial magnetosheath (e.g. *West and Buck, 1976; Scholer et al., 1981*). Also, plasma elements originating from the magnetosheath have been observed inside the terrestrial magnetosphere (e.g. *Woch and Lundin, 1992; Yamauchi et al., 1993; Lu et al., 2004*). More recently, *Karlsson et al. (2012)* studied the three-dimensional morphology of localized density enhancements observed by Cluster satellites in the magnetosheath and analysed their importance for the penetration of the terrestrial magnetopause.

The interest for the interaction of plasma elements with magnetic discontinuities as the magnetopause is raised by recent statistical studies of the dynamical properties of large amplitude transient dynamic pressure enhancements or jets (*Archer and Horbury, 2013; Plaschke et al., 2013*). These studies show that the magnetosheath inhomogeneities are dominated by velocity increases with respect to the background plasma (up to 15 times the background level). *Archer and Horbury (2013)* show that about 82% of the magnetosheath jets exhibit also an excess of density. As discussed by *Plaschke et al. (2013)*, a large fraction of the high-speed jets are propagating anti-sunward in the frontside magnetosheath and are likely to interact with the magnetopause.

The physical mechanisms that mix the two different plasma populations, solar wind and magnetospheric, and also the role played by both the interplanetary magnetic field and the geomagnetic field continue to represent an active research topic in the physics of planetary magnetospheres. Therefore, the studies of plasma-field interaction are of great importance for understanding of the transfer of mass, momentum and energy at the interface between the solar wind and the terrestrial magnetosphere.

Starting with the second half of the 1950's, the propagation of plasma elements across transverse magnetic fields has been investigated extensively by numerous laboratory experiments (e.g. *Bostick, 1956; Wetstone et al., 1960*). All the experiments performed in different geometries of the magnetic field evidenced the formation of a polarization electric field at the boundaries of the plasma cloud that enable its forward convection across the magnetic field. At the beginning of the 1960's, *Schmidt (1960)*

developed a theoretical model that is able to explain the propagation across transverse magnetic fields of non-diamagnetic plasma elements with a large dielectric constant. According to *Schmidt's* model, a plasma cloud injected into a non-uniform increasing magnetic field is slowed-down and eventually stopped and reflected backwards when the magnetic field becomes larger than a certain critical value. This process, called adiabatic breaking, has been confirmed later in the laboratory experiments carried out by and *Demidenko et al.* (1967, 1969, 1972).

Lemaire (1977, 1985) applied the theoretical kinetic model of *Schmidt* (1960) to investigate the penetration of solar wind plasmoids into the terrestrial magnetosphere. Thus, the impulsive penetration mechanism has been developed in order to describe the dynamics of plasma irregularities at the Earth's magnetopause. Similar to the model of *Schmidt* (1960), the impulsive penetration mechanism is a kinetic model that uses the guiding center approximation to describe the self-consistent motion of electrons and ions during their interaction with the transverse magnetic field. A detailed review of the impulsive penetration mechanism is given by *Echim and Lemaire* (2000).

Numerical simulations have been widely used to investigate the plasma interaction with transverse magnetic fields. *Galvez* (1987) developed one-dimensional electrostatic particle-in-cell simulations to study the dynamics of a non-diamagnetic plasma element injected in vacuum across a uniform magnetic field. His results revealed the polarization of the plasma cloud and its propagation across the background magnetic field, in agreement with the theoretical model of *Schmidt* (1960). Later on, two-dimensional electrostatic particle-in-cell simulations have been performed by *Livesey and Pritchett* (1989). Note that both *Galvez* (1987) and *Livesey and Pritchett* (1989) have considered only large gyroradius beams, i.e. the width of the beam is small compared with the ion Larmor radius. The first three-dimensional electromagnetic particle-in-cell simulations of plasma elements injected in transverse magnetic fields have been carried out by *Neubert et al.* (1992). This time the authors analyzed the dynamics of small gyroradius clouds, i.e. the width of the beam is large compared with the ion Larmor radius, across a uniform magnetic field in vacuum and in the presence of a background plasma. The total simulation time considered by *Neubert et al.* (1992) covered two ion cyclotron periods. More recently, *Hurtig et al.* (2003) and *Gunell et al.* (2009) have studied the plasma motion across curved magnetic field lines with three-dimensional electrostatic particle-in-cell simulations. All five aforementioned particle-in-cell numerical simulations are listed below for comparison.

The plasma-field interaction is by its own nature a three-dimensional problem. Indeed, there is (i) convection along one direction, (ii) self-polarization along the direction that is normal to the background magnetic field and the initial injection velocity and (iii) expansion along the third direction parallel to the external magnetic field. Thus, three-dimensional geometries allow the simultaneous investigation of the change of momentum along the x-axis, the formation of the space charge layers along the y-axis and the plasma expansion along the z-axis. The numerical simulations

INTRODUCTION

discussed in the third chapter of my thesis are performed using a three-dimensional full-electromagnetic relativistic particle-in-cell code. The plasma clouds considered here are large compared with the ion Larmor radius and the total simulation time covers up to four ion cyclotron periods. No background plasma is taken into account due to the limited computational resources. I tested uniform and non-uniform magnetic field profiles. The non-uniform magnetic field is unidirectional and is increasing along the injection direction over a transition region with a length scale of few ion Larmor radii. No electric field is assumed initially.

Particle-in-cell simulations identified in the literature that investigate the interaction of plasma elements with transverse magnetic fields. The following notations are used: E = electrostatic code, EM = electromagnetic code, h = cloud's width along the direction normal to both the background magnetic field and the initial injection velocity, r_{Li} = ion Larmor radius.

| Simulation | Simulation geometry | Magnetic field configuration | Plasma cloud lateral width | Surrounding medium |
|------------------------------------|---------------------|------------------------------|---------------------------------|-----------------------------|
| <i>Galvez, 1987</i> | 1D – E | uniform $\beta \ll 1$ | $h = 3.3r_{Li}$ | vacuum |
| <i>Livesey and Pritchett, 1989</i> | 2D – E | uniform $\beta \ll 1$ | $h \ll r_{Li}$ | vacuum background plasma |
| <i>Neubert et al., 1992</i> | 3D – EM | uniform $\beta \ll 1$ | $h \gg r_{Li}$ | vacuum background plasma |
| <i>Hurtig et al., 2003</i> | 3D – E | curved $\beta \ll 1$ | $h \ll r_{Li}$ | vacuum |
| <i>Gunell et al., 2009</i> | 3D – E | curved $\beta \ll 1$ | $h = 0.5r_{Li}$ $h = r_{Li}$ | vacuum |

Chapter 1

Kinetic effects at the boundaries of a proton stream injected into a transverse magnetic field: test-kinetic simulations

In the first chapter of my thesis I investigate the physical mechanisms that lead to the formation of ring-shaped and non-gyrotropic velocity distribution functions (VDFs) at the edges of a proton cloud streaming across a transverse non-uniform magnetic field. The velocity distribution function is numerically reconstructed using the forward and backward Liouville approaches of the test-kinetic simulation method. A key feature of the test-kinetic simulations discussed here is the formation of an energy-dispersed structure (EDS) where the energy content varies with the distance from the center of the stream. The EDS is characterized by non-Maxwellian velocity distribution functions. The results presented in Chapter 1 of my thesis have already been published (*Voitcu and Echim, 2012; Voitcu et al., 2012*) and blocks of text and figures from the two papers will be reused here.

1.1 Vlasov equation

The space and time evolution of the velocity distribution function, f , for each component species, α , of a collisionless plasma is described by the Vlasov equation (*Delcroix and Bers, 1994*):

$$\frac{\partial f_\alpha}{\partial t} + \vec{v} \cdot \frac{\partial f_\alpha}{\partial \vec{r}} + \frac{q_\alpha}{m_\alpha} (\vec{E} + \vec{v} \times \vec{B}) \cdot \frac{\partial f_\alpha}{\partial \vec{v}} = 0 \quad (1.1)$$

where the electric and magnetic fields are due to both external and internal plasma charges and currents. A self-consistent solution of equation (1.1) is obtained when the electromagnetic field is computed from Maxwell's equations:

$$\begin{aligned} \nabla \times \vec{B} &= \mu_0 \left(\vec{J}_{\text{ext}} + \vec{J}_{\text{int}} + \epsilon_0 \frac{\partial \vec{E}}{\partial t} \right) \\ \nabla \times \vec{E} &= -\frac{\partial \vec{B}}{\partial t} \\ \nabla \cdot \vec{B} &= 0 \\ \nabla \cdot \vec{E} &= \frac{\rho_{\text{ext}} + \rho_{\text{int}}}{\epsilon_0} \end{aligned} \quad (1.2)$$

where ρ_{ext} and ρ_{int} are the external and internal plasma charge densities, while \vec{J}_{ext} and \vec{J}_{int} are the external and internal plasma current densities. The internal source terms ρ_{int}

and \vec{J}_{int} in equation (1.2) are computed from the zeroth and first order moments of the velocity distribution function of each component species:

$$\begin{aligned}\rho_{int}(\vec{r}, t) &= \sum_{\alpha} q_{\alpha} \int_{-\infty}^{+\infty} f_{\alpha}(\vec{r}, \vec{v}, t) d^3\vec{v} \\ \vec{J}_{int}(\vec{r}, t) &= \sum_{\alpha} q_{\alpha} \int_{-\infty}^{+\infty} \vec{v} f_{\alpha}(\vec{r}, \vec{v}, t) d^3\vec{v}\end{aligned}\quad (1.3)$$

where the integration is performed over the entire three-dimensional velocity space. As can be noticed, obtaining a solution of the non-linear partial differential equation (1.1) is not straightforward in most of the problems of practical interest. The Vlasov equation (1.1) coupled with Maxwell's equations (1.2) describes the velocity distribution function of each plasma component species and treats self-consistently the coupling between the plasma dynamics, external forces and electromagnetic field. In the following we use the method of characteristics to compute the velocity distribution function in a prescribed configuration of the electromagnetic field.

1.2 The test-kinetic simulation method

The test-kinetic simulations are based on numerical integration of test-particle trajectories in prescribed electric and magnetic fields and can be classified in four different approaches according to *Marchand* (2010): (i) trajectory sampling, (ii) forward Monte Carlo, (iii) forward Liouville and (iv) backward Liouville. The latter two will be described below. The test-kinetic method is a useful tool to study the kinetic structure of plasmas using prescribed electric and magnetic fields provided either by theoretical models, magnetohydrodynamic simulations or experimental data. The usefulness of the method is evident. It provides a description at the microscopic level that is consistent with electromagnetic configurations determined at a macroscopic level, theoretically or experimentally. I will use both forward and backward Liouville approaches to analyze the kinetic structure of a proton cloud injected into a given magnetic field, assuming that the initial velocity distribution function is known.

The characteristics of the Vlasov equation for collisionless plasmas can be obtained by solving the Newton-Lorentz equation of motion for a system of charged particles injected into given profiles of the electric and magnetic fields (*Delcroix and Bers, 1994*):

$$\frac{d^2\vec{r}}{dt^2} = \frac{q}{m} \left(\vec{E} + \frac{d\vec{r}}{dt} \times \vec{B} \right) \quad (1.4)$$

This is equivalent to Liouville's theorem applied to the velocity distribution function f , which states that the numerical value of f remains unchanged at each point along a test-particle orbit:

$$\frac{df}{dt} = 0 \quad (1.5)$$

One can compute numerically any number of Vlasov equation characteristics and then map the velocity distribution function along them by applying Liouville's theorem.

1.2.1 The forward Liouville approach

In the forward approach one defines a uniform grid of guiding centers with $N_x \times N_y$ nodes placed inside the so-called “source region” from where test-particles are injected into the simulation domain. The velocity distribution function is prescribed in the source region. To each of the $N_x \times N_y$ mesh points, n_p particles are “attached” with the initial velocities $(v_{x0}, v_{y0}, v_{z0})_i$ distributed according to the velocity distribution function defined for the source region. In order to reconstruct the VDF in other regions of the simulation domain, $6 \times n_p \times N_x \times N_y$ equations of motion (1.4) are numerically integrated in the time range $t > 0$ and provide $3 \times n_p \times N_x \times N_y$ components of the final test-particles velocities $(v_x, v_y, v_z)_i$ at time t . These velocities define a scattered distribution of points in the three-dimensional velocity space.

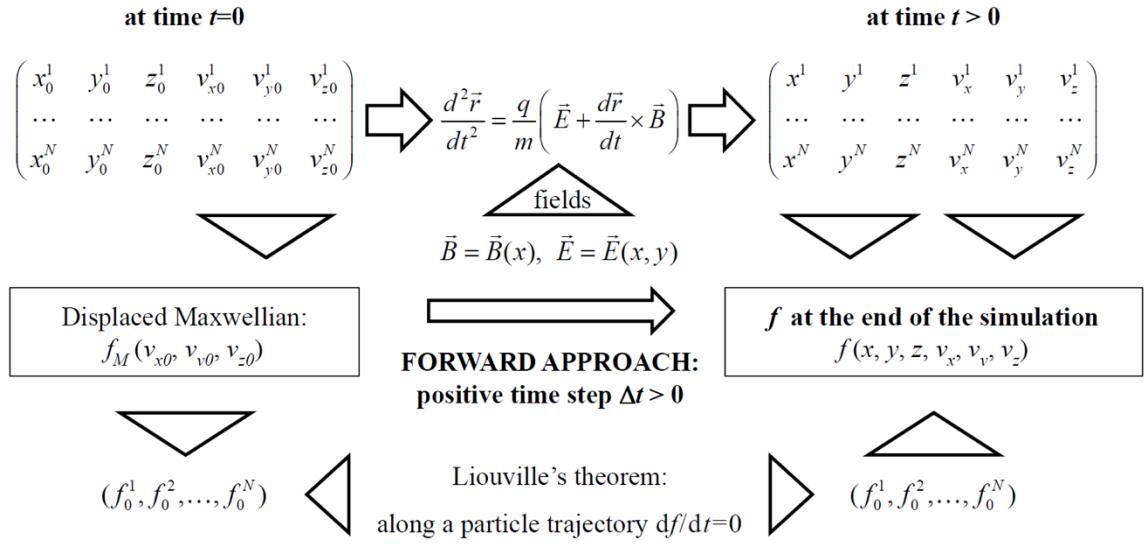


Figure 1.1 – Schematic diagram of the forward Liouville approach; a positive time-step is used to integrate test-particle orbits in given electric and magnetic fields.

Since the velocity distribution function does not change along each of the orbits, the value of f in each point of the velocity space defined by the final velocities $(v_x, v_y, v_z)_i$ is equal to the value of the initial distribution function computed at $t=0$ for the initial velocities $(v_{x0}, v_{y0}, v_{z0})_i$, as stated by the Liouville theorem (1.5). This is basically the procedure to Liouville map the three-dimensional velocity distribution function from a point in configuration space to another, when the profiles of the electric and magnetic fields are known. In practice we need a sufficient number of characteristics to achieve a reasonable sampling of the velocity space. Therefore, we “collect” the VDF from a bin in the three-dimensional configuration space. The procedure outlined above is applied at time t in those spatial bins of the configuration space populated by a sufficiently large number of particles such that a satisfactory sampling of f to be obtained. A schematic diagram describing the forward Liouville approach is shown in Figure 1.1.

1.2.2 The backward Liouville approach

A limitation of the forward approach is its reduced spatial resolution resulting from the binning of the spatial domain in cells whose size depends on the total number of test-particles and the resolution desired in the velocity space. When one needs a very good spatial resolution then better results are obtained by the backward approach.

In the backward approach a three-dimensional velocity grid $(v_x, v_y, v_z)_i$ with N_v vertices is constructed at a precise position in the configuration space. A test-particle is assigned to each vertex of the grid and its equation of motion is integrated backward in time back to $t=0$. To each node of the grid a single test-particle is assigned. The initial velocities of the test-particles are precisely equal to the velocities corresponding to the grid vertices. Thus, the particles are injected in the system from the spatial region where the distribution function is unknown, contrary to the forward approach that considers particles injected from a source region and propagated forward in time until they reach the region where the VDF needs to be computed.

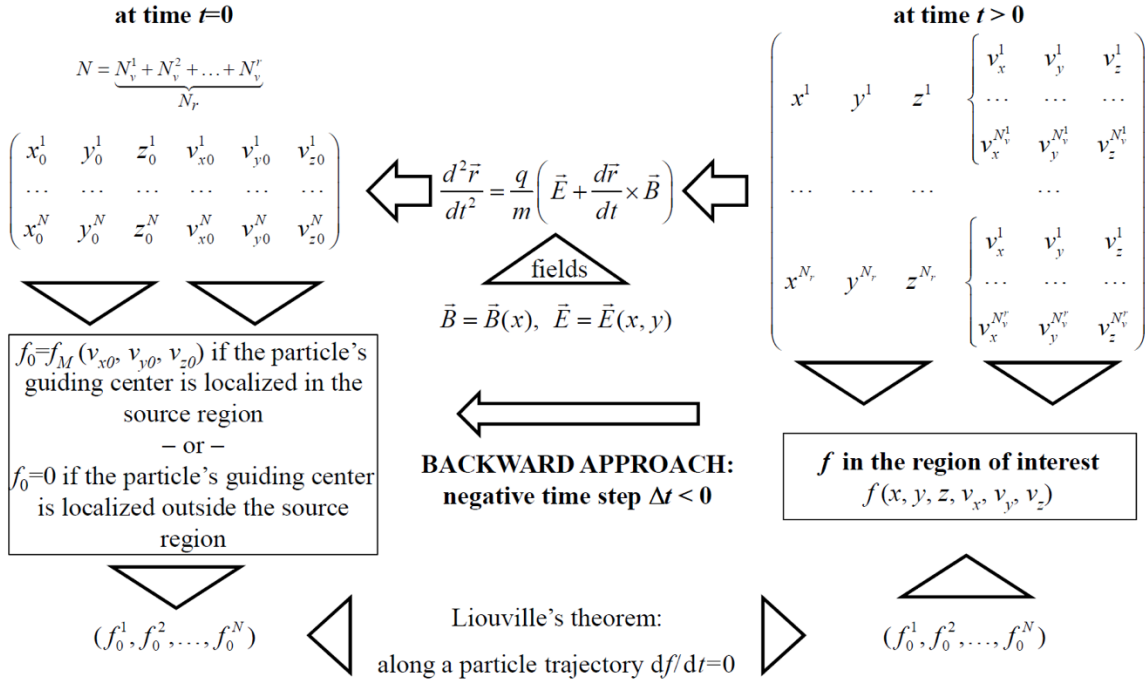


Figure 1.2 – Schematic diagram of the backward Liouville approach; a negative time-step is used to integrate test-particle orbits in given electric and magnetic fields.

In order to reconstruct the velocity distribution function with the backward approach, the $6 \times N_v$ equations of motion (1.4) are numerically integrated backward in time, thus providing $3 \times N_v$ components $(v_{x0}, v_{y0}, v_{z0})_i$ of the test-particles velocities at time $t=0$. If the particle's i guiding center is localized inside the source region, at time $t=0$, we assign to that particle the numerical value of the distribution function computed at $t=0$ for the velocity components $(v_{x0}, v_{y0}, v_{z0})_i$. Otherwise, the value of the VDF is set to zero. Using Liouville's theorem (1.5) we assign to each vertex of the grid, $(v_x, v_y, v_z)_i$, the numerical value of the distribution function computed at $t=0$. In this way the VDF is

determined on the discrete mesh in the 3D velocity space. This procedure is applied at time t for N_r points of interest in the configuration space. A schematic diagram describing the backward Liouville approach is shown in Figure 1.2.

It should be mentioned that in both forward and backward approaches, the source region is defined in terms of the guiding centers positions and not based on the actual positions of the particles. More exactly, in the forward approach we define at $t=0$ a uniform grid of guiding centers and we compute the actual positions of all the particles assigned to those guiding centers based on their initial velocities and fields configuration in the injection region (Northrop, 1963):

$$\vec{r} = \vec{r}_{gc} + \frac{m}{qB^2} \vec{B} \times \vec{w}_\perp \quad (1.6)$$

where \vec{r} is the position of a particle with the guiding center localized in \vec{r}_{gc} , while the last right term in equation (1.6) is the Larmor radius vector; \vec{w}_\perp is the gyration velocity in the perpendicular plane to the magnetic field of induction \vec{B} . A schematic diagram is shown in Figure 1.3. The blue circles illustrate different orbits of the particles (green dots) that gyrate around their guiding centers (red dots). It can be noticed that even though the initial distribution of sources (guiding centers) is structured as a uniform grid, the particles are randomly localized inside and nearby the source region at $t=0$. In this way a more realistic initial distribution of particles in the configuration space is obtained, in contrast with the more straightforward possibility of injecting the particles directly from the grid nodes. In the backward approach, the source region is also defined based on guiding centers positions in order to have consistency with the forward approach. Only that this time the equation (1.6) is applied to compute the guiding centers positions, since the final positions of the particles at the end of the simulation, i.e. at $t=0$ in the backward approach, are known.

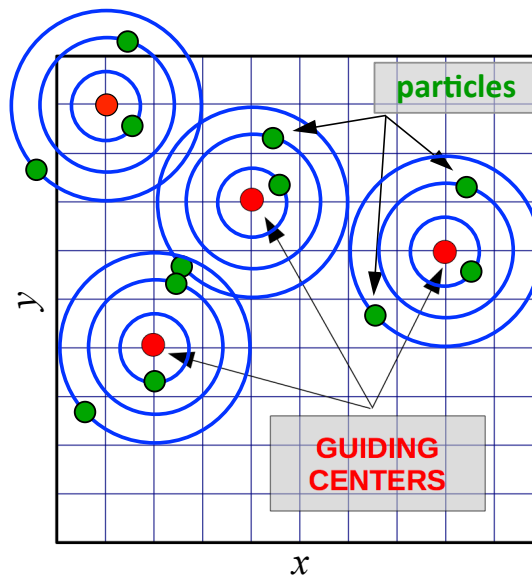


Figure 1.3 – Schematic diagram of the source region defined in terms of guiding centers positions. The blue circles illustrate different orbits of the particles (green dots) that gyrate around their guiding centers (red dots).

1.3 Simulation setup

In the test-kinetic simulations the magnetic and electric fields introduced in equation (1.4) are prescribed a priori. The magnetic field used in our computations is stationary, it varies with the x -coordinate and is confined everywhere in the yOz plane:

$$\vec{B}(x) = \frac{\vec{B}_1}{2} \operatorname{erfc}\left(\frac{x}{L}\right) + \frac{\vec{B}_2}{2} \left[2 - \operatorname{erfc}\left(\frac{x}{L}\right) \right] \quad (1.7)$$

where \vec{B}_1 is the asymptotic field in the left hand side of the transition region ($x \rightarrow -\infty$), \vec{B}_2 is the asymptotic field in the right hand side ($x \rightarrow +\infty$) and L represents the characteristic scale length of the transition region. This type of magnetic profile has been obtained self-consistently from kinetic models of one-dimensional tangential discontinuities (TDs) (e.g. *Sestero, 1964; Lemaire and Burlaga, 1976; Roth et al., 1996*). The magnetic profile will be hereinafter also termed *discontinuity* although there is no discontinuous variation of it inside the simulation domain. We investigate a particular configuration of the B-field, namely an antiparallel profile, which is obtained by setting $B_y=0$ and $B_{2z}=-B_{1z}$ in (1.7). In this case the B-field is everywhere parallel to Oz and changes sign at $x=0$.

The electric field is everywhere normal to the magnetic field and is derived from the two-dimensional Laplace equation solved in the xOy plane:

$$\frac{\partial^2 \Phi}{\partial x^2} + \frac{\partial^2 \Phi}{\partial y^2} = 0 \quad (1.8)$$

The equation (1.8) is integrated on a rectangular domain defined by $x_L \leq x \leq x_R$ and $y_B \leq y \leq y_T$. The following Neumann boundary conditions are considered:

$$\begin{aligned} \left. \frac{\partial \Phi}{\partial x} \right|_{x=x_L} &= \left. \frac{\partial \Phi}{\partial x} \right|_{x=x_R} = 0 \\ \left. \frac{\partial \Phi}{\partial y} \right|_{y=y_B} &= \left. \frac{\partial \Phi}{\partial y} \right|_{y=y_T} = -V_0 B_z(x) \end{aligned} \quad (1.9)$$

where V_0 is the plasma bulk velocity at the left hand side of the transition region. The boundary conditions (1.9) have been chosen such that the electric field at $y=y_B$ and $y=y_T$ sustains a quasi-uniform electric drift in the x direction: $E_y(x)/B_z(x)=V_0$. The boundary conditions at $x=x_L$ and $x=x_R$ correspond to a vanishing E_x component at the two sides of the simulation domain. The electric field obtained from equations (1.8) and (1.9) is a two-dimensional generalization of the one-dimensional electric field used in previous test-particle simulations (*Echim and Lemaire, 2003*). Taking $x_R=-x_L$ and $y_T=-y_B$, the electric field intensity has the E_x and E_y components:

$$\begin{aligned} E_x(x, y) &= -\frac{\pi}{2x_L} \sum_{m=1}^{\infty} \eta_m \cos\left(\frac{m\pi x}{2x_L}\right) \sinh\left(\frac{m\pi y}{2x_L}\right) \\ E_y(x, y) &= -\frac{\pi}{2x_L} \sum_{m=1}^{\infty} \eta_m \sin\left(\frac{m\pi x}{2x_L}\right) \cosh\left(\frac{m\pi y}{2x_L}\right) \end{aligned} \quad (1.10)$$

where $m=1, 3, 5$, etc. The η_m coefficients are given by:

$$\eta_m = \frac{2x_L V_0 B_{1z}}{\pi^2 \cosh\left(\frac{m\pi y_B}{2x_L}\right)} \int_{-\pi}^{+\pi} \operatorname{erf}\left(\frac{2x_L}{\pi L} \theta\right) \sin(m\theta) d\theta \quad (1.11)$$

The solution of Laplace's equation (1.8) with boundary conditions (1.9) may be viewed as an electric field simulating the one sustained by space-charge layers forming at the boundaries of a moving non-diamagnetic plasma element in the presence of a magnetic field (e.g. *Schmidt, 1960; Galvez et al., 1990*) and illustrated by the particle-in-cell simulations described in the third chapter of the thesis.

The simulations presented here have been performed for an electromagnetic field configuration scaled to reproduce parameters typical for the terrestrial magnetotail. The magnetic field profile would correspond to a tangential discontinuity. A possible origin of the electric field can be a localized perturbation of the dawn-dusk electric field. Another region of the magnetosphere where such electric and magnetic fields could be observed is the magnetopause.

The initial velocity distribution function specified for the particles injected from the source region is described by a displaced Maxwellian:

$$f_M(v_{x0}, v_{y0}, v_{z0}) = N_0 \left(\frac{m}{2\pi k_B T_0} \right)^{3/2} e^{-\frac{m[(v_{x0}-V_0)^2 + v_{y0}^2 + v_{z0}^2]}{2k_B T_0}} \quad (1.12)$$

where V_0 is the average velocity parallel to the positive x-axis and perpendicular to the magnetic field, while N_0 and T_0 are the density and temperature of protons. In both forward and backward approaches the initial ($t=0$) source region, where the velocity distribution function is known, is localized in the left hand side of the transition region in the xOy plane perpendicular to the magnetic field. A schematic diagram of the simulation setup is shown in Figure 1.4.

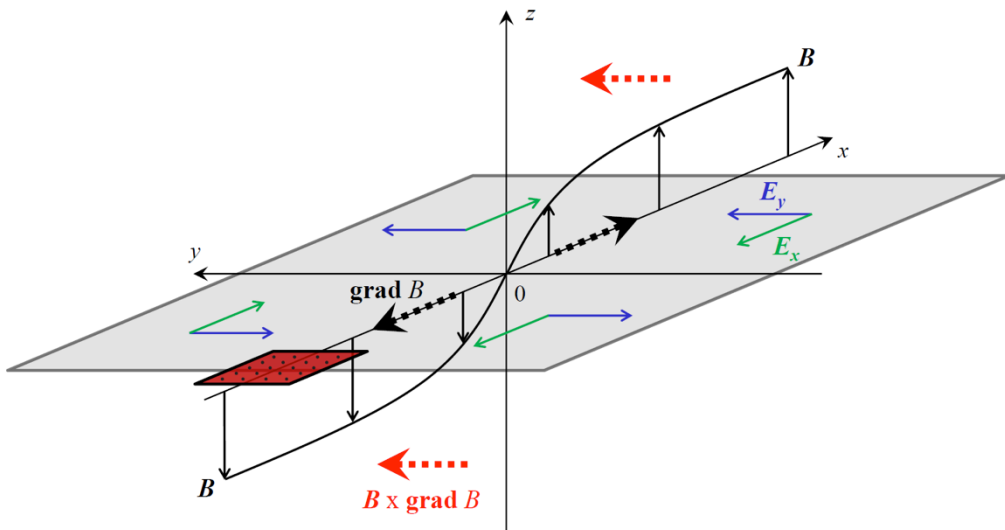


Figure 1.4 – Schematic diagram of the simulation geometry. The source region (red rectangle) where the initial velocity distribution function is known is localized in the xOy plane perpendicular to the magnetic field, at the left hand side of the transition region.

1.4 Numerical results: forward Liouville approach

1.4.1 Ring-shaped and non-gyrotropic VDFs observed by Cluster satellites in the terrestrial magnetosphere

Lee et al. (2004) and *Wilber et al. (2004)* have thoroughly analysed data from the four Cluster spacecrafts (*Escoubet et al., 1997*) on 1st of October 2001 and discussed the kinetic properties of the plasma in the vicinity of the neutral sheet. It is shown that the current sheet became very thin, of the order of the Larmor radius of a 5 keV proton gyrating into a magnetic field of 10 nT. The thinning of the current sheet coincided with observations of highly anisotropic ion VDFs; the $B_{y,GSM}$ component turned from negative to positive values (*Lee et al., 2004*). Examples of ion VDFs corresponding to these observations are illustrated in Figure 1.5 and show projections in the space of perpendicular velocities at three different moments of time.

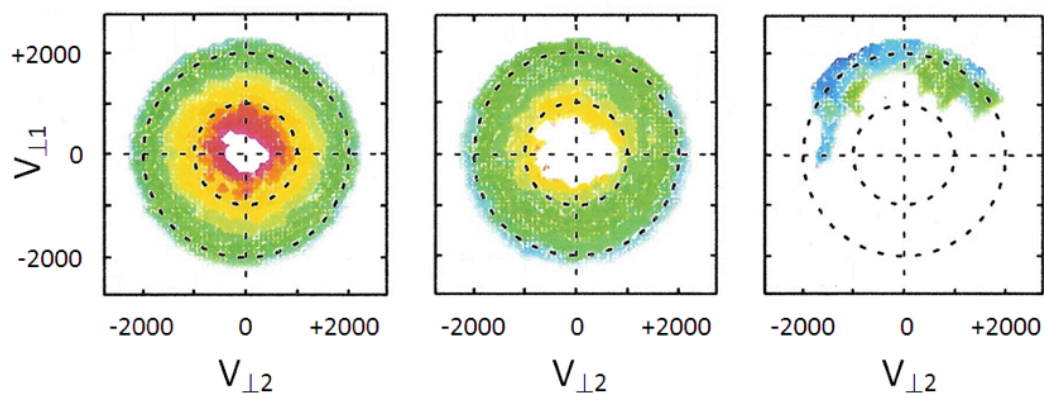


Figure 1.5 – Example of ring-shaped and non-gyrotropic (crescent-like) ion VDFs observed by Cluster (C1) CIS instruments (*Reme et al., 1997*) at 09:25:40 UT (left panel), 09:36:32 UT (middle panel) and 09:46:11 UT (right panel) on 1st of October 2001. All panels illustrate sections in the velocity plane perpendicular to the local magnetic field; the units are km/s on both axes (from *Lee et al., 2004*).

Before the thinning of the current sheet, the proton velocity distribution functions observed by Cluster spacecraft (see Figure 1.5) are nearly isotropic with a small central cavity. Nevertheless, later on, the velocity distribution function, although remains still gyrotropic, shows that a significantly larger central region of the velocity space is voided of particles. The distribution function becomes highly non-gyrotropic toward the end of the analysed time interval, with the ions being restricted to a limited sector in the space of perpendicular velocities. Similar features of velocity distribution functions have been reported by observations of ion shell or ring-shaped velocity distribution functions in the plasma sheet (*Nakamura et al., 1991*) or plasma sheet boundary layer – PSBL (*Nakamura et al., 1992*), triggering instabilities, waves and auroral emissions (*Olsson et al., 2004; Keiling et al., 2006; Ashour-Abdalla et al., 2006*).

Based on test-particle simulations without any electric field, *Lee et al. (2004)* explained the crescent-shaped non-gyrotropic velocity distribution functions as an effect of the remote sensing of particles with Larmor radius larger than the thickness of the

neutral sheet. The velocities of the test-particles simulated by *Lee et al. (2004)* had the initial velocities distributed according to a Maxwellian distribution function with a low-energy cut-off matching the observed velocity distribution functions. The VDF in various regions of the simulation domain has been computed by accumulating particles passing through the corresponding spatial cell in 25 ion Larmor periods and not by tracing VDFs along integrated orbits as in this study.

1.4.2 Case I: Antiparallel magnetic field and non-uniform electric field

Inspired by the previous example of experimental and numerical results we performed test-kinetic simulations for the setup described in section 1.2, similar to the one imagined by *Lee et al. (2004)*. The test-kinetic method adopted here enables the direct computation of the velocity distribution function by Liouville mapping. The antiparallel magnetic field is shown in Figure 1.6 (left panel), while the non-uniform electric field is shown in Figure 1.6 (right panel). This simulation geometry may be viewed as describing a neutral sheet and a superimposed electric field with E_y changing sign whenever the B_z reverses sign. One important aspect of our electromagnetic configuration is that although B_z changes sign at $x=0$, the gradient-B drift remains parallel to $+Oy$ since ∇B also changes sign at $x=0$.

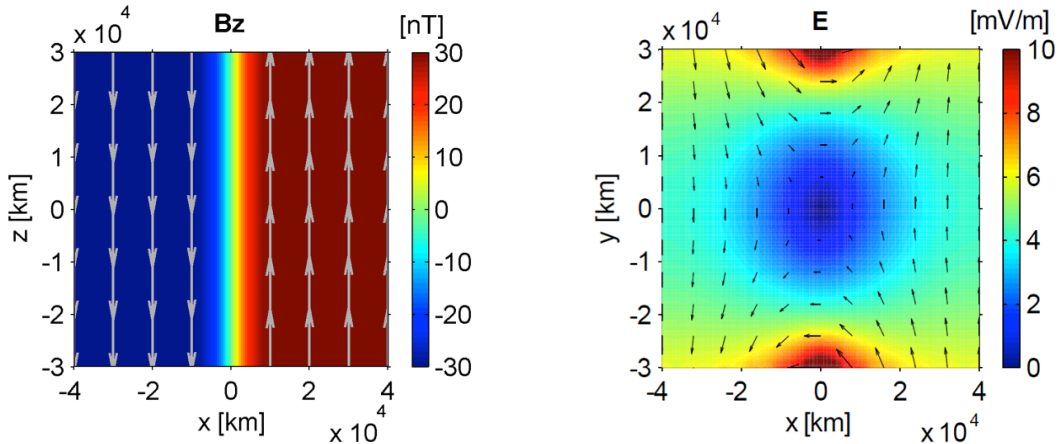


Figure 1.6 – *Left panel*: magnetic field profile in the simulation domain; the B-field is unidirectional and changes orientation at $x=0$. *Right panel*: electric field profile in the simulation domain; E_y changes sign whenever B_z reverses sign. The simulation domain is limited by: $-40000 \text{ km} \leq x \leq +40000 \text{ km}$, $-30000 \text{ km} \leq y \leq +30000 \text{ km}$.

Our numerical experiment consists in injecting test-particles on the left side of the neutral sheet ($x < 0$, see Figure 1.6 – left panel) and integrating their orbits until they intersect the magnetic transition region. The initial velocity distribution function of the test-particles is given by the drifting Maxwellian (1.12) without any low-energy cut-off. All the trajectories are integrated numerically over a time interval t . The simulation domain is defined between $[-40000, +40000]$ km along the x-axis and $[-30000, +30000]$ km along the y-axis, the particles that reach regions outside these limits are removed from the simulation. We use the forward Liouville approach (see Figure 1.1) to compute the VDF of the test-protons. The input parameters assumed are given in Table 1.1.

Table 1.1 – Input parameters of the test-kinetic simulations: N_0 , $k_B T_0$, V_0 are the density, thermal energy and average velocity of the drifting Maxwellian (1.12); B_{1z} , B_{2z} are the asymptotic values of the magnetic field; L is the length scale of the TD; R_L is the Larmor radius of the thermal protons; T_L is the proton cyclotron period; $N_x \times N_y$ is the number of injection sources; n_p is the number of test-particles injected from each source; x_0 , y_0 are the coordinates of the first source; dx_0 , dy_0 are the separation distances between sources along Ox and Oy .

| | N_0 [m ⁻³] | $k_B T_0$ [keV] | V_0 [km/s] | B_{1z} [nT] | B_{2z} [nT] | L [km] | R_L [km] | T_L [s] | $N_x=N_y$ | n_p | x_0, y_0 [km] | dx_0, dy_0 [km] |
|----------------|-----------------------------|--------------------|-----------------|------------------|------------------|-------------|---------------|--------------|-----------|-------|--------------------|----------------------|
| Case I | 10^4 | 3 | 200 | -30 | +30 | 6000 | 260 | 2.2 | 12 | 20000 | -20000, -550 | 200, 100 |
| Case II | 10^4 | 7 | 200 | +30 | +90 | 6000 | 400 | 2.2 | 12 | 75000 | -20000, -1100 | 200, 200 |

In Figure 1.7 we illustrate the positions of the protons in the xOy plane, perpendicular to the magnetic field, after 120 seconds of gyration and drift (roughly 55 gyration periods). The local number density is color coded; one density value is assigned to each bin of a 2D mesh of 60x60 spatial cells. After 120 seconds the protons are still in the region with a smooth variation of the magnetic and electric fields, on the left side of the discontinuity, and continue to drift towards the discontinuity. The spatial variation of the VDF in various regions of the cloud is shown in Figure 1.8. As expected, in the central region of the cloud the VDF is a drifting Maxwellian similar to the initial one.

After another 100 seconds of drift, the protons move inside the transition region where they interact with the non-uniform field. Their positions in the xOy plane, perpendicular to the magnetic field, are shown in Figure 1.9 for $t=225$ seconds (or roughly 100 proton gyro-periods). The overall shape of the proton cloud is deformed and shows significant asymmetries; the test-protons are scattered in the positive direction of the y -axis. While initially the spatial scale of the proton cloud in the y -direction was roughly 6000 km, after 225 seconds the cloud expands over 20000 km in the positive direction of y -axis. We assign this asymmetric expansion of the cloud to the positive gradient-B drift (*Northrop, 1963*):

$$\vec{V}_{\nabla B} = \frac{mw_{\perp}^2}{2qB^3} \vec{B} \times \nabla B \quad (1.13)$$

where w_{\perp} is the perpendicular velocity in the guiding center frame of reference.

Indeed, in the geometry chosen here the gradient-B drift described by equation (1.13) is the most important one. This charge and energy dependent gradient-B drift acts inside the transition region where the electromagnetic field is non-uniform. The VDF of protons in various spatial bins inside the cloud is computed for each spatial bin defined in the xOy plane and identified by the combination of letters (rows) and numbers (columns) in Figure 1.9. The size of a spatial bin is defined such that it contains a large number of particles for a good sampling of the VDF. The bins of the mesh shown in Figure 1.9 have a spatial resolution of 280 km in x -direction and 2500 km in y -direction, adapted to the geometry of the cloud and the total number of simulated particles.

The spatial variation of the VDF in the bins illustrated in Figure 1.9 is shown in Figure 1.10. These results evidence a key feature of the proton velocity distribution function: the formation of a cavity in the central region of the perpendicular velocities

space. An example is given by the ring-shaped velocity distribution functions obtained in the lateral spatial bins D3, E3, D4 and E4. The size of the central, low-energy cavity has the tendency to increase with the distance from the center of the ion cloud; the central void of particles is larger close to the upper boundary (i.e. for larger y -values) than in the center (compare, for instance, the VDFs of bins E3 and E4). The kinetic properties of the front and trailing edge of the proton cloud show additional interesting features. The velocity distribution function is highly non-gyrotropic on the front-side and trailing edge of the cloud, as illustrated by the VDFs obtained for instance in spatial bins A4, B4, G4 and H4, shown in Figure 1.10. These aspects will be discussed in more detail below.

Further, Figure 1.11, Figure 1.13, Figure 1.15 and Figure 1.17 show the positions of the protons in the xOy plane after 275, 300, 350 and 600 seconds of gyration and drift illustrating the subsequent stages of the interaction of the proton cloud/beam with the region of magnetic field gradient. The proton cloud continues to drift towards the right side of the discontinuity. The overall shape of the cloud is strongly deformed and shows significant asymmetries. The spatial variation of the velocity distribution functions corresponding to the cloud's position illustrated by Figure 1.11, Figure 1.13, Figure 1.15 and Figure 1.17 are shown in Figure 1.12 for $t=275$ s, Figure 1.14 for $t=300$ s, Figure 1.16 for $t=350$ s and Figure 1.18 for $t=600$ s. These results obtained confirm that the ring-shaped VDFs observed at the edges of the proton cloud/beam are preserved even when the cloud exit outside the region of magnetic transition. In some sense they are a "hallmark" imprinted on the cloud's kinetic structure by the interaction with the TD.

In Figure 1.15 one can identify the formation of two proton populations with different dynamics: P1, a population that is captured in the interior of the discontinuity and P2, a population that penetrates inside the discontinuity and moves across it into the right side. The formation of these two populations is an effect of the combination of the electric drift and gradient-B drift acting inside the simulation domain.

As shown in Figure 1.10, Figure 1.12, Figure 1.14, Figure 1.16 and Figure 1.18, the lateral edges of the cloud (in the direction perpendicular both to \vec{V} and \vec{B}) are mainly populated by the most energetic particles of the cloud and the velocity distribution functions in these regions are ring-shaped. The physical mechanism that explains the formation of the central cavity in the velocity space and the creation of a ring-shaped distribution in the space of perpendicular velocities is related to the gradient-B drift. Indeed, the particles with a larger perpendicular thermal energy are deflected by $\vec{V}_{\nabla B}$ to larger distances along the y -axis (see (1.13)). The velocities of the particles deflected by the gradient-B drift populate the ring shaped VDFs observed, e.g., in bins D3, D4, D5, E3, E4, E5, F4, F5 of Figure 1.10. The protons with smaller thermal velocities are deflected less by $\vec{V}_{\nabla B}$ and therefore their number decreases in the positive direction of the y -axis, away from the center of the cloud. The regions close to the edges are virtually not accessible to particles with small thermal energy. Thus, the velocity space corresponding to the smaller energies is void and a cavity is formed in the central part of the VDF (see bins D3, D4, D5, E3, E4, E5, F4, F5 of Figure 1.10).

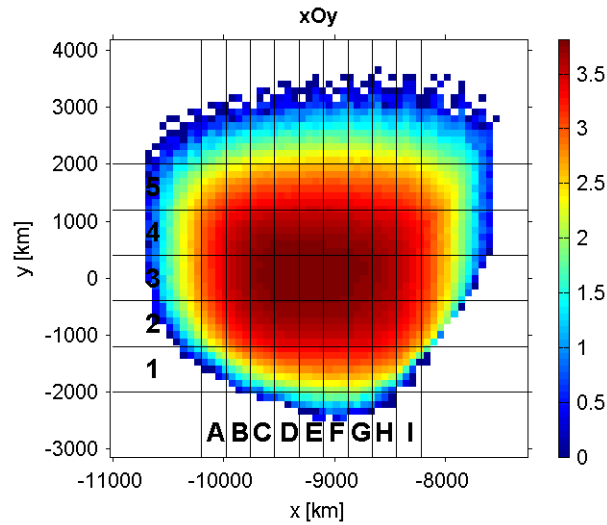


Figure 1.7 – Distribution of protons in the xOy plane after 120 seconds ($\sim 55T_L$) from injection in the electromagnetic field illustrated in **Figure 1.6**. The local value of the number density is color coded. The cloud moved in a region of virtually uniform electric and magnetic fields. The spatial mesh on which the VDF is reconstructed is also shown; each bin is identified by a combination of letters and numbers as shown on the left side and bottom side of the figure.

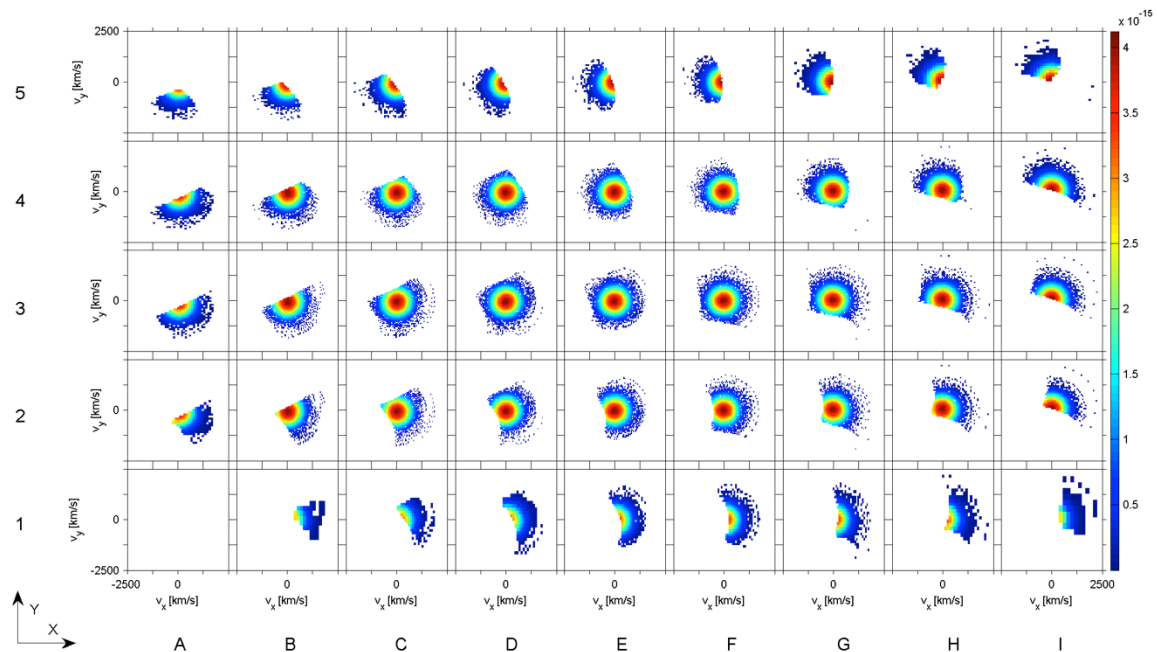


Figure 1.8 – Projection in the space of perpendicular velocities, for $v_z=0$, of the Liouville mapped velocity distribution functions of protons in the cloud at $t=120$ seconds. The spatial bins are defined in **Figure 1.7**. One notes the drifting Maxwellian VDF obtained in the central core of the cloud and non-gyrotropic VDFs at the edges of the cloud; the latter result from the large Larmor radius particles with gyro-centers inside the cloud. Note the different regions of the velocity space populated in bins C1–I1 compared to C5–I5.

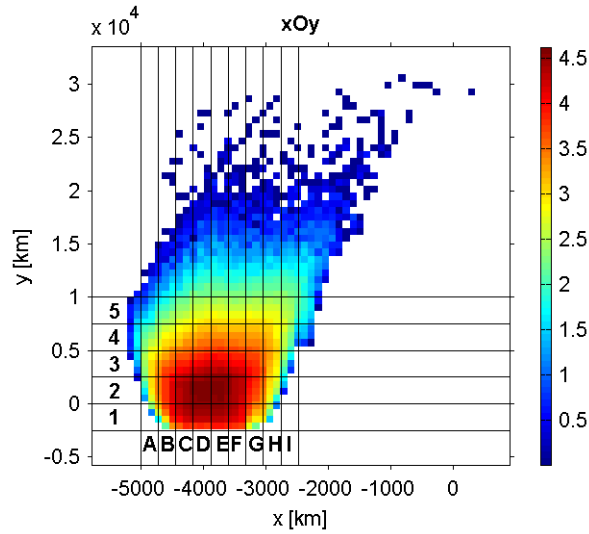


Figure 1.9 – Distribution of protons in the xOy plane after 225 seconds ($\sim 100T_L$) from injection in the electromagnetic field illustrated in **Figure 1.6**. The local value of the number density is color coded. The cloud has spent some time in the region of non-uniform fields and its shape is elongated into the $+y$ -direction under the action of the gradient-B drift. The spatial mesh on which the VDF is reconstructed is also shown.

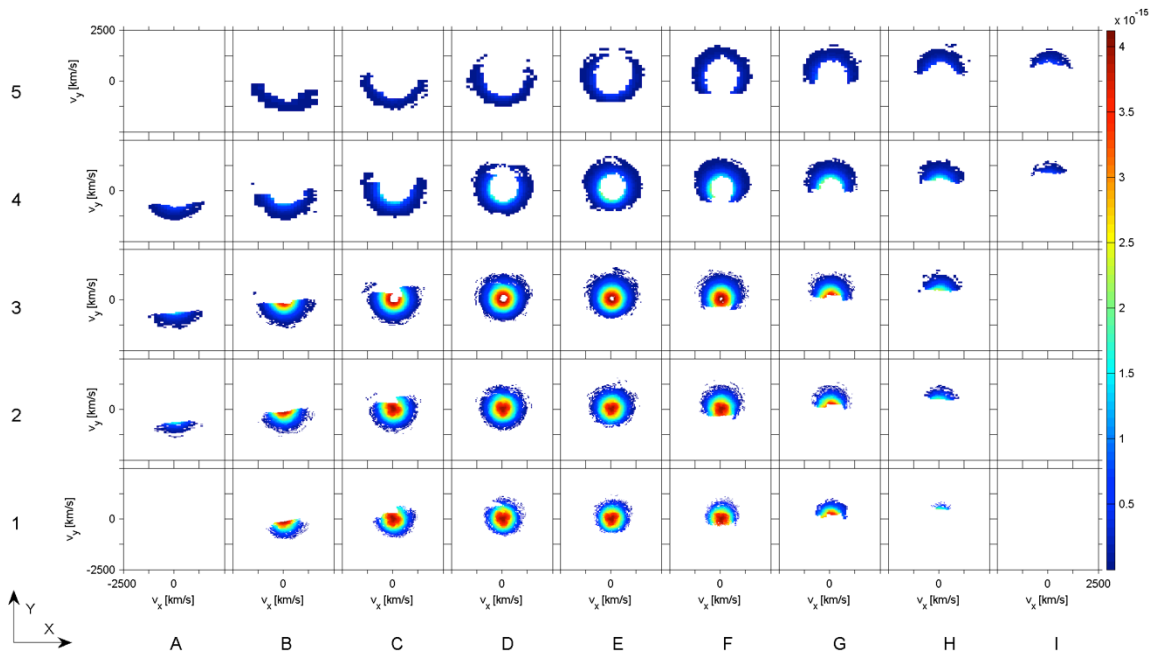


Figure 1.10 – Projection in the space of perpendicular velocities, for $v_z=0$, of the Liouville mapped velocity distribution functions of protons in the cloud at $t=225$ seconds. The spatial bins are defined in **Figure 1.9**. A drifting Maxwellian VDF is obtained in the core of the cloud, in bins D1–F1, D2–F2. Ring-shaped VDFs are obtained close to the edges of the cloud, bins D4–F4, E5–F5. Crescent-like VDF are obtained close to the trailing and leading edges, A2–A4, B4–B5, C4–C5, G4–G5, H4–H5, I4–I5.

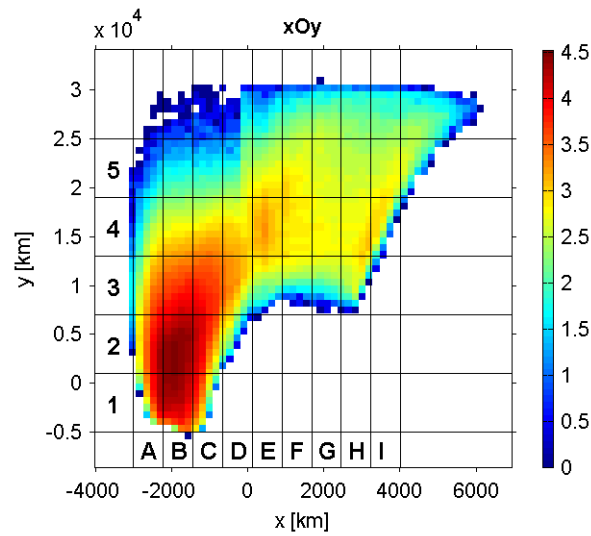


Figure 1.11 – Distribution of protons in the xOy plane after 275 seconds ($\sim 125T_L$) from injection in the electromagnetic field illustrated in **Figure 1.6**. This snapshot illustrates the initial stage of the interaction between the proton cloud and the region of the most rapid variation of B ; some parts of the cloud intersected the plane $x=0$ where $B=0$. The local value of the number density is color coded. The spatial mesh on which the VDF is reconstructed is also shown.

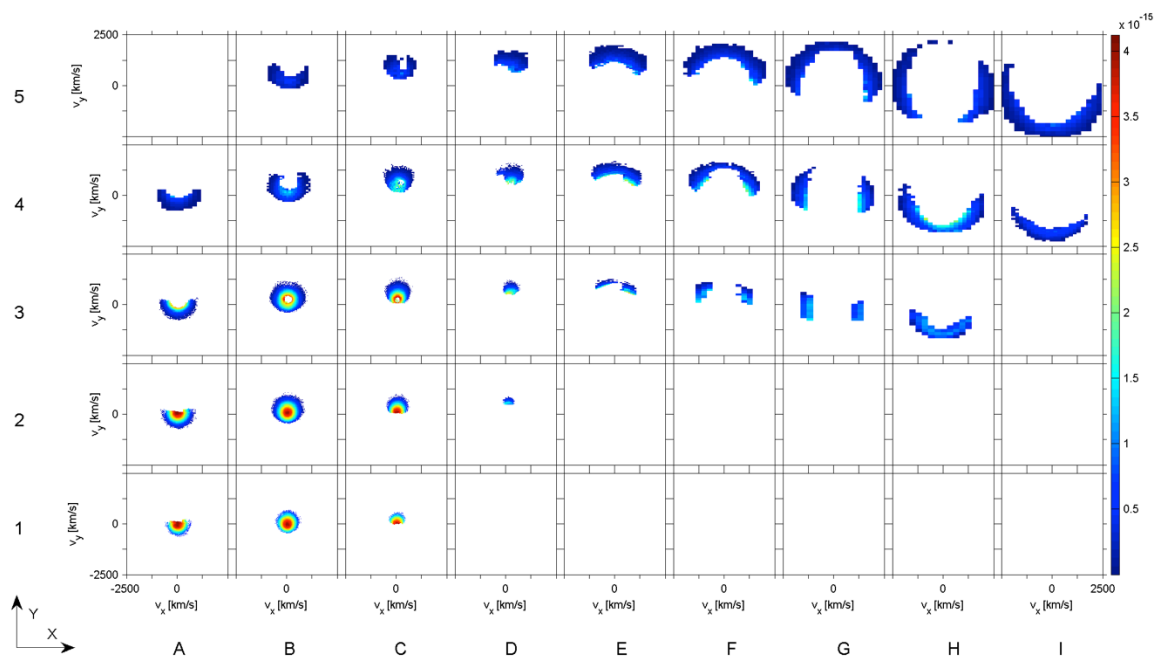


Figure 1.12 – Projection in the space of perpendicular velocities, for $v_z=0$, of the Liouville mapped velocity distribution functions of protons in the cloud at $\Delta t=275$ seconds. The spatial bins are defined in **Figure 1.11**. During this initial stage of the interaction of the cloud with the discontinuity one identifies the Maxwellian core of the cloud (bins B1–B2) and non-gyrotropic VDFs at the leading edge (e.g. bins D5–I5).

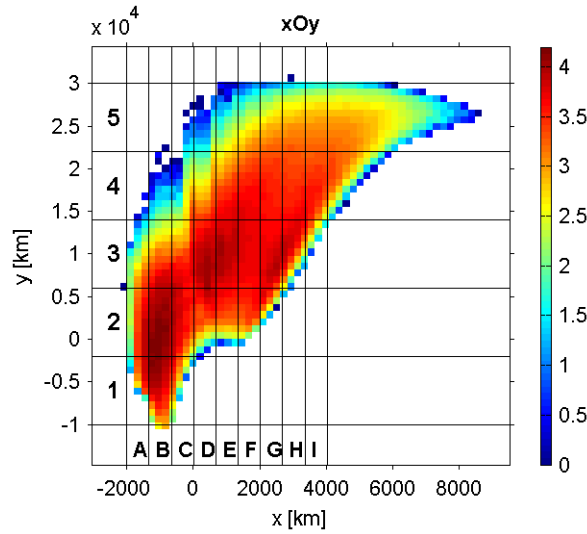


Figure 1.13 – Distribution of protons in the xOy plane after 300 seconds ($\sim 135T_L$) from injection in the electromagnetic field illustrated in **Figure 1.6**. The local value of the number density is color coded. The spatial mesh on which the VDF is reconstructed is also shown. The figure illustrates a later stage of the interaction between the cloud and the central region of the discontinuity where the magnetic field vanishes. A significant number of protons moved in the region of positive B_z .

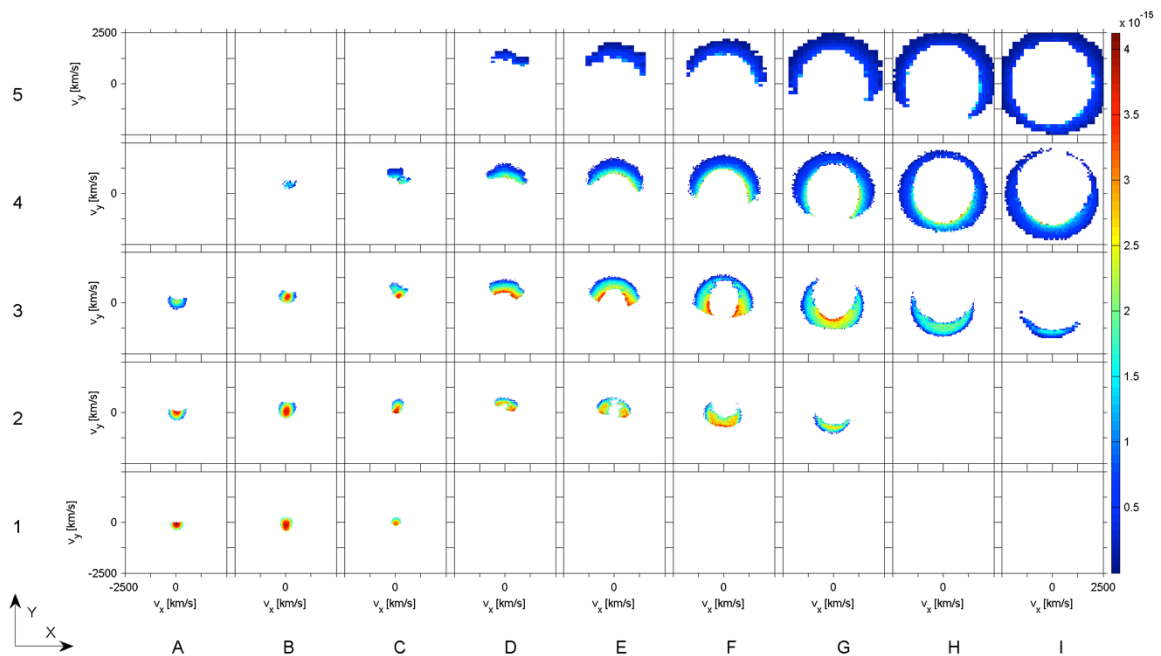


Figure 1.14 – Projection in the space of perpendicular velocities, for $v_z=0$, of the Liouville mapped velocity distribution functions of protons at $\Delta t=300$ seconds. The spatial bins are defined in **Figure 1.13**. We note that in the region of positive B_z the VDFs of protons are ring-shaped (bins G4–I4, H5–I5) or crescent-like (bins G3–I3, E5–G5).

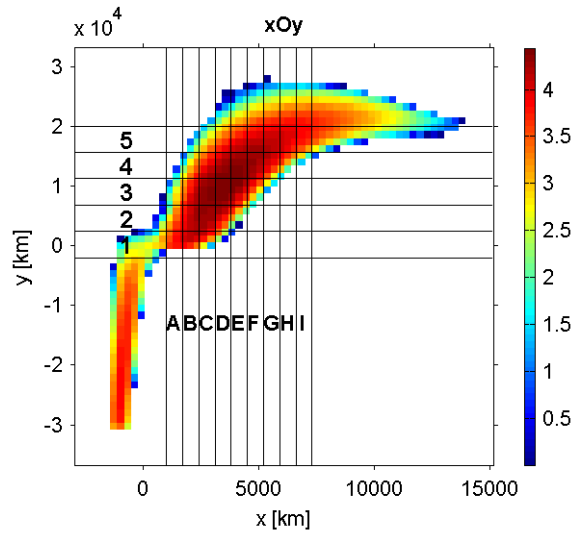


Figure 1.15 – Distribution of protons in the xOy plane after 350 seconds ($\sim 160T_L$) from injection in the electromagnetic field illustrated in **Figure 1.6**. The local value of the number density is color coded. The spatial mesh on which the VDF is reconstructed is also shown. One notes the splitting of the cloud into two populations: population P1 that does not cross the surface where $B=0$ and remains trapped in some region on the left side of the discontinuity ($x < 0$) and respectively population P2 that penetrates into the right side of the magnetic discontinuity. At later stages the two populations disconnect. In the reminder of the paper we follow only P2.

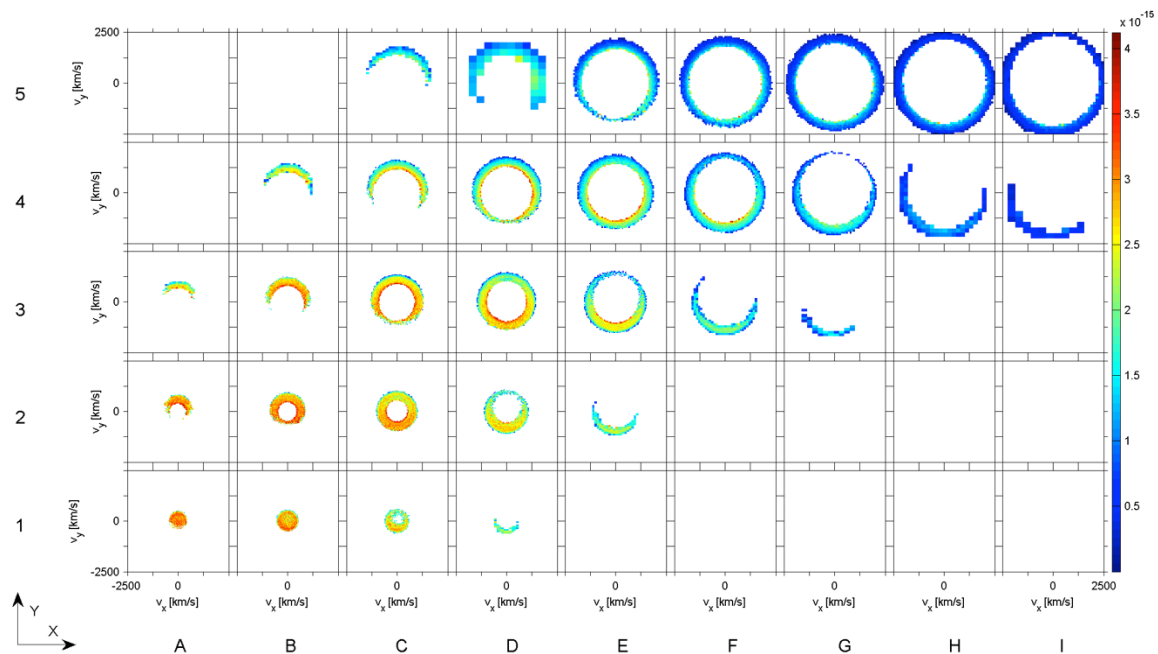


Figure 1.16 – Projection in the space of perpendicular velocities, for $v_z=0$, of the Liouville mapped velocity distribution functions of protons in the cloud at $\Delta t=350$ seconds. The spatial bins are defined in **Figure 1.15**. Only VDFs of the P2 population are shown. Ring-shaped and crescent-like VDFs are observed in the large majority of spatial bins.

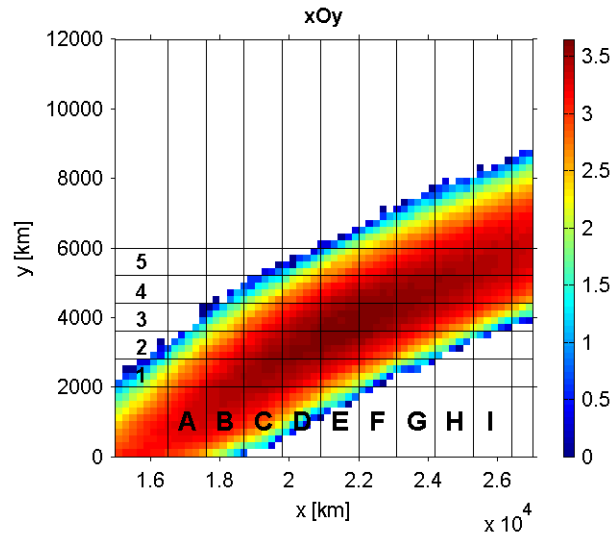


Figure 1.17 – Distribution of protons of the population P2 in the xOy plane after 600 seconds ($\sim 270T_L$) from injection in the electromagnetic field illustrated in **Figure 1.6**. The local value of the number density is color coded. The spatial mesh on which the VDF is reconstructed is also shown. The protons move in a region of uniform magnetic and electric field, on the right side of the discontinuity.

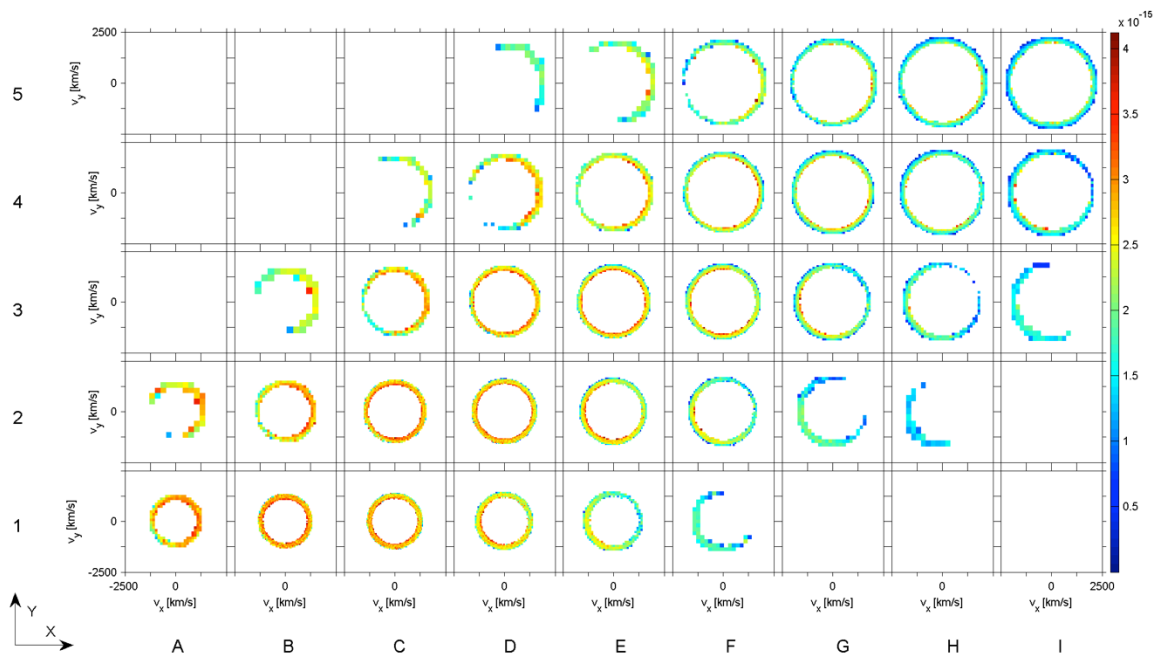


Figure 1.18 – Projection in the space of perpendicular velocities, for $v_z=0$, of the Liouville mapped velocity distribution functions of protons in the cloud at $\Delta t=600$ seconds. The spatial bins are defined in **Figure 1.17**. All the VDFs obtained for this stage of propagation are either ring-shaped or crescent-like, a signature of the interaction of the cloud with the region of magnetic field gradient.

An additional key feature associated with the same physical process is the formation of a velocity-dispersion structure at the edges of the cloud. Since grad-B drift displaces most efficiently the particles with higher thermal velocities, the outer edges of the proton cloud/beam are populated by the particles with the highest energies. Thus, the kinetic energy of the protons decreases from the outer layers towards the core of the cloud. This velocity dispersion is revealed for instance by the VDFs in bins F5, F4, F3, F2, F1 of Figure 1.10. Our simulations results suggest a mechanism to explain the formation of velocity-dispersed ion structures based on the gradient-B drift that can imprint energy-dispersed features in regions close to the boundaries of spatially confined plasmas. This mechanism is additional to the ones proposed in the literature (e.g. *Zelenyi et al.*, 1990; *Keiling et al.*, 2004; *Sauvaud and Kovrazhkin*, 2004).

The kinetic properties of the front-side and trailing edge of the proton cloud show interesting additional kinetic features. The proton velocity distribution function is non-gyrotropic in these regions and it has a crescent shape with increased phase density in certain areas of the perpendicular velocities space. This effect is seen, for instance, in bins A3, A4, H2-H5 of Figure 1.10, A3, A4, H3, H4, I4 and I5 of Figure 1.12, A2, A3, H3 and I3 of Figure 1.14, A2, A3, D1, E2, F3, G3, H4, I4 of Figure 1.16. These crescent-like shaped VDFs observed at the front and trailing edges of the cloud are an effect due to the remote sensing of the protons with guiding centers localized in the interior of the cloud and whose Larmor radius is large enough to enable the orbit to penetrate along x in regions behind and ahead of the bulk of the cloud. For example, most of the particles localized in bins D1, E2, G3 and I4 from Figure 1.16 have a negative gyration velocity v_y due to the clockwise gyration of protons in the positive B-field. At the same time the particles in bins A3, B4, C5 shown in Figure 1.16 have a positive gyration velocity v_y due also to the clockwise gyration. Therefore, the gyro-phase restricted effect observed at the front-side and trailing edge region can be associated with the remote sensing of particles whose guiding centers pertain to the interior of the cloud. Similar conjectures have been made by *Lee et al.* (2004) for in-situ data from the magnetospheric tail and by *Meziane et al.* (2003) for high energy ions near the terrestrial foreshock.

1.4.3 Case II: Parallel magnetic field and uniform electric field

In order to confirm the findings on the effects of the gradient-B drift on the formation of ring-shaped and non-gyrotropic velocity distribution functions, we carried out additional test-kinetic simulations. We use a unidirectional, non-uniform and increasing magnetic field and a uniform electric field. The magnetic field is everywhere parallel to the positive z -axis and its magnitude increases from 30 to 90 nT without changing of sign. The electric field is computed as a convection field determined by the orientation and the magnitude of the asymptotic magnetic field \vec{B}_1 and the bulk velocity \vec{V}_0 of plasma on the left side of the transition region:

$$\vec{E} = \vec{B}_1 \times \vec{V}_0 = \text{const.} \quad (1.14)$$

Thus, in this case the electric field is everywhere parallel to the positive y -axis. The input parameters assumed for this simulation are given in Table I. The positions of the test-protons in the xOy plane, at the end of the simulation, are shown in Figure 1.19. The local number density is color coded and represented on a spatial mesh of 80×80 bins.

In Figure 1.19 it is shown that the protons are scattered in the direction of the gradient-B drift, i.e. the positive y -axis. Figure 1.20 illustrates the spatial variation of the velocity distribution function of protons. The spatial resolution used to compute the VDF is equal to 150 km along x -direction and 3000 km along y -direction. The results show that ring-shaped VDFs similar to the ones obtained in case I are obtained in bins D3, D4, E3, E4, F3 and F4. The size of the central cavity formed in the perpendicular velocities space increases as we approach to the upper edge of the cloud. Crescent-like, non-gyrotopropic distribution functions are obtained on the front and trailing edge of the cloud, similar to case I (see for instance the VDFs corresponding to the bins I1 to I5 and to the bins A1 to A5). The results obtained in case II, for a parallel magnetic field and a uniform electric field confirm the role of the gradient-B drift on the formation of non-Maxwellian distribution functions. They also demonstrate that the kinetic effects found with these simulations are not dependent on a particular configuration of the electric and magnetic fields.

The simulations discussed here are based on input parameters (velocity distribution functions, magnetic field) consistent with experimental data from the terrestrial magnetosphere and emphasize the role of the gradient-B drift at sharp transitions to contribute to the formation of non-Maxwellian distribution functions (ring-shaped and crescent-like) as those observed by Cluster in the plasma sheet.

The velocity distribution functions obtained numerically show similarities with those observed experimentally by Cluster satellites in the terrestrial magnetotail. We compared the proton velocity distribution functions measured by Cluster CIS instruments and shown in Figure 1.5, with the proton velocity distribution functions computed numerically using our test-kinetic approach and illustrated in Figure 1.16 and Figure 1.20, and found relevant similarities. Both measured and computed VDFs have cavities in the central region of the perpendicular velocities space, like those illustrated by the left and middle panels of Figure 1.5 and respectively by the VDFs corresponding to the spatial bins C2 and D3 from Figure 1.16. In our simulations the central cavity results from of a physical process related to the spatial dispersion of particles due to the gradient-B drift and is not due to an ad-hoc low energy cut-off imposed onto the initial velocity distribution function of the test-particles. On the other hand, crescent-like, non-gyrotopropic VDFs are revealed by satellite data (right panel from Figure 1.5) and also by our simulated data (e.g. bins E2 and G3 from Figure 1.16, or bins H4-H5 and I4-I5 from Figure 1.20). This kinetic effect is a consequence of the remote sensing, in regions outside the cloud, of particles whose guiding centers are found inside the cloud.

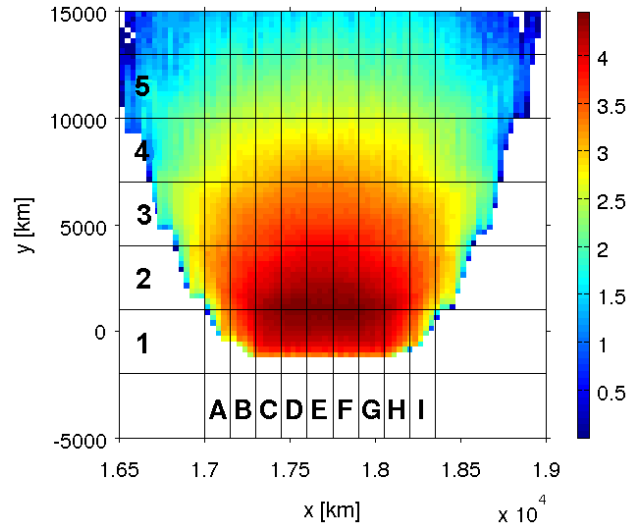


Figure 1.19 – Distribution of protons in the xOy plane after 360 seconds ($\sim 160T_L$) from injection on the left side in the case of a unidirectional, non-uniform, parallel magnetic field and a uniform electric field. The local value of the number density is color coded. The spatial mesh on which the VDF is reconstructed is also shown. The deformation of the shape of the cloud is due to the gradient-B drift.

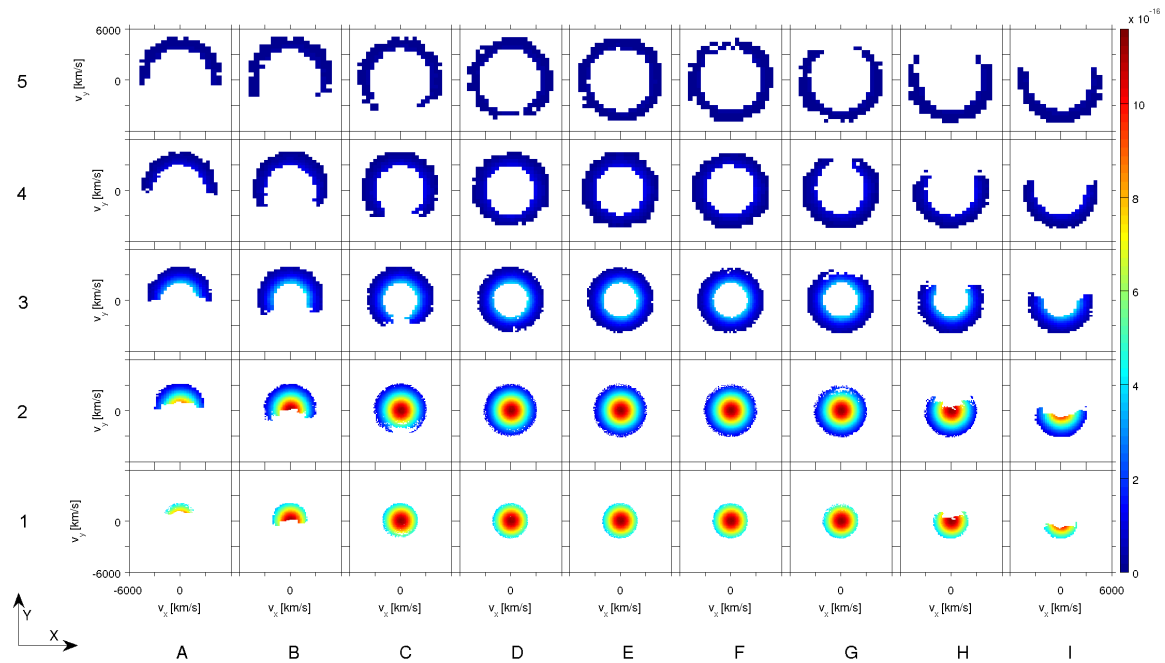


Figure 1.20 – Projection in the space of perpendicular velocities, for $v_z=0$, of the Liouville mapped velocity distribution functions of protons in the cloud at $\Delta t=600$ seconds for a parallel magnetic field and a uniform electric field. Spatial bins are defined in **Figure 1.19**. Note the formation of the central cavity due to the gradient-B drift in bins of the upper three rows; non-gyrotropic VDFs are obtained in bins from the column A, B, C, G, H and I.

1.5 Comparison between forward and backward results

In the following, we compare the velocity distribution functions computed at $t=225$ seconds with both forward and backward Liouville approaches. Nine spatial bins have been selected in order to reconstruct the velocity distribution function with the two approaches. In Figure 1.21 we illustrate the number density of the test-protons in the xOy plane, perpendicular to the magnetic field, at $t=225$ s, together with the nine spatial bins considered; Figure 1.21 represents a zoom in Figure 1.9.

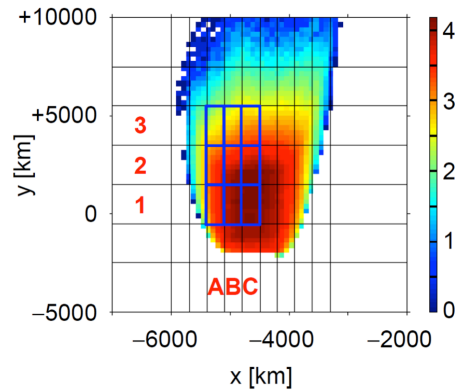


Figure 1.21 – Proton density distribution in the xOy plane, perpendicular to the magnetic field, at $t=225$ s ($\sim 100T_L$) obtained with the forward approach. The local number density is color coded using a 2D mesh of 60×60 cells. The blue rectangles indicate the spatial bins used to compute the VDF shown in **Figure 1.22**.

The velocity distribution function of protons computed at $t=225$ seconds using the forward approach is shown in Figure 1.22. The VDF inside the cloud is computed for each bin defined by the blue rectangles in the xOy plane and identified by the combination of letters (columns) and numbers (rows) in Figure 1.21. The corresponding velocity distribution functions obtained using the backward approach are shown in Figure 1.23. The VDF is computed for the central point of each spatial bin defined by the blue rectangles in the xOy plane illustrated in Figure 1.21.

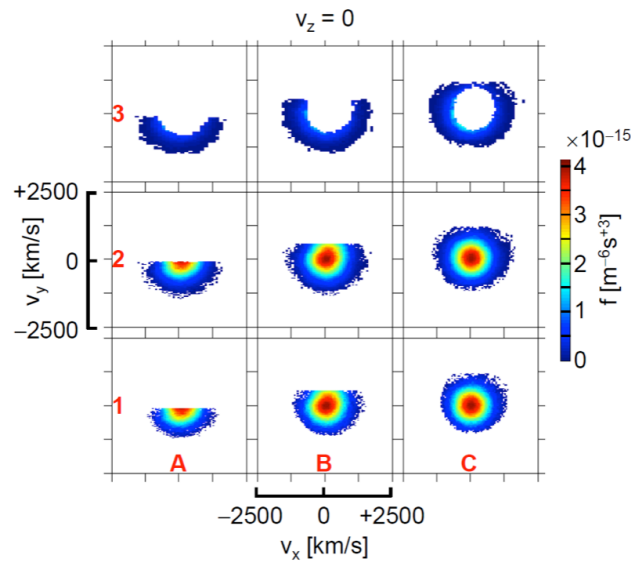


Figure 1.22 – Velocity distribution functions obtained at $t=225$ s ($\sim 100T_L$) using the forward approach in the spatial bins indicated by blue rectangles in **Figure 1.21**. The plots correspond to $v_z=0$ cross-sections.

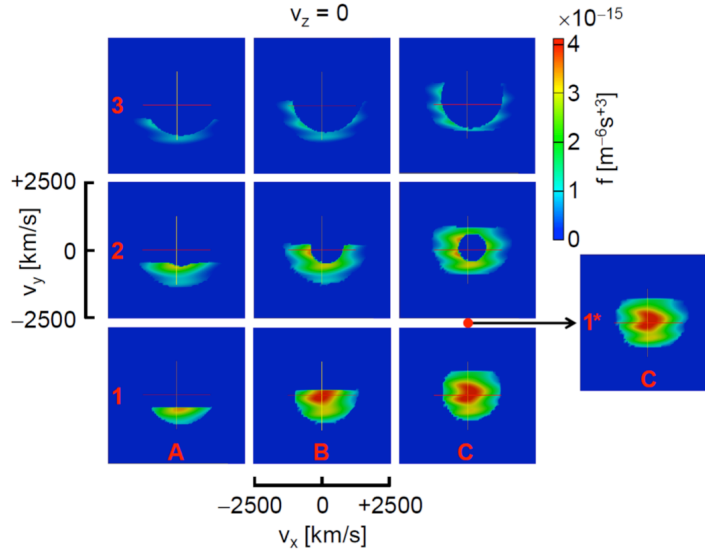


Figure 1.23 – VDFs obtained at $t=225 \text{ s}$ ($\sim 100T_L$) using the backward approach for the central points of the bins indicated by blue rectangles in **Figure 1.21**. C1* is the middle point between C1 and C2.

There are significant differences between the forward and backward approaches as illustrated by Figure 1.22 and Figure 1.23. Nevertheless, the velocity distribution function, f , has the same variation tendency in both cases, i.e. (i) it is ring-shaped close to the upper boundary (i.e. for larger y -values) while in the center is approximately Maxwellian (comparing, for instance, f corresponding to C1 and C3 in Figure 1.22 and Figure 1.23) and (ii) the anisotropy of the velocity distribution function is more pronounced close to the trailing edge of the cloud (i.e. for smaller x -values) than in the center (for example, comparing f for A2 and B2 in Figure 1.22 and Figure 1.23). The explanation for the differences observed is related to the different methods used to compute the distribution function with forward and backward approaches. In the forward approach f is sampled over a spatial bin whose size is defined such that it contains a large enough number of particles and the statistical error resulting from sampling is minimized. On the other hand, in the backward approach the computation of f for a precise point in configuration space is free from statistical errors; in our case, f is computed for the central point of each spatial bin defined for the forward method. The strength of the backward approach is related to its ability to produce detailed velocity distribution functions at precise locations without statistical sampling errors. The essential difference between the forward and backward approaches is that the former necessarily relies on spatial binning and sampling, while the latter can be calculated at precise locations in space. In many cases, the backward approach can lead to filamentary structures in velocity (or momentum) space, while such structures are always attenuated in the forward approach, owing to the spatial averages involved. In contrary to the backward approach, the forward Liouville approach enables the computation of both the velocity distribution function and general dynamics of the particle cloud while advancing an initial distribution of particles into a non-uniform configuration of the magnetic and electric fields. Thus, the strength of the forward approach is related to its ability to investigate the evolution of a specific plasma source.

A solution to eliminate these differences and to obtain comparable distribution functions would involve spatial averages of f by a proper quadrature scheme applied in the backward approach. For that purpose, the velocity distribution function obtained using the backward approach is numerically integrated over a rectangular domain in the xOy plane corresponding to the spatial bin used to compute the distribution function using the forward approach. The resulting averages are presented in Figure 1.24 for each bin defined by the blue rectangles in the xOy plane (see Figure 1.21). The averages are computed by the trapezoidal integration rule with 10×10 points applied in each spatial bin. The resulting averaged distribution functions are closer to those given by the forward approach, as expected. Nevertheless, there are still some notable differences particularly for bins B2 and C2 (see Figure 1.24). These two bins are localized in a region characterized by a pronounced spatial variation of the velocity distribution function, as can be seen from Figure 1.23 by comparing f for C1* and C2 (C1* is the middle point between C1's and C2's centres). On the other hand, the results obtained for bin C1 using both forward and backward approaches are very similar since the spatial variation of the distribution function for that region is smooth (see f for C1 and C1* in Figure 1.23). The differences observed for the bins localized in regions with sharp spatial variation of the VDF can be explained by analyzing in more detail the sampling method of the forward approach and the averaging method of the backward approach. In order to better understand the differences between the two, a schematic representation is shown in Figure 1.25 and Figure 1.26.

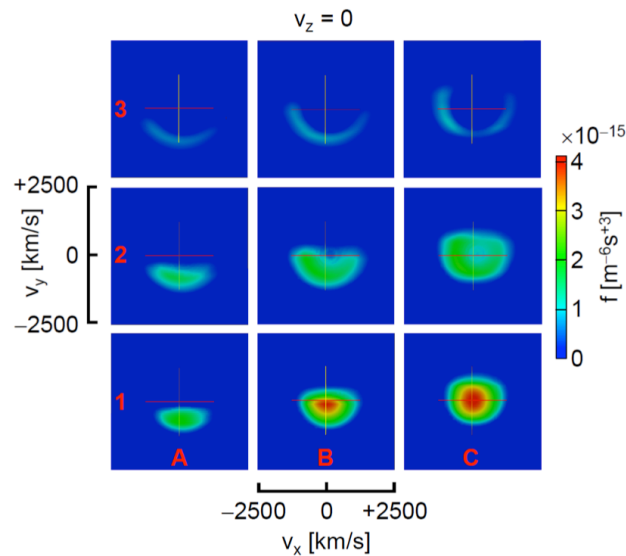


Figure 1.24 – Velocity distribution functions obtained at $t=225$ s ($\sim 100T_L$) with the backward approach by averaging over the spatial bins indicated with blue rectangles in **Figure 1.21**.

Let us consider the problem of calculating the velocity distribution function for a spatial bin that is localized in a region of the configuration space characterized by a steep spatial variation of f along Oy direction. The VDF is computed using both forward and backward approaches; for the latter approach, the averaging method is used. We divide the spatial bin in two areas, A and B, characterized by two distinct velocity distribution functions, as shown in Figure 1.25 and Figure 1.26. In area A the velocity

distribution function is the inner core of a Maxwellian distribution function, f_A , while in area B we retrieve the outer shell of the same Maxwellian distribution, f_B .

For simplicity, let us assume that f does not vary significantly in either A or B. By using the forward approach, the particles localized in the both areas A and B will have the velocities distributed according to their respective velocity distribution functions. Thus, the less energetic particles will be found in area A, while the most energetic ones will be found in area B (see Figure 1.25). This simplified model corresponds roughly to our simulation results. All particles localized inside the entire spatial bin will be distributed in velocity space as follows. Particles originating from area A, i.e. the less energetic ones, will be found in the central regions of velocity space, while particles originating from area B, i.e. the most energetic ones, will be found in the outer regions of velocity space.

In order to reconstruct the velocity distribution function by using the forward approach, a uniform grid in velocity space is defined. For each velocity bin j centred in \vec{v}_j , the corresponding distribution function $f_{\text{FWD}}(\vec{v}_j)$ is computed by averaging over all numerical values “attached” to each particle i localized inside the considered bin:

$$f_{\text{FWD}}(\vec{v}_j) = \frac{1}{n_j} \sum_{i=1}^{n_j} f_j^i(\vec{v}_j^i) \quad (1.15)$$

where \vec{v}_j^i is the velocity of particle i localized inside the velocity bin j and n_j is the total number of particles inside bin j . Among these n_j particles, let n_j^A be the ones from area A and n_j^B those from area B such that $n_j = n_j^A + n_j^B$. Thus, equation (1.15) becomes:

$$f_{\text{FWD}}(\vec{v}_j) = \frac{1}{n_j} \left(\sum_{i_A=1}^{n_j^A} f_j^{i_A}(\vec{v}_j^{i_A}) + \sum_{i_B=1}^{n_j^B} f_j^{i_B}(\vec{v}_j^{i_B}) \right) \quad (1.16)$$

where $f_j^{i_A}(\vec{v}_j^{i_A}) = f_A(\vec{v}_j^{i_A})$, since all i_A particles are localized inside area A and likewise $f_j^{i_B}(\vec{v}_j^{i_B}) = f_B(\vec{v}_j^{i_B})$, as all i_B particles belongs to area B. Furthermore, we consider that all velocity bins are small enough such that $f_A(\vec{v}_j^{i_A}) = f_A(\vec{v}_j)$ and $f_B(\vec{v}_j^{i_B}) = f_B(\vec{v}_j)$. In this way, f computed using the forward approach for the velocity bin centred on \vec{v}_j is:

$$f_{\text{FWD}}(\vec{v}_j) = \frac{n_j^A}{n_j} f_A(\vec{v}_j) + \left(1 - \frac{n_j^A}{n_j} \right) f_B(\vec{v}_j) \quad (1.17)$$

In order to compute the velocity distribution function using the backward approach, we define a uniform grid in configuration space having $n \times n$ points that cover the entire area of the spatial bin to be sampled (see Figure 1.26). For each velocity vertex j centred in \vec{v}_j , the corresponding distribution function $f_{\text{BWD}}(\vec{v}_j)$ is computed by averaging over all numerical values f_j^i “attached” to each point i of the spatial grid:

$$f_{\text{BWD}}(\vec{v}_j) = \frac{1}{n^2} \sum_{i=1}^{n^2} f_j^i(\vec{v}_j) \quad (1.18)$$

Considering that m grid points are localized inside area A, while the other n^2-m grid points are localized inside area B, equation (1.18) becomes:

$$f_{\text{BWD}}(\vec{v}_j) = \frac{1}{n^2} \left(\sum_{i_A=1}^m f_j^{i_A}(\vec{v}_j) + \sum_{i_B=m+1}^{n^2} f_j^{i_B}(\vec{v}_j) \right) \quad (1.19)$$

where $f_j^{i_A}(\vec{v}_j) = f_A(\vec{v}_j)$, since all i_A grid points are localized inside area A, and similarly $f_j^{i_B}(\vec{v}_j) = f_B(\vec{v}_j)$. Therefore, f computed using the backward approach for the velocity bin centred on \vec{v}_j is given by:

$$f_{\text{BWD}}(\vec{v}_j) = \frac{m}{n^2} f_A(\vec{v}_j) + \left(1 - \frac{m}{n^2} \right) f_B(\vec{v}_j) \quad (1.20)$$

We should mention that the average value (1.20) has been obtained simply by computing the arithmetic mean of all n^2 function's values instead of integrating the velocity distribution function over the entire spatial bin using a 2D trapezoidal integration rule, as it is done in our simulations. Also, we considered a uniform grid in velocity space for the backward approach, while in our simulations an unstructured grid has been used to compute the velocity distribution function. These simplifications should not have major consequences on the final results.

In order to compare the velocity distribution functions obtained from both forward and backward approaches we considered three representative velocity bins, designated a , b and c and centred at \vec{v}_a , \vec{v}_b and \vec{v}_c (see Figure 1.25 and Figure 1.26), to compute the numerical values of f given by equations (1.17) and (1.20). These three velocity bins have been chosen such that: $f_A(\vec{v}_a) \neq 0$ and $f_B(\vec{v}_a) = 0$, $f_A(\vec{v}_b) = f_B(\vec{v}_b) \neq 0$, while $f_A(\vec{v}_c) = 0$ and $f_B(\vec{v}_c) \neq 0$. Therefore, from equations (1.17) and (1.20), we obtain the values of f computed with both forward and backward approaches for velocity bins a , b and c . The results are given in Table 1.2 and show that the velocity distribution function given by the backward approach is smaller than the one obtained from the forward approach for velocity bins a and c , while for bin b both values are equal.

Table 1.2 – Values of f obtained with both forward and backward approaches for three selected velocity bins centered at a , b and c .

| \vec{v}_j | $f_{\text{FWD}}(\vec{v}_j)$ | $f_{\text{BWD}}(\vec{v}_j)$ |
|-------------|-----------------------------------|--|
| \vec{v}_a | $f_A(\vec{v}_a)$ | $\frac{m}{n^2} f_A(\vec{v}_a) < f_A(\vec{v}_a)$ |
| \vec{v}_b | $f_A(\vec{v}_b) = f_B(\vec{v}_b)$ | $f_A(\vec{v}_b) = f_B(\vec{v}_b)$ |
| \vec{v}_c | $f_B(\vec{v}_c)$ | $\left(1 - \frac{m}{n^2} \right) f_B(\vec{v}_c) < f_B(\vec{v}_c)$ |

By applying this algorithm to all velocity space bins, a Maxwellian distribution function is obtained with the forward approach, as can be seen in Figure 1.25. However, f obtained with the backward approach presents a cavity in the central region of velocity

space, as can be seen in Figure 1.26. Similar results are obtained, for instance, for bin C2 of our simulations depicted in Figure 1.22 and Figure 1.24, which is localized in a region characterized by a steep spatial variation of the velocity distribution function. Indeed, with the forward approach a Maxwellian distribution is obtained for bin C2, while with the backward approach the distribution function is characterized by a central cavity in velocity space. Thus, the simplified model described in Figure 1.25 and Figure 1.26 explains the differences obtained between forward and backward approaches in spatial regions characterized by sharp gradients of f .

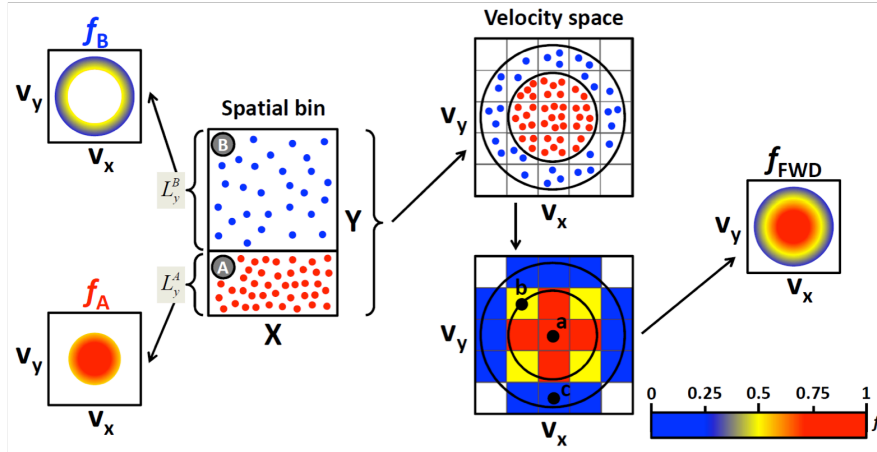


Figure 1.25 – Schematic diagram illustrating the sampling method used to compute the velocity distribution function with the forward Liouville approach.

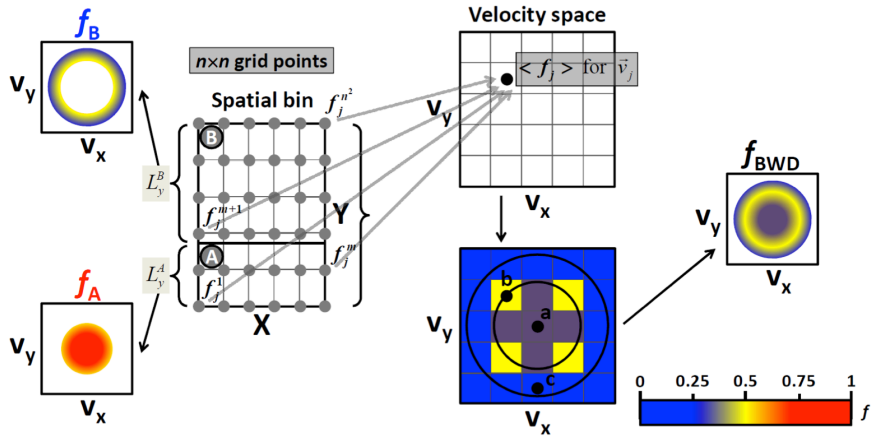


Figure 1.26 – Schematic diagram illustrating the averaging method used to compute the velocity distribution function with the backward Liouville approach.

The velocity distribution functions given by equation (1.17), for the forward approach, and (1.20), for the backward approach, have similar mathematical expressions except for the weight coefficients of f_A and f_B . In the forward approach the weight coefficients are expressed in terms of n_j^A/n_j , i.e. the ratio of the number of particles localized inside velocity bin j and pertaining to spatial area A to the total number of particles localized inside velocity bin j . In the backward approach the weight coefficients are expressed in terms of m/n^2 , i.e. the ratio of grid points number localized

inside area A to total number of grid points localized inside the entire spatial bin. By analyzing the n_j^A/n_j ratio we can conclude that this quantity depends on the position of bin j in velocity space. On the other hand, m/n^2 is equal to the ratio of region A area to entire spatial bin area, which is independent on the position of bin j in velocity space:

$$\frac{m}{n^2} = \frac{\text{Area}(A)}{\text{Area}(\text{bin})} = \frac{L_y^A}{L_y} \quad (1.21)$$

where L_y^A indicates the width of area A along the y-axis, while L_y represent the width of the entire spatial bin. Thus, the weight coefficients corresponding to forward and backward distribution functions are not equal in general and the results provided by the two approaches may also be different, independently of the number of particles injected in the forward simulations or the number of grid points used in the averaging scheme for the backward simulations.

The main point that distinguishes the averaging method (1.20) from the sampling method (1.17) is that, in the backward approach, to a given point in velocity space correspond n^2 points in the configuration space that cover the entire area of the spatial bin. In the forward approach however, a given bin in velocity space may originate from only a subset of points in configuration space localized in a certain area of the spatial bin. Therefore, in order to calculate the numerical value of the distribution function at a certain bin in velocity space, the backward averaging method (1.20) will take into account the contribution from the entire spatial bin, while the forward sampling method (1.17) will take into account the contribution of only a part of the considered spatial bin, thus possibly leading to different results. Nevertheless, f_{FWD} given by equation (1.17) would be equal to f_{BWD} given by equation (1.20) if $m=n^2$. This condition is satisfied if we increase the size of region A such that it will cover the entire area of the spatial bin. Only in this case n_j^A/n_j will also be equal to n_j for all velocity space bins and the weight coefficients corresponding to forward and backward distribution functions will be equal. Therefore, by increasing the size of area A it is possible to obtain converging results with both approaches as long as the initial assumption is satisfied, i.e. there are no significant spatial variations of f along area A. We should note that this assumption will always be satisfied for region B since the size of this area continually decreases, as the size of A increases. Indeed, in the simplified model described in Figure 1.25 and Figure 1.26 we keep the total area of the bin, i.e. $\text{Area}(A)+\text{Area}(B)$, constant. Therefore, if we increase the area of A, the area of B will decrease accordingly such that the total area of the bin to remain unchanged. In this case, since the area of B is decreasing, there will be no significant spatial variations of f along that region and the initial assumption is fulfilled.

This result can be generalized for three-dimensional bins with spatial variations of the velocity distribution function along all three coordinate axes. In this case the forward and backward approaches will return similar results only for those spatial bins which are small enough such that the following inequality to be satisfied simultaneously along all three coordinates axes:

$$L_i \cdot \left| \frac{\partial f}{\partial x_i} \right| \ll f \quad (1.22)$$

where $i = 1, 2, 3$ for the x, y, z axes respectively. On the other hand, with bins covering regions of configuration space characterized by sharp spatial gradients of f , the forward and backward approaches will generally provide different results.

1.6 Conclusions

In the first chapter of my thesis I have imagined a configuration of the electromagnetic field that enables the investigation of the dynamics of a proton cloud/beam injected across sheared electric and magnetic fields. The parallel component of the electric field is everywhere equal to zero and the perpendicular component is computed by solving Laplace's equation on a two-dimensional rectangular grid (case I) or is constant and uniform (case II). We analysed the individual motion of particles and the Liouville mapping of an initial velocity distribution function of the protons. The test-particles move across regions with sharp variations of a sheared antiparallel (case I) or parallel (case II) magnetic field. The global dynamics of the cloud is asymmetric due to the gradient of B drift that is oriented in the $+Oy$ direction. The asymmetry is imprinted on the cloud morphology while it traverses the transition region. However, the cloud remains asymmetric at large distances from the magnetic transition region, in the region of uniform field.

The asymmetry of the cloud is retrieved in its kinetic structure. Indeed, the layer formed at the outer edge of the cloud, in the positive y -direction perpendicular to the bulk velocity and magnetic field, is populated by particles whose velocities varies with the distance from the cloud's core, forming an energy-dispersed structure. This kinetic feature is obtained in both simulations, case I and II, when the magnetic field profile is parallel and antiparallel. The test-kinetic simulations illustrate that the energy of the particles increases towards the fringe of the cloud. We have shown that this effect is due to the gradient-B drift that efficiently disperses protons in the $+Oy$ direction, proportionally to their kinetic energy.

The reconstruction of the velocity distribution function shows the formation of a central cavity in the space of the perpendicular velocities. Such ring-shaped distribution functions are obtained in spatial bins localised close or within the outer energy-dispersed layer. Since the particles with a smaller thermal energy are less deflected they populate mainly the core of the cloud at lower y -coordinates where the velocity distribution function is close to a Maxwellian. On the front-side and in the trailing edge of the cloud the velocity distribution function is non-gyrotropic and has a crescent like shape in some of the spatial bins. This anisotropy is an effect due to the remote sensing of particles whose guiding centers pertain to the inner cloud.

One of the advantages of the forward Liouville approach is that it enables the investigation of the VDFs and also gives an idea of the general dynamics of the cloud while convecting in the non-uniform field configuration. A disadvantage of the forward method is that the velocity distribution function is reconstructed for spatial bins with rather coarse dimensions imposed by the total number of simulated particles.

The main conclusions of our study do not necessarily depend on the particular profile of the electric field nor on the existence of a mechanism able to inject clouds of ions in the neutral sheet. This is confirmed by the results obtained in case II where the electric field is uniform. Our simulations have been performed for a configuration that reproduces some typical parameters for the terrestrial plasma sheet investigated previously by *Lee et al. (2004)* and *Wilber et al. (2004)*. In our simulations, however, we introduce an electric field and a finite sized cloud of test-particles. A possible origin of the electric field treated in our simulations may be the launching of bursty bulk flows (BBFs) in the plasma sheet and considering their propagation across the neutral sheet (*Liu, 2001*), or the ballooning instability (*Pritchett and Coroniti, 1999*), or the propagation of bubbles in the geomagnetic tail related also to BBFs formation (*Birn et al., 2004*). Testing of any of these mechanisms is beyond the scope of this work. But in all the three scenarios mentioned above a localised perturbation of the dawn-dusk, cross-tail, electric field is observed and can be considered a possible source for the prescribed electric field used in simulations.

Although we did not show the projections of the VDFs in the plane of velocities including the parallel direction, the phase space density is equally distributed in the parallel and anti-parallel direction of the magnetic field. The proton cloud expands along the magnetic field lines due to the parallel velocity component assigned initially. In a realistic magnetospheric configuration the particles with the larger positive parallel velocities moving along B , populating the upper half of the cloud, will be reflected by the mirror force at some ionospheric altitude and will travel back thus filling some regions of the negative parallel velocity space.

The formation of the energy-dispersed structure and of the ring-shaped velocity distribution function is a kinetic effect obtained at the edges of a localized plasma cloud. In a magnetotail geometry when the cloud/stream moves in the z_{GSE} direction, the B-field being mainly along the x_{GSE} , the ring-shaped VDFs and the energy-dispersed structure will be observed at the lateral edges in the y_{GSE} direction. Thus, the localization of the non-Maxwellian velocity distribution functions and possibly their properties would depend on the local magnetic field and the global geometry of the cloud itself. In a future study we shall investigate in detail this relationship.

The test-kinetic simulations discussed in the first chapter of my thesis suggest a physical mechanism that can explain the formation of an energy-dispersed structure at the edges of a proton beam interacting with a non-uniform electromagnetic field. We have also identified kinetic effects contributing to the formation of ring-shaped and non-gyrotropic velocity distribution functions. Although these results are obtained for two prescribed configurations of the electromagnetic field their relevance is more general.

Our study emphasizes the role of the gradient-B drift on the edges of plasma structures; the gradient-B drift is acting in any region with a non-uniform magnetic field, like for instance, X-lines or X-planes. In more complex geometries and for time dependent situations additional first order drifts may be included. Nevertheless, the main results of our study should remain valid as all the first order drifts depend on the kinetic energy of the particle. This is a key property emphasized by the kinetic effects described in this thesis. A preliminary comparison with in-situ data from the terrestrial magnetosphere show a rather good correlation and more in-depth data comparisons will be done in the future.

We compared the velocity distribution functions obtained with the forward and backward approaches for different regions of the proton cloud. In the forward approach f is sampled over a spatial bin that needs to be populated by a sufficiently large number of particles so as to reduce statistical errors. On the other hand, in the backward approach f is computed without statistical errors, at precise positions in configuration space. In order to compare the distribution functions obtained with both approaches, a spatial averaging of f is needed. The velocity distribution function given by the backward approach is numerically integrated over a rectangular domain corresponding to the spatial bin used to compute the distribution function with the forward approach.

Our simulation results show that there are significant differences between the distribution functions given by forward and backward approaches. The differences are observed especially for spatial bins from regions with a steep spatial variation of the velocity distribution function, while in regions with smooth variations of f the two approaches provide similar results. The differences and similarities can be explained by a careful examination of the sampling method used in the forward approach and the averaging method used in the backward approach. The main difference between the two computational methods is due to the approach used to estimate the velocity distribution function in a spatial bin: the backward method uses an averaging method that takes into account the contribution of the entire spatial bin to calculate the distribution function for a certain bin in velocity space, while, in certain cases, the forward sampling method effectively only takes into account the contribution from a part of the bin considered. The two approaches lead to similar results when averages are calculated over bins in which the VDF varies smoothly in configuration space.

Chapter 2

Kinetic simulations of tangential discontinuities

In the second chapter of my thesis I investigate the kinetic structure of a one-dimensional tangential discontinuity (TD) using one-dimensional particle-in-cell (PIC) simulations and comparison with theoretical kinetic models. I consider three different cases: (i) *TD without velocity shear* across the discontinuity and different asymptotic densities and temperatures, (ii) *TD with velocity shear* in the perpendicular direction to the magnetic field and equal asymptotic densities and temperatures and (iii) a *plasma slab* moving across a transverse external magnetic field and a background stagnant plasma with equal densities and temperatures.

2.1 Particle-in-cell simulation method

In particle-in-cell simulations (*Birdsall and Langdon, 1991*) plasma dynamics is studied by following the trajectories of a large number of particles in their self-consistent electric and magnetic fields. The limited computing infrastructure, even nowadays, makes it practically impossible to simulate the same number of particles per Debye sphere as in real plasmas. Therefore, in particle-in-cell simulations, real particles are replaced by *finite-size superparticles* with the mass and charge much larger than those of real particles. The finite-size superparticles may be viewed as charge clouds that can pass freely through each other without changing their internal charge distribution. The use of charge clouds instead of point particles plays a key role in smoothing the short-range electrostatic interactions between particles while keeping the same long-range behavior as in real plasmas (*Langdon and Birdsall, 1970*). The benefit of working with finite-size superparticles is that the same real plasma parameter can be achieved even with a smaller number of simulated particles. In order to simulate the same plasma system as in reality, the charge density, the mass density and the thermal energy density of superparticles must match the same values as those of the real particles (*Matsumoto and Omura, 1984*).

The self-consistent electromagnetic field is computed in PIC simulations from the Maxwell's equations that are solved using finite-differences in both space and time with a centered-difference scheme. In explicit particle-in-cell codes, the discretization of space and time cannot be done arbitrarily, but must fulfill certain requirements. The most restrictive requirement is given by the Courant condition that enforces an upper limit to the time-step Δt for a given grid spacing Δx (*Birdsall and Langdon, 1991*):

$$c \cdot \Delta t < \Delta x \quad (2.1)$$

where c is the speed of light in vacuum. Moreover, the time-step must resolve the electron plasma oscillations too. In order to avoid the numerical instabilities that can rise due to the discretization of the configuration space, the grid spacing must resolve the electrons Debye length λ_D (*Birdsall and Langdon, 1991*):

$$\Delta x < 3\lambda_D \quad (2.2)$$

These very strict requirements for the discretization of space and time, expressed by inequalities (2.1) and (2.2), can generate large simulation runtimes, especially for problems with spatial and temporal scales much larger than the Debye length and the plasma period.

The electrical charge of a finite-size particle is distributed by interpolation over the spatial mesh used to compute the electromagnetic field. With a first order interpolation scheme, the charge q of the superparticle is distributed among its neighboring grid points i and $i+1$ as follows (*Birdsall and Langdon, 1991*):

$$q_i = \frac{x_{i+1} - x}{\Delta x} q, \quad q_{i+1} = \frac{x - x_i}{\Delta x} q \quad (2.3)$$

where x is the central position of the particle, while q_i and q_{i+1} are the electrical charges assigned to the grid points i and $i+1$ localized at $x_i = i \cdot \Delta x$ and $x_{i+1} = (i+1) \cdot \Delta x$. In order to achieve the momentum conservation and to avoid the non-physical acceleration of the particles by the so-called *self-force*, the same interpolation scheme and the same grid points that have been used to distribute the charges over the spatial grid must be reused to compute the electric and magnetic fields in the actual positions of the particles. For a first order interpolation scheme we have:

$$\vec{E}(x) = \frac{x_{i+1} - x}{\Delta x} \vec{E}_i + \frac{x - x_i}{\Delta x} \vec{E}_{i+1} \quad (2.4)$$

where \vec{E}_i and \vec{E}_{i+1} are the values of the electric field at the grid points i and $i+1$. The same formula is used also for the magnetic field.

The simulations presented here are performed using an adapted version of the one-dimensional particle-in-cell code KEMPO1 (*Omura and Matsumoto, 1993; Omura, 2007*). KEMPO1 is a 1d3v PIC code, i.e. only one spatial coordinate is considered, but all the three components of the velocity vector are taken into account. The self-consistent electromagnetic field is computed from the Ampère and Faraday's laws:

$$\begin{aligned} \frac{\partial \vec{E}}{\partial t} &= \frac{1}{\epsilon_0} \left(\frac{\nabla \times \vec{B}}{\mu_0} - \vec{J} \right) \\ \frac{\partial \vec{B}}{\partial t} &= -\nabla \times \vec{E} \end{aligned} \quad (2.5)$$

where \vec{J} is the total current density in the plasma, while ϵ_0 and μ_0 are the electrical permittivity and the magnetic permeability of the vacuum. Equations (2.5) are solved numerically by a finite-differences method using a centered-difference scheme that enables the computation of the fields at any given time by knowing their values at the previous time-step, for all the grid points inside the simulation domain (*Omura and Matsumoto, 1993*). The finite-difference scheme is summarized below:

$$\begin{aligned}
 E_{x,i+1/2}^{t+\Delta t} &= E_{x,i+1/2}^t - J_{x,i+1/2}^{t+\Delta t/2} \Delta t \\
 E_{y,i}^{t+\Delta t} &= E_{y,i}^t + \left(-J_{y,i}^{t+\Delta t/2} - c^2 \frac{B_{z,i+1/2}^{t+\Delta t/2} - B_{z,i-1/2}^{t+\Delta t/2}}{\Delta x} \right) \Delta t \\
 E_{z,i+1/2}^{t+\Delta t} &= E_{z,i+1/2}^t + \left(-J_{z,i+1/2}^{t+\Delta t/2} + c^2 \frac{B_{y,i+1}^{t+\Delta t/2} - B_{y,i}^{t+\Delta t/2}}{\Delta x} \right) \Delta t \\
 B_{y,i}^{t+\Delta t/2} &= B_{y,i}^{t-\Delta t/2} + \frac{E_{z,i+1/2}^t - E_{z,i-1/2}^t}{\Delta x} \Delta t \\
 B_{z,i+1/2}^{t+\Delta t/2} &= B_{z,i+1/2}^{t-\Delta t/2} - \frac{E_{y,i+1}^t - E_{y,i}^t}{\Delta x} \Delta t
 \end{aligned} \tag{2.6}$$

As can be seen in equations (2.6), two staggered grid sets are used for both space and time discretization. The E_y and B_y components of the electric and magnetic fields are defined in full-integer grid points localized at $x_i = i \cdot \Delta x$, while the E_x , E_z and B_z components are given in half-integer grid points localized at $x_{i+1/2} = (i+1/2) \cdot \Delta x$. The time discretization is done at full-integer time-steps, $t_n = n \cdot \Delta t$, for the electric field and at half-integer time-steps, $t_{n+1/2} = (n+1/2) \cdot \Delta t$, for the magnetic field. The current density is defined in the same grid points as the electric field and at the same time-steps as the magnetic field. Since the geometry of the code is one-dimensional, the B_x component of the magnetic field is constant in space and time. Therefore, taking into account that we are interested in configurations typical for tangential discontinuities where the normal component of the magnetic field is zero, we set the value of B_x equal to zero.

The total current density at any given time and in any grid point is computed from the individual contribution of each superparticle to a certain grid point inside the simulation domain. In the case of J_y and J_z components of the current density, the contribution of each finite-size superparticle is distributed among its neighboring grid points by linear interpolation:

$$\begin{aligned}
 J_{y,i\mp 1/2}^{t+\Delta t/2} &= \sum_p \frac{|x_{i\pm 1/2} - x_p^{t+\Delta t/2}|}{\Delta x} q_p v_{y,p}^{t+\Delta t/2} \\
 J_{z,i\mp 1/2}^{t+\Delta t/2} &= \sum_p \frac{|x_{i\pm 1/2} - x_p^{t+\Delta t/2}|}{\Delta x} q_p v_{z,p}^{t+\Delta t/2}
 \end{aligned} \tag{2.7}$$

where p indexes all the particles that are localized between the grid points $i-1/2$ and $i+1/2$ at time $t+\Delta t/2$; v_y and v_z are the velocity components of the p particle at $t+\Delta t/2$. The J_x component of the total current density is computed by the *current deposition of particles* technique in order to ensure the fulfilment of the charge continuity equation at each time-step during the simulation (Villasenor and Buneman, 1992):

$$\frac{\rho_i^{t+\Delta t} - \rho_i^t}{\Delta t} + \frac{J_{x,i+1/2}^{t+\Delta t/2} - J_{x,i-1/2}^{t+\Delta t/2}}{\Delta x} = 0 \tag{2.8}$$

where ρ_i is the electrical charge density computed from equation (2.3). $J_{x,i+1/2}$ at $t+\Delta t/2$ is thus obtained by taking into account the amount of charge that crosses over the half-integer grid point $i+1/2$ between t and $t+\Delta t$.

The equation of motion for each particle:

$$\begin{aligned}\frac{dx}{dt} &= v_x \\ \frac{d\vec{v}}{dt} &= \frac{q}{m}(\vec{E} + \vec{v} \times \vec{B})\end{aligned}\quad (2.9)$$

is discretized in time using the leap-frog method:

$$\begin{aligned}\frac{x^{t+\Delta t} - x^t}{\Delta t} &= v_x^{t+\Delta t/2} \\ \frac{\vec{v}^{t+\Delta t/2} - \vec{v}^{t-\Delta t/2}}{\Delta t} &= \frac{q}{m} \left(\vec{E}^t + \frac{\vec{v}^{t-\Delta t/2} + \vec{v}^{t+\Delta t/2}}{2} \times \vec{B}^t \right)\end{aligned}\quad (2.10)$$

and it is solved explicitly by using the Buneman-Boris technique in three steps, as shown below (*Birdsall and Langdon, 1991*):

$$\begin{aligned}\vec{v}_1 &= \vec{v}^{t-\Delta t/2} + \frac{q\Delta t}{2m} \vec{E}^t \\ \vec{v}_2 &= \vec{v}_1 + \frac{2}{1+b^2} (\vec{v}_1 + \vec{v}_1 \times \vec{b}) \times \vec{b} \\ \vec{v}^{t+\Delta t/2} &= \vec{v}_2 + \frac{q\Delta t}{2m} \vec{E}^t\end{aligned}\quad (2.11)$$

where $\vec{b} = (q\Delta t / 2m)\vec{B}^t$. The computation of the velocity at time $t+\Delta t/2$ using the equations (2.11) ensures the strict conservation of the kinetic energy of a particle during the pure gyration motion from $t-\Delta t/2$ to $t+\Delta t/2$, i.e. $|\vec{v}_1| = |\vec{v}_2|$ in (2.11). The position of a particle along the x-axis at $t+\Delta t$ is given by:

$$x^{t+\Delta t} = x^t + v_x^{t+\Delta t/2} \Delta t \quad (2.12)$$

where v_x is computed from equations (2.11). Since the simulation code KEMPO1 is one-dimensional, only one spatial coordinate is considered. However, all the three velocity components are taken into account. KEMPO1 is a relativistic particle code and therefore the relativistic equation of motion is actually solved instead of equation (2.9):

$$\frac{d\vec{u}}{dt} = \frac{q}{m_0} \left(\vec{E} + \frac{1}{\gamma} \vec{u} \times \vec{B} \right) \quad (2.13)$$

where we used the notation $\vec{u} = \gamma \vec{v}$, γ is the relativistic factor and m_0 is the rest mass of the particle. Nevertheless, the procedure described above still applies, but this time for \vec{u} in equation (2.13).

A schematic diagram of a one-dimensional particle-in-cell simulation cycle is shown in Figure 2.1 (*Birdsall and Langdon, 1991*). The equation of motion (2.9) for each charged particle initialized at $t=0$ is integrated numerically over the time-step Δt using the explicit formulas (2.11) and (2.12). Having the new positions and velocities of all the

particles inside the simulation domain, the charge and current densities are computed for the grid points using the linear interpolation schemes (2.3) and (2.7); for J_x the current deposition technique is used. The Maxwell's equations (2.5) are then integrated over the one-dimensional spatial mesh to obtain the electromagnetic field explicitly at $t+\Delta t$, as shown in (2.6). The interpolation scheme (2.4) is used to calculate the electric and magnetic fields in the position of each particle. The equation of motion is integrated again over the time-step Δt , resulting the updated set of positions and velocities. The cycle is continued until the end of the simulation. The time-step Δt must fulfill the Courant condition (2.1) of numerical stability. Also, the grid spacing Δx must resolve the electron Debye length according to inequality (2.2).

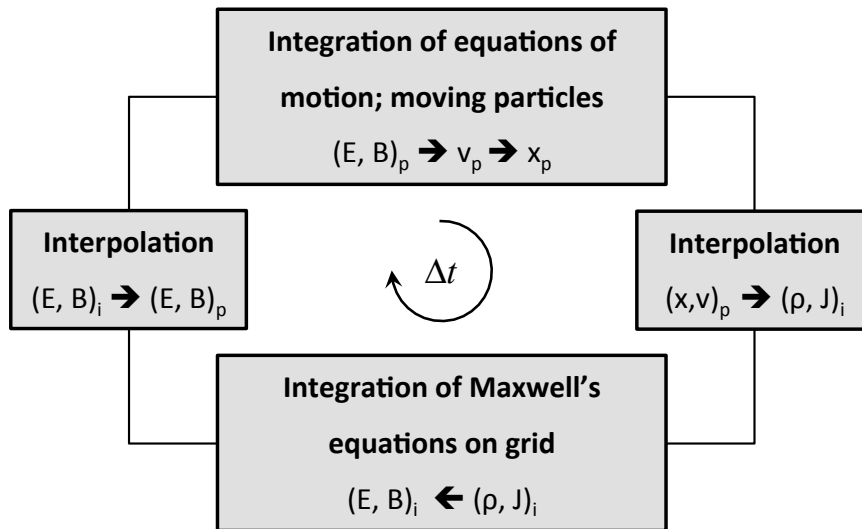


Figure 2.1 – A typical cycle in a one-dimensional particle-in-cell simulation code. The quantities computed in the position of each particle are indexed with p , while the grid quantities are indexed with i (adapted from *Birdsall and Langdon, 1991*).

2.2 Simulation setup

The simulation domain is defined in the x -direction between $0 \leq x \leq L$ and is split in two regions of equal widths that are filled initially with the same number of electrons and protons, forming the left ($x < L/2$) and right ($x > L/2$) plasma populations. We study three different cases.

In the first case we consider a tangential discontinuity without velocity shear at the interface between two plasma populations at rest and with different densities and temperatures. The configuration of this case is illustrated schematically by Figure 2.2. In the second case, the two asymptotic plasmas have equal densities and temperatures, but there is a variation of the bulk velocity in the direction perpendicular to the magnetic field; this is the case of a tangential discontinuity with velocity shear (see Figure 2.3 for the simulation geometry). In the last case, we simulate a plasma slab streaming across a transverse magnetic field in the presence of a background stagnant plasma with equal densities and temperatures (see Figure 2.4 for the setup of the simulation).

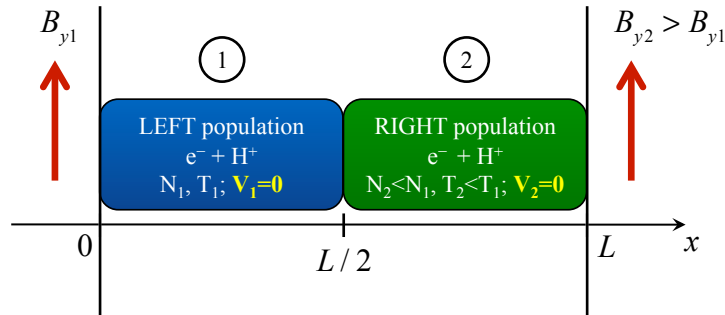


Figure 2.2 – Schematic diagram of the simulation geometry for case A: *tangential discontinuity without velocity shear*. In this case there is no asymptotic variation of the plasma bulk velocity across the discontinuity and the two plasma populations have different asymptotic densities and temperatures.

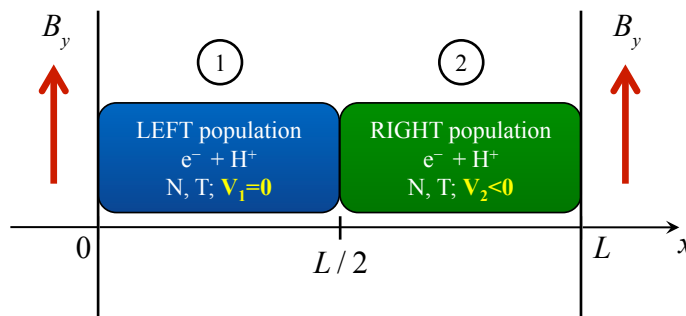


Figure 2.3 – Schematic diagram of the simulation geometry for case B: *tangential discontinuity with velocity shear*. In this case the plasma bulk velocity varies in the perpendicular direction to the magnetic field, but the two populations have equal asymptotic densities and temperatures.

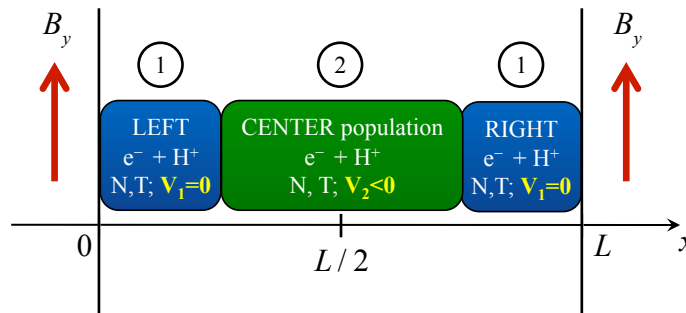


Figure 2.4 – Schematic diagram of the simulation geometry for case C: *plasma slab*. In this case the central plasma population is streaming across a transverse magnetic field and a background stagnant plasma with equal densities and temperatures.

Initially, the electrons and the protons are uniformly distributed along the x -axis inside the simulation domain. In all three cases discussed here, the initial velocity distribution function is given by an isotropic/displaced Maxwellian with the same temperature for both electrons and protons. In the second and third cases, the average velocity for the right population (case B) and for the central population (case C) is parallel to the negative z -axis and perpendicular to the magnetic field. The velocities of the particles at $t=0$ are distributed according to the isotropic/displaced Maxwellian distribution function.

In the first simulated case, the plasma density for the left population, N_1 , is one order of magnitude larger than the one for the right population, N_2 . The temperature of the left population, T_1 , is two times larger than the one corresponding to the right population, T_2 . For the other two cases, B and C, the densities and the temperatures of the two plasmas are equal. The initial uniform magnetic field is oriented along the positive y-axis everywhere inside the simulation domain for all three cases. In the last two cases, a convection electric field, $E_0=V_0B_0$, is initialized for the right region (case B) and for the central region (case C) of the simulation domain. Otherwise, the initial electric field is set to zero everywhere. The plasma and field parameters for all the three cases considered are given in Table 2.1.

Table 2.1 – Plasma and field parameters for the three cases considered in the second chapter: N = number density, T = temperature, V_z = bulk velocity, B_y = magnetic induction and E_x = electric field intensity at $t=0$ for case A (see **Figure 2.2**), case B (see **Figure 2.3**) and case C (see **Figure 2.4**); indices “1” and “2” denote the values corresponding to the two plasma regions illustrated in the aforementioned figures.

| | N_1 | N_2 | T_1 | T_2 | V_{z1} | V_{z2} | B_{y1} | B_{y2} | E_{x1} | E_{x2} |
|------------------------|--------------------|--------|-------|-------|----------|----------|----------|----------|----------|----------|
| | [m ⁻³] | | [keV] | | [km/s] | | [nT] | | [mV/m] | |
| Case A | 10^6 | 10^5 | 20 | 10 | 0 | 0 | 180 | 218 | 0 | 0 |
| Cases B & C | 10^6 | 10^6 | 20 | 20 | 0 | -1000 | 500 | 500 | 0 | -500 |

The boundary conditions assumed for the three cases discussed here are (i) reflective for particles, while the fields are kept fixed at their initial value, in cases A and B, and (ii) periodic for both particles and fields, in case C. The particles that leave the simulation domain will be relocated inside the domain as follows:

- cases A and B:
 - if $x_p < 0$ then $x_p := -x_p$ and $v_p := -v_p$
 - if $x_p > L$ then $x_p := 2L - x_p$ and $v_p := -v_p$
- case C:
 - if $x_p < 0$ then $x_p := x_p + L$
 - if $x_p > L$ then $x_p := x_p - L$

where x_p and v_p are the position and the velocity of the particle moving outside the simulation domain at any given time. On the other hand, all the grid quantities will be updated at the boundaries of the simulation domain such that the following equalities to be satisfied at any given time during the simulation:

- cases A and B:

$$G_{x=0}^{t>0} = G_{x=0}^{t=0} \text{ and } G_{x=L}^{t>0} = G_{x=L}^{t=0}$$
- case C:

$$G_{x+L}^t = G_x^t$$

where the grid quantity G can be the electric field, the magnetic field or the total current density. All these boundary conditions are applied at each time-step during the simulation after the integration of the equation of motion, for particles, and after the integration of Maxwell’s equations, for fields.

The simulation parameters for the three cases considered are given in Table 2.2. The total number of particles per species is 131,072 in case A, 262,144 in case B and 4,194,304 in case C. This corresponds to a number of 512 electrons and protons per grid cell in the first two cases and to 8192 particles per grid cell in case C. The grid cell has a width of 1.5 electron Debye lengths in all the three cases. The length of the simulation domain covers 5 ion gyration radii in the first case and 28 ion gyration radii in the last two cases. The total simulation time varies between 3 (case A) and 5 (cases B and C) ion Larmor periods. The ion-to-electron mass-ratio used is 16.

Table 2.2 – Simulation parameters for cases A, B and C: nx = number of grid points, nt = number of time-steps, L = length of the simulation domain, r_L = Larmor radius, T = total simulation time, T_L = Larmor period, λ_D = Debye length, Δx = grid spacing, Δt = time-step, c = speed of light in vacuum; “ e ” and “ i ” indices designates the electrons and ions corresponding quantities. In case A the gyration radius and the cyclotron period are computed for the left population (see **Figure 2.2**).

| | nx | nt | L/r_{Le} | L/r_{Li} | T/T_{Le} | T/T_{Li} | $\Delta x/\lambda_{De}$ | $c\Delta t/\Delta x$ |
|------------------------|------|--------|------------|------------|------------|------------|-------------------------|----------------------|
| Case A | 256 | 262144 | 20 | 5 | 54 | 3 | 1.5 | 0.9 |
| Cases B & C | 512 | 131072 | 112 | 28 | 76 | 5 | 1.5 | 0.9 |

2.3 Numerical results

2.3.1 Evaluation of the intrinsic particle-in-cell noise

In the following we discuss the intrinsic statistical noise that is typical to particle-in-cell numerical simulations. For this purpose, we analyze the space and time evolution of a uniform plasma in the presence of constant electric and magnetic fields. Initially, the entire simulation domain is filled with electrons and protons having a number density of 10^6 m^{-3} and a temperature of 20 keV. Their velocity distribution function is a displaced Maxwellian with the average velocity oriented along the negative z-axis and equal to 500 km/s. The magnetic field equals 200nT and is pointing along $+Oy$, while a convection electric field of 100 mV/m is considered at the beginning of the simulation. The initial conditions together with other input parameters are summarized in Table 2.3.

Table 2.3 – Input parameters for the test-simulations with a variable number of particles: N = number density, T = temperature, V_z = bulk velocity, B_y = magnetic induction, E_x = electric field intensity, nx = number of grid points, nt = number of time-steps, Δx = grid spacing, Δt = time-step and ion-to-electron mass ratio m_i/m_e ; λ_D is the Debye length and c is speed of light in vacuum; “ e ” and “ i ” indices designates the electrons and ions corresponding quantities.

| $N_e=N_i$ [m^{-3}] | $T_e=T_i$ [keV] | $V_{ze}=V_{zi}$ [km/s] | B_y [nT] | E_x [mV/m] | nx | nt | $\Delta x/\lambda_{De}$ | $c\Delta t/\Delta x$ | m_i/m_e |
|----------------------------------|--------------------|---------------------------|---------------|-----------------|------|------|-------------------------|----------------------|-----------|
| 10^6 | 20 | -500 | 200 | -100 | 512 | 2048 | 1.5 | 0.9 | 16 |

We performed three numerical experiments with (i) 4096 particles per cell, (ii) 65536 particles per cell and (iii) 262144 particles per cell. For the beginning, we analyzed the plasma and electromagnetic field evolution over a short time scale of ~ 8 electron plasma periods. Then we increased the simulation time to cover approximately 1000

electron plasma periods or, equivalently, nearly 4 ion gyration periods, but with less few simulated particles. The boundary conditions assumed here are reflective for particles, while the fields are kept fixed at their initial value, as discussed in the previous section.

In Figure 2.5 we illustrate the space and time evolution of the electric field for the first simulation. The number of particles per cell in this case was equal to 4096. A notable feature of these simulations are the high amplitude fluctuations, one order of magnitude larger than the actual value of the electric field, observed throughout the entire simulation domain. In order to identify the origin of these electrostatic fluctuations, we analyzed also the space and time evolution of the net charge density computed as $(n_e - n_i)/n_i$, where n_e and n_i are the electron and ion number densities. For each grid cell of the simulation domain, we computed time-averages by taking the arithmetic mean of all instantaneous values of the electric field and the net charge density:

$$\langle Q_i \rangle = \frac{1}{nt} \sum_{n=1}^{nt} Q_i(t_n = n \cdot \Delta t) \quad (2.14)$$

with i indexing the grid points along the x-axis; Q is the physical quantity that will be time-averaged. In our case we apply equation (2.14) for both the E_x component of the electric field and the net charge density $(n_e - n_i)/n_i$. The results obtained are shown in Figure 2.6 where on the left column we have the net charge density at the end of the simulation (blue plot) and its time-averaged profile (red plot), while on the right we have the same profiles but for the electric field. Each row of panels corresponds to one of the three numerical experiments performed, i.e. with 4096 particles per cell (top panels), 65536 particles per cell (middle panels) and 262144 particles per cell (bottom panels).

The large amplitude fluctuations are clearly evidenced for both the net charge density and the electric field intensity (see blue lines in Figure 2.6). On the other hand, it can be easily noticed that these oscillations are removed by time averaging the simulation results (see red lines in Figure 2.6). Their amplitude is considerably reduced when much more particles are loaded into the simulation domain. Indeed, by increasing the number of electrons and ions by 64 times, the amplitude of the electric field and net charge density fluctuations has been reduced by one order of magnitude (compare top and bottom panels of Figure 2.6). Consequently, the time-averaged profiles are also smoother when more simulation particles are considered.

We increased the simulation time to span more than 1000 electron plasma periods. On the other hand, in order to maintain a satisfactory computing time, we reduced the number of particles to 512 per cell. In this case we use 256 grid cells instead of 512 as in the previous three cases. In Figure 2.7 we show the variation profile of the net charge density (left panel) and of the electric field (right panel) at the end of the simulation (blue lines) and computed by time-averaging (red lines). As can be noticed, the fluctuations are present even after approximately four ion Larmor periods from the beginning of the simulations. As expected, their amplitude is larger now than previously since the number of particles diminished. In this case too, by taking time-averages, we obtain smoother profiles for both quantities.

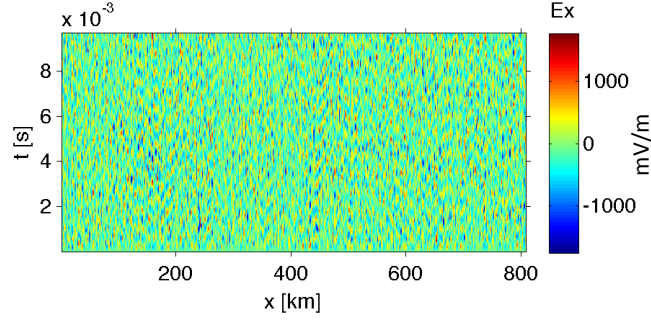


Figure 2.5 – Space and time evolution of the E_x component of the electric field when 4096 particles per grid cell are loaded into the simulation domain. The simulation time covers 8 electron plasma periods.

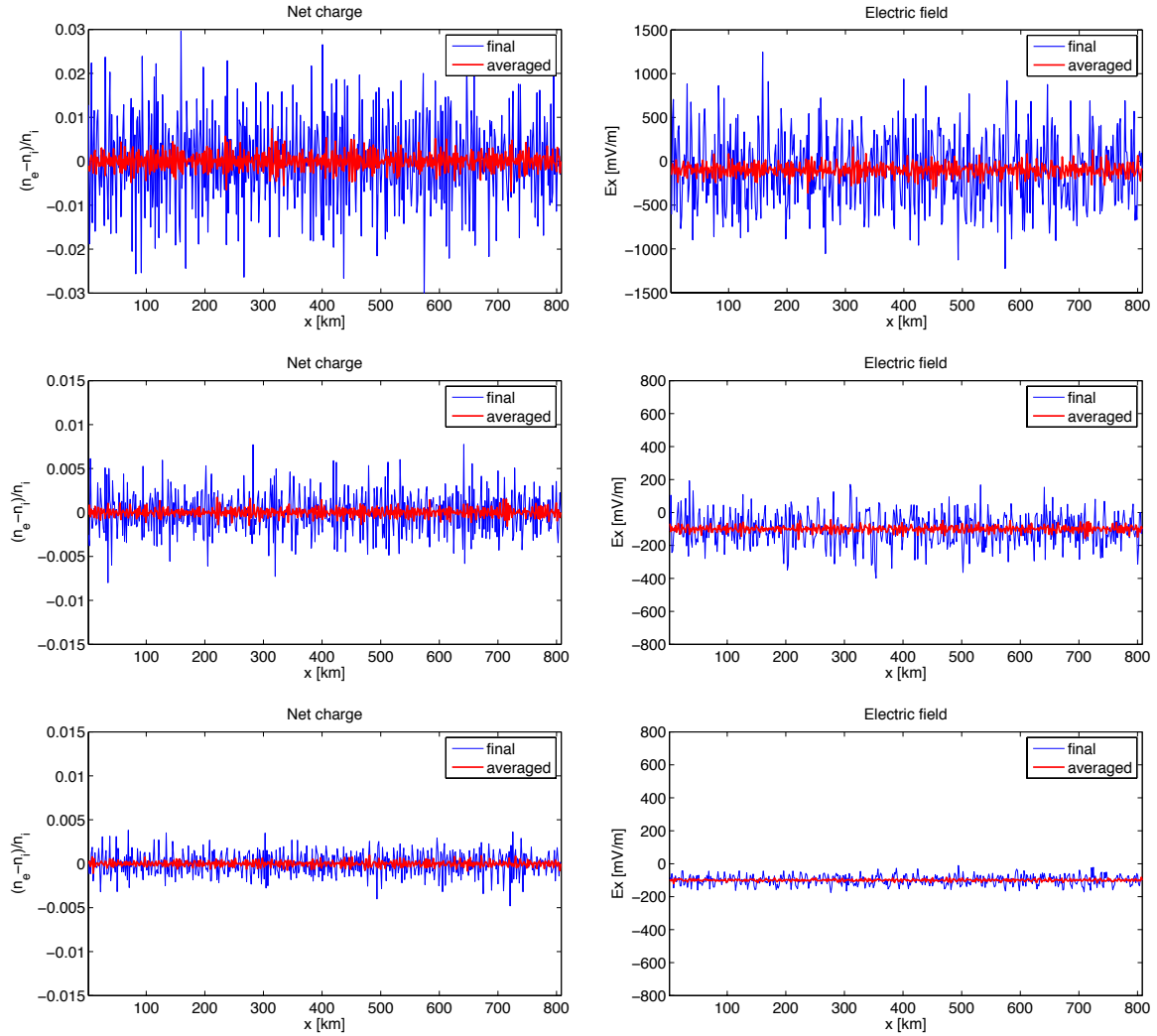


Figure 2.6 – Net charge density (left column) and electric field intensity (right column) obtained with 4096 particles per cell (top panels), 65536 particles per cell (middle panels) and 262144 particles per cell (bottom panels). The blue lines show the results obtained at the end of the simulations, while the red ones illustrate the time-averaged profiles. The total simulation time covers ~ 8 electron plasma periods.

The results suggest that the observed electrostatic fluctuations are related to the number of particles of the simulation. Their large amplitudes are significantly reduced (i) by increasing the number of particles and (ii) by taking time-averages. Therefore, we conclude that these fluctuations could be in fact a statistical (electrostatic) white noise.

To emphasize the nature of the statistical noise observed, we calculated the time histograms of the net charge density and electric field deviations from their averaged values:

$$\delta Q_i(t) = Q_i(t) - \langle Q_i \rangle \quad (2.15)$$

for the central region of the simulation domain ($x=202$ km). The results obtained are shown in Figure 2.8 for the net charge density (left panel) and for the electric field (right panel). The histograms have been fitted using a normal distribution with mean $\mu \approx 0$ and standard deviation $\sigma \approx 0.029$ for the net charge density and $\sigma \approx 1218$ mV/m for the electric field (see red lines in Figure 2.8). The time-deviations from mean have a gaussian distribution confirming that the large amplitude fluctuations evidenced in our simulations are indeed a white statistical noise. Note that that the time interval chosen for averaging must be much larger with respect to the plasma frequency. Indeed, our numerical tests revealed that only when $nt \cdot \Delta t \gg 1/\nu_p$ (ν_p is the plasma frequency) the high amplitude statistical fluctuations are indeed a gaussian white noise. The results obtained here clearly justify the time averaging procedure (2.14).

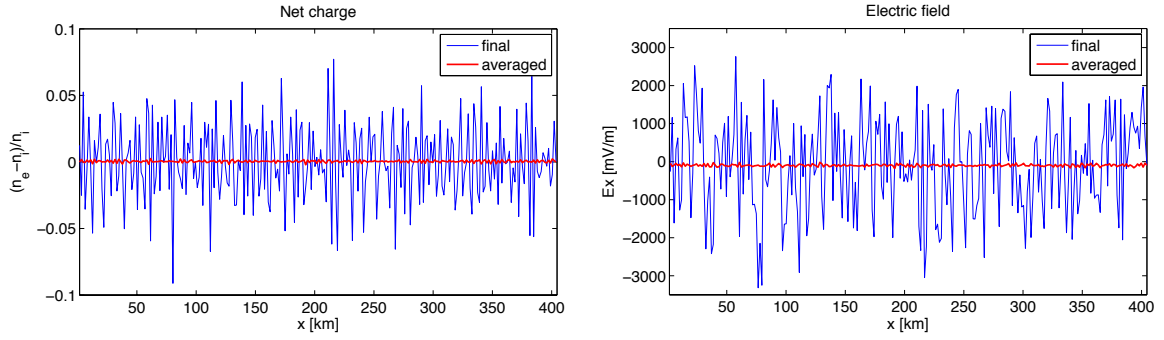


Figure 2.7 – Net charge density (left column) and electric field intensity (right column) obtained with 512 particles per cell for a total simulation time that covers ~ 1000 electron plasma periods or, equivalently, ~ 4 ion Larmor periods. The blue lines show the results obtained at the end of the simulations, while the red ones illustrate the time-averaged profiles.

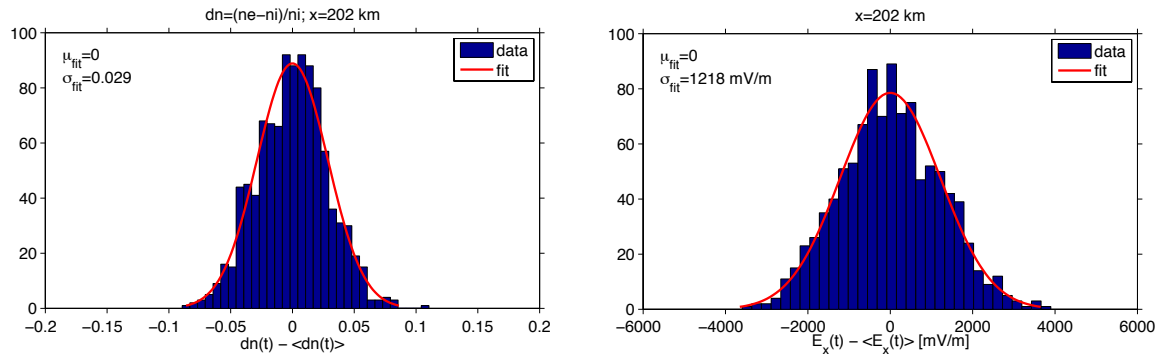


Figure 2.8 – Histograms of the net charge density (left panel) and electric field intensity (right panel) deviations from their time-averaged values, computed for the central region of the simulation domain ($x=202$ km). The red line illustrates the fitting curve of the histogram using a normal distribution.

The gaussian noise present in our simulations is not limited only to the net charge density or the E_x component of the electric field, but it was observed for all the plasma and electromagnetic field parameters analyzed. On the other hand, we performed

additional numerical experiments, but not discussed here, and have shown that the amplitude of the statistical noise is not influenced by the ion-to-electron mass ratio or by the width of a grid cell compared to the electron Debye length. Note that the time-averaging procedure discussed here should be used with care since it could interfere with the physics. Indeed, we should consider time-averages only for the problems that are stable over time and when time-dependent effects are not of interest.

2.3.2 Case A: Tangential discontinuity without velocity shear

We simulate a tangential discontinuity without velocity shear (*Sestero, 1964*), i.e. there is no asymptotic variation of the plasma bulk velocity across the discontinuity and the two plasma populations have different densities and temperatures, as illustrated schematically in Figure 2.2. The input parameters are given in Table 2.1 and Table 2.2.

Figure 2.9 shows the numerical results obtained for case A. On the first row of panels we have the E_x component of the electric field, the second row shows the B_y component of the magnetic field, on the third row we show the electron number density, while at the bottom of the figure we plot the net electrical charge inside the plasma computed as $(n_e - n_i)/n_i$ ratio, where n_e and n_i are the electron and ion number densities. The first column shows the time history of the aforementioned physical quantities, on the second one we illustrate the time-averaged profiles, while on the last column we show the results obtained with a theoretical kinetic model of tangential discontinuities developed by *Roth et al. (1996)*. Note that the kinetic model is run for precisely the same asymptotic parameters as the PIC simulations. The theoretical model is based on steady-state solutions of the Vlasov equation and can provide the equilibrium structure of tangential discontinuities in collisionless plasmas. It is a generalized one-dimensional model that is able to describe tangential discontinuities with and without velocity shear. A full description of the model is given in the paper of *Roth et al. (1996)*.

From the space and time evolution of the electromagnetic field shown in Figure 2.9 (left column, first two panels) we note that the transition profiles of the electric and magnetic fields are established very quickly, soon after the beginning of the simulation. The electric field is very noisy and it is characterized by high amplitude fluctuations that are one order of magnitude larger than the electric field predicted by the theoretical kinetic model. The noise is reduced by time-averaging, as shown also in the previous section. To confirm the gaussian nature of the electrostatic noise for this particular simulation geometry, we show in Figure 2.10 the time histogram of the electric field deviation from its averaged value for the central region of the simulation domain ($x \approx 200$ km). The histogram has been fitted using a normal distribution with mean $\mu \approx 0$ and standard deviation $\sigma \approx 600$ mV/m (see the red line in Figure 2.10). The time-averaging procedure (2.14) has been applied to all physical quantities of interest in our simulations. The computation of time-averages of the PIC results is justified also by the temporal stability of the PIC solution and by the fact that we compare our numerical results with a theoretical steady state model of a tangential discontinuity.

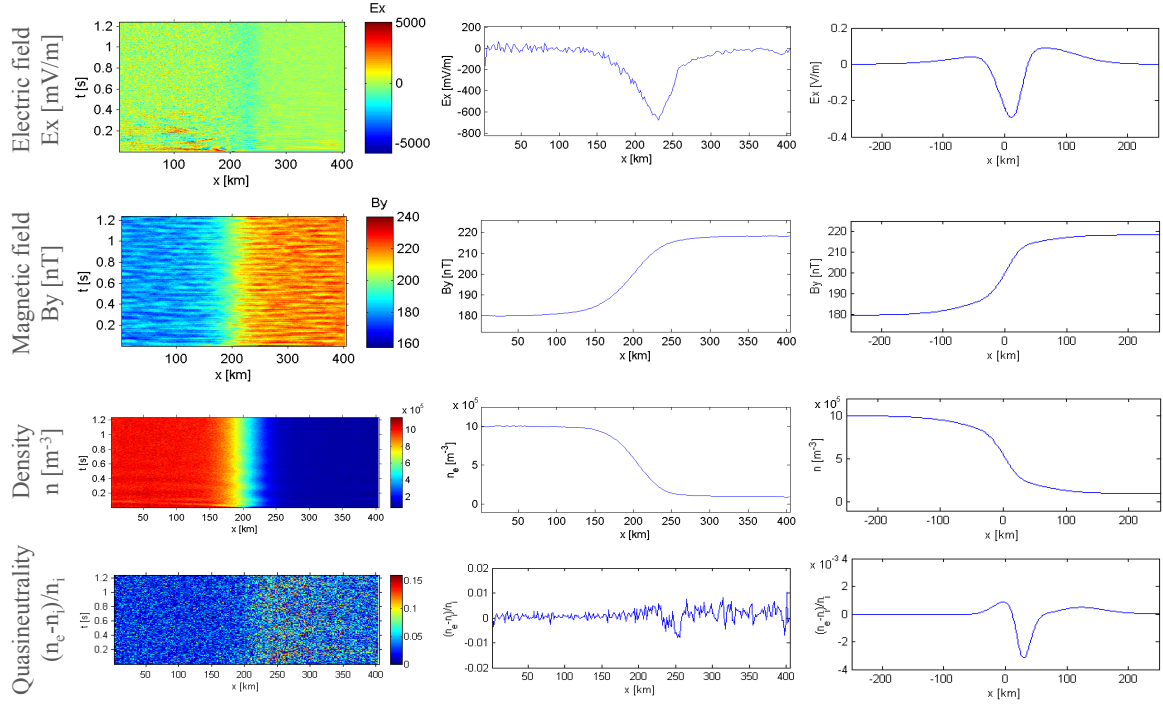


Figure 2.9 – Simulation results for a tangential discontinuity without velocity shear (case A). On the left column we show the time history for the electric field (first row), the magnetic field (second row), the electron number density (third row) and the net electrical charge (fourth row). The second column shows the time-averaged profiles, while on the last column we have the results of a theoretical kinetic model for a tangential discontinuity (Roth *et al.*, 1996).

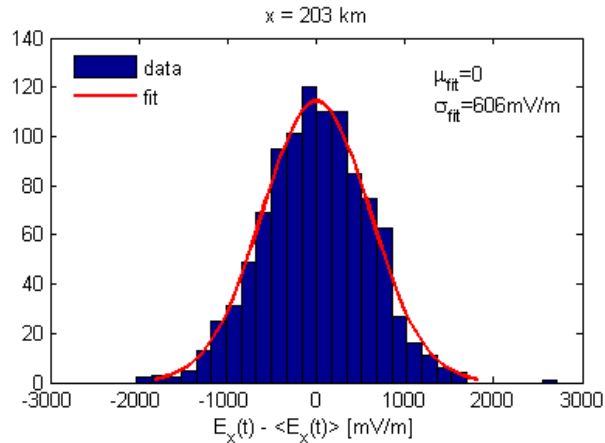


Figure 2.10 – Histogram of the electric field deviation from average, $E_x(t) - \langle E_x(t) \rangle$, computed for the central region of the simulation domain ($x \approx 200$ km). The red line illustrates the fitting curve of the histogram using a normal distribution with mean $\mu \approx 0$ and standard deviation $\sigma \approx 600$ mV/m. The averaged electric field is equal to ~ 300 mV/m.

The time-averaged profiles shown in Figure 2.9 for the electromagnetic field (middle column, first two panels) and for the plasma number density (middle column, third panel) have the typical features of a tangential discontinuity and are in agreement with the theoretical solution (third column, first three panels) computed using the model developed by Roth *et al.* (1996) for the same input parameters as the ones used in simulation. The panels from the last row of Figure 2.9 illustrate to what extent the plasma quasineutrality condition is fulfilled at each time-step of the simulation (left

panel) and also on average (middle panel). The results reveal the electric polarization of the plasma inside the transition region and the formation of a positive space charge layer in the central area of the simulation domain ($x \approx 250$ km). The polarization of the discontinuity is in agreement with the theoretical model as can be seen in the bottom-right panel of Figure 2.9. Nevertheless, the value of the $(n_e - n_i)/n_i$ ratio given by our simulations is 2.5 times larger than the one calculated with the theoretical model. Also, the same discrepancy is found for the electric field. We assume that the too low number of particles loaded into the simulation causes this mismatch between the numerical result and the theoretical solution.

2.3.3 Case B: Tangential discontinuity with velocity shear

The simulation geometry for the case of a tangential discontinuity with velocity shear (*Sestero, 1966*) is shown in Figure 2.3. In this simulation the plasma bulk velocity varies in the direction perpendicular to the magnetic field and the two plasma populations have equal densities and temperature. Inside the right half of the simulation domain the electrons and protons are initialized with a non-zero average velocity pointing along the negative z-axis, while the particles from the left half of the simulation domain are at rest. The input parameters for case B are given in Table 2.1 and Table 2.2.

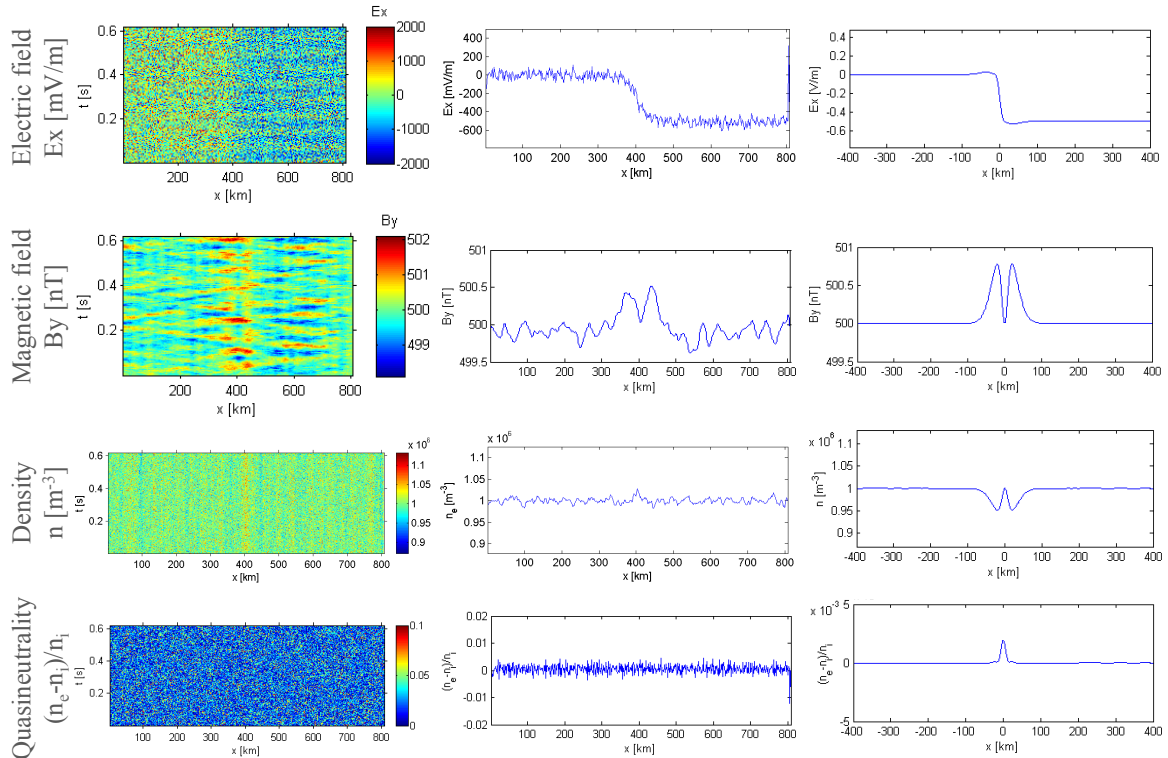


Figure 2.11 - Simulation results for a tangential discontinuity with velocity shear (case B). On the left column we show the time history for the electric field (first row), the magnetic field (second row), the electron number density (third row) and the net electrical charge (fourth row). The second column shows the time-averaged profiles, while on the last column we have the results of a theoretical kinetic model for a tangential discontinuity (*Roth et al., 1996*).

Figure 2.11 illustrates the numerical results obtained with the same distribution of panels as in Figure 2.9. Initially, the electric and the magnetic fields, the electron and ion number densities and the plasma bulk velocity are characterized by infinitesimal transition profiles at the boundary between the two different plasma regions. Soon after the start of the simulation, the system evolves to transition region of finite width with a scale length of approximately 3.5 ion gyration radii. Similarly to the previous case, all the physical quantities are characterized by an intense statistical noise, especially the E_x component of the electric field (upper-left panel). Taking time averages, the amplitude of these fluctuations are significantly reduced (see upper-middle panel).

The simulated profiles of the electric and magnetic fields (middle column, first two panels) are similar to the theoretical solutions (right column, first two panels). On the other hand, the number density and the net electrical charge, i.e. $(n_e - n_i)/n_i$ ratio, are strongly affected by the large statistical noise (middle column, last two panels). The averaged profiles of the density and net charge (right column, last two panels) are not similar to the theoretical ones. A possible explanation is the rather small number of simulated particles. This result emphasizes the critical role played by the number of particle loaded into the simulation and illustrate that a too small number of particles can generate incomplete results.

In Figure 2.12 we show the time-averaged profile of the ions bulk velocity across the discontinuity computed as the ratio between the ion current density J_{zi} and the ion charge density ρ_i . In the right asymptotic region of the simulation domain ($x > 450$ km) we obtain a bulk velocity of approximately 1000 km/s that points along the negative direction of the z-axis, in agreement with the input value.

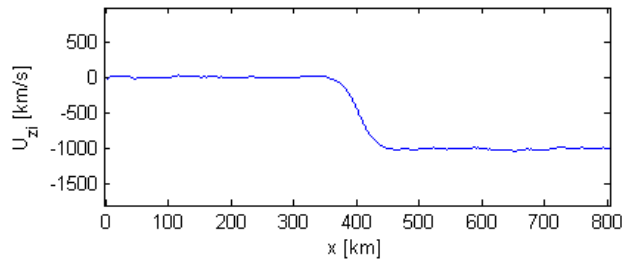


Figure 2.12 – The simulated profile of the ions bulk velocity for case B. The transition layer between the left asymptotic region ($V_z=0$) and the right asymptotic region ($V_z=-1000$ km/s) has a width of approximately 3.5 ion Larmor radii.

2.3.4 Case C: Plasma slab streaming across a transverse magnetic field

In the last case we simulate the motion of a plasma slab across a transverse uniform magnetic field in the presence of a background plasma. The geometry of the problem is shown in Figure 2.4. The plasma localized in the central region of the simulation domain is similar to a jet with the bulk velocity perpendicular to the magnetic field. The jet is immersed into a stationary background plasma that has the same density and temperature. The input parameters are given in Table 2.1 and Table 2.2.

The numerical results obtained for case C are shown in Figure 2.13 with the same distribution of panels as in the two previous cases, aside from the last column that was not included here. At $t=0$, the background plasma and the jet are separated by infinitesimal discontinuities in the electric field and in the bulk velocity that are localized in $x=200$ km and $x=600$ km. As in the previous two cases, we use time averages to reduce the statistical noise and smooth the transition profiles. Two finite width asymmetric boundary layers are formed at the edges of the plasma jet. The left boundary layer is centered in $x \approx 200$ km and has a width of approximately 221 km ($\sim 7.6r_{Li}$), while the right boundary layer is localized in $x \approx 625$ km and has a width of approximately 296 km ($\sim 10.2r_{Li}$), where r_{Li} is the ion Larmor radius.

The two asymmetric boundary layers are distinguished more clearly in Figure 2.14 where we show the time-averaged profile of the ion bulk velocity. It can be noticed that the plasma localized in the lateral regions of the simulation domain ($x < 90$ km and $x > 770$ km) is stationary, while the “central” plasma is streaming along the negative direction of the z-axis with a convection velocity of approximately 1000 km/s, consistent with the initial input of the simulation (see Table 2.1). On the other hand, Figure 2.14 shows the formation of two plasma “wings” at the edges of the slab that are characterized by a small positive bulk velocity with respect to the slab’s convection velocity. Similar results have been obtained by *Echim et al.* (2005) using a two-dimensional steady-state theoretical kinetic model (*Echim, 2004*).

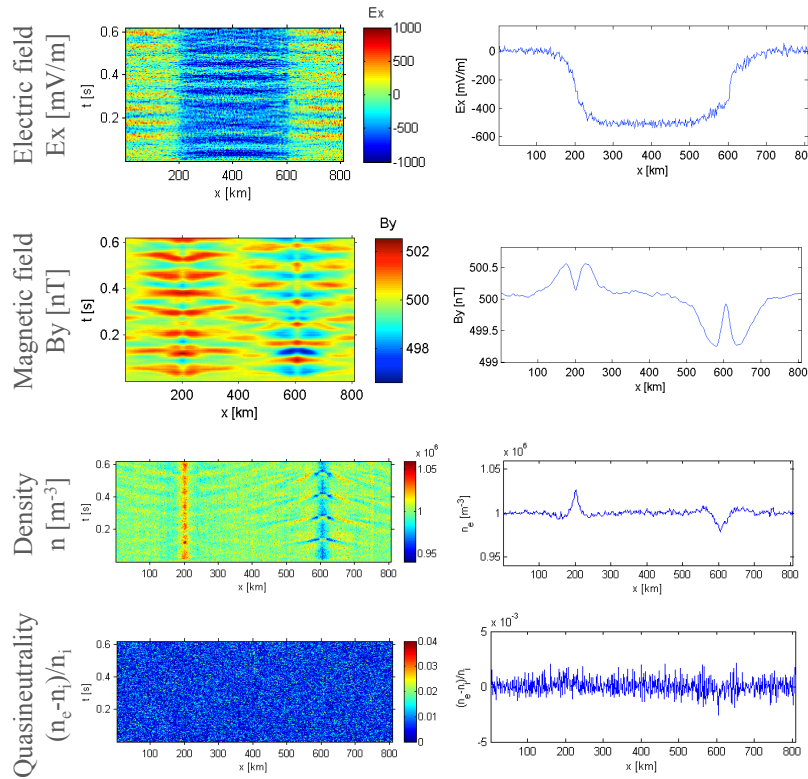


Figure 2.13 – Simulation results for a plasma slab streaming across a transverse magnetic field (case C). On the left column we show the time history for the electric field (first row), the magnetic field (second row), the electron number density (third row) and the net electrical charge (fourth row), while on the right column we show the time-averaged profiles.

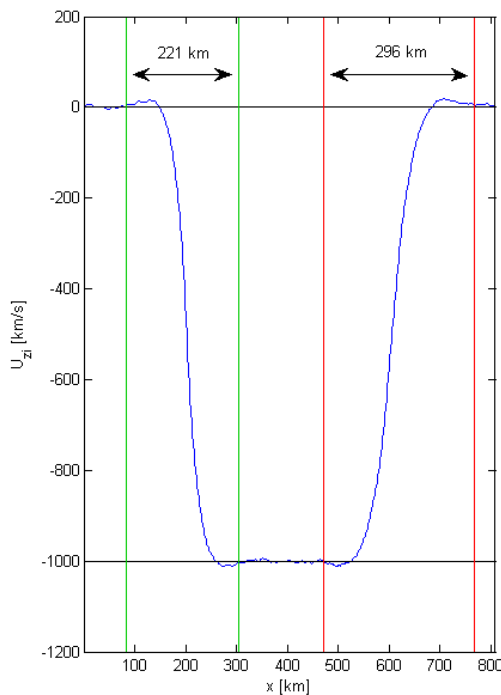


Figure 2.14 – The simulated profile of the ions bulk velocity for case C. Two asymmetric boundary layers are formed at the edges of the plasma slab. The left boundary layer has a width of approximately 7.6 ion Larmor radii, while the right boundary layer has a width of approximately 10.2 ion Larmor radii.

2.4 Conclusions

In this chapter I have investigated the space and time evolution of the plasma and electromagnetic field parameters at the interface between two magnetized plasmas having different macroscopic properties by using one-dimensional particle-in-cell simulations. Three cases have been analyzed: (i) a tangential discontinuity without velocity shear, (ii) a tangential discontinuity with velocity shear and (iii) a plasma slab moving across a transverse magnetic field. I have used an adapted version of the KEMPO1 electromagnetic PIC code (*Omura and Matsumoto, 1993; Omura, 2007*) to compute the transition profiles across the simulation domain for different physical quantities of interest as the magnetic field, the electric plasma, the electron and ion number densities and the plasma bulk velocity. Also, we checked to what extent the plasma quasineutrality condition is fulfilled through the entire simulation. We initialized a number of electrons and protons per grid cell varying from 512 to 8192 particles, for an ion-to-electron mass-ratio equal to 16. The time span of the simulation is of the order of few ion Larmor periods.

The numerical results obtained using particle-in-cell simulations reveal that the infinitesimal discontinuity assumed initially for all the three cases considered here, evolves to a finite width transition region with a scale of the order of ion Larmor radius. The transition region has properties typical for a tangential discontinuity and it was stable over the simulation time of 3-5 ion cyclotron periods. Since the code is not parallelized our computing resources were quite limited. We used a relatively small

number of particles that leads to a significantly large numerical noise, especially for the electric field and for the net electrical charge. By taking time-averages, we were able to reduce the statistical noise and to smooth the transition profiles for the plasma parameters and for the electromagnetic field. On the other hand, we emphasized the critical role played by the number of particles initialized inside the simulation domain.

The time-averaged simulated profiles have been compared with a steady-state theoretical solution of a tangential discontinuity using identical input parameters. The theoretical kinetic model used (*Roth et al.*, 1996) can provide the equilibrium structure of one-dimensional TDs with and without velocity shear. The results of our simulations are in relatively good agreement with the theoretical solutions. To our knowledge, this is the first time when theoretical kinetic models are directly compared with particle-in-cell simulations conducted under the same initial and asymptotic conditions.

The numerical experiments carried out into the second chapter of my thesis played the role of an intermediate step for the transition from test-kinetic to three-dimensional full-particle simulations. The primary goal was to simulate self-consistently plasma configurations typical to the study of plasma elements dynamics across transverse magnetic fields for which theoretical solutions are available.

Chapter 3

Three-dimensional particle-in-cell simulations of plasma elements transported across transverse non-uniform magnetic fields

In this chapter of my thesis I discuss the three-dimensional electromagnetic particle-in-cell simulations devoted to the investigation of the interaction of a localized plasma element/cloud with a transverse magnetic field. The plasma cloud is streaming in vacuum and perpendicular to a background magnetic field. The simulations demonstrate the crucial role of plasma processes taking place in the boundary layers at the edges of the plasma cloud for the propagation across the ambient magnetic field. The effects of magnetic field gradients are also analyzed and discussed.

3.1 Three-dimensional particle-in-cell simulations

The simulations presented here are performed using a modified version of the three-dimensional particle-in-cell code TRISTAN (*Buneman, 1993*). TRISTAN is a full electromagnetic explicit 3d3v PIC code, i.e. all three spatial coordinates and all three velocity components are solved. The electromagnetic field is discretized in space according to the Yee lattice (*Yee, 1966*) shown in Figure 3.1. Thus, the E_x, E_y, E_z and the B_x, B_y, B_z components of the electric and magnetic fields are computed numerically from Maxwell's equations in the staggered grid points located at:

$$\begin{aligned} E_x(i+1/2, j, k) & & E_y(i, j+1/2, k) & & E_z(i, j, k+1/2) \\ B_x(i, j+1/2, k+1/2) & & B_y(i+1/2, j, k+1/2) & & B_z(i+1/2, j+1/2, k) \end{aligned} \quad (3.1)$$

where i, j, k indexes the number of grid points inside the simulation domain along the Ox, Oy and Oz axes. The Ampère and Faraday's laws:

$$\begin{aligned} \frac{\partial \vec{E}}{\partial t} &= \frac{1}{\epsilon_0} \left(\frac{\nabla \times \vec{B}}{\mu_0} - \vec{J} \right) \\ \frac{\partial \vec{B}}{\partial t} &= -\nabla \times \vec{E} \end{aligned} \quad (3.2)$$

are solved numerically using finite-differences method with a centered-difference scheme in order to obtain the electromagnetic field on the Yee lattice shown in Figure 3.1. In equation (3.2), \vec{J} is the total current density in the plasma, while ϵ_0 and μ_0 are the electrical permittivity and the magnetic permeability of the vacuum. All the simulations included in the present chapter are performed with periodic boundary conditions for the electric and magnetic fields (see Appendix A).

The time-step and the grid spacing used to solve the Maxwell's equations with finite-differences must satisfy the Courant condition of numerical stability which takes the following form for a three-dimensional problem (*Birdsall and Langdon, 1991*):

$$\frac{1}{(c \cdot \Delta t)^2} > \frac{1}{(\Delta x)^2} + \frac{1}{(\Delta y)^2} + \frac{1}{(\Delta z)^2} \quad (3.3)$$

where Δx , Δy , Δz represents the grid spacing along the Ox , Oy and Oz axes, Δt is the time-step and c is the speed of light in vacuum. In TRISTAN, the same grid spacing is used for all the three spatial coordinates, i.e. $\Delta x = \Delta y = \Delta z$. In this case, the inequality (3.3) is reduced to a more simplified form:

$$c \cdot \Delta t < \Delta x / \sqrt{3} \quad (3.4)$$

which is even more restrictive here than in the one-dimensional case (see Chapter 2). Also, the time-step must resolve the electron plasma frequency, while the grid spacing must be of the order of the electron Debye length λ_D (*Birdsall and Langdon, 1991*):

$$\Delta x < 3\lambda_D \quad (3.5)$$

to avoid the numerical instabilities related to the discretization of the configuration space.

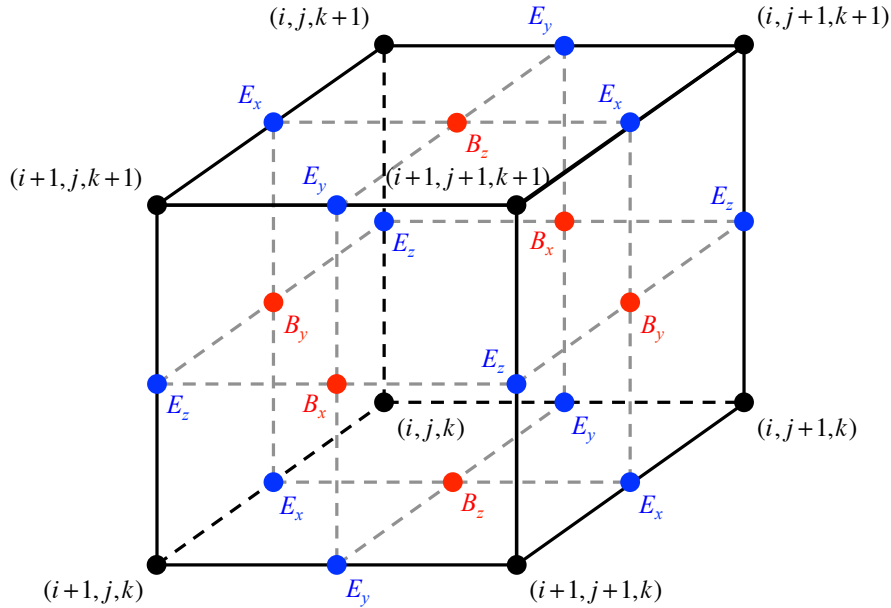


Figure 3.1 – Yee lattice (*Yee, 1966*) used to solve the Maxwell's equations using finite-differences method with a centered-difference scheme. The electric field is computed at the locations shown by blue dots, while the magnetic field is computed at the locations shown by red dots (adapted from *Yee, 1966*).

The electric charge of a finite-size superparticle is distributed among its eight neighboring grid points as a function of the distance between the exact position of the particle and the grid points, following the *volume weighting method* (*Buneman, 1993*). This latter is a first order interpolation scheme that operates in all the three spatial coordinates and is a three-dimensional generalization of the linear interpolation scheme used in the one-dimensional PIC simulations described in Chapter 2. In order to avoid the self-force, the volume weighting method together with the same grid points used to distribute the charges over the grid is also applied further to compute the electric and magnetic fields in the actual positions of the particles (see Appendix A for details).

The total current density is obtained from the so-called *current deposition of particles method* (Villasenor and Buneman, 1992). All the three components of the current density, both for electrons and ions, are calculated as the amount of charge that crosses the faces of the grid cells used to integrate the Maxwell's equations by finite-differences (see Appendix A for details). The current deposition of particles method ensures the conservation of the electric charge at each time-step during the simulation:

$$\frac{\partial \rho}{\partial t} + \nabla \cdot \vec{J} = 0 \quad (3.6)$$

where ρ is the electric charge density.

The positions \vec{r} and velocities \vec{v} of the particles are obtained by integrating numerically the relativistic equation of motion:

$$\begin{aligned} \frac{d\vec{r}}{dt} &= \frac{1}{\gamma} \vec{u} \\ \frac{d\vec{u}}{dt} &= \frac{q}{m} \left(\vec{E} + \frac{1}{\gamma} \vec{u} \times \vec{B} \right) \end{aligned} \quad (3.7)$$

where we used the notation $\vec{u} = \gamma \vec{v}$, $\gamma = 1 / \sqrt{1 - v^2 / c^2}$ is the relativistic factor and m is the rest mass of a particle. The equations (3.7) are discretized by using the leap-frog method. The velocity at a given time is computed explicitly with the *Buneman-Boris technique* (Birdsall and Langdon, 1991). The boundary conditions for particles are periodic.

The normalization of temporal and spatial scales used in TRISTAN code is defined such that the following quantities are equal to unity:

$$\Delta x = 1, \quad \Delta t = 1, \quad e / m_e = 1, \quad \epsilon_0 = 1 \quad (3.8)$$

where e is the elementary charge and m_e is the electron mass. A detailed description of the normalization scheme used in our simulations is given in Appendix B.

A schematic diagram illustrating the three-dimensional particle-in-cell simulation cycle implemented in TRISTAN is shown in Figure 3.2. At the beginning of the simulation, the positions and velocities of the particles and also the electric and magnetic fields are initialized according to the specific initial conditions that define the problem to study. It is important to check that the initial electromagnetic field satisfies the Maxwell's equations. Once the initialization is done, the equation of motion (3.7) is integrated numerically over the time-step Δt , for each simulated particle. Prior to the computation of particles' trajectories, a half-update of the magnetic field is performed, i.e. the Faraday's law is integrated in time over $\Delta t/2$, in order to provide the fields at the same instance of time for the integration of equation (3.7). This step is required since the electric and magnetic fields are staggered in time due to the centered-difference discretization applied for the Maxwell's equations. Thus, the new positions and velocities of the particles are determined and the total current density is computed by the current deposition technique. Periodic boundary conditions are applied for the particles that intersect the boundaries and leave the simulation domain. Further, the Ampère and Faraday's laws (3.2) are integrated over the three-dimensional spatial mesh shown in

Figure 3.1. The volume weighting method is then used to calculate the electric and magnetic fields in the position of each simulated particle. Periodic boundary conditions are considered also for the electromagnetic field. After updating the fields on the positions of the particles, the equation of motion is integrated again over the time-step Δt , thus providing the new set of positions and velocities. The cycle is continued until the condition that defines the end of the simulation is satisfied. The time-step and the grid spacing used must fulfill the numerical stability conditions expressed by the inequalities (3.4) and (3.5). A description of the formulas used in our 3D-PIC code is given in Appendix A.

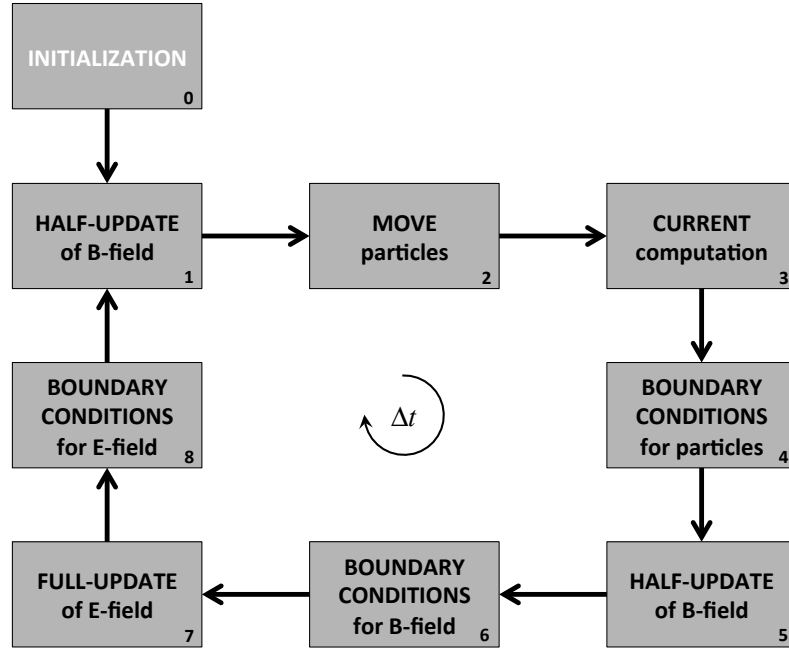


Figure 3.2 – Schematic diagram of a three-dimensional particle-in-cell simulation cycle. Each of the 8 steps illustrated above are performed iteratively until the end of the simulation. The time-step Δt must fulfill the Courant condition of numerical stability (adapted from *Cai et al.*, 2003).

3.2 The simulation setup

The simulation domain is defined between $[3, mx-2]$ along the Ox axis, $[3, my-2]$ along the Oy axis and $[3, mz-2]$ along the Oz axis, where mx , my , mz are the number of grid points along the three coordinate axes, with the grid spacing $\Delta x = \Delta y = \Delta z = 1$. The initial positions of the particles, electrons and protons that form the three-dimensional plasma element, are uniformly distributed inside the simulation domain over a rectangular region of width w_x along the Ox axis, w_y along the Oy axis and w_z along the Oz axis. A schematic diagram of the simulation geometry is shown in Figure 3.3.

The initial velocity distribution function (VDF) for both species is a displaced Maxwellian with an average velocity \vec{V}_0 parallel to the positive x -axis. The electrons and protons velocities are initialized according to their corresponding displaced Maxwellian distribution function. The background magnetic field \vec{B}_0 is constant and it is oriented along the positive direction of the z -axis and perpendicular to the initial bulk velocity of the

plasma element. We consider two different profiles for the external magnetic field: (i) an uniform field and (ii) a non-uniform field that varies with the x -coordinate over a finite width transition region having the length scale $x_2 - x_1$:

$$B_0(x) = \begin{cases} B_1, & \text{for } x < x_1 \\ B_1 + (B_2 - B_1) \frac{x - x_1}{x_2 - x_1}, & \text{for } x_1 \leq x \leq x_2 \\ B_2, & \text{for } x > x_2 \end{cases} \quad (3.9)$$

where B_1 is the asymptotic field in the left hand side of the transition region ($x < x_1$), while B_2 is the asymptotic field in the right hand side ($x > x_2$). At $t=0$, the electric field is set to zero everywhere inside the simulation domain.

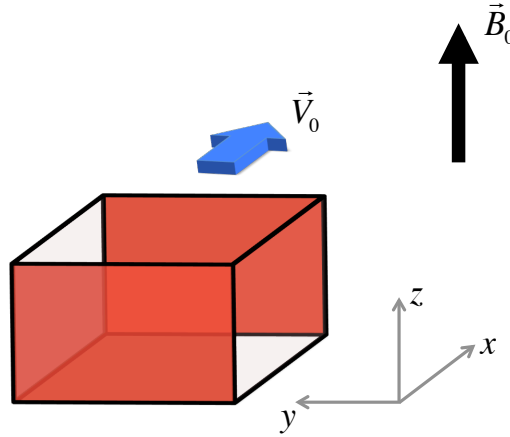


Figure 3.3 – Schematic diagram of the simulation setup. The three-dimensional plasma element/cloud (red rectangular box) is injected with a non-zero bulk velocity (blue arrow), in vacuum, across a transverse magnetic field (black arrow).

In the following section I discuss the results of numerical simulations of a *small Larmor radius plasma cloud*, i.e. a plasma cloud whose transversal dimension is much larger than the ion gyration radius. The cloud is injected in vacuum across two different profiles of the transverse magnetic field, i.e. uniform and non-uniform. I analyze and discuss five different cases.

In the first two cases I simulate the dynamics of a plasma element with the initial bulk velocity $V_0=0$ (case I) and $V_0 \neq 0$ (case II) immersed into a uniform magnetic field. These cases are devoted to “calibrate” the simulation and test that the results are correct for problems whose solution is known a priori. In the last three cases I investigate the role of the initial velocity on the dynamics of the cloud in a non-uniform magnetic field. The simulations describe the convection of a plasma element into the non-uniform magnetic field given by equation (3.9) with an initial slow speed (case III), intermediate speed (case IV) and fast speed (case V) plasma bulk velocity. The input parameters for all simulated cases are given in Table 3.1 and Table 3.2. The plasma element is formed from only electrons and protons. The physical quantities are expressed in normalized units, as discussed in Appendix B. Periodic boundary conditions for both particles and fields have been considered throughout all the simulations performed here.

Table 3.1 – Input parameters for all the simulations discussed in Chapter 3: m_i/m_e is the ion-to-electron mass ratio; T_e/T_i is the electron-to-ion temperature ratio; β_e is the plasma-beta parameter for electrons; ε is the dielectric constant of the plasma element; w_x, w_y, w_z are the widths of the plasma element along Ox, Oy, Oz axes; r_{Li} is the ion Larmor radius; Δx is the grid spacing; λ_D is the electron Debye length; Δt is the time-step; c is the speed of light in vacuum; N_c is the number of particles per grid-cell at $t=0$.

| | m_i/m_e | T_e/T_i | β_e | ε | w_x/r_{Li} | w_y/r_{Li} | w_z/r_{Li} | $\Delta x/\lambda_D$ | $c\Delta t/\Delta x$ | N_c |
|------------------|-----------|-----------|-----------|---------------|--------------|--------------|--------------|----------------------|----------------------|-------|
| All cases | 36 | 25 | 0.02 | 126 | 40 | 40 | 24 | 2.5 | 0.5 | 200 |

Table 3.2 – Input parameters for the five cases and the three sub-cases shown in Chapter 3: V_0 is the initial plasma bulk velocity; V_{Ti} is the ion thermal speed, $V_{Ti}=(2k_B T_i/m_i)^{1/2}$; B_1 and B_2 are the asymptotic magnetic fields defined in equation (3.9); x_1 and x_2 define the non-uniform magnetic field region given by equation (3.9); r_{Li} is the ion Larmor radius; x_0, y_0, z_0 gives the starting position of the plasma element along the Ox, Oy, Oz axes; m_x, m_y, m_z are the number of grid points along the Ox, Oy, Oz axes; T is the total simulation time; T_{Li} is the ion Larmor period.

| | V_0/V_{Ti} | $(B_2-B_1)/B_1$ | $(x_2-x_1)/r_{Li}$ | x_1 | x_0 | y_0 | z_0 | m_x | m_y | m_z | T/T_{Li} |
|------------------|--------------|-----------------|--------------------|-------|-------|-------|-------|-------|-------|-------|------------|
| Case I | 0 | 0 | – | – | 23.5 | 53.5 | 138.5 | 155 | 155 | 305 | 0.1 |
| Case II | 4.60 | 0 | – | – | 23.5 | 53.5 | 138.5 | 155 | 155 | 305 | 2 |
| Case III | 1.15 | 50% | 5 | 79 | 23.5 | 103.5 | 238.5 | 155 | 255 | 505 | 3.75 |
| Case IV-1 | 2.30 | 50% | 5 | 159 | 103.5 | 78.5 | 188.5 | 255 | 205 | 405 | 3 |
| Case IV-2 | 2.30 | 10% | 5 | 159 | 103.5 | 78.5 | 188.5 | 255 | 205 | 405 | 3 |
| Case IV-3 | 2.30 | 67% | 32 | 159 | 103.5 | 78.5 | 188.5 | 255 | 205 | 405 | 3 |
| Case V | 4.60 | 50% | 5 | 85 | 23.5 | 53.5 | 138.5 | 155 | 155 | 305 | 2 |

3.3 Numerical results

3.3.1 Case I: Stationary plasma element in uniform magnetic field

This first case is devoted to a plasma element at rest in a uniform and constant magnetic field and is performed in order to check whether the three dimensional code provides meaningful results for a simple physical situation. The input parameters for case I are given in Table 3.1 and Table 3.2. All the physical quantities used here are expressed in normalized units (see Appendix B). We analyze in detail the evolution of the plasma element during a time interval spanning the first three electron Larmor periods.

Figure 3.4 shows the initial number density of the plasma element. Two relevant cross-sections are illustrated inside the simulation domain: in the left panel the electron number density is shown in the xOy plane perpendicular to the background magnetic field, for $z=153$; in the right panel the electron number density is shown in the xOz plane parallel to the background magnetic field, for $y=78$. Initially, the electrons and ions have the same number density. As can be noticed in Figure 3.4, the initial shape of the plasma element is a rectangular box with uniform density. The velocity distribution function, at $t=0$, inside the central region of the plasma element is shown in Figure 3.5 for both electrons (left panel) and ions (right panel). The distribution functions are computed as histograms in a 2D cross-section of the three-dimensional velocity space for $v_z=0$; the histograms are computed in a spatial region defined by $46 \leq x \leq 51$, $68.5 \leq y \leq 88.5$ and $3 \leq z \leq 303$. Figure 3.5 shows that the initial VDF is an isotropic Maxwellian with zero average velocity.

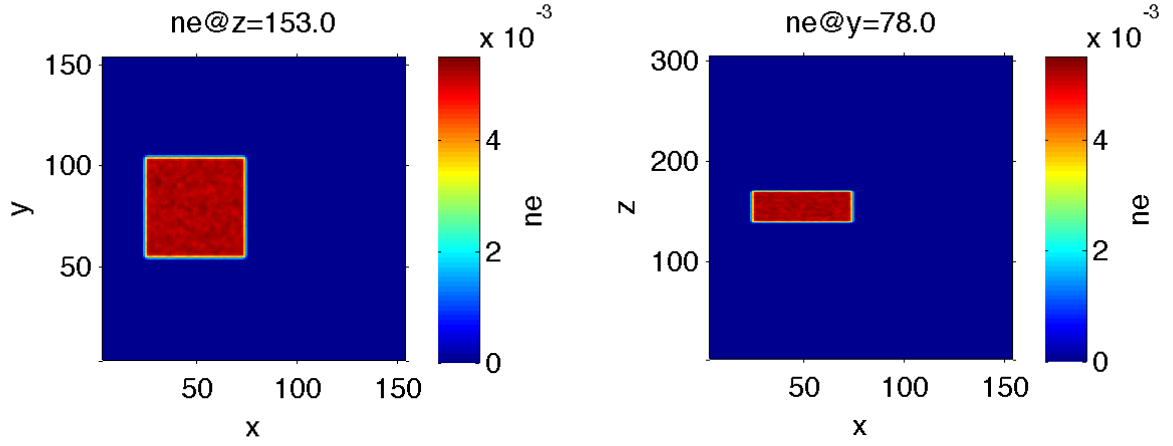


Figure 3.4 – Initial number density of electrons in the xOy (left panel) and xOz (right panel) sections of the simulation domain. The uniform background magnetic field is parallel to the z -axis. The ions and electrons are initialized with the same number density. At $t=0$ the three-dimensional plasma element has a rectangular shape and a uniform density.

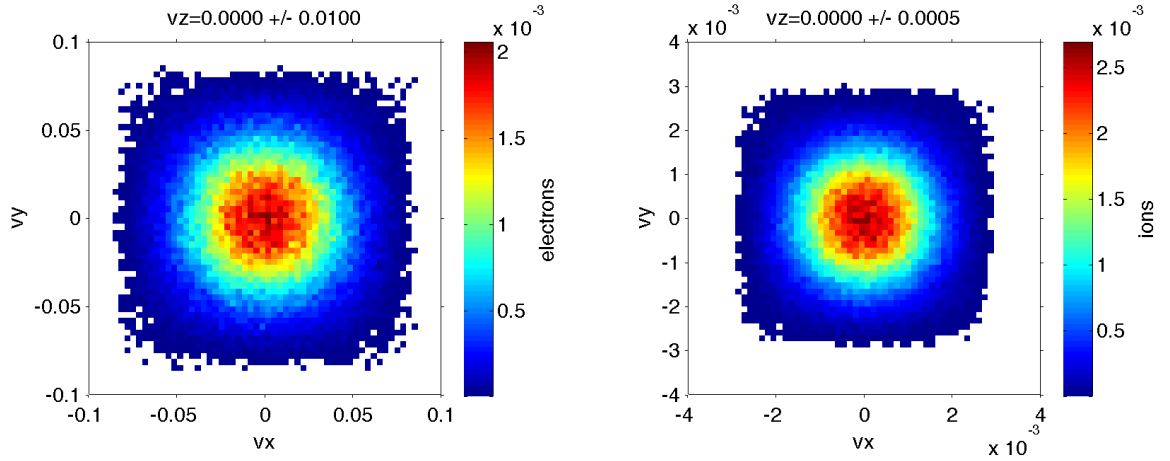


Figure 3.5 – Initial velocity distribution function of electrons (left panel) and ions (right panel) in the $v_z=0$ section perpendicular to the background magnetic field. The VDFs are computed in the central region of the plasma element for $46 \leq x \leq 51$, $68.5 \leq y \leq 88.5$ and $3 \leq z \leq 303$. Note that the initial velocity distribution function of both electrons and ions is an isotropic Maxwellian with zero average velocity.

In Figure 3.6 and Figure 3.7 we illustrate the number densities of electrons n_e (top panels) and ions n_i (middle panels) and also the net charge density computed as $n_i - n_e$ (bottom panels) in the xOy plane perpendicular to the background magnetic field (Figure 3.6), for the cross-section $z=153$, and in the xOz plane parallel to the background magnetic field (Figure 3.7), for the cross-section $y=78$. On the left column of the two figures we show the results obtained at $t=T_{Le}/2$, while on the right column we have the results at $t=3T_{Le}$, where T_{Le} represents the electron Larmor period. The electric field corresponding to the same cross-sections and to the same moments of time as in the two aforementioned figures is shown in Figure 3.8 (E_x and E_y components perpendicular to the background magnetic field) and in Figure 3.9 (parallel component E_z).

At the early stages of the simulation ($t \ll T_{Le}$), the particles located at the edges of the plasma element will move outward with respect to the central core of the cloud.

Therefore, the plasma will expand in vacuum due to the thermal motion of both electrons and ions. Having a higher thermal velocity than the ions, the electrons will expand more rapidly and space charge layers will be formed at the boundaries of the plasma element. Indeed, as can be noticed in Figure 3.6 and Figure 3.7 (bottom-left panels), at a half of the electron Larmor period, the plasma cloud can be divided into three different main regions: (i) a quasineutral core with equal number densities for both electrons and ions, (ii) a positive charge layer of protons surrounding the quasineutral core and (iii) a negative charge layer of electrons at the outer edges of the plasma cloud. Both space charge layers have a width of the order of few electron/ion Larmor radii. As a consequence, an outward directed electric field is formed at the boundaries of the plasma element, as can be seen in Figure 3.8 and Figure 3.9. The net charge density fluctuations observed inside the quasineutral core of the plasma cloud are in fact due to a statistical noise introduced by the limited number of particles loaded into the simulation domain. By increasing the number of simulated particles one would reduce the amplitude of these fluctuations.

At later stages of the simulation ($T_{Le}/2 < t \ll T_{Li}$), the two space charge layers will evolve differently in the plane perpendicular and parallel to the magnetic field. Let's analyze now the dynamics of the plasma cloud in the perpendicular plane to the background magnetic field. The Lorentz force deflects the electrons and eventually stops the outward expansion. Simultaneously, the ions are accelerated by the outward directed electric field and, in combination with the thermal motion, will continue to expand to larger radial distances than the electrons. Thus, the two space charge boundary layers will develop opposite polarities now than in the early stages of the simulation. When the ions also become magnetized, at $t > T_{Li}/2$, their thermal expansion is hindered by the gyration motion in the background magnetic field. Nevertheless, on average, a positive charge layer will persist at the outer edges of the plasma cloud since the ion Larmor radius is larger than the one of electrons. Note however that this effect is reduced in our simulations as the proton-to-electron mass ratio has been altered from 1836 to 36 in order to be able to perform a large enough number of simulation iterations and to cover simulation times of the order of the proton Larmor period.

From the inspection of the net charge density in the xOy plane perpendicular to the background magnetic field at $t=3T_{Le}$ (see Figure 3.6, bottom-right panel), one can notice that the structure of the plasma cloud has changed, compared to the early stages of the simulation. A negative charge layer now surrounds the quasineutral core, while at the outer edges of the plasma cloud a positive layer is formed. Moreover, by a closer look at the bottom-right panel of Figure 3.6, we can notice that a slightly negative charge density is distinguished at the outer boundary of the ion charge layer. The electric field has a more complicated structure now than in the early stages of the simulation (see Figure 3.8, right panels). An alternating inward-outward electric field is observed at the edges of the plasma element in the xOy plane. In our computations the electron r_{Le} and ion r_{Li} Larmor radii have comparable values, i.e. $r_{Li}/r_{Le}=1.2$. Therefore,

since the electron and ion Larmor scales are approximately equal, the two space charged boundary layers are not well separated and, as a consequence, an inward directed electric field is not clearly evidenced at the edges of the plasma cloud for $t > T_{Le}$. Nevertheless, the numerical experiments performed using a larger r_{Li}/r_{Le} ratio emphasized the presence of an inward directed electric field at the outer boundaries of the plasma cloud for time scales larger than the electron Larmor period and up to $1.5T_{Li}$.

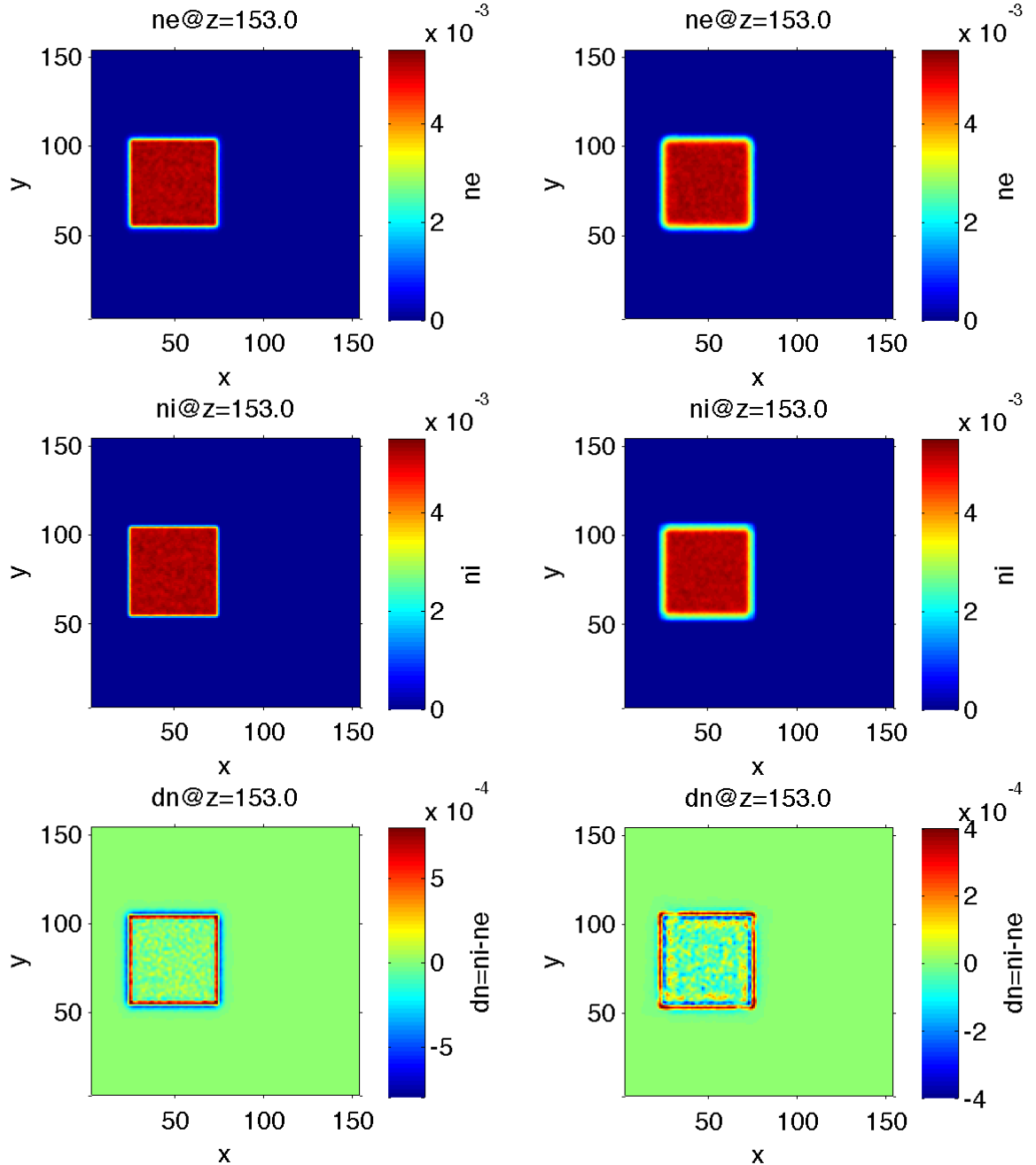


Figure 3.6 – Number densities of electrons n_e (top panels) and ions n_i (middle panels) and the electric charge separation computed as $n_i - n_e$ (bottom panels) at $t=T_{Le}/2$ (left column) and $t=3T_{Le}$ (right column), where T_{Le} is the electron Larmor period; xOy central sections perpendicular to the background magnetic field are shown.

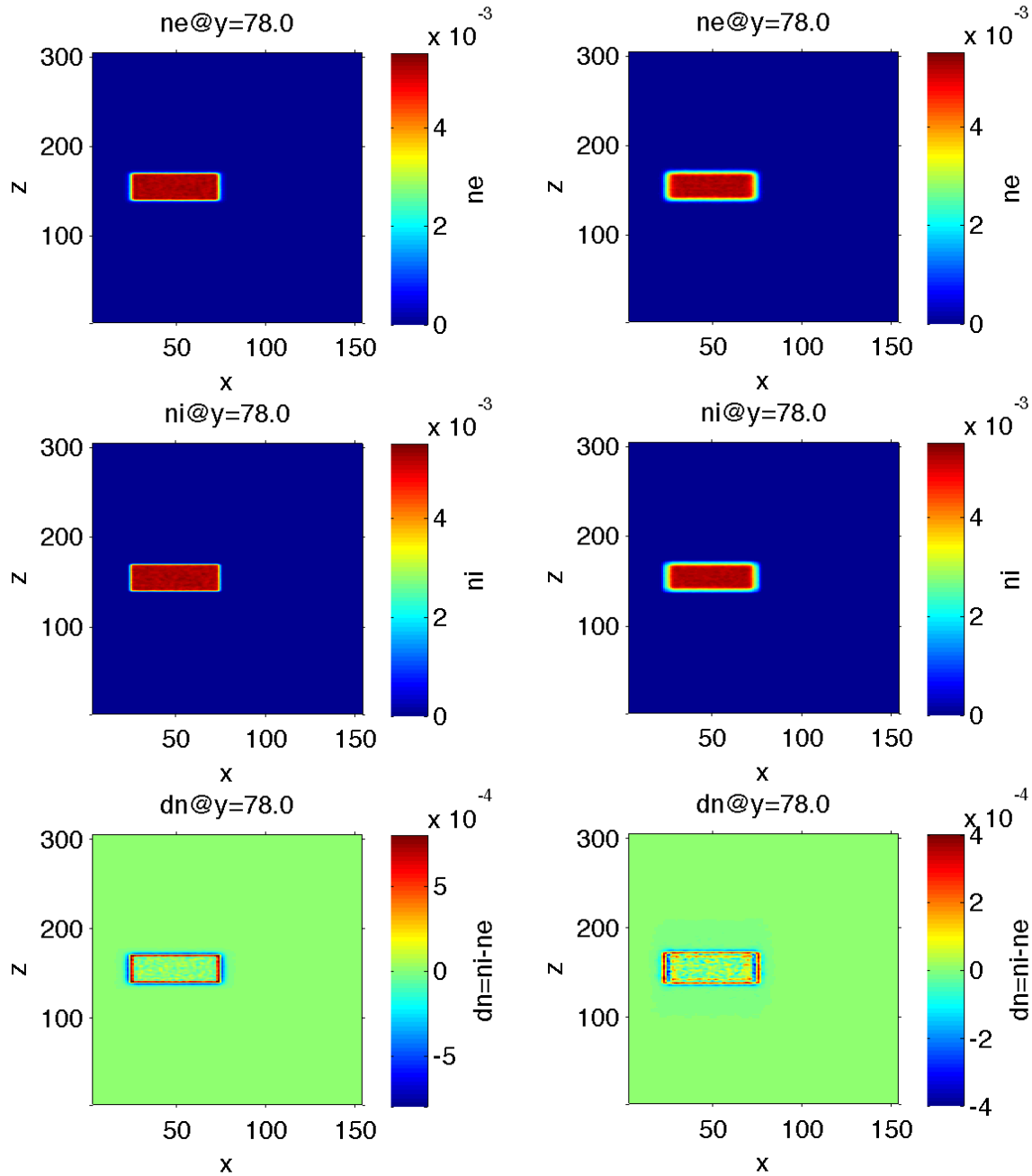


Figure 3.7 – Number densities of electrons n_e (top panels) and ions n_i (middle panels) and the charge separation computed as $n_i - n_e$ (bottom panels) at $t = T_{Le}/2$ (left column) and $t = 3T_{Le}$ (right column), where T_{Le} is the electron Larmor period; xOz central sections parallel to the ambient magnetic field are shown.

The plasma dynamics along the Oz axis parallel to the background magnetic field has a different evolution from that in the xOy plane perpendicular to \vec{B}_0 . The parallel electric field created by the thermal motion of particles along the magnetic field lines (see Figure 3.9) will tend to reduce the expansion rate of the plasma cloud in the positive and negative directions of the z -axis. Indeed, the electrons located at the edges of the plasma element will be slowed-down by the outward parallel electric field, while the ions will be accelerated. As a result, the charge separation between the two species will decrease and consequently the parallel electric field will be less intense (see Figure 3.9). Nevertheless, the particles expansion along the magnetic field lines will continue to

exist and the plasma number density in the perpendicular plane to the background magnetic field will decrease drastically. After only few ion Larmor periods the particles reach the boundaries of the simulation domain and the number density inside the central core of the plasma element is one order of magnitude smaller than it is initially. The degradation of the plasma element along the magnetic field lines has a significant impact on the propagation of a plasma element across a transverse magnetic field, as it will be discussed further in the other simulated cases.

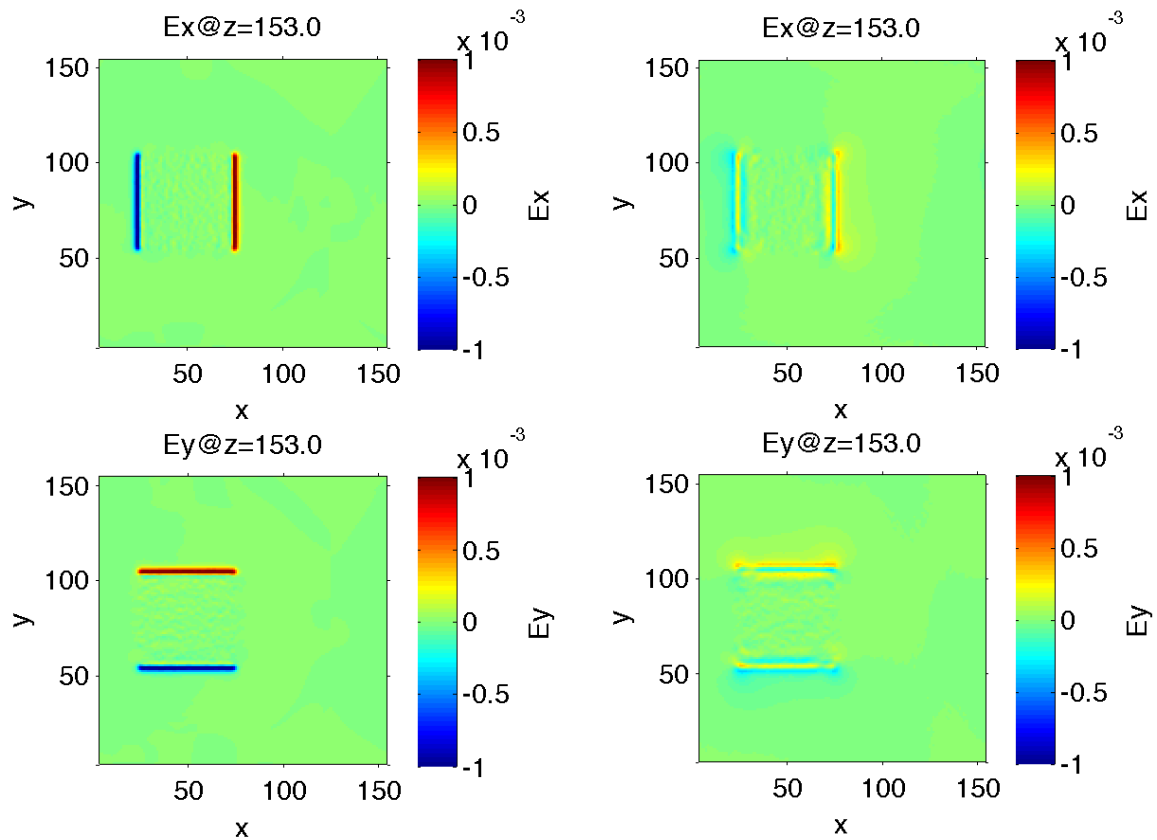


Figure 3.8 – E_x (top panels) and E_y (bottom panels) components of the electric field at $t=T_{Le}/2$ (left column) and $t=3T_{Le}$ (right column), where T_{Le} is the electron Larmor period; xOy central sections perpendicular to the background magnetic field are shown.

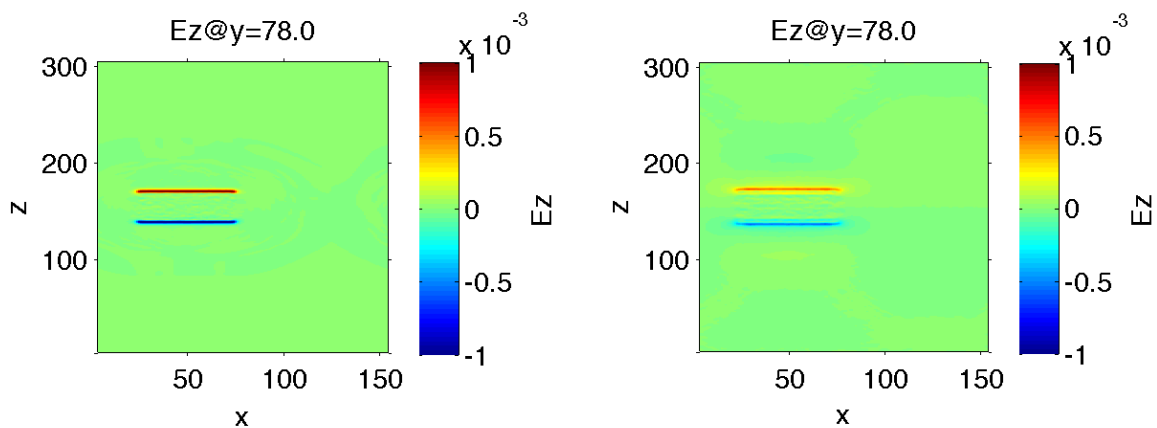


Figure 3.9 – E_z component of the electric field at $t=T_{Le}/2$ (left panel) and $t=3T_{Le}$ (right panel), where T_{Le} is the electron Larmor period; xOz central sections parallel to the background magnetic field are shown.

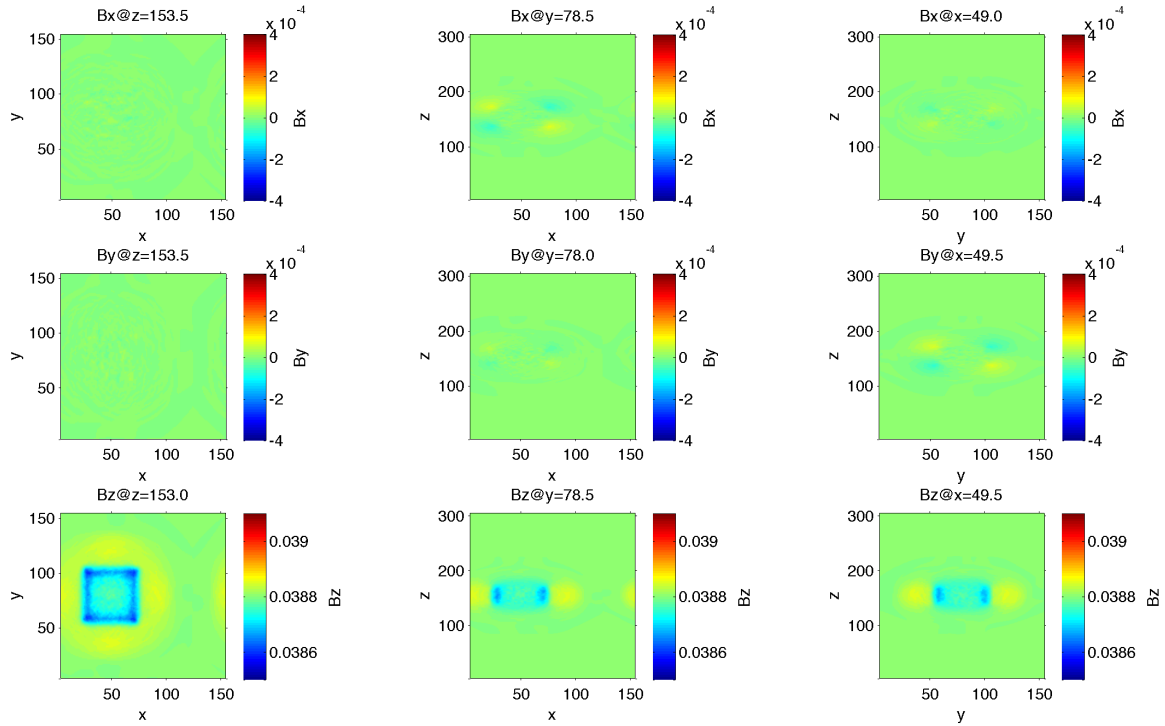


Figure 3.10 – The B_x (top panels), B_y (middle panels) and B_z (bottom panels) components of the magnetic field, at $t=T_{Le}/2$ (T_{Le} is the electron Larmor period), in the xOy plane (left column), xOz plane (middle column) and yOz plane (right panel) inside the simulation domain, for the cross-sections specified in the title of each of the nine plots.

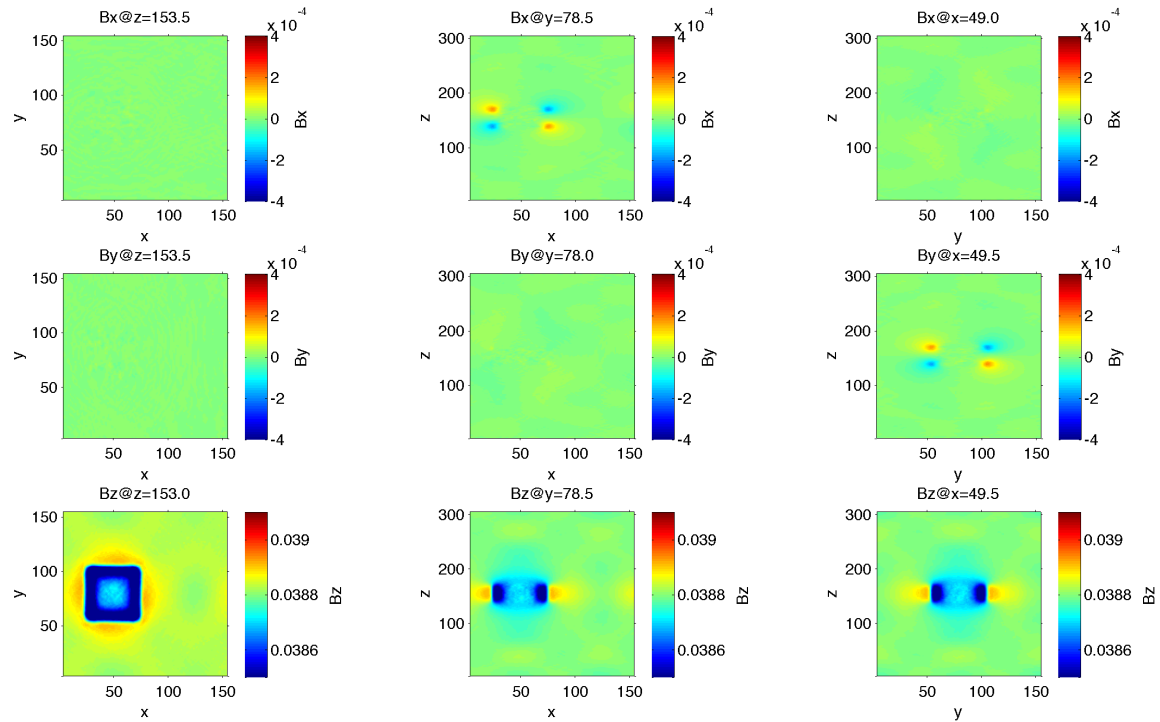


Figure 3.11 – The B_x (top panels), B_y (middle panels) and B_z (bottom panels) components of the magnetic field, at $t=3T_{Le}$ (T_{Le} is the electron Larmor period), in the xOy plane (left column), xOz plane (middle column) and yOz plane (right panel) inside the simulation domain, for the cross-sections specified in the title of each of the nine plots.

The magnetic field for nine different cross-sections inside the simulation domain is shown in Figure 3.10 for $t=T_{Le}/2$ and in Figure 3.11 for $t=3T_{Le}$. We illustrate the B_x (top panels), B_y (middle panels) and B_z (bottom panels) components of the magnetic field in the xOy plane (left column), xOz plane (middle column) and yOz plane (right column), for the cross-sections specified at the top of each plot. By analyzing the top and middle panels of Figure 3.10 and Figure 3.11, we can notice that the B_x and B_y components of the magnetic field are two orders of magnitude smaller than the ambient magnetic field oriented along the positive z -axis. Indeed, since the β -parameter of the plasma cloud is of the order of 10^{-2} , the self-consistent contribution of electrons and ions to the total magnetic field is negligible. Nevertheless, a diamagnetic cavity is formed in the actual position of the plasma cloud, as can be observed in the bottom panels of Figure 3.10 and Figure 3.11. Inside the diamagnetic cavity the B_z component of the total magnetic field decreased by less than 1% from the background magnetic field value B_0 ($B_0=0.0388$ normalized units).

In Figure 3.12 we present the J_x (top panels) and J_y (bottom panels) components of the total current density, at $t=T_{Le}/2$ (left column) and $t=3T_{Le}$ (right column), for a central cross-section in the xOy plane perpendicular to the background magnetic field. An electric current flows at the boundaries of the plasma element along the positive x -axis at the top edge of the cloud ($J_x>0$), along the negative y -axis at the right edge ($J_y<0$), along the negative x -axis at the bottom edge ($J_x<0$) and along the positive y -axis at the left edge of the cloud ($J_y>0$). This is a diamagnetic current, \vec{J}_D , that flows wherever there is a kinetic pressure gradient inside the plasma (Chen, 1974):

$$\vec{J}_D = \frac{\vec{B} \times \nabla p}{B^2} \quad (3.10)$$

where $p=n_e k_B T_e + n_i k_B T_i$ is the total kinetic pressure, T_e and T_i are the electron and ion temperatures, while k_B is the Boltzmann's constant. Indeed, in our simulations there is a pressure gradient at the plasma-vacuum boundaries that is pointing radially inwards with respect to the center of the cloud. Therefore, the $\vec{B} \times \nabla p$ current will be positive at the top and the left edges of the plasma element and negative at the bottom and the right edges, in agreement with the numerical results obtained.

Besides the diamagnetic current (3.10) circulating around the quasineutral core of the plasma element, there is an additional current directed radially outward with respect to the center of the cloud. It is positive at the right ($J_x>0$) and top ($J_y>0$) edges of the plasma element and negative at the left ($J_x<0$) and bottom ($J_y<0$) edges. This current is related to the thermal expansion of the electrons and ions at the plasma-vacuum interface, as discussed previously. The gyration motion in the plane perpendicular to the magnetic field has a direct effect on the expansion of the electrons at the boundaries of the plasma cloud. Thus, the radially directed flux of electrons at the edges of the cloud will oscillate with the Larmor frequency from positive to negative \vec{J}_D values. On the other hand, for $t \ll T_{Li}$, the flux of ions at the boundaries of the plasma is pointing radially

outward with respect to the center of the cloud; the ions are virtually not magnetized at these early moments of the simulation. This behavior is well illustrated in Figure 3.13 and Figure 3.14 where we plot the dependencies $J_x=J_x(x)$ (Figure 3.13) and $J_y=J_y(y)$ (Figure 3.14) at $t=T_{Le}/4$ (top panels), $t=T_{Le}/2$ (middle-top panels), $t=2.5T_{Le}$ (middle-bottom panels) and $t=3T_{Le}$ (bottom panels), for both electrons (left column) and ions (right column). It can be noticed that indeed the electron current density is oscillating in the xOy plane perpendicular to \vec{B}_0 , while the ions continue to expand radially outward over the three electron Larmor periods simulated here. At $t=T_{Le}/2$, the current is carried only by the electrons since their thermal velocity is higher than for the ions. This effect is shown in the top panels of Figure 3.13 and Figure 3.14. On the other hand, at $t=3T_{Le}$, the electron and ion currents at the edges of the plasma cloud are flowing in opposite directions. At this time, the current density for the ions being a bit larger than for the electrons, a small radially outward total current density exists at the outer boundaries of the plasma element, as can be observed also in Figure 3.12. The current density fluctuations observed inside the quasineutral core of the plasma cloud are related also to the limited number of particles loaded into the simulation domain, similar to the statistical noise observed for the net charge density. As indicated previously, an increased number of simulated particles should reduce the amplitude of these fluctuations.

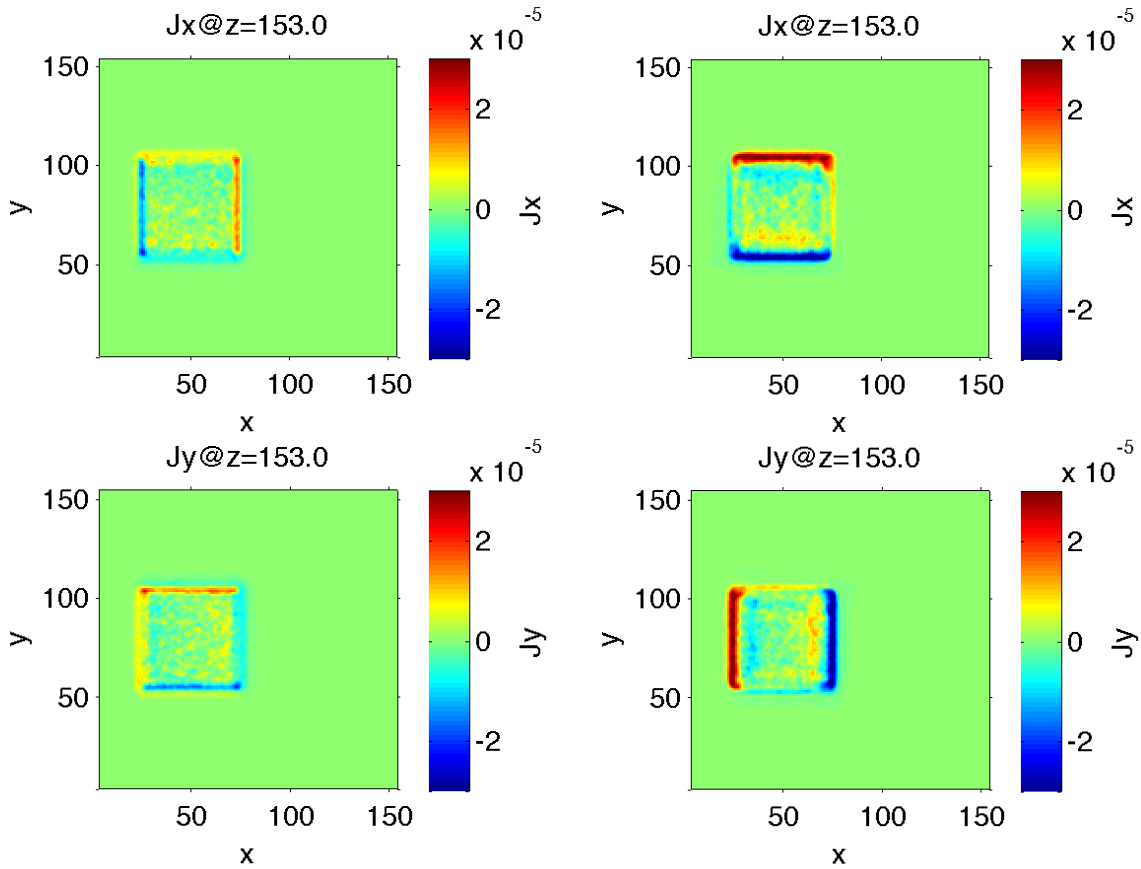


Figure 3.12 – J_x (top panels) and J_y (bottom panels) components of the total current density at $t=T_{Le}/2$ (left column) and $t=3T_{Le}$ (right column), where T_{Le} is the electron Larmor period; xOy central sections perpendicular to the background magnetic field are shown.

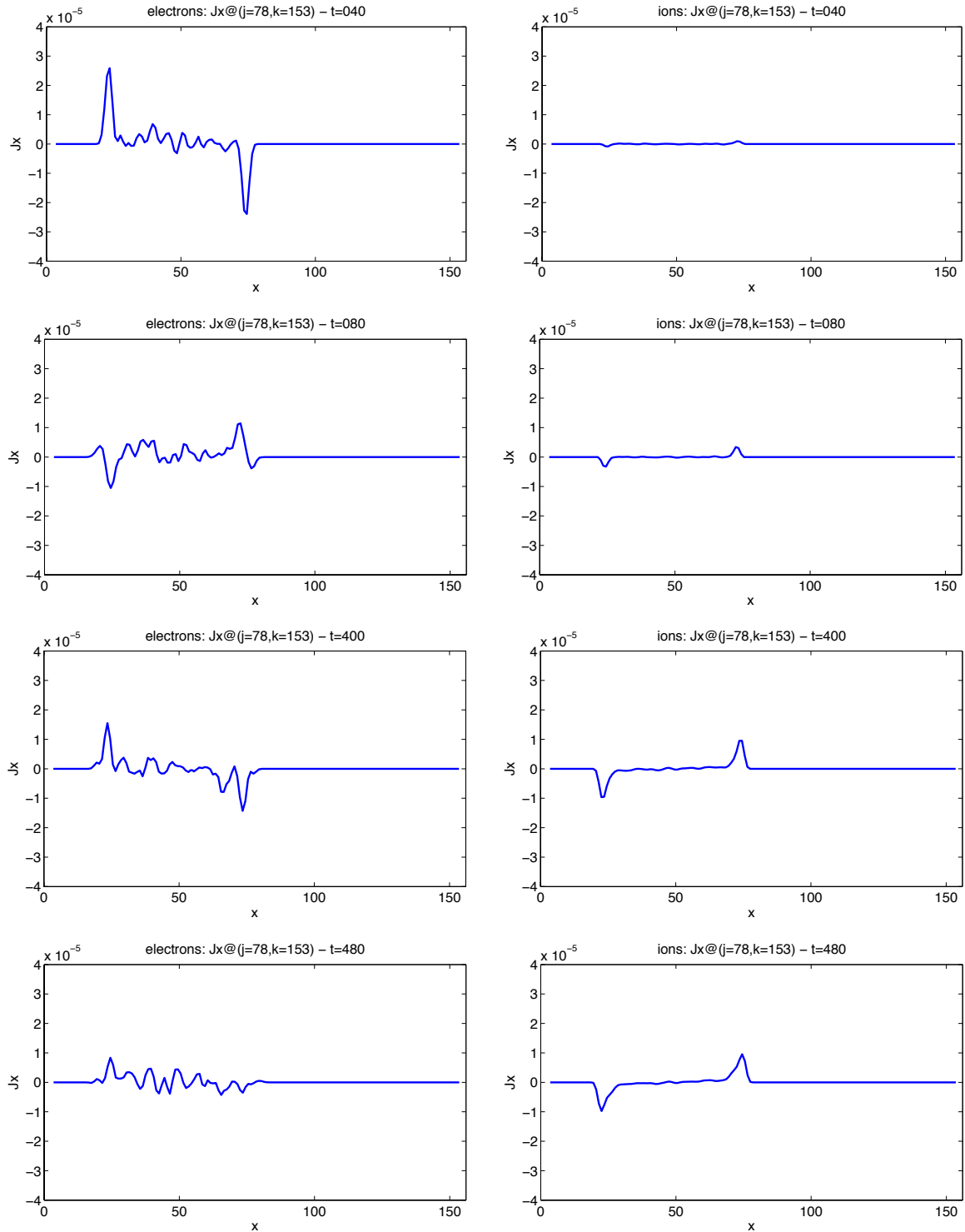


Figure 3.13 – Variation with x of the J_x component of the current density for electrons (left panels) and ions (right panels) at $t=T_{Le}/4$ (top panels), $t=T_{Le}/2$ (middle-top panels), $t=2.5T_{Le}$ (middle-bottom panels) and $t=3T_{Le}$ (bottom panels), where T_{Le} is the electron Larmor period. The dependence $J_x=J_x(x)$ is shown for $y=78$ and $z=153$.

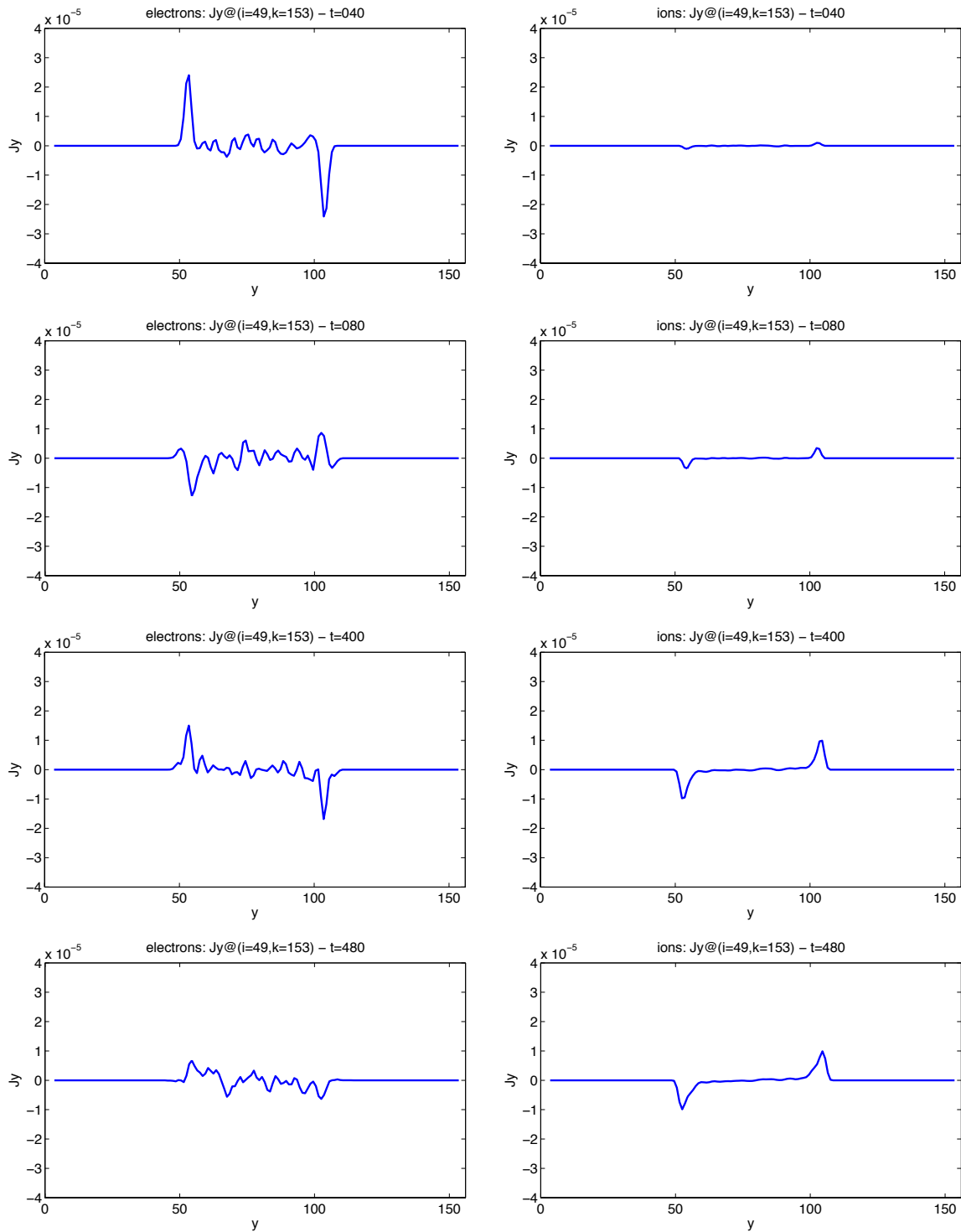


Figure 3.14 – Variation with y of the J_y component of the current density for electrons (left panels) and ions (right panels) at $t=T_{Le}/4$ (top panels), $t=T_{Le}/2$ (middle-top panels), $t=2.5T_{Le}$ (middle-bottom panels) and $t=3T_{Le}$ (bottom panels), where T_{Le} is the electron Larmor period. The dependence $J_y=J_y(y)$ is shown for $x=49$ and $z=153$.

In Figure 3.16 and Figure 3.17 we show the velocity distribution function of both electrons (Figure 3.16) and ions (Figure 3.17) at $t=3T_{Le}$. The VDFs are computed as two-dimensional velocity histograms in the (v_x, v_y) plane perpendicular to the background magnetic field for $v_z=0$. Five spatial bins have been selected to calculate the velocity distribution functions and are marked with black rectangles in Figure 3.15 where we illustrate a zoom in the top-right panel of Figure 3.6. The bins are located at the following positions in the xOy plane: (left bin) $21 \leq x \leq 26$ and $68.5 \leq y \leq 88.5$; (right bin) $71 \leq x \leq 76$ and $68.5 \leq y \leq 88.5$; (top bin) $38.5 \leq x \leq 58.5$ and $101 \leq y \leq 106$; (bottom bin) $38.5 \leq x \leq 58.5$ and $51 \leq y \leq 56$; (middle bin) $46 \leq x \leq 51$ and $76 \leq y \leq 81$. All five spatial bins extend in the Oz direction, i.e. $3 \leq z \leq 303$. Each (v_x, v_y) plot in Figure 3.16 and Figure 3.17 corresponds to a spatial bin illustrated in Figure 3.15.

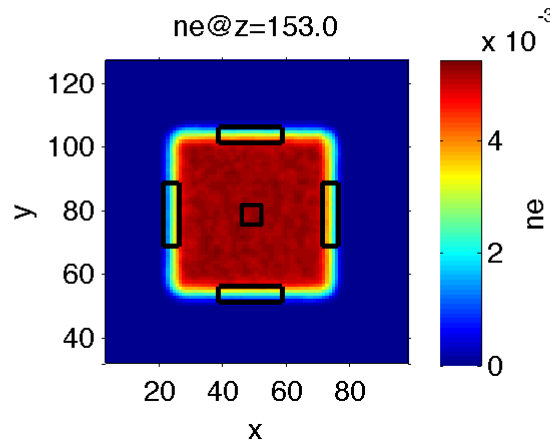


Figure 3.15 – Number density of electrons at $t=3T_{Le}$, where T_{Le} is the electron Larmor period, in the xOy central section perpendicular to the background magnetic field. This is a zoom in the top-right panel of **Figure 3.6**. The five black rectangles mark the spatial bins used to compute the velocity distribution function for both electrons and ions.

The velocity distribution function inside the central region of the plasma element is an isotropic Maxwellian with zero average velocity, for both electrons and ions. When one compares the middle panels of Figure 3.16 and Figure 3.17 with Figure 3.5, one notices the similarities with the initial VDF. On the other hand, at the edges of the plasma cloud the velocity distribution function is non-Maxwellian. Indeed, the VDFs of both electrons and ions for the left, right, top and bottom spatial bins are anisotropic with an increased density in certain regions of the perpendicular velocity space. For instance, the electrons localized inside the right spatial bin have a positive average velocity along the Oy axis (see right panel of Figure 3.16), while the ones inside the left bin have a negative average velocity along the Oy axis (see left panel of Figure 3.16). This effect is induced by the diamagnetic drift of electrons flowing in the $\nabla p \times \vec{B}$ direction at the boundaries of the plasma element. In the case of ions, the velocity distribution function at the edges of the cloud is a displaced Maxwellian with a long high-energy tail (see Figure 3.17). Unlike the electrons, the ions are still unmagnetized at the very early stages of the simulation. As a result, the gyration motion in the perpendicular plane to

the magnetic field does not have yet a significant effect on the trajectories of the ions. Thereby, the features of the velocity distribution function observed at the left, right, top and bottom spatial bins emphasize the radially outward thermal expansion of the ions at the boundaries of the plasma element. The formation of the high-energy tail is due to the acceleration of the ions by the outward directed electric field acting at the edges of the cloud (see Figure 3.8).

The numerical experiment performed in the first case shown here played the role of a key-test for our PIC-3D simulation code in a plasma-field configuration that is of interest for my PhD thesis. The main goal was to simulate the early evolution of a stationary plasma element immersed in a uniform magnetic field and to recover what is already known about this topic. The numerical results obtained here confirm and generalize to three-dimensions the detailed simulations published previously by *Galvez et al. (1988)* that have been performed using a two-dimensional electrostatic particle-in-cell code.

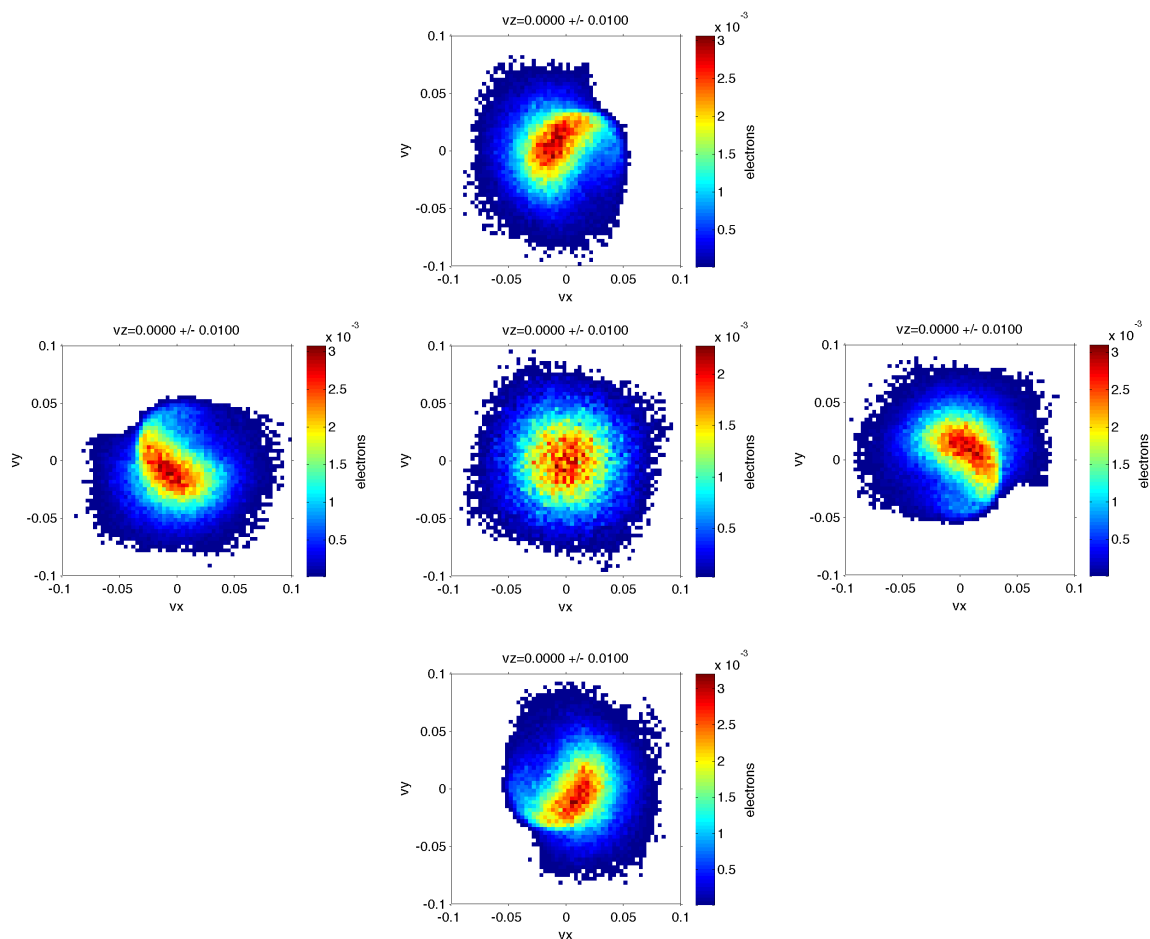


Figure 3.16 – Velocity distribution function of electrons at $t=3T_{Le}$ in the $v_z=0$ section perpendicular to the background magnetic field; T_{Le} is the electron Larmor period. Each of the five (v_x, v_y) panels correspond to a certain spatial bin that covers the entire simulation domain along the z -axis. The bins locations in the xOy plane are shown with black rectangles in **Figure 3.15**.

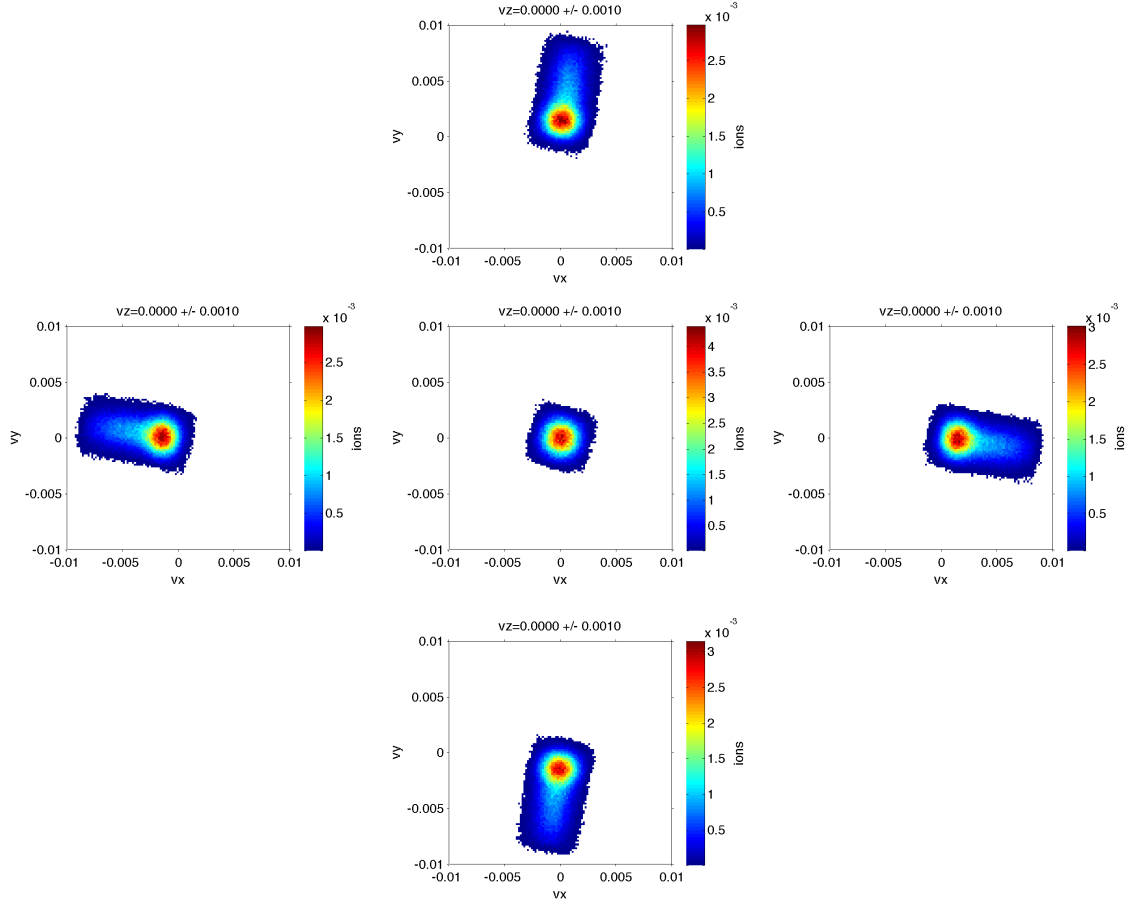


Figure 3.17 – Velocity distribution function of ions at $t=3T_{Le}$ in the $v_z=0$ section perpendicular to the background magnetic field; T_{Le} is the electron Larmor period. Each of the five (v_x, v_y) panels correspond to a certain spatial bin that covers the entire simulation domain along the z -axis. The bins locations in the xOy plane are shown with black rectangles in **Figure 3.15**.

3.3.2 Case II: Plasma element streaming across a uniform magnetic field

In the second case we simulate the dynamics of a plasma cloud streaming with a non-zero bulk velocity, $V_0 \neq 0$, across a uniform background magnetic field, $B_0 = \text{const.}$, as shown in Figure 3.3. The input parameters for case II are given in Table 3.1 and Table 3.2. All the physical quantities are expressed in normalized units (see Appendix B). We analyze the evolution of the plasma and electromagnetic field over two ion Larmor periods.

When a low- β plasma element is injected across a transverse magnetic field, two space charge layers will be formed at the lateral edges of the plasma element along the $\vec{V}_0 \times \vec{B}_0$ direction, as shown in Figure 3.18 (panel b), since the electrons and ions are gyrating in opposite directions in the perpendicular plane to the magnetic field (see Figure 3.18, panel a). Therefore, a polarization electric field, \vec{E}_p , will form inside the quasineutral bulk of the plasma, as described by *Schmidt* (1960):

$$\vec{E}_p = -\vec{V}_0 \times \vec{B}_0 \quad (3.11)$$

where \vec{V}_0 is the initial bulk velocity of the plasma element injected perpendicular to the ambient magnetic field \vec{B}_0 . Under some circumstances, the polarization electric field

(3.11) will enable the convection of the plasma across the magnetic field with approximately the injection velocity. The first requirement is that the kinetic energy density of the plasma element to be much larger than the polarization electric field energy density or, equivalently, that the dielectric constant of the plasma, ϵ , to be very large compared to unity (*Livesey and Pritchett, 1989*):

$$\epsilon = 1 + \frac{\omega_{pi}^2}{\omega_{Li}^2} \gg 1 \quad (3.12)$$

where ω_{pi} is the ion plasma frequency and ω_{Li} is the ion Larmor frequency. Moreover, in order to have the quasineutrality condition fulfilled inside the bulk of the plasma cloud, a second requirement must be accomplished (*Livesey and Pritchett, 1989*):

$$\epsilon \gg \sqrt{\frac{m_i}{m_e}} \quad (3.13)$$

where m_i and m_e are the ion and electron masses. An additional condition necessary to enable the polarization of the plasma element is that the two space charge layers to be much thinner compared to the width of the cloud (*Livesey and Pritchett, 1989*). Under these circumstances, the plasma element will stream across the background magnetic field with the bulk velocity \vec{V}_p (*Livesey and Pritchett, 1989*):

$$\vec{V}_p = \left(1 - \frac{1}{\epsilon}\right) \vec{V}_0 \quad (3.14)$$

which is approximately equal to the injection velocity when $\epsilon \gg 1$.

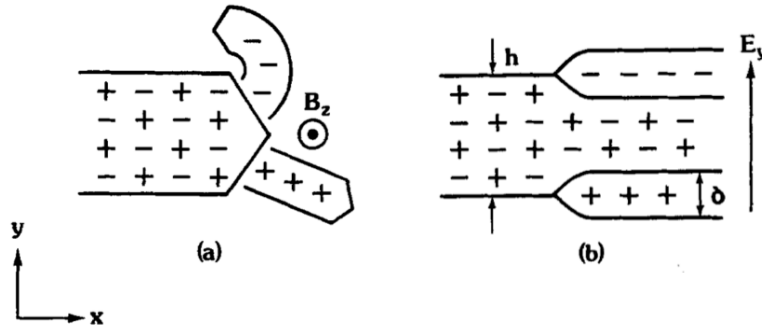


Figure 3.18 – Schematic diagram of the two space charge layers forming at the edges of a plasma beam injected across a transverse background magnetic field. Panel (a) illustrate the trajectories of the electrons and ions immediately after injection, while panel (b) shows the polarization electric field inside the quasineutral plasma core (adapted from *Livesey and Pritchett, 1989*).

In Figure 3.19 we show the variation along the y-axis of the net charge density (top panels) and of the E_y component of the electric field (bottom panels), at $t=T_{Le}/4$, for case I where $V_0=0$ (left column) and for case II where $V_0 \neq 0$ (right column). As it was described in the previous section, at the early stages of the simulation (for time intervals shorter than the electron Larmor period) the plasma element can be divided into three main regions: (i) a quasineutral core with equal number densities for both electrons and ions, (ii) a positive charge layer surrounding the quasineutral core and (iii) a negative charge layer at the outer edges of the plasma cloud. These features can be easily

observed for both simulated cases in the top panels of Figure 3.19. Inside the quasineutral core of the plasma cloud there are statistical fluctuations of the net charge density due to the limited number of simulated particles considered.

A closer examination of the space charge density profiles shown in Figure 3.19 reveals the polarization of the plasma element when is streaming perpendicular to the background magnetic field (see top-right panel), in contrast to the first case where the plasma is at rest (see top-left panel). Indeed, the total net charge density in case II is slightly positive at the bottom edge of the cloud (for $45 \leq y \leq 55$) and slightly negative at the top edge of the cloud (for $100 \leq y \leq 110$). On the other hand, in case I, the two aforementioned boundaries show no net charges on average. As a result, a polarization electric field, $E_y \approx V_0 B_0$, is formed inside the quasineutral core of the plasma element in case II (see bottom-right panel). Instead, in case I when plasma is at rest, no electric field is observed inside the main bulk of the cloud (see bottom-left panel). This polarization electric field will enable the forward convection of the plasma element across the magnetic field.

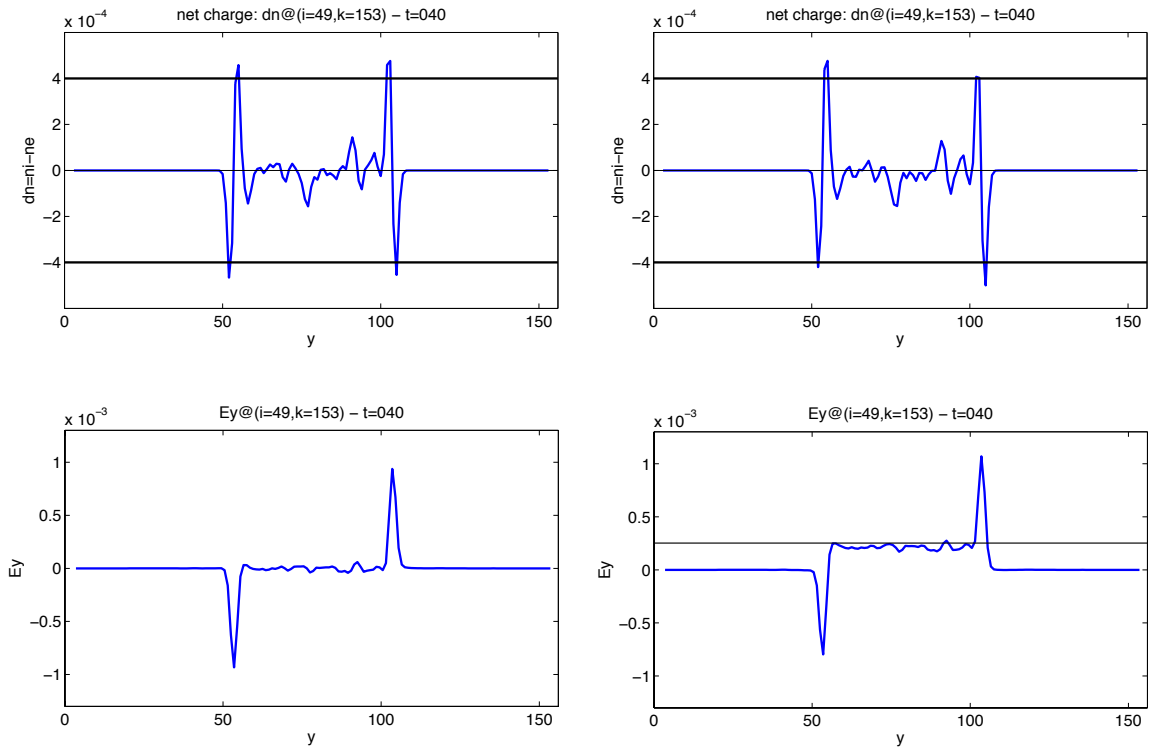


Figure 3.19 – Variation along the y -axis of the net charge density (top panels) and of the E_y component of the electric field (bottom panels), at $t = T_{Le}/4$, for case I (left column) and case II (right column); T_{Le} is the electron Larmor period. The black line in the bottom-right panel marks the value of the polarization electric field given by equation (3.11), i.e. $E_y = V_0 B_0$.

In Figure 3.20 and Figure 3.21 we show the number density of electrons n_e (top panels) and ions n_i (middle panels) and also the net charge density computed as $n_i - n_e$ (bottom panels) in the xOy plane (left column), xOz plane (middle column) and yOz plane (right column), at $t = T_{Li}$ (Figure 3.20) and $t = 2T_{Li}$ (Figure 3.21), where T_{Li} is the ion

Larmor period. The numerical results obtained clearly illustrate the propagation of the plasma element across the ambient magnetic field. During the entire simulation time that takes two ion gyration periods, the plasma cloud traveled along the positive direction of the x-axis over a distance of about 56 ion Larmor radii, which indicates an average convection velocity of approximately $4.46V_{Ti}$ ($V_{Ti}=(2k_B T_i/m_i)^{1/2}$ is the ion thermal velocity at $t=0$), almost equal to the initial injection velocity ($V_0=4.6V_{Ti}$); compare, for instance, the left panel of Figure 3.4 with the top-left panel of Figure 3.21.

At the same time, the plasma is expanding rapidly along both parallel and antiparallel directions of the background magnetic field. The most energetic particles already reached the edges of the simulation domain along the z-axis after two ion cyclotron periods. However, the main bulk of the plasma is still located well inside the simulation domain at $t=2T_{Li}$ (see Figure 3.21). As a consequence of the thermal expansion of particles along the z-axis, the number density in the xOy plane perpendicular to the background magnetic field is decreasing significantly in time. Indeed, after only one ion gyration period, the number density of both electrons and ions in the $z=153$ cross-section is approximately 2.5 times smaller than the initial value (compare Figure 3.20 with Figure 3.4). At the end of the simulation, for $t=2T_{Li}$, the plasma cloud became 5 times more tenuous than it was initially (compare Figure 3.21 with Figure 3.4). The net charge density inside the simulation domain is shown in the bottom panels of both Figure 3.20 and Figure 3.21. It can be noticed that there are statistical fluctuations in all three cross-sections xOy, xOz and yOz due to the small number of particles loaded into the simulation.

The bulk velocity of the plasma element in different cross-sections inside the simulation domain is shown in Figure 3.22 (for $t=T_{Li}$) and Figure 3.23 (for $t=2T_{Li}$). We illustrate the V_x component (top panels), the V_y component (middle panels) and the V_z component (bottom panels) in the xOy plane (left column), xOz plane (middle column) and yOz plane (right panel). The plasma bulk velocity \vec{V} is computed from the average velocities of both electrons \vec{V}_e and ions \vec{V}_i :

$$\vec{V} = \frac{m_e n_e \vec{V}_e + m_i n_i \vec{V}_i}{m_e n_e + m_i n_i} \quad (3.15)$$

with \vec{V}_e and \vec{V}_i given by:

$$\vec{V}_e = \frac{\vec{J}_e}{q_e n_e}, \quad \vec{V}_i = \frac{\vec{J}_i}{q_i n_i} \quad (3.16)$$

where \vec{J}_e and \vec{J}_i are the electron and ion current densities, while q_e and q_i are the electric charges of the two species. In order to avoid the unrealistically large bulk velocities that could arise in those spatial bins populated with too few particles, we apply the equation (3.15) only for the grid cells having a number density of at least 5% from the initial value. By analyzing the results obtained, it can be noticed that after two ion Larmor periods from the beginning of the simulation, the plasma element continues to stream along the positive x-axis with almost the injection velocity V_0 (see top panels

of Figure 3.22 and Figure 3.23). Indeed, the V_x component of the bulk velocity (3.15) in the central region of the plasma cloud is $\sim 0.95V_0$ at $t=2T_{Li}$, only with 10% smaller than the theoretical value predicted by equation (3.14), i.e. $V_p=0.96V_0$. The value of V_p at $t=2T_{Li}$ has been computed by taking into account that the central plasma density decreased ~ 5 times since the beginning of the simulation and therefore the dielectric constant of the plasma is approximately 5 times smaller than the initial one. On the other hand, we can observe that the plasma element is expanding rapidly along both positive and negative directions of the Oz axis (see bottom-middle and bottom-right panels of Figure 3.22 and Figure 3.23). The V_z component of the plasma bulk velocity close to the edges of the cloud along the z -axis, at $t=2T_{Li}$, is approximately $+5V_{Ti}$ in $z\approx 240$ and $-5V_{Ti}$ in $z\approx 60$. Instead, inside the center of the cloud, the plasma bulk velocity along the Oz axis is zero.

In Figure 3.24 and Figure 3.25 we illustrate the E_x (top panels), E_y (middle panels) and E_z (bottom panels) components of the electric field in the xOy plane (left column), xOz plane (middle column) and yOz plane (right column) inside the simulation domain, at $t=T_{Li}$ (Figure 3.24) and $t=2T_{Li}$ (Figure 3.25). The polarization electric field established inside the quasineutral core of the plasma is illustrated by the middle panels of Figure 3.24 and Figure 3.25. The intensity of the polarization E-field is not uniform inside the main bulk of the plasma element and shows significant fluctuations. This variability is better emphasized in Figure 3.26 where is illustrated the temporal evolution of E_y along the y -axis, between $t=T_{Li}$ and up to $t=2T_{Li}$, for $x=110$ and $z=153$. The source of these fluctuations is more likely the limited number of particles loaded into the simulation domain. Further investigations with a significantly larger number of particles should clarify their origin. On the other hand, the E_y component of the electric field is not strictly confined inside the main bulk of the plasma, but it extends also to the nearby regions. At the end of the simulation the electric field interferes with the boundaries of the simulation box, as can be noticed, for instance, in the middle-left panel of Figure 3.25. In order to avoid unphysical effects of the boundaries, we enlarged the size of the simulation domain in our further runs.

In Figure 3.27 we show the B_x (top panels), B_y (middle panels) and B_z (bottom panels) components of the magnetic field, at the end of the simulation ($t=2T_{Li}$), in the xOy plane (left column), xOz plane (middle column) and yOz plane (right column), for the cross-sections specified in the title of each plot. The B_x and B_y components of the magnetic field are less than 1% smaller than the background magnetic field B_0 pointing along the positive z -axis (see top and middle panels of Figure 3.27). Also, inside the actual position of the plasma element, the B_z component of the magnetic field is approximately 0.25% smaller than B_0 . Indeed, a small diamagnetic cavity can be observed in the bottom panels of Figure 3.27. As expected, the self-consistent contribution of the particles to the total magnetic field is negligible since a low-beta plasma cloud is considered in our simulations.

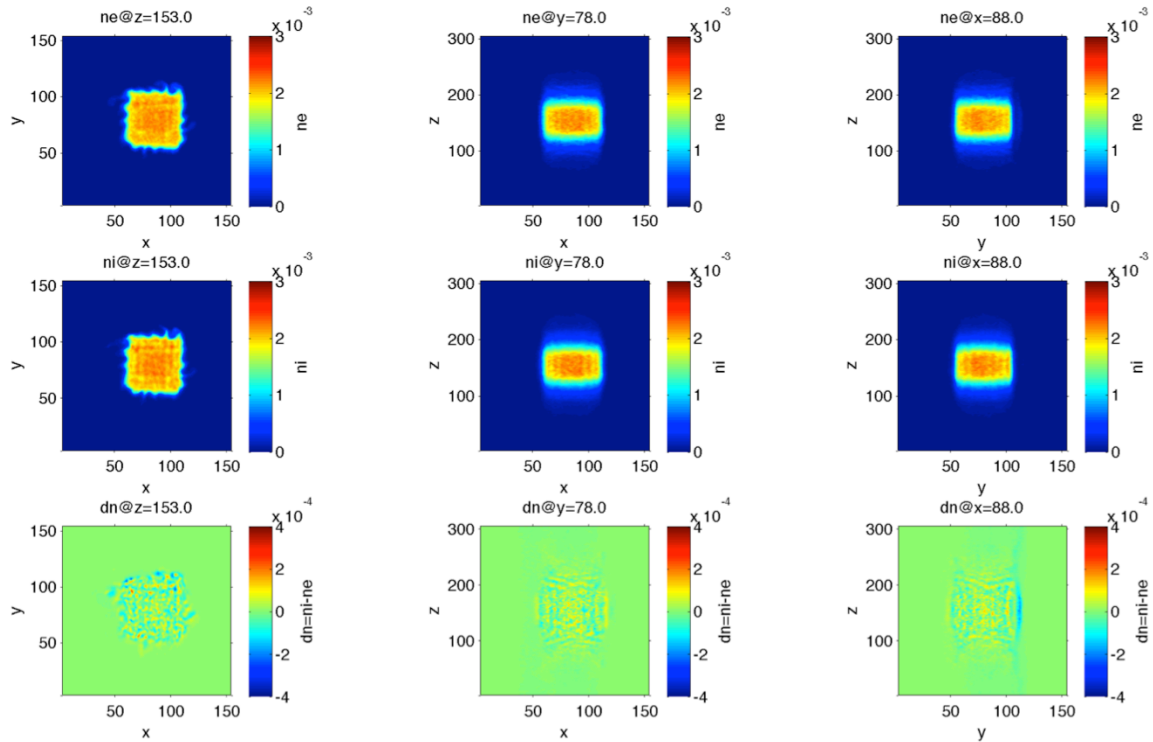


Figure 3.20 – Number density of electrons n_e (top panels) and ions n_i (middle panels) and the charge separation computed as $n_i - n_e$ (bottom panels) in the xOy plane (left column), xOz plane (middle column) and yOz plane (right column), at $t = T_{Li}$ (T_{Li} is the ion Larmor period), for the cross-sections indicated in the title of each plot.

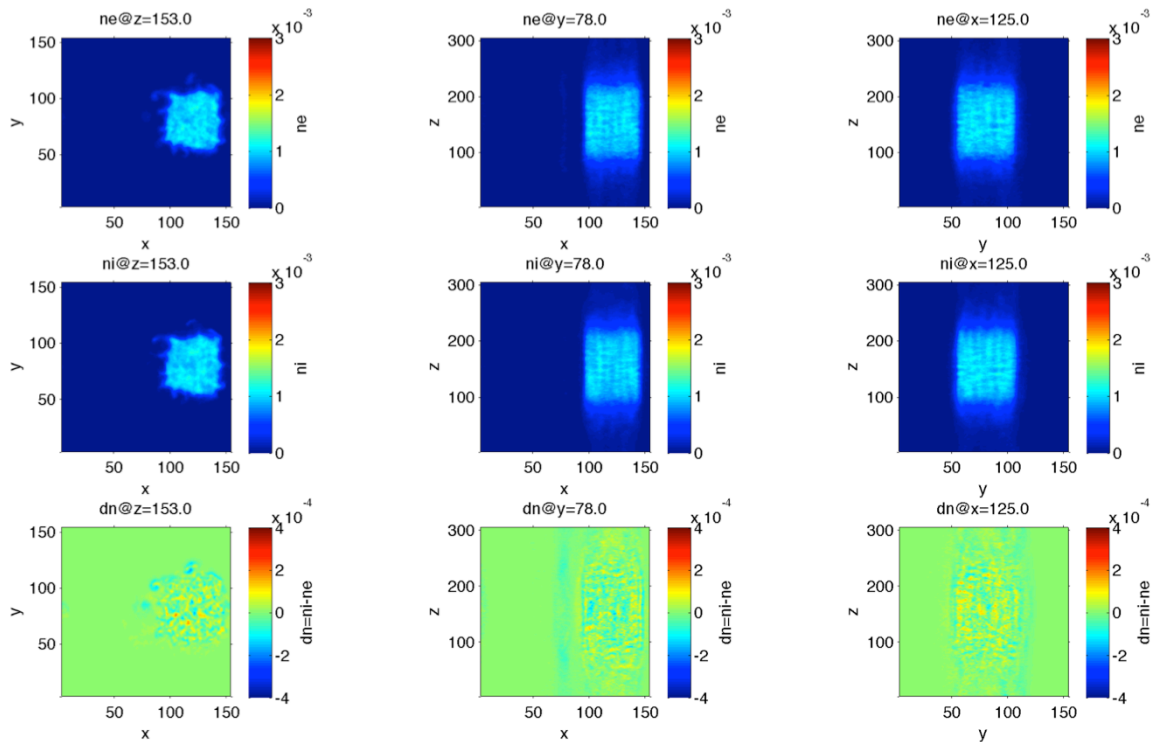


Figure 3.21 – Number density of electrons n_e (top panels) and ions n_i (middle panels) and the charge separation computed as $n_i - n_e$ (bottom panels) in the xOy plane (left column), xOz plane (middle column) and yOz plane (right column), at $t = 2T_{Li}$ (T_{Li} is the ion Larmor period), for the cross-sections indicated in the title of each plot.

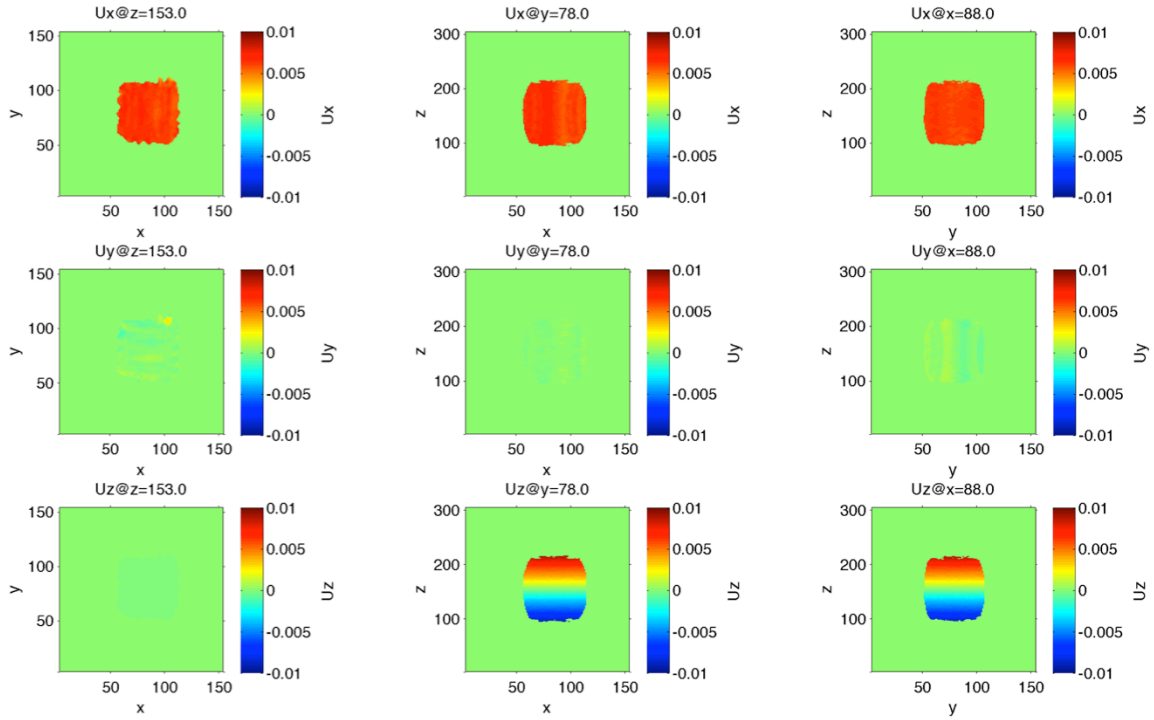


Figure 3.22 – U_x (top panels), U_y (middle panels) and U_z (bottom panels) components of the plasma bulk velocity in the xOy plane (left column), xOz plane (middle column) and yOz plane (right column), at $t=T_{Li}$ (T_{Li} is the ion Larmor period), for the cross-sections indicated in the title of each plot.

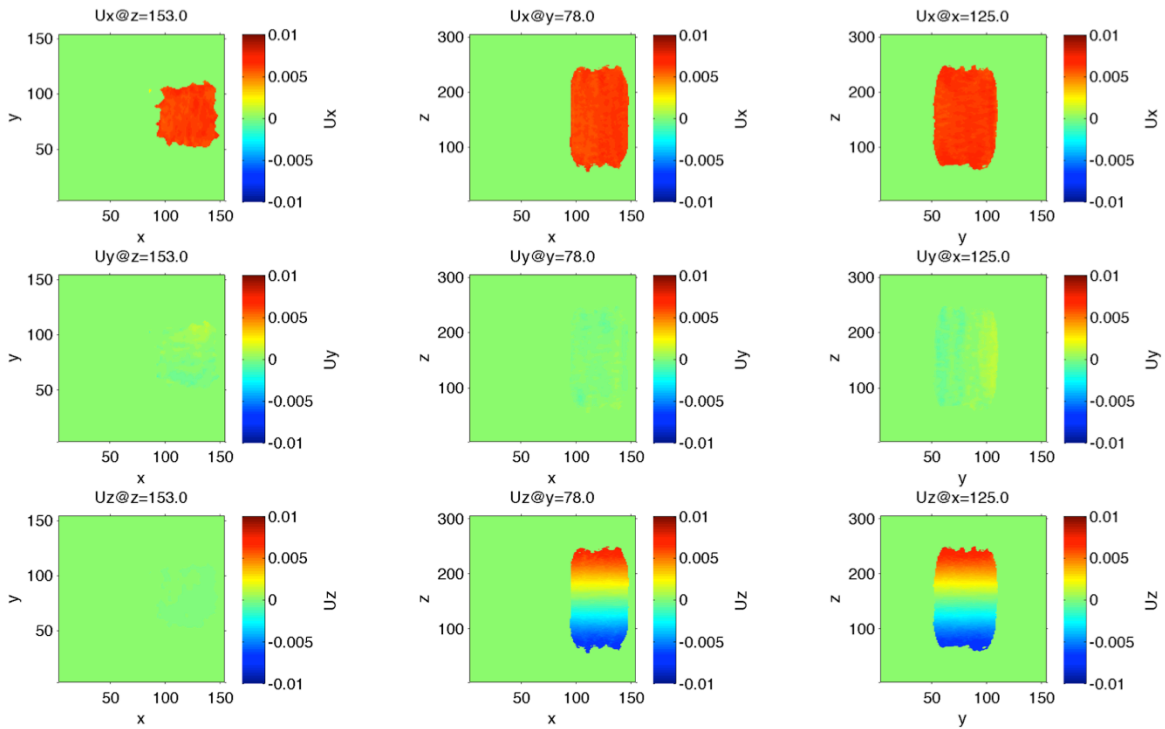


Figure 3.23 U_x (top panels), U_y (middle panels) and U_z (bottom panels) components of the plasma bulk velocity in the xOy plane (left column), xOz plane (middle column) and yOz plane (right column), at $t=2T_{Li}$ (T_{Li} is the ion Larmor period), for the cross-sections indicated in the title of each plot.

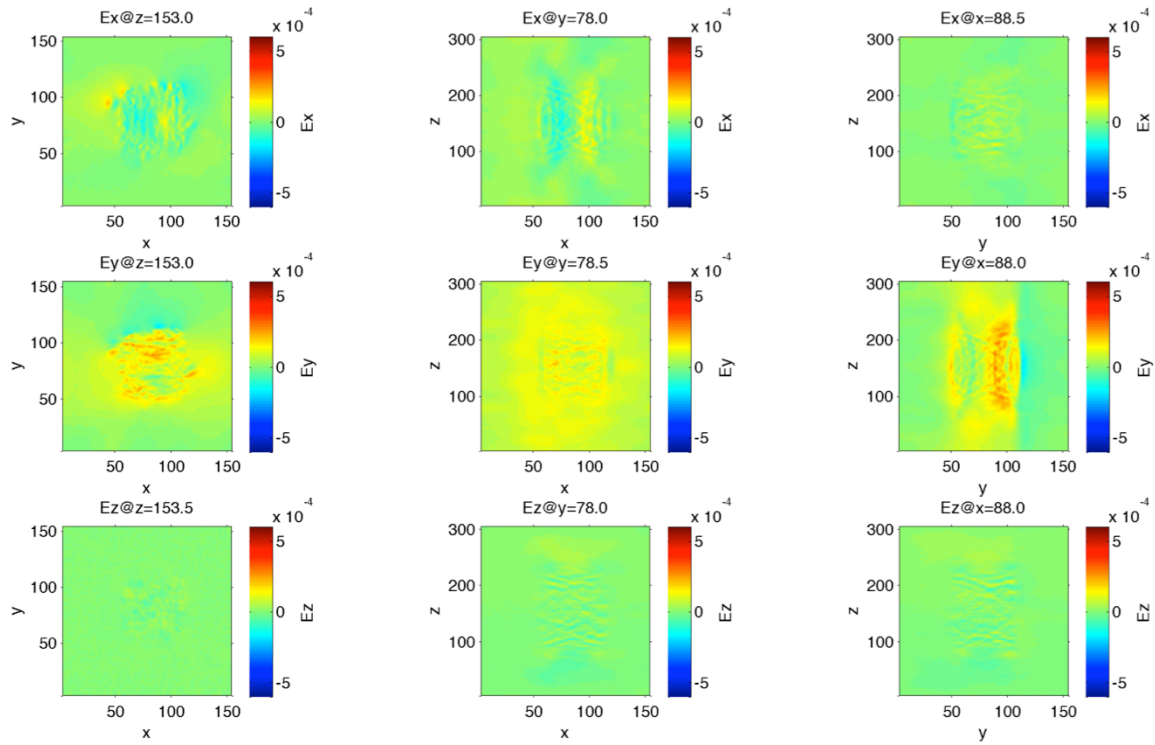


Figure 3.24 – E_x (top panels), E_y (middle panels) and E_z (bottom panels) components of the electric field in the xOy plane (left column), xOz plane (middle column) and yOz plane (right column), at $t=T_{Li}$ (T_{Li} is the ion Larmor period), for the cross-sections indicated in the title of each plot.

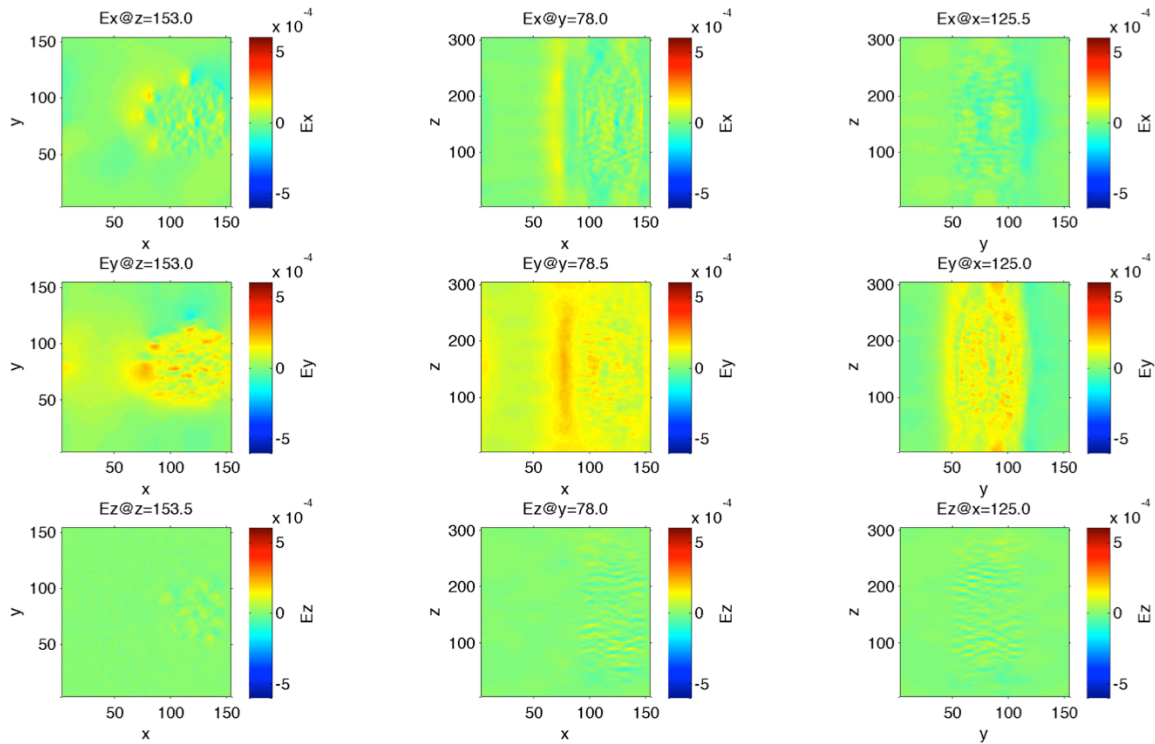


Figure 3.25 – E_x (top panels), E_y (middle panels) and E_z (bottom panels) components of the electric field in the xOy plane (left column), xOz plane (middle column) and yOz plane (right column), at $t=2T_{Li}$ (T_{Li} is the ion Larmor period), for the cross-sections indicated in the title of each plot.

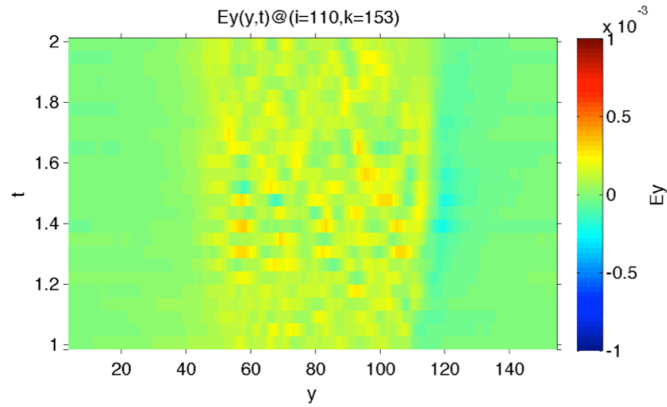


Figure 3.26 – Variation over time of the polarization electric field, E_y , along the y -axis between $t=T_{Li}$ and $t=2T_{Li}$, where T_{Li} is the ion Larmor period; the representation is made for $x=110$ and $z=153$.

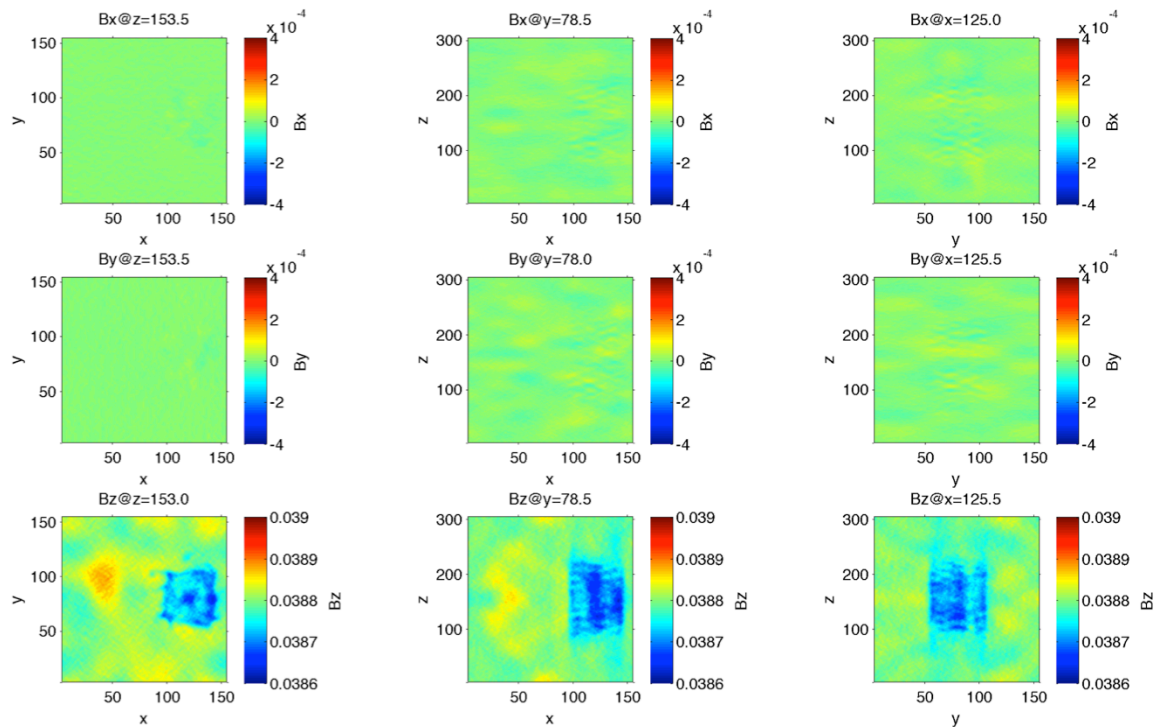


Figure 3.27 – B_x (top panels), B_y (middle panels) and B_z (bottom panels) components of the magnetic field in the xOy plane (left column), xOz plane (middle column) and yOz plane (right column), at $t=2T_{Li}$ (T_{Li} is the ion Larmor period), for the cross-sections indicated in the title of each plot.

3.3.3 Case III: Low speed plasma element injected across a non-uniform transverse magnetic field – impenetrable magnetic barrier

In the third case we simulate the interaction of a low- β plasma element with the non-uniform background magnetic field given by equation (3.9). A schematic diagram of the simulation setup is shown in Figure 3.3 where $B_0=B_0(x)$. We consider here a slow speed plasma cloud having the injection velocity, V_0 , equal to $1.15V_{Ti}$, where V_{Ti} is the ion thermal speed. The input parameters for case III are given in Table 3.1 and Table 3.2. All the physical quantities are expressed in normalized units (see Appendix B for more details about the normalization scheme used here). We analyze the evolution of the plasma and electromagnetic field over almost four ion cyclotron periods.

The background magnetic field, B_0 , is stationary and varies with the x-coordinate across a transition region that covers 5 ion gyration radii. The spatial profile of $B_0=B_0(x)$ is shown in Figure 3.28. As can be noticed, the magnetic field increases linearly between two asymptotic values, B_1 on the left hand side of the transition region (upstream, $x<79$) and B_2 at the right hand side (downstream, $x>85$). Initially, the plasma cloud is localized on the left hand side of the transition region where the background magnetic field is uniform. At the beginning of the simulation, the injection velocity has a non-zero component along the positive x-axis such that the plasma element will stream towards the transition region where the magnetic field is increasing by 50% from its asymptotic value B_1 .

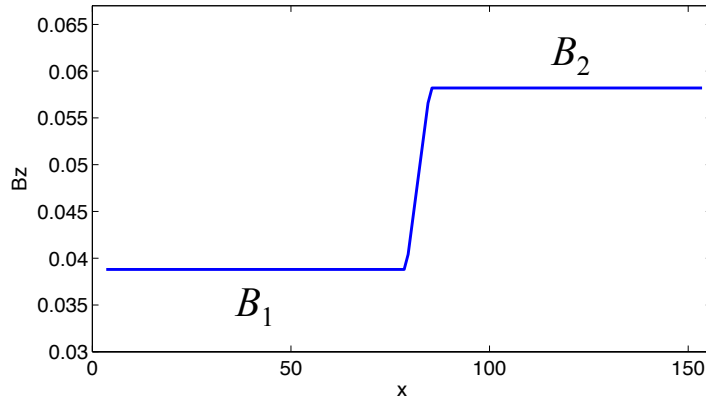


Figure 3.28 – Background magnetic field profile inside the simulation domain. The B-field is oriented along the positive z-axis and increases linearly with x-coordinate over a transition region having the width of $5r_{Li}$ (r_{Li} is ion Larmor radius in the left hand side of the transition region).

In Figure 3.29 we show the initial number density of the plasma element for two different cross-sections inside the simulation domain. In the left panel we illustrate the electron number density in the xOy plane perpendicular to the background magnetic field, for $z=253$, while in the right panel the electron number density is shown in the xOz plane parallel to the background magnetic field, for $y=128$. Initially, the electrons and ions have equal number densities. The non-uniform magnetic field region is marked with two black straight lines in both xOy and xOz planes. As can be noticed, the rectangular plasma element is localized initially on the left hand side of the transition region where the magnetic field is constant ($B=B_1$).

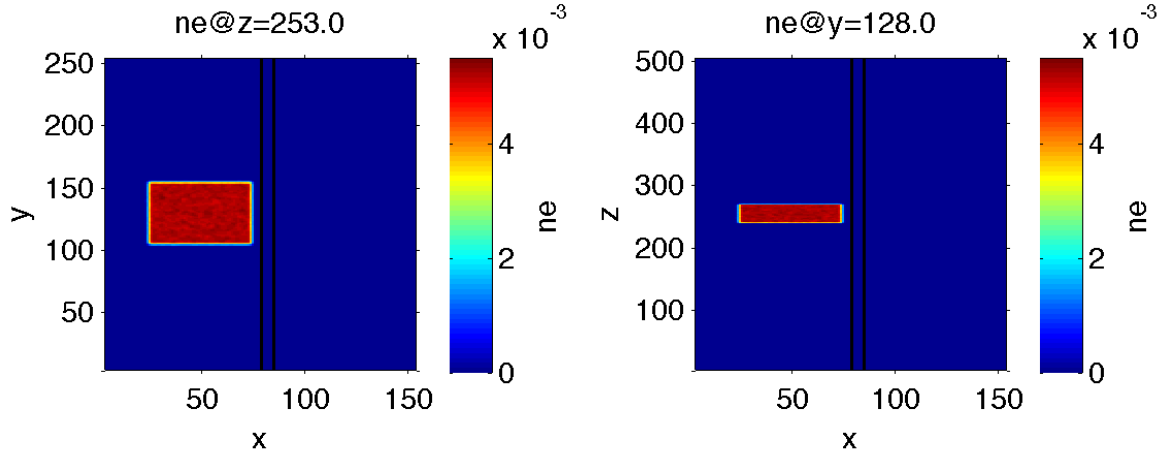


Figure 3.29 – Initial number density of electrons in the xOy (left panel) and xOz (right panel) central sections of the simulation domain. The non-uniform background magnetic field is oriented along the positive direction of the z -axis. The two black lines mark the position of the transition region where the magnetic field increases linearly from B_1 up to $B_2=1.5B_1$. The ions and electrons are initialized with the same number density. At $t=0$ the three-dimensional plasma element has a rectangular shape and is localized on the left hand side of the transition region.

In Figure 3.30 and Figure 3.31 we illustrate the number density of electrons (top panels) and ions (bottom panels) in the xOy plane (Figure 3.30) and xOz plane (Figure 3.31), at $t=T_{Li}$ (left column), $t=2T_{Li}$ (middle-left column), $t=3T_{Li}$ (middle-right column) and $t=3.75T_{Li}$ (right column). The non-uniform magnetic field region is marked with two black straight lines in all panels shown. After two ion Larmor periods the front edge of the plasma element moved into the transition region where the magnetic field increases significantly (see middle-left panels of Figure 3.30). However, the cloud cannot cross over and the convection motion along the x -axis is fully stopped (see middle-right and right panels of Figure 3.30). Moreover, the front-side plasma is pushed back and simultaneously deflected along the negative and positive directions of the y -axis. At the same time, the electrons and ions are expanding rapidly along both parallel and antiparallel directions of the background magnetic field. Nevertheless, at $t=3.75T_{Li}$, the main bulk of the plasma is still located inside the simulation box (see right panel of Figure 3.31). As a result, the number density of both species, for $z=253$ cross-section, is approximately 10 times smaller at the end of the simulation than initially (compare right panels of Figure 3.30 with left panel of Figure 3.29).

In Figure 3.32 we show the U_x (top panels) and U_y (bottom panels) components of the plasma bulk velocity (3.15) in the xOy plane, for $z=253$ cross-section, at $t=T_{Li}$ (left column), $t=2T_{Li}$ (middle-left column), $t=3T_{Li}$ (middle-right column) and $t=3.75T_{Li}$ (right column). At the early stages of the simulation, the plasma element is moving along the positive x -axis with approximately the injection velocity, as can be seen in the Figure 3.32 (top-left panel). Later on, the convection of the front-side plasma along the Ox axis is suppressed ($V_x \approx 0$), while the entire plasma cloud is significantly slowed down (see Figure 3.32, middle-left panel). At later simulation instants, when $t \geq 3T_{Li}$, the V_x component of the bulk velocity in the front edge of the cloud is negative (see Figure

3.32, last top-right panels). Simultaneously, a non-zero V_y component is evidenced at the lateral edges of the cloud along the y -axis, i.e. for small y values $V_y < 0$ and for large y values $V_y > 0$ (see Figure 3.32, last bottom-right panels). Up to the end of the simulation, the entire plasma element is stopped and the particles are deflected along the perpendicular direction to both the ambient magnetic field and the injection velocity.

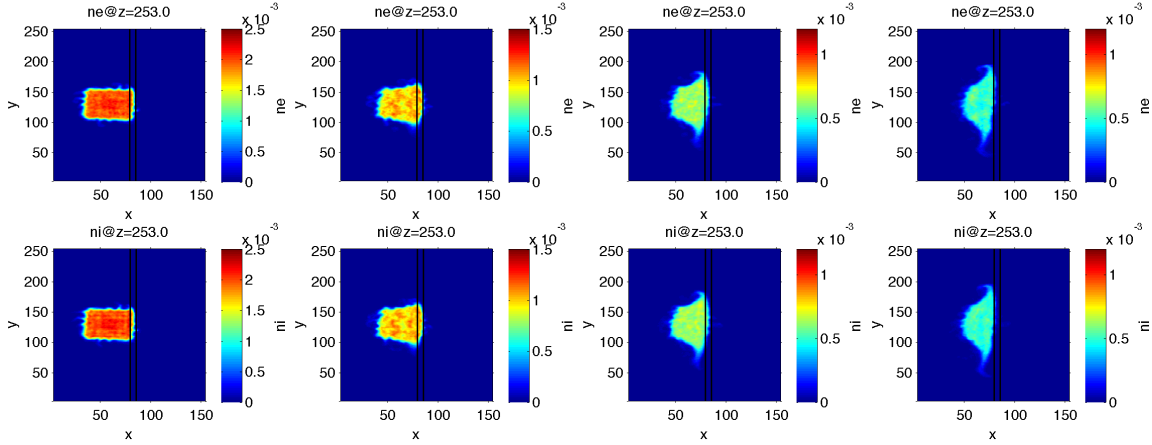


Figure 3.30 – Number density of electrons (top panels) and ions (bottom panels) at $t=T_{Li}$ (left column), $t=2T_{Li}$ (middle-left column), $t=3T_{Li}$ (middle-right column) and $t=3.75T_{Li}$ (right column); T_{Li} is the ion Larmor period in the left hand side of the transition region. The two black lines mark the position of the transition region where the magnetic field is non-uniform. The xOy plane perpendicular to the background magnetic field is shown here, for $z=253$ cross-section.

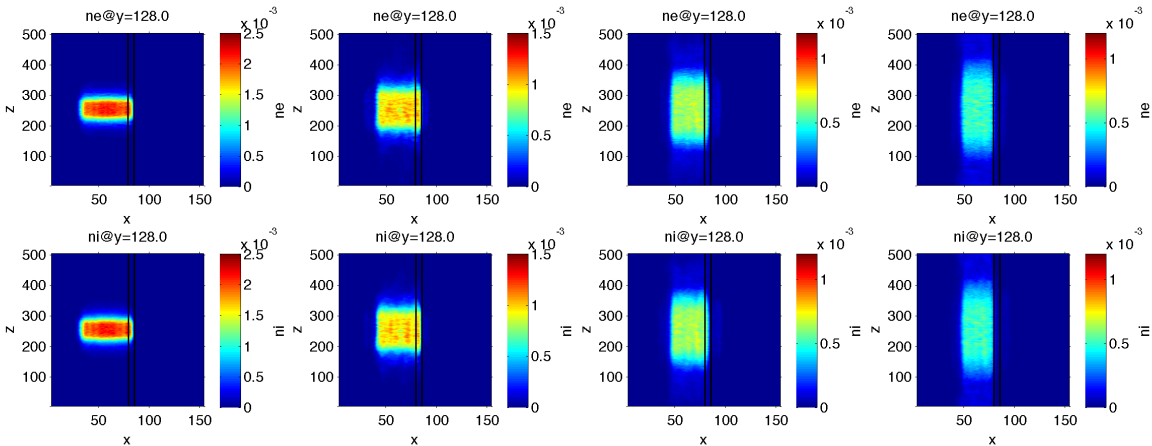


Figure 3.31 – Number density of electrons (top panels) and ions (bottom panels) at $t=T_{Li}$ (left column), $t=2T_{Li}$ (middle-left column), $t=3T_{Li}$ (middle-right column) and $t=3.75T_{Li}$ (right column); T_{Li} is the ion Larmor period in the left hand side of the transition region. The two black lines mark the position of the transition region where the magnetic field is non-uniform. The xOz plane perpendicular to the background magnetic field is shown here, for $y=128$ cross-section.

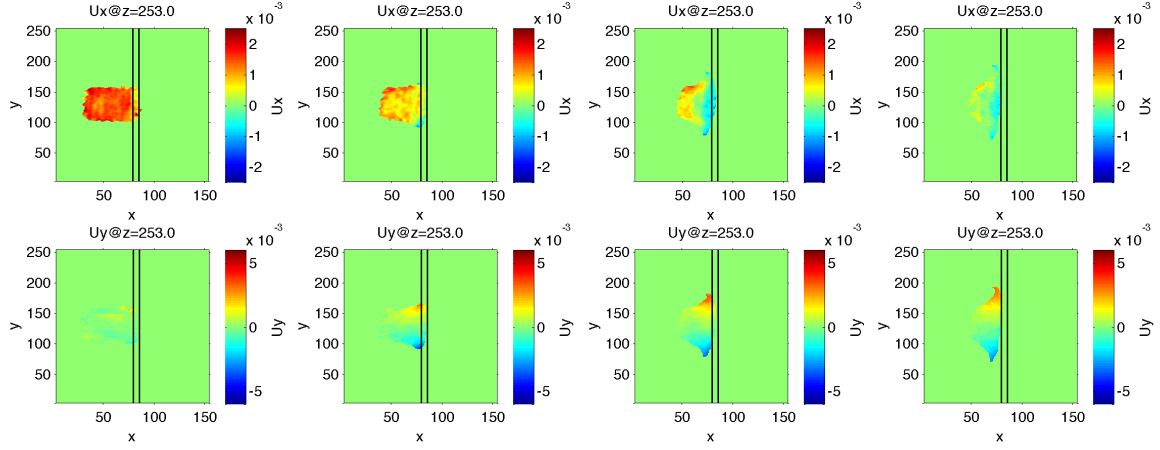


Figure 3.32 – V_x (top panels) and V_y (bottom panels) components of the plasma bulk velocity at $t=T_{Li}$ (left column), $t=2T_{Li}$ (middle-left column), $t=3T_{Li}$ (middle-right column) and $t=3.75T_{Li}$ (right column); T_{Li} is the ion Larmor period in the left hand side of the transition region. The two black lines mark the position of the transition region where the B-field is non-uniform. The xOy plane perpendicular to the background magnetic field is shown here, for $z=253$ cross-section.

The simulation results obtained here clearly emphasize the physical process of adiabatic breaking that takes place when a non-diamagnetic plasma element is streaming into an increasing transverse magnetic field (e.g. *Demidenko, 1967; Lemaire, 1985*). Let us assume that the first-order guiding center approximation is valid and the magnetic moment, μ , of electrons and ions is an adiabatic invariant (*Alfven, 1953*):

$$\mu_\alpha = \frac{m_\alpha w_\perp^2}{2B} = \text{const.} \quad (3.17)$$

where w_\perp is the gyration velocity of a particle with mass m in the perpendicular plane to the magnetic field of strength B ; α is the species index. Also, let us consider that the dielectric constant of the plasma is much larger than unity. Under these circumstances, the plasma convection velocity, $V(x)$, across a non-uniform magnetic field, $B(x)$, satisfies the following equation (*Lemaire, 1985*):

$$\frac{(m_e + m_i)}{2} V^2(x) + (\overline{\mu_e} + \overline{\mu_i}) B(x) = \text{const.} \quad (3.18)$$

where $V(x)$ is in fact the zero order drift velocity:

$$\vec{U}_E = \frac{\vec{E} \times \vec{B}}{B^2} \quad (3.19)$$

The bars over the magnetic moments μ_e and μ_i in equation (3.18) indicate averaging over the velocity distribution functions of electrons and ions. Since the magnetic moment is an adiabatic invariant, the equation (3.18) can be rewritten as (*Lemaire, 1985*):

$$(m_e + m_i) V^2 + m_e \overline{w_{\perp e}^2} + m_i \overline{w_{\perp i}^2} = \text{const.} \quad (3.20)$$

This equality reveals the conservation of the total kinetic energy in the perpendicular plane to the magnetic field (convection + gyration for both species). It clearly shows that when the magnetic field increases, convection energy is converted into gyration energy and therefore the plasma element is slowed down. There is a critical magnetic field, B_c ,

for which all the convection energy is transformed into gyration energy and the plasma is stopped. The value of B_c in x_c can be obtained by setting $V(x_c)=0$ in equation (3.18). This leads to (Lemaire, 1985):

$$B_c(x_c) = \frac{(m_e + m_i)V_0^2 + m_e \overline{w_{\perp e0}^2} + m_i \overline{w_{\perp i0}^2}}{2(\overline{\mu_e} + \overline{\mu_i})} \quad (3.21)$$

When the plasma element reaches the critical point x_c , the magnetic field B_c acts like a barrier that prevents the further convection of the cloud along the x-axis. This process of adiabatic breaking has been verified in the past by different laboratory experiments (Demidenko et al., 1967, 1969).

Our numerical simulations sustain the physical mechanism described above. Indeed, the critical magnetic field obtained from (3.21) for the plasma parameters considered in this case is equal to $B_c=1.06B_1$. Nevertheless, the magnetic field increases across the discontinuity from B_1 to $B_2=1.5B_1$. Thus, the asymptotic magnetic field B_2 is larger than the critical value B_c or in other words the magnetic barrier is too steepen and the plasma element is not able to penetrate the transition region since its initial energy is not large enough. Therefore, the cloud is stopped and pushed back along the negative direction of the x-axis by the $-(\overline{\mu_e} + \overline{\mu_i})\nabla B$ force (Lemaire, 1985) acting inside the transition region (see top-right panel of Figure 3.32). In addition to the adiabatic breaking process observed, the dynamics of the plasma element along the Oy axis shows additional interesting features. As the plasma enters into the non-uniform magnetic field region, it is virtually deflected along both positive and negative y -direction (see bottom-right panel of Figure 3.32).

In order to understand the physical mechanism responsible for this effect, we analyze in more detail the electrodynamics of the cloud when it interacts with the magnetic barrier. We illustrate on the top panels of Figure 3.33 the E_x component of the electric field, in the xOy plane perpendicular to \vec{B}_0 , at $t=3T_{Li}$ (left column) and $t=3.75T_{Li}$ (right column). One can notice that a region with a negative E_x component of the electric field is formed at the front-left hand side edge of the plasma cloud (for $y>110$); at the same time, a region with a positive E_x component of the electric field is formed at the front-right hand side edge (for $y<110$). The zero order drift produced by this component of the electric field is along $+Oy$ for $y>110$ (where $V_y>0$) and along $-Oy$ for $y<110$ (where $V_y<0$). This is true for electrons and ions.

In the bottom panels of Figure 3.33 we show the $U_{E,y}$ component of the zero-order drift velocity (3.19) computed at the same time instants and for the same cross-sections as the E_x field. $U_{E,y}$ is calculated only for the grid cells that have a number density equal to at least 5% of the initial value. The same constraint is applied to the computation of the bulk velocity (3.15). One can notice that on average the plasma cloud has a positive $U_{E,y}$ component of the electric drift velocity at the front-left hand side of the plasma element; the cloud has a negative $U_{E,y}$ at the front-right hand side edge. The fluctuations observed in the xOy plane are most probably related to the limited number of particles loaded into the simulation.

When one compares the bottom panels of Figure 3.33 with the last two bottom-right panels of Figure 3.32, one can see that the values of $U_{E,y}$ are smaller than those of V_y at the very lateral edges of the cloud, while inside the inner regions the $U_{E,y}$ and V_y velocities are similar. It is known (Echim and Lemaire, 2005; Lundin et al., 2005) that sharp kinetic boundaries of the order of the electrons or ion Larmor radius are sites where the frozen-in theorem is broken and there is a decoupling between the so-called convection velocity, equal to the electric drift, and the actual plasma bulk velocity derived from the real moments of the velocity distribution function. Since the edges at the front-side of the cloud are dominated by particles with higher energies (this is discussed in the next paragraphs), their bulk velocity is different than that of the particles inside the core of the cloud. The latter can indeed be approximated by the convection (or frozen-in or electric drift) velocity given by equation (3.19).

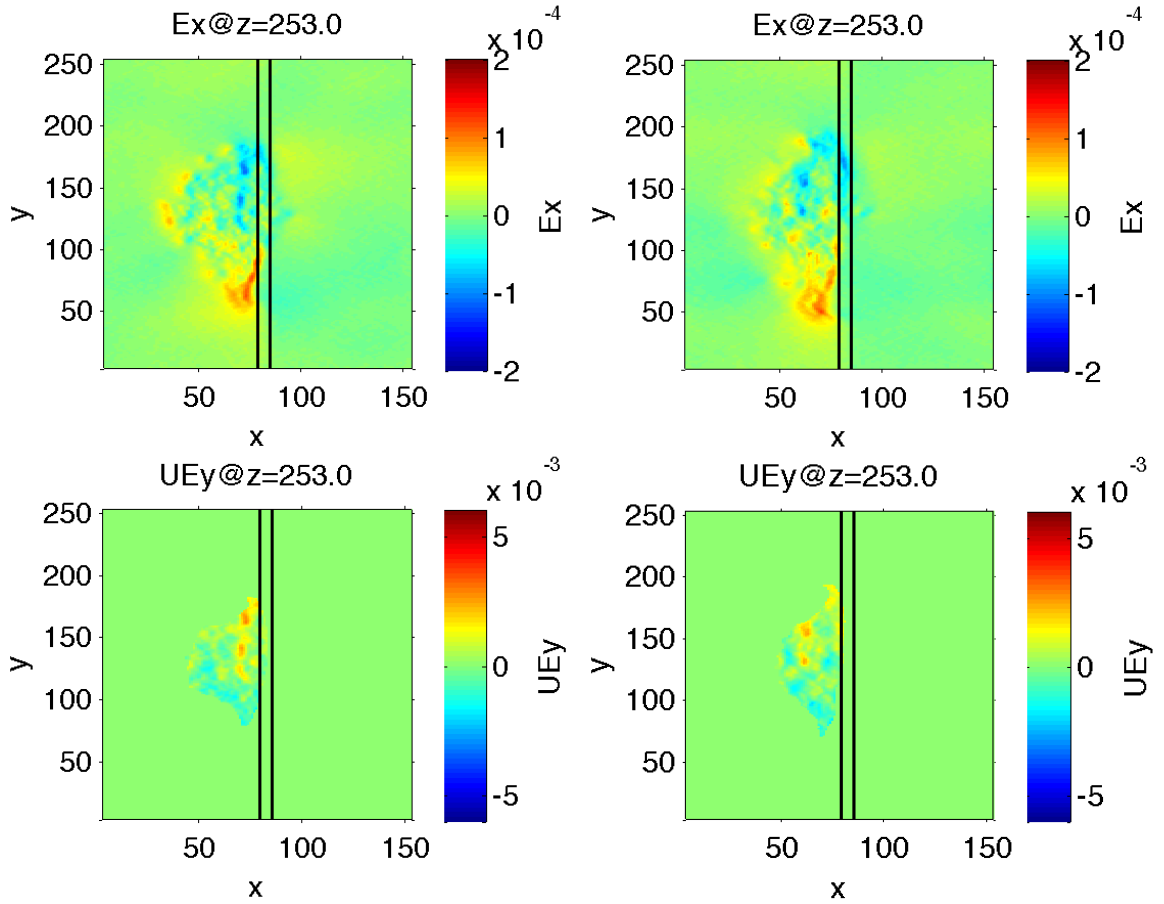


Figure 3.33 – E_x component of the electric field (top panels) and $U_{E,y}$ component of the zero-order drift (bottom panels) in the xOy plane perpendicular to the ambient magnetic field, for $t=3T_{Li}$ (left column) and $t=3.75T_{Li}$ (right column); T_{Li} is the ion Larmor period in the left hand side of the transition region. The two black lines mark the position of the transition region where the magnetic field is non-uniform. The zero-order drift is computed only for those grid cells having a number density of at least 5% from its initial value, otherwise the value of $U_{E,y}$ is set to zero.

Let us discuss further the origin of the E_x component of the electric field that contributes to the deflection of the plasma element in the direction perpendicular to both the background magnetic field and the initial injection velocity. In the left panel of Figure 3.34 we show the net charge density in the xOy plane perpendicular to the magnetic field at $t=3T_{Li}$. The non-uniform magnetic field region is marked with two black straight lines, while the initial position of the plasma element is indicated by a black rectangle. Note, however, that in order to better illustrate the polarization charges at the edges of the plasma element, we assigned a net charge equal to zero inside the quasineutral core of the cloud. The actual value of the net charge in the core is different from zero most likely due to a gaussian numerical noise controlled by the limited number of particles introduced in the simulation.

It can be noticed that the front-edge of the plasma element is electrically polarized. Indeed, after three ion cyclotron periods from the beginning of the simulation, a positive space charge layer is formed in the lateral region of the propagation front (for $y>110$), while a negative layer is evidenced in the opposite lateral region (for $y<110$). One should also notice that the situation is reversed in the regions of the cloud that did not yet interact with the magnetic interface. Indeed, the lateral edge ($y>125$) of the plasma core localized outside the magnetic barrier (at $x<70$) is negatively polarized, while the opposite lateral edge ($y<125$ and $x<70$) is positively charged. The polarization in the left hand side of the cloud, between the front edge and the rest of the cloud, sustains a positive E_x in the region defined by $65<x<85$ and $y<110$. Similarly a region of negative E_x is formed in the parcel of the cloud defined by $65<x<85$ and $y>110$. A schematic diagram of the left panel of Figure 3.34 is shown in the right panel of the same figure.

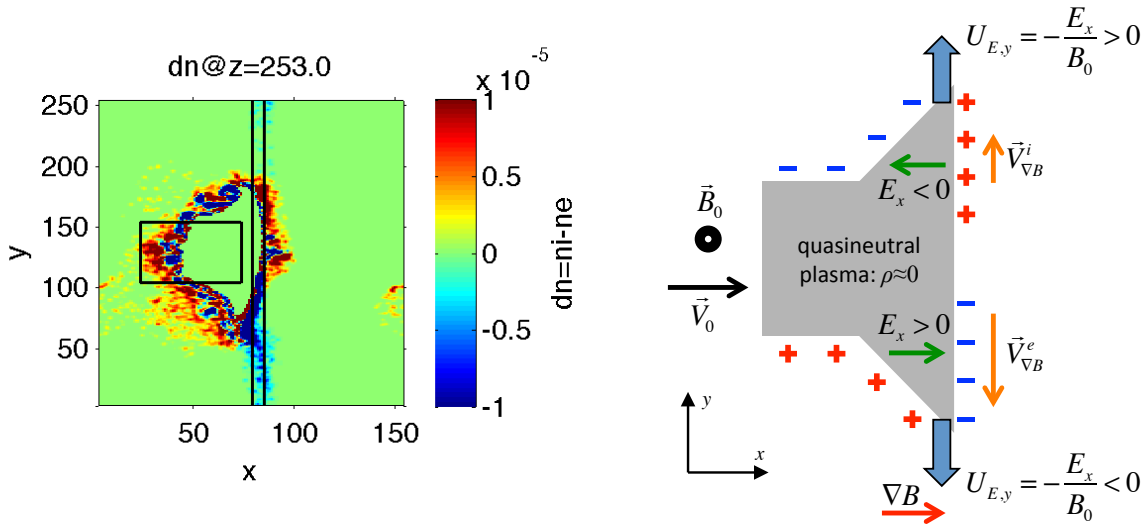


Figure 3.34 – (Left panel) Net charge density in the xOy plane perpendicular to the ambient magnetic field at $t=3T_{Li}$; T_{Li} is the ion Larmor period at the left hand side of the transition region. The non-uniform magnetic field region is marked with the two black straight lines, while the initial position of the plasma cloud is shown by a black rectangle. The net charge in the core of the cloud has been artificially assigned to zero in order to remove the numerical noise and emphasize the effects in the lateral edges. (Right panel) Schematic diagram of the plasma polarization when it interacts with the increasing magnetic field.

The polarization of the front-side boundary of the plasma cloud is a consequence of the charge dependent gradient-B drift (1.13) acting inside the transition region where the magnetic field is non-uniform. Indeed, in this region the grad-B drift velocity deflects ions along $+Oy$ and electrons $-Oy$. As the front-edge of the plasma element starts to interact with the non-uniform magnetic field (at $t \approx T_{Li}$, see top-left panel of Figure 3.30) the electrons and ions are scattered in opposite directions along the y -axis. From $t = T_{Li}$ and up to $t = 3T_{Li}$, the high-energy front-side ions having an initial gyration velocity of approximately $1.8V_{Ti}$ are scattered along $+Oy$ direction over a distance of only $2r_{Li}$. Instead, the much more hotter electrons are scattered along $-Oy$ direction over a distance of $\sim 35r_{Li}$, nearly equal to the initial width of the plasma element w_y (see Table 3.1). As a result, a sufficiently large charge separation is generated and the propagation front of the plasma element is polarized as shown in Figure 3.34.

It is important to note that the grad-B drift (1.13) deflects more efficiently the most energetic particles than the thermal ones. The latter are however the most numerous since the initial velocity distribution function is a Maxwellian. Nevertheless, they are much less scattered along y -axis. Therefore, when one looks at the density of the electrons and ions in Figure 3.30, one sees that both species are scattered in the positive and negative directions of the y -axis. This is a confirmation that the driver of the deflection is not charge dependent. Our interpretation outlined above is that the high energy particles of the cloud arrive first at the magnetic barrier and, since they are not able to penetrate, they start drifting in the Oy direction “pushed” by the gradient-B drift. This charge dependent drift establishes a polarization in the front edge of the cloud, with ions populating the region at larger y -values and electrons populating the region at smaller y -values. These space charge layers in the front side persist and develop in time since the particles have not enough energy to penetrate the magnetic barrier. Thus, a second polarization field is built between the front edge and the rest of the cloud. This polarization enables a negative E_x within the parcels of the cloud at larger y that did not yet interact with the magnetic barrier. The situation is reversed for the parcels at smaller y , as indicated in Figure 3.34. The electric drift due to this E_x component deflects the cloud in the positive and respective negative Oy directions at the left hand side (for larger y -values) and respectively right hand side (for smaller y -values) of the cloud. Thus, the action of the two drifts, the gradient-B drift and zero-order electric drift, cannot be disentangled. They act together and contribute to the global deflection of the cloud along the magnetic barrier. The higher energy particles provide the polarization in the front and at the lateral edges of the cloud; this polarization eventually deflects all the particles in the cloud by the zero-order drift. This is a kinetic, non-MHD, effect that demonstrates the crucial role of Larmor scale processes for plasma dynamics in non-uniform electromagnetic fields.

3.3.4 Case IV: Intermediate speed plasma element injected across a non-uniform transverse magnetic field – penetration of the magnetic barrier

In order to achieve simulation conditions that enable the penetration of the magnetic barrier, we increased the injection velocity of the plasma element by a factor of 2, i.e. $V_0/V_{Ti}=2.3$, where V_{Ti} is the ion thermal speed. The input parameters for case IV-1 are given in Table 3.1 and Table 3.2. All the physical quantities are expressed in normalized units (see Appendix B details). The evolution of the plasma cloud across the non-uniform magnetic field region is tracked over three ion Larmor periods.

The initial number density is shown in Figure 3.35. In the left panel we illustrate the electrons density in the xOy plane perpendicular to the background magnetic field, at $z=203$, while in the right panel we show the density in the xOz plane, at $y=103$. The non-uniform magnetic field region is marked with two black straight lines in both planes. In order to reduce the effects of the boundaries, we fix now the simulation boundaries along the Ox axis even further away from the plasma element than previously. The particles are initialized in the central area of the simulation box where the magnetic field is uniform.

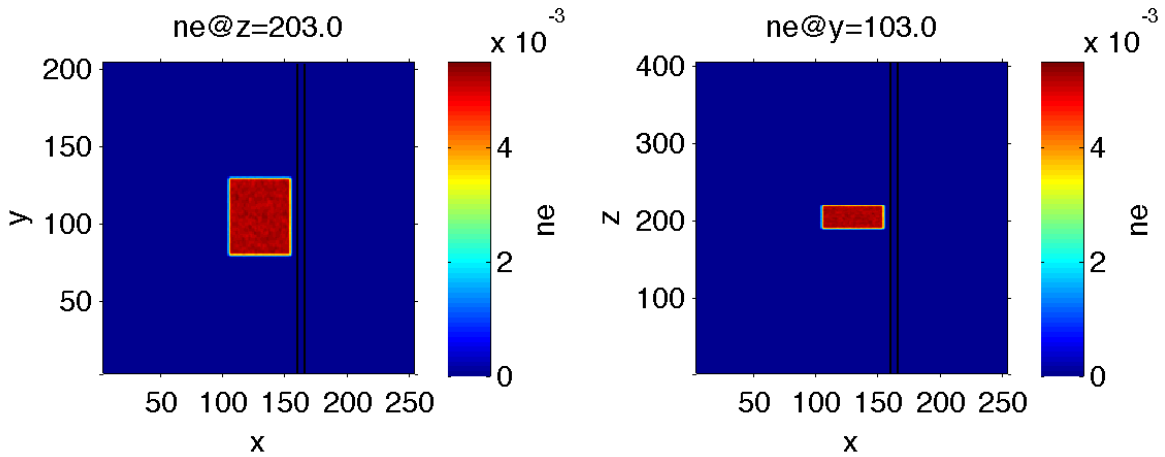


Figure 3.35 – Initial number density of electrons in the xOy (left panel) and xOz (right panel) sections of the simulation domain. The non-uniform background magnetic field is oriented along the positive direction of the z -axis. The two black lines mark the position of the transition region where the magnetic field increases linearly from B_1 up to $B_2=1.5B_1$. The ions and electrons are initialized with the same number density. At $t=0$ the three-dimensional plasma element has a rectangular shape and is localized on the left hand side of the transition region.

Figure 3.36 shows the time evolution of the number density of electrons (top panels) and ions (bottom panels) in the xOy plane perpendicular to the background magnetic field, at $t=1.5T_{Li}$ (left column) and $t=3T_{Li}$ (right column). It can be noticed that even though the injection velocity is two times larger now than in the previous case, the plasma element still cannot penetrate the magnetic barrier. Indeed, from $t=1.5T_{Li}$ and up to $t=3T_{Li}$, the propagation front is localized slightly into the right side of the transition region, but is not moving anymore along the x -axis. Moreover, as in the previous case, the plasma is deflected along both positive and negative Oy directions.

The dynamics of the plasma element is well described in Figure 3.37 where we illustrate the U_x (top panels) and U_y (bottom panels) components of the bulk velocity

(3.15) in the xOy plane, for $z=203$, at $t=1.5T_{Li}$ (left column) and $t=3T_{Li}$ (right column). To avoid the unrealistically large bulk velocities that could arise in those spatial bins populated with too few particles, we apply the equation (3.15) only for the grid cells that have a number density at least 5% from the initial value. After three ion cyclotron periods from the beginning of the simulation, the central core of the plasma cloud is at rest ($V_x \approx 0$ for $90 \leq y \leq 125$), while the lateral edges are pushed backwards along the x -axis, i.e. $V_x < 0$ for $y < 90$ and $y > 125$ (see top-right panel of Figure 3.37). On the other hand, the top-lateral edge of the cloud ($y > 125$) has a positive V_y component, while for the bottom-lateral edge $V_y < 0$ (see bottom-right panel of Figure 3.37). The results obtained here illustrate again the adiabatic breaking process discussed in the previous case. Even though the injection velocity is twice as large than in the third simulated case, the magnetic barrier is still too high and the plasma element cannot penetrate the transition region. Indeed, the critical magnetic field (3.21) is $B_c = 1.23B_1$, while the magnetic field in the right side of the transition region is $B_2 = 1.5B_1$. Therefore, the cloud is stopped and pushed back along the negative direction of the x -axis, while is deflected along $\pm Oy$.

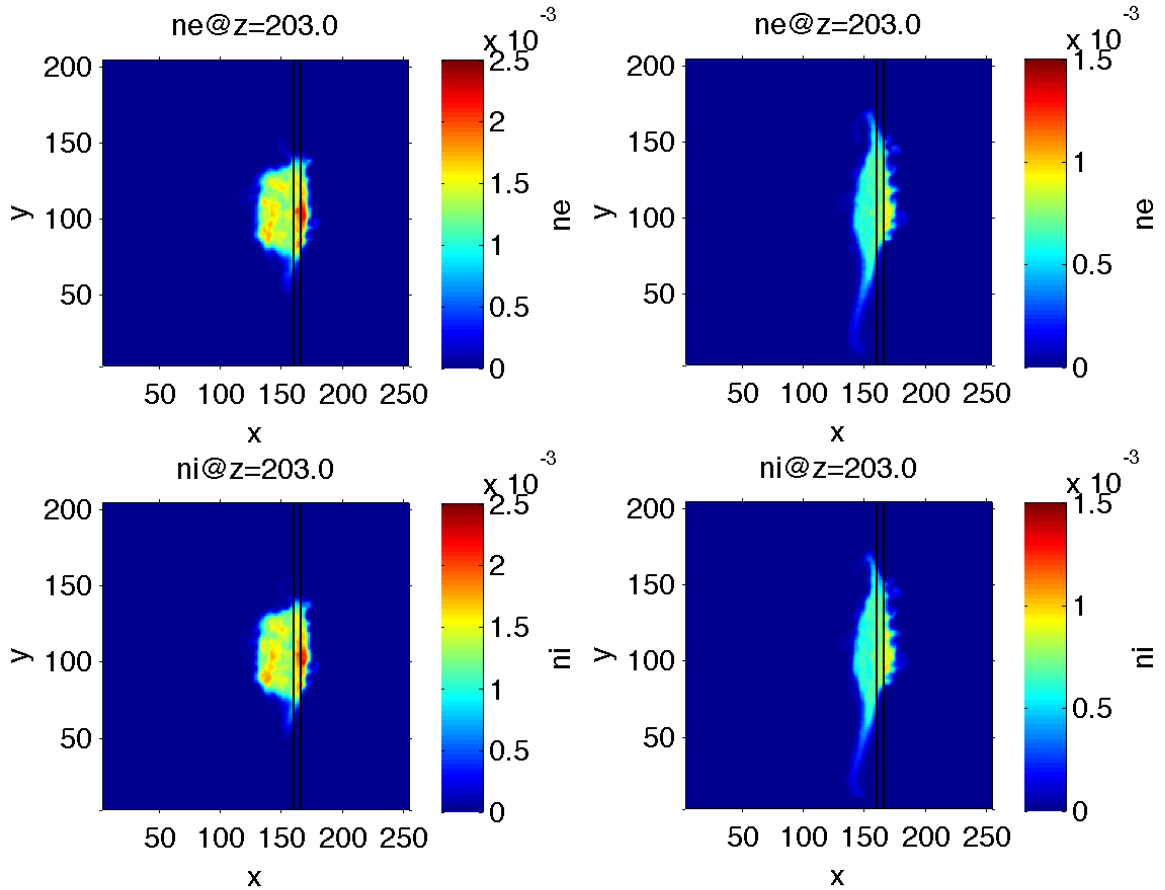


Figure 3.36 – Number density of electrons (top panels) and ions (bottom panels) at $t=1.5T_{Li}$ (left column) and $t=3T_{Li}$ (right column); T_{Li} is the ion Larmor period in the left hand side of the transition region. The two black lines mark the position of the transition region where the magnetic field is non-uniform. The xOy plane perpendicular to the background magnetic field is shown here, for $z=203$.

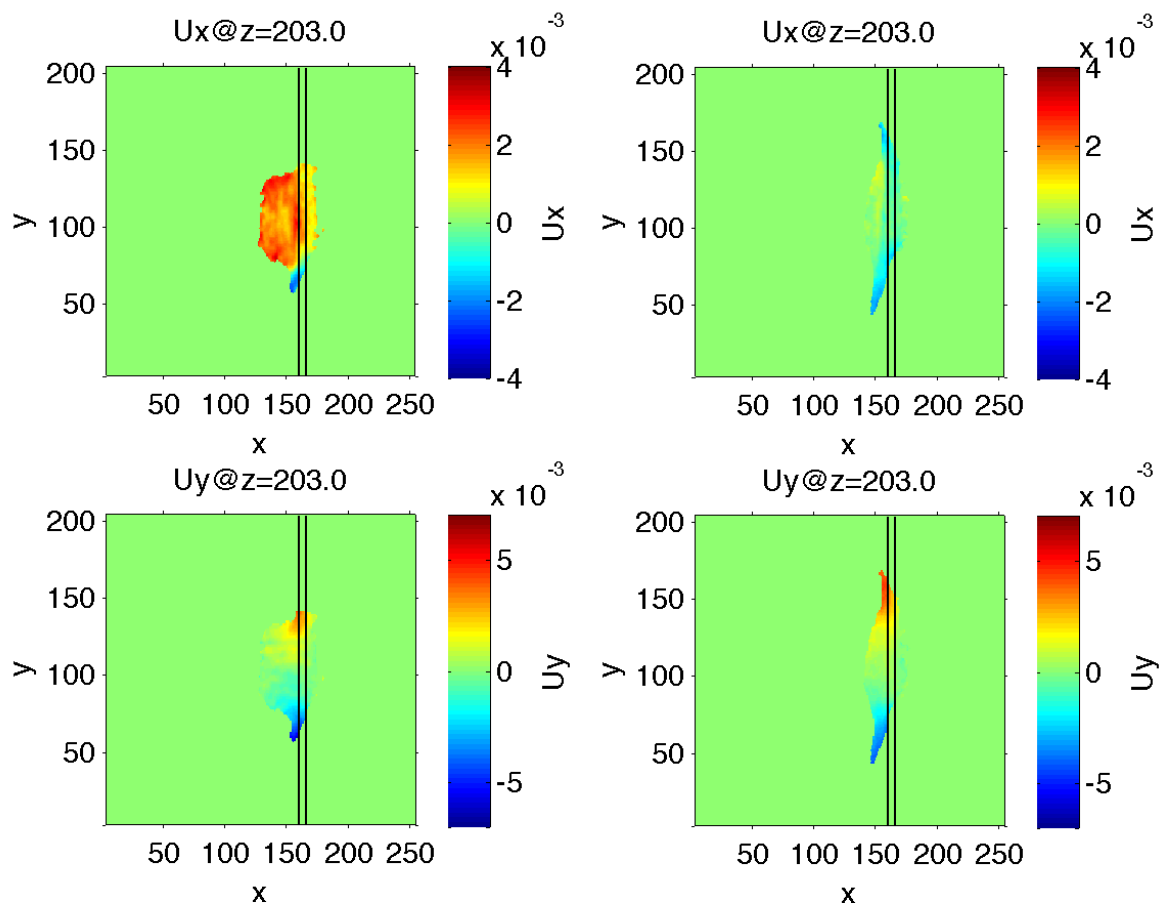


Figure 3.37 – V_x (top panels) and V_y (bottom panels) components of the plasma bulk velocity in the xOy plane perpendicular to the ambient magnetic field, for $t=1.5T_{Li}$ (left column) and $t=3T_{Li}$ (right column); T_{Li} is the ion Larmor period in the left hand side of the transition region. The two black lines mark the position of the transition region. The bulk velocity is computed only for those grid cells having a number density of at least 5% from its initial value, otherwise its value is set to zero.

The magnetic barrier is overcome by the plasma element when we reduce the value of the asymptotic field at the right hand side of the transition region by a factor of ~ 1.4 , i.e. to $B_2=1.1B_1$. These conditions are implemented in case IV-2; see Table 3.1 and Table 3.2 for the input parameters. In this simulation the height of the magnetic barrier is smaller than the critical field $B_c=1.23B_1$.

In Figure 3.38 we show the number density of electrons (top panels) and ions (bottom panels), at the end of the simulation ($t=3T_{Li}$), in the xOy plane perpendicular to the background magnetic field (left column) and in the xOz plane (right column). The plasma element is able to move across the region of sharp magnetic variation, fully penetrates the magnetic barrier and moves into the right hand side of the transition region (one could call this “magnetospheric” side, if the magnetic barrier is seen as an analogy of the magnetopause).

The plasma is expanding rapidly along Oz axis and the most energetic particles already reached the boundaries of the simulation box. Nevertheless, most of the electrons and ions are still well inside the simulation domain. The main core of the plasma element is ~ 7 times more tenuous now ($t=3T_{Li}$) than at $t=0$.

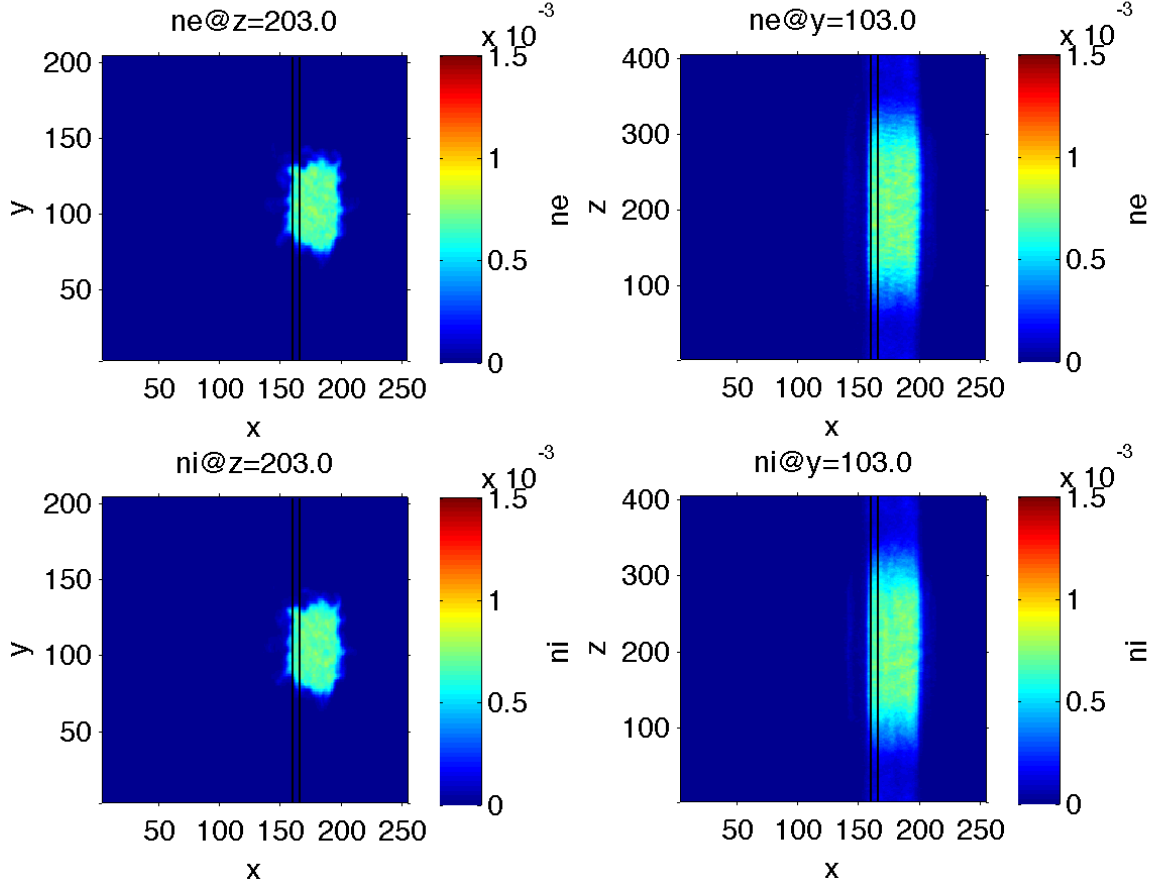


Figure 3.38 – Number density of electrons (top panels) and ions (bottom panels) in the xOy (left column) and xOz (right column) planes, at the end of the simulation, i.e for $t=3T_{Li}$; T_{Li} is the ion Larmor period at the left hand side of the transition region. The two black lines mark the position of the transition region where the magnetic field is non-uniform.

The plasma bulk velocity at $t=3T_{Li}$ is shown in Figure 3.39. The left column illustrate the V_x component in the xOy plane for $z=203$, while the right column shows V_x in the xOz plane for $y=103$. As in the previous cases, the plasma bulk velocity is computed from (3.15) only for the grid cells that have a number density at least 5% from the initial value. The plasma element is braked; it moves downstream the magnetic discontinuity with a bulk velocity smaller than the initial one. To better illustrate the adiabatic breaking of the cloud, we show in Figure 3.40 the spatial variation of the forward velocity in the y -direction field, $V_x=V_x(y)$, for $x=182$ and $z=203$. The black line indicates the average value of the plasma bulk velocity shown with blue color, while the red one is the initial injection velocity. The ratio between the final and initial velocity is equal to $V_x/V_0 \approx 0.7$. This result illustrates again the effectiveness of the adiabatic breaking process. In this case the plasma cloud has enough convection energy to penetrate the magnetic barrier, but part of it is converted into gyration energy in the stronger magnetic field at the right hand side of the transition region, as suggested by laboratory and theoretical arguments (e.g. *Demidenko et al., 1967, 1969; Lemaire, 1985*). The theoretical value of the final plasma bulk velocity downstream the magnetic sharp transition computed from equation (3.18) is $V_x=0.73V_0$, in good agreement with theoretical models (*Lemaire, 1985*).

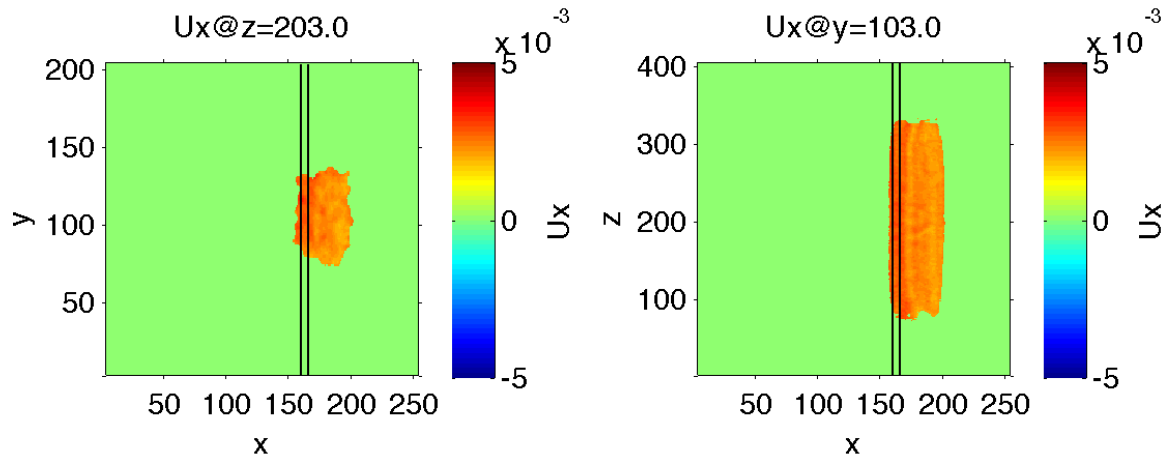


Figure 3.39 – Plasma bulk velocity (the V_x component) in the xOy plane (left panel) and xOz plane (right panel) at $t=3T_{Li}$; T_{Li} is the ion Larmor period at the left hand side of the transition region. The two black lines mark the position of the transition region where the magnetic field is non-uniform.

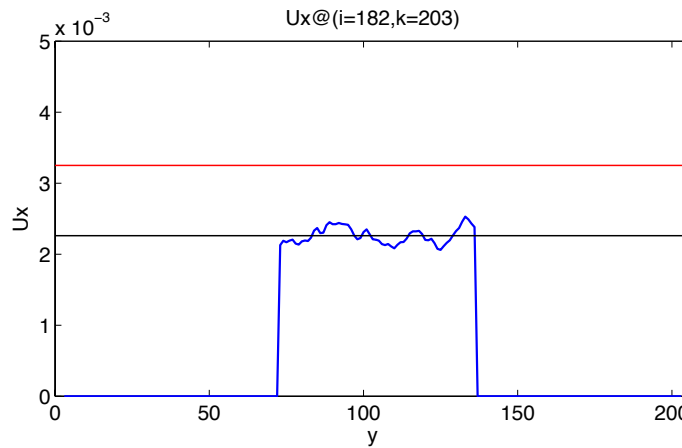


Figure 3.40 – Forward plasma bulk velocity as a function of the y -coordinate, $V_x=V_x(y)$, for $x=182$ and $z=203$. The black line corresponds to the average value of the plasma bulk velocity, while the red one represents the initial injection velocity.

In an additional simulation, the case IV-3, the thickness of the magnetic discontinuity (the “magnetopause”) increased from $5r_{Li}$ to $32r_{Li}$. The magnetic field gradient is however kept unmodified. The input parameters for this case are given in Table 3.1 and Table 3.2.

We analyzed the propagation of the plasma element over three ion Larmor periods from the beginning of the simulation. The numerical results obtained are shown in Figure 3.41. On the first and second columns we illustrate the number density for electrons and ions in the xOy plane perpendicular to the ambient magnetic field, while on the third and fourth columns we show the V_x and V_y components of the plasma bulk velocity for the same cross-sections as in the first two columns. We present the results at $t=0.5T_{Li}$ (first line), $t=1T_{Li}$ (second line), $t=1.5T_{Li}$ (third line), $t=2T_{Li}$ (fourth line), $t=2.5T_{Li}$ (fifth line) and $t=3T_{Li}$ (sixth line). The plasma bulk velocity is computed only for the grid cells having a number density of at least 5% from the initial value. The non-uniform magnetic field region is marked with two black straight lines in all 24 panels shown.

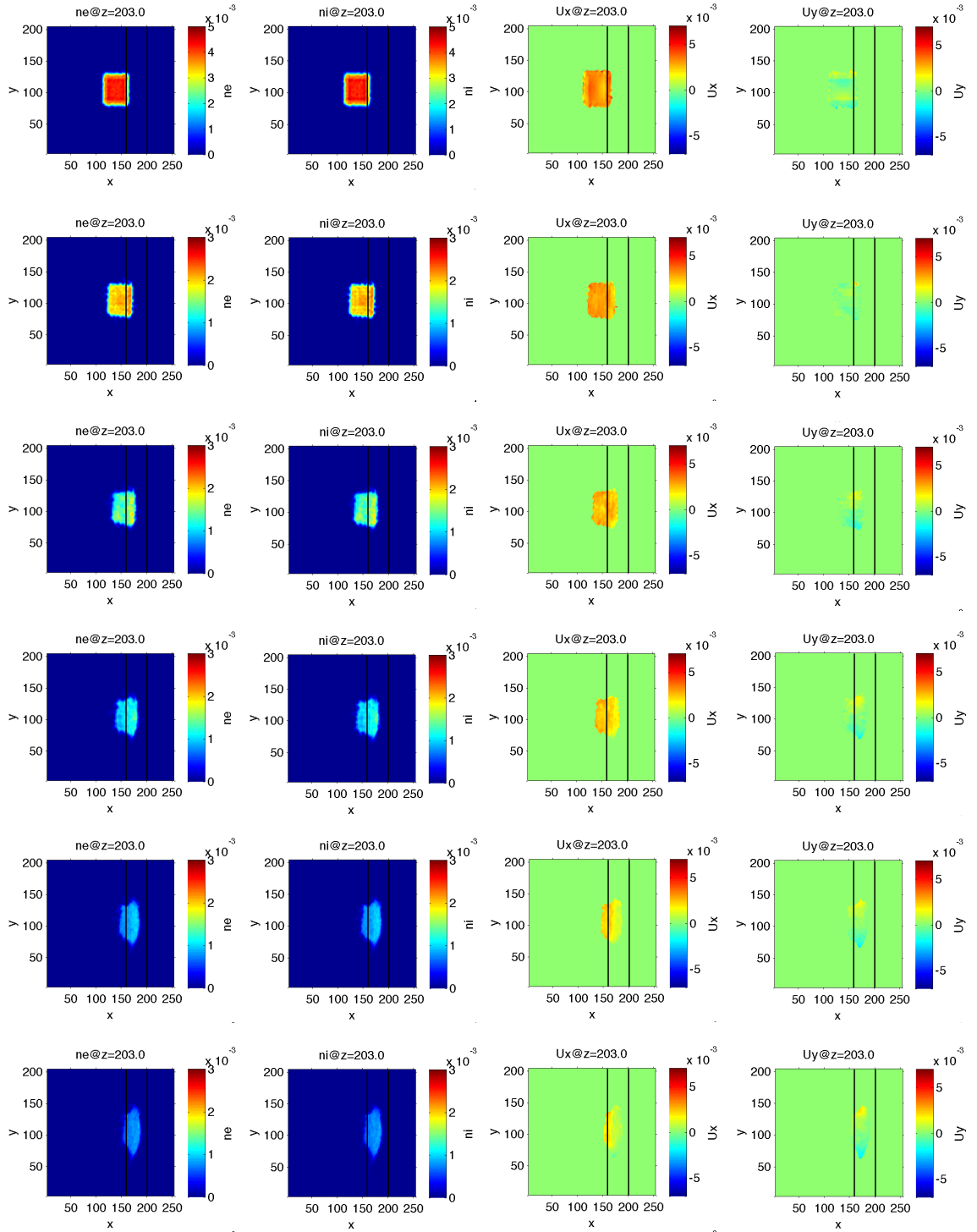


Figure 3.41 – Number density of electrons (first column) and ions (second column) and also the V_x (third column) and V_y (fourth column) components of the plasma bulk velocity, in the xOy plane perpendicular to the magnetic field, at $t=0.5T_{Li}$ (first line), $t=1T_{Li}$ (second line), $t=1.5T_{Li}$ (third line), $t=2T_{Li}$ (fourth line), $t=2.5T_{Li}$ (fifth line) and $t=3T_{Li}$ (sixth line); T_{Li} is the ion Larmor period in the left hand side of the transition region. The two black lines mark the position of the transition region where the magnetic field is non-uniform. The bulk velocity is computed only for those grid cells having a number density of at least 5% from its initial value, otherwise V_x and V_y are set to zero.

The front-side of the plasma element enters into the transition region at $t \approx 0.5T_{Li}$ and after $3T_{Li}$ the entire cloud moved inside the non-uniform magnetic field area (see first two columns of Figure 3.41). The convection velocity decreases significantly as the plasma is advancing into the stronger magnetic field as shown in Figure 3.41 (third column). At the end of the simulation, after three ion Larmor periods, the V_x component of the bulk velocity is much smaller than initially, i.e. $V_x = 0.15V_0$. In this case too, the plasma is deflected also along both the positive and negative Oy directions (see first and last columns of Figure 3.41). In order to emphasize even more clearly the adiabatic breaking mechanism of our simulations, we illustrate in Figure 3.42 the variation of the plasma streaming velocity across the non-uniform magnetic field. Let us rewrite the equation (3.18) in the following more compacted form:

$$1 - \left[\frac{V(x)}{V_0} \right]^2 = \frac{2(\bar{\mu}_e + \bar{\mu}_i)B_1}{(m_e + m_i)V_0^2} \left[\frac{B(x)}{B_1} - 1 \right] \quad (3.22)$$

where the constant in the right term of equation (3.18) is expressed as a function of the plasma and field parameters at the left hand side of the transition region. Equation (3.22) provides a linear dependence of the quantity $(1 - V/V_0)^2$ as a function of $B/B_1 - 1$, at a given x . We computed the V_x component of the plasma bulk velocity at the front edge of the plasma cloud from the simulation data obtained in case IV-3, for the time snapshots illustrated in Figure 3.41.

From equation (3.9), we calculated the magnetic field in the front-side position of the plasma cloud. Thus, a set of 7 pairs $V_x - B$ is obtained for the front edge of the plasma element. In Figure 3.42 we show the resulting plot of $(1 - V_x/V_0)^2$ as a function of $B/B_1 - 1$ (blue dots). The red line illustrates a linear fit of the simulation data with equation (3.22). The coefficient of determination R^2 for the linear fit is equal to 0.94 and indicates that indeed the data fulfill equation (3.22). This is a quantitative confirmation of the adiabatic breaking mechanism from 3D-PIC simulation of a plasma element transported in a non-uniform background magnetic field.

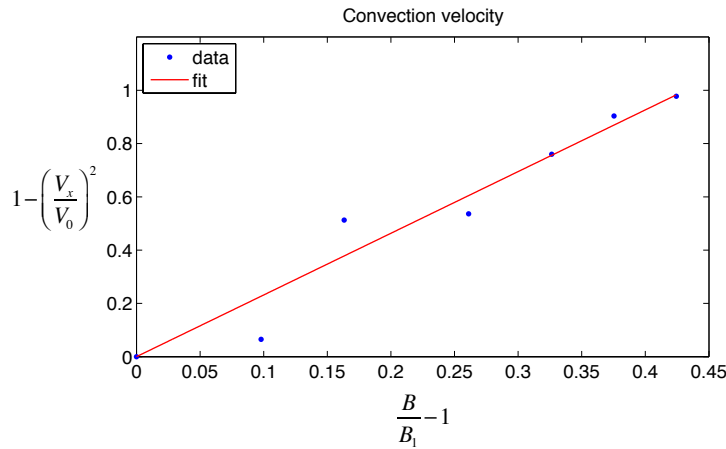


Figure 3.42 – Plasma convection velocity V_x as a function of the magnetic field strength B in the following representation, i.e. $(1 - V_x/V_0)^2$ as a function of $B/B_1 - 1$ for seven pairs $V_x - B$ obtained at the propagation front of the plasma element at different moments of the interaction with the magnetic discontinuity (blue dots). The red line shows the linear fitting of the simulation data with equation (3.22). The coefficient of determination R^2 for the linear fit is equal to 0.94.

3.3.5 Case V: Fast speed plasma element injected across a non-uniform transverse magnetic field – penetration of the magnetic barrier

In the last case we use the initial plasma parameters similar to the second simulation, i.e. case II, and introduce a gradient of the magnetic field as shown in Figure 3.28. The initial injection velocity is two times larger here than in the previous simulation (case IV). The plasma stream is supersonic $V_0=1.35V_s$, where V_s is given by (Chen, 1974):

$$V_s = \sqrt{\frac{k_B T_e}{m_i}} \quad (3.23)$$

The height of the magnetic barrier is identical to the one considered in cases III and IV-1, i.e. $B_2=1.5B_1$, when no penetration was possible. The magnetic field increases linearly by 50% from the asymptotic left value over a scale length of ~ 5 ion gyration radii. The input parameters are given in Table 3.1 and Table 3.2.

The dynamics of the cloud was investigated at several moments of time as shown by Figure 3.43 that illustrates the number density of electrons (top panels) and ions (bottom panels) in the xOy plane perpendicular to the magnetic field, at $t=0$ (left column), $t=0.65T_{Li}$ (middle-left column), $t=1.55T_{Li}$ (middle-right column) and $t=2T_{Li}$ (right column). After less than one ion Larmor period from the beginning of the simulation, at $t=0.65T_{Li}$, the front edge of the plasma element already arrived in the vicinity of the magnetic transition region. The density increases at the propagation front of the cloud, for both electrons and ions (see middle-left panels of Figure 3.43), as an effect of the subsonic slowing-down of the cloud by the magnetic barrier. This density enhancement is propagating backwards (along negative x -axis). At the end of the simulation, the entire cloud crossed the discontinuity and moved into the right side of the transition region. Its width along the x -axis is significantly diminished (see right panels of Figure 3.43). Thus, the interaction of the supersonic plasma with the magnetic barrier led to the compression of the entire cloud along the injection direction.

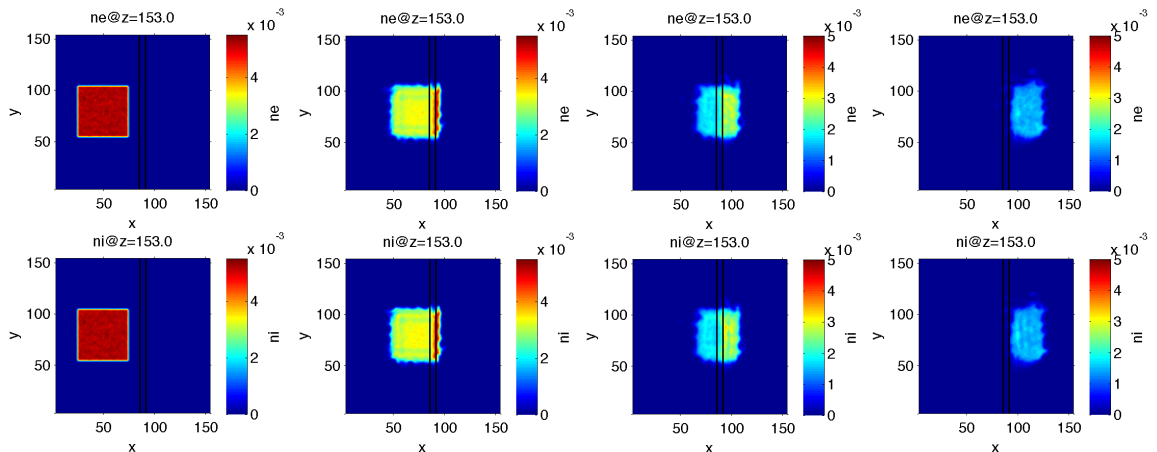


Figure 3.43 – Number density of electrons (top panels) and ions (bottom panels) at $t=0$ (left column), $t=0.65T_{Li}$ (middle-left column), $t=1.55T_{Li}$ (middle-right column) and $t=2T_{Li}$ (right column); T_{Li} is the ion Larmor period in the left hand side of the transition region. The two black lines mark the position of the transition region where the magnetic field is non-uniform. The xOy plane perpendicular to the background magnetic field is shown here, for $z=153$ cross-section.

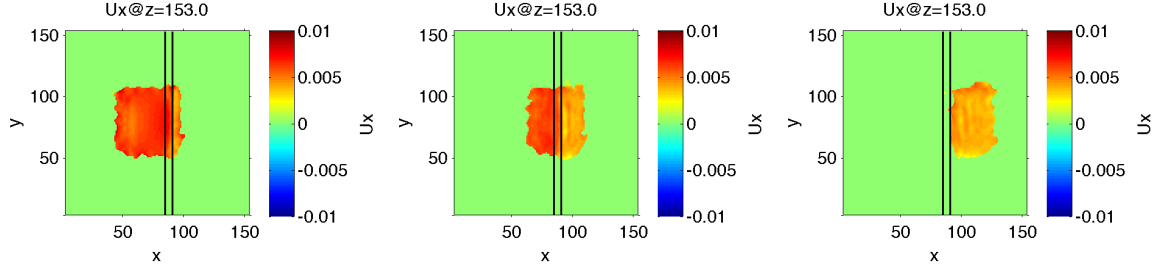


Figure 3.44 – V_x component of the plasma bulk velocity at $t=0.65T_{Li}$ (left column), $t=1.55T_{Li}$ (middle column) and $t=2T_{Li}$ (right column); T_{Li} is the ion Larmor period in the left hand side of the transition region. The two black lines mark the position of the transition region where the B-field is non-uniform. The xOy plane perpendicular to the background magnetic field is shown here, for $z=153$.

In Figure 3.44 we illustrate the V_x component of the plasma bulk velocity in the xOy plane, for $z=153$, at $t=0.65T_{Li}$ (left column), $t=1.55T_{Li}$ (middle column) and $t=2T_{Li}$ (right column). The plasma bulk velocity is computed only for those grid cells having a density of at least 5% from its initial value. As the plasma cloud crosses the transition region, it is slowed down as shown in the left and middle panels of Figure 3.44. After two ion cyclotron periods from the beginning of the simulation, the entire plasma element is braked to subsonic speeds and is streaming with a lower velocity into the right hand side region where the magnetic field is uniform. The convection velocity is 60% smaller now than it was initially (see right panel of Figure 3.44).

In order to better understand the interaction of the supersonic plasma element with the non-uniform increasing magnetic field, we analyzed how the plasma and field parameters varies along the initial injection direction. In Figure 3.45 we show the variation along the x -axis, for $y=77$ and $z=153$, of the electron number density n_e (top panel), plasma convection velocity V_x (middle panel) and magnetic field B_z (bottom panel), at $t=1.55T_{Li}$. We illustrate here only the values corresponding to the central region of the plasma element, i.e. from $x=68$ to $x=104$. The grey rectangle indicates the transition region with a non-uniform magnetic field, while the red line on the middle panel mark the ion sound speed (3.23). As can be noticed, when the supersonic plasma flow is interacting with the magnetic barrier, the streaming velocity decreases to subsonic values, while the number density is increasing (see top and middle panels of Figure 3.45). Indeed, on average, the plasma convection velocity at the left side of the transition region is equal to $\sim 1.25V_s$, while on the right $V_x \approx 0.83V_s$. Thus, the V_x velocity is reduced across the non-uniform B-field region by ~ 1.5 times. On the other hand, the number density is increased with approximately the same ratio as the bulk velocity. Also, for this simulated case, the magnetic field increases by 50% over ~ 5 ion Larmor radii, i.e. $B_2/B_1=1.5$ (see bottom panel of Figure 3.45). It should be mentioned that the B_x and B_y components of the magnetic field are practically equal to zero during the entire simulation time. By analyzing the numerical results obtained, we can conclude that a perpendicular shock is formed when the supersonic plasma element is interacting with the magnetic barrier. There is a compression of the plasma at the shock and the flow is slowed-down to subsonic velocities.

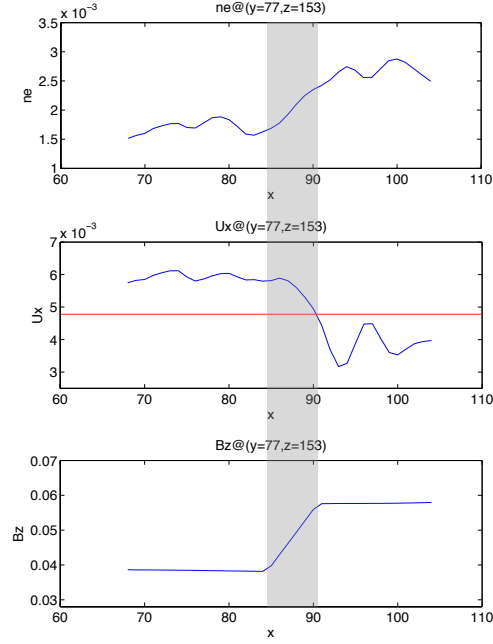


Figure 3.45 – Variation along the x -axis, for $y=77$ and $z=153$, of the electron number density n_e (top panel), plasma convection velocity V_x (middle panel) and magnetic field B_z (bottom panel), at $t=1.55T_{Li}$. We illustrate here only the values corresponding to the central region of the plasma element, i.e. from $x=68$ to $x=104$. The grey rectangle indicates the transition region with a non-uniform magnetic field, while the red line on the middle panel mark the ion sound speed V_s .

3.4 Conclusions

In this chapter I studied the interaction of three-dimensional plasma elements with transverse magnetic fields by using full-electromagnetic particle-in-cell simulations. I considered a non-diamagnetic plasma cloud that is streaming in vacuum across a constant background magnetic field. No electric fields are assumed initially inside the simulation domain. Two different profiles of the external magnetic field are discussed in our simulations: (i) a uniform field and (ii) a non-uniform field that varies along the initial injection direction over a finite width transition region with a length scale of ~ 5 ion gyration radii. The initial velocity distribution function of both electrons and protons is a displaced Maxwellian with an average velocity oriented perpendicular to the ambient magnetic field. Several cases have been analyzed and discussed. For the beginning, in the first two cases, plasma elements with zero/non-zero bulk velocities are immersed into a uniform external magnetic field. Further, in cases III–V, a non-uniform magnetic field profile is considered with three different plasma injection velocities, i.e. $V_0=1.15V_{Ti}$ (slow speed cloud), $V_0=2.30V_{Ti}$ (intermediate speed cloud) and $V_0=4.60V_{Ti}$ (fast speed cloud). The space and time evolution of the plasma and electromagnetic field have been analyzed and discussed over a time interval varying from 2 to ~ 4 ion cyclotron periods. It should be mentioned that initially the plasma element is a rectangular shape box with uniform density. The simulation geometry considered here allows the simultaneous investigation of the change of momentum along the x -axis, the formation of the space charge layers along the y -axis and the plasma expansion along the z -axis.

It should be mentioned that the periodic boundary conditions used in our simulations could induce undesired effects inside the simulation domain. To reduce the possible influence of the periodic boundaries on the dynamics of the plasma and the electromagnetic field, we tried to keep the edges of the simulation domain as far as possible from the plasma cloud. Moreover, the simulations have been stopped when a significant number of particles reached the boundaries of the domain.

In the first case I study the early dynamics of a stationary plasma element ($V_0=0$). The results obtained indicated that shortly after the beginning of the simulation, for $t > T_{Le}/2$, the plasma element can be divided into three main different regions in the perpendicular plane to the magnetic field: (i) a quasineutral core with equal number densities for both electrons and ions, (ii) a negative charge layer surrounding the quasineutral core and (iii) a positive charge layer at the outer edges of the cloud. As a consequence, perpendicular electric fields are generated locally, while inside the quasineutral core of the plasma no electric fields have been evidenced. *Galvez et al.* (1988), using a two-dimensional electrostatic PIC code, have made similar conjectures on the plasma expansion across a uniform magnetic field. Also, our results illustrate that a diamagnetic current is flowing around the boundaries of the cloud and a small diamagnetic cavity is formed in the xOy plane. Indeed, in the actual position of the cloud the total magnetic field is decreased by less than 1% with respect to the background field (we simulate low- β plasmas). On the other hand, the plasma element is expanding rapidly along the parallel direction to the magnetic field by thermal motion. As a result, a parallel electric field is formed at the edges of the cloud along the z -axis.

In the second case the plasma cloud is streaming across the uniform magnetic field. It has been shown that after less than one electron cyclotron period from the beginning of the simulation, a polarization electric field is formed inside the quasineutral core of the cloud, in agreement with the theoretical kinetic model of *Schmidt* (1960) and in contrast with the previous case where no electric fields have been observed inside the main bulk of the plasma. This polarization electric field is sustained by the space charge layers forming at the boundaries of the cloud along the perpendicular direction to both the magnetic field and the plasma convection velocity. After two ion gyration periods from the beginning of the simulation, the plasma element continues to stream along the positive x -axis with almost the injection velocity. Up to the end of the simulation, due to the thermal expansion of particles along the magnetic field, the plasma density became five times smaller than initially.

In the third case the plasma element is injected across a non-uniform magnetic field that is confined inside a transition region with a scale length of ~ 5 ion Larmor radii. After two ion Larmor periods from the beginning of the simulation, the front edge of the plasma element is localized inside the transition region where the magnetic field is by 50% larger than at the injection position. It has been shown that the cloud cannot cross the transition region and the convection motion is fully stopped. Moreover, the front-side plasma is pushed back and simultaneously deflected along the negative and positive

directions of the y -axis. At the same time, the electrons and ions are expanding rapidly along both parallel and antiparallel directions of the background magnetic field. The simulation results obtained here clearly emphasize the physical process of adiabatic breaking that takes place when a non-diamagnetic plasma element is streaming into an increasing transverse magnetic field and are in good agreement with theoretical kinetic models (*Schmidt, 1960; Lemaire, 1985*).

In order to force the penetrability of the transition region, the injection velocity of the plasma element has been increased by a factor of 2 in case IV-1. Yet, the height of the magnetic barrier is still too large and the plasma cloud cannot penetrate the non-uniform magnetic field region. Therefore, to enable the penetration in case IV-2, the asymptotic field into the right hand side of the transition region has been reduced under the theoretical critical value for which all the convection energy is transformed into gyration energy and no further transport across the magnetic field is possible. The simulation results obtained clearly evidenced the crossing of the magnetic barrier. After three ion gyration periods from the beginning of the simulation the main bulk of the cloud is located inside the right hand side of the transition region where the field is uniform. To better illustrate the adiabatic breaking mechanism, we increased the width of the transition region, in case IV-3, from $5r_{Li}$ to $32r_{Li}$ without changing the magnetic field gradient. During the three ion Larmor periods simulated here, I analyzed the variation of the plasma streaming velocity with the strength of the non-uniform magnetic field. The results obtained are in good agreement with the theoretical solution (*Lemaire, 1985*).

In the fifth case the convection velocity of the plasma element is supersonic, i.e. $V_0=1.35V_s$, and the height of the magnetic barrier is identical to the one considered in cases III and IV-1 where no penetration was possible. This time the cloud is twice as fast than in the previous case IV. The results obtained show that a perpendicular shock is formed when the supersonic plasma element is interacting with the magnetic barrier. Indeed, we observed a compression of the plasma at the shock and the flow was slowed-down to subsonic velocities. By the end of the simulation ($t=2T_{Li}$), the entire cloud is located at the right side of the transition region and its width along the x -axis is significantly diminished. Thus, the interaction of the supersonic plasma with the magnetic barrier led to the compression of the entire cloud along the injection direction.

The numerical results presented here confirm the formation of the polarization electric field in the perpendicular direction to the initial plasma bulk velocity and the background magnetic field, as predicted theoretically by *Schmidt (1960)*. I evidenced the adiabatic breaking process advocated previously by theoretical kinetic models and revealed in laboratory experiments. To my knowledge this is the first time that the interaction of a plasma element/jet with a magnetic field discontinuity is investigated with three-dimensional particle-in-cell simulations.

Chapter 4

Summary and conclusions

In my PhD thesis I have simulated with test-kinetic and particle-in-cell methods the interaction of non-diamagnetic plasma elements with transverse magnetic fields. I have considered plasma and electromagnetic field configurations typical for the terrestrial magnetosphere. The numerical results obtained in the present thesis are important for understanding the physical processes responsible for the transfer of mass, momentum and energy in space plasmas.

In the first chapter of my thesis I studied the kinetic effects at the boundaries of a proton stream injected across a non-uniform transverse magnetic field typical for one-dimensional tangential discontinuities. The Liouville mapping method has been applied to compute the velocity distribution function with both forward and backward test-kinetic simulation approaches. The electric and magnetic fields are prescribed a priori from the beginning of the simulation. The particles are moving across regions with sharp variations of a parallel/antiparallel magnetic field. Two different profiles of the electric field have been taken into account, i.e. (i) a uniform profile and (ii) a non-uniform one computed from Laplace's equation. The electric field profiles considered here enable the propagation of the proton stream across the transverse magnetic field. The initial velocity distribution function of the protons is a displaced Maxwellian with the average velocity perpendicular to the magnetic field direction.

The overall evolution of the proton cloud is asymmetric due to the gradient-B drift acting inside the transition region where the magnetic field is non-uniform. It has been shown that the features imprinted to the cloud morphology by its interaction with the magnetic discontinuity are preserved even at large distances from the transition region where the field is uniform. The asymmetry of the cloud is retrieved in its kinetic structure and an energy-dispersed structure is formed. The particles' energy increases towards the fringe of the cloud in the perpendicular direction to the bulk velocity and magnetic field. Ring-shaped velocity distribution functions are obtained at the outer edges of the cloud. We have shown that this effect is due to the gradient-B drift that efficiently disperses protons proportionally to their kinetic energy. In the front-side and in the trailing edge of the cloud we evidenced the formation of non-gyrotropic velocity distribution functions due to the remote sensing of particles whose guiding centers pertain to the inner cloud.

The numerical results obtained in the first chapter suggest a physical mechanism that can explain the formation of energy-dispersed structures at the edges of proton beams interacting with non-uniform magnetic fields. I have identified kinetic effects that lead to

the formation of ring-shaped and non-gyrotropic velocity distribution functions within the energy dispersed structures. Although the results were obtained for two particular configurations of the prescribed electromagnetic field, their relevance is more general.

For a consistency check, the forward results have been cross-checked with the backward method. It has been shown that in general the two approaches provide similar results. Nevertheless, we demonstrated that there are significant differences between the distribution functions computed with the two approaches, especially in those regions of configuration space that are characterized by a steep spatial variation of the velocity distribution function.

In the second chapter of my thesis I studied the kinetic structure of tangential discontinuities by using one-dimensional electromagnetic particle-in-cell simulations. Three problems have been considered, namely (i) a tangential discontinuity without velocity shear and different asymptotic densities and temperatures, (ii) a tangential discontinuity with velocity shear where the plasma bulk velocity varies in the perpendicular direction to the magnetic field and the asymptotic densities and temperatures are equal, and (iii) a plasma slab moving across a transverse magnetic field and a background stagnant plasma with equal densities and temperatures. For all three problems considered, the space and time evolution of the plasma and electromagnetic field parameters have been analyzed and discussed.

The numerical results obtained here revealed the formation of a finite width transition region at the interface of two magnetized plasmas with different macroscopic parameters. The transition region has properties typical for a tangential discontinuity with a scale length of few ion Larmor radius and it is stable over the entire simulation time of 3–5 ion cyclotron periods. We emphasized the critical role played by the number of particles initialized inside the simulation domain. It has been shown that a small number of particles alters significantly the results. By taking time-averages, we were able to reduce the statistical electrostatic noise and to smooth the transition profiles for the plasma and electromagnetic field parameters.

The time-averaged simulated profiles have been compared with the kinetic solution of a steady-state theoretical model (*Roth et al.*, 1996). The kinetic solution provides the equilibrium structure of a one-dimensional tangential discontinuity starting from first principles. Identical input parameters have been considered in both the 1D PIC simulations and the 1D kinetic model. The PIC results are in good agreement with the kinetic solutions and provide an independent validation of the hypothesis assumed by these models. It is important to point out that the kinetic models assume particular expressions for the solution of the Vlasov equations based on the so-called “cut-off” functions (see *Lemaire and Burlaga*, 1976; *Roth et al.*, 1996; *Echim et al.*, 2005). It was believed that these functions were rather arbitrary and that are a limitation of the model. The PIC simulations obtained solutions quite similar to the kinetic ones and thus provide an important validation.

In the third chapter of my thesis I studied the interaction of a small Larmor radius plasma element/cloud with transverse magnetic fields in configurations typical for the terrestrial magnetosphere. For this purpose I used three-dimensional electromagnetic particle-in-cell simulations. The plasma elements considered here are streaming into vacuum and perpendicular to a background uniform/non-uniform magnetic field. In the latter case, the magnetic field is unidirectional and increases linearly along the injection direction. No electric fields are assumed initially. Various cases have been investigated.

First, the plasma element is injected into a uniform magnetic field. A non-uniform magnetic field typical to a tangential discontinuity was considered too. I have chosen three different injection velocities that describe two subsonic flows and one supersonic flow. The simulation geometry considered here allowed the simultaneous investigation of the change of momentum along the x-axis, the formation of the space charge layers along the y-axis and the plasma expansion along the z-axis.

The results included in the third chapter of my thesis confirmed the formation of the polarization electric field along the perpendicular direction to the initial plasma bulk velocity and to the background magnetic field, as predicted theoretically by *Schmidt* (1960). I have shown that the penetration of a magnetic discontinuity is not possible if the height of the barrier is larger than a certain critical value. The latter is the total magnetic field for which the entire initial convection energy is converted into gyration energy in the stronger magnetic field. When the magnetic barrier is too steep, the plasma is pushed back and simultaneously deflected along the negative and positive directions of the y-axis, perpendicular to both the background magnetic field and initial injection direction.

It has been shown that the transition region can be penetrated by reducing the height of the magnetic barrier or by increasing the initial injection velocity. The simulation results obtained clearly emphasize the adiabatic breaking mechanism and are in good agreement with the theoretical kinetic models (*Schmidt*, 1960; *Lemaire*, 1985).

The original contributions of my PhD thesis are listed below:

- I identified a new physical mechanism that can explain the formation of an energy-dispersed structure with ring-shaped and non-gyrotropic distribution functions at the edges of a proton cloud interacting with a non-uniform transverse magnetic field (*Voitcu and Echim*, 2012).
- I compared for the first time the forward and backward Liouville approaches corresponding to the test-kinetic simulation method and we have shown that the two approaches provide different results when the velocity distribution function varies rapidly in the configuration space (*Voitcu et al.*, 2012).
- I have simulated for the first time a tangential discontinuity using a full-particle code. The results obtained provide an independent validation of the hypothesis assumed by the theoretical models of tangential discontinuities. To our knowledge, this is for the

SUMMARY AND CONCLUSIONS

first time when theoretical kinetic models are directly compared with numerical simulations performed under the same initial and asymptotic conditions.

- I have simulated three-dimensional plasma clouds interacting with transverse magnetic fields using a full electromagnetic particle-in-cell code over time intervals three times larger than in the previous similar numerical simulations. This is for the first time when the interaction of a plasma element/jet with a magnetic field discontinuity is investigated with three-dimensional particle-in-cell simulations. We evidenced physical processes advocated previously by theoretical models and revealed in laboratory experiments.

Several future perspectives can be taken into account to improve and develop this work further. An important step would be to simulate a significantly larger number of particles to reduce the amplitude of the electrostatic statistical noise. On the other hand, more appropriate boundary conditions should be considered in order to eliminate the possible unwanted effects related to the fields periodicity in our simulations. Other important step would be to take into account the presence of a background plasma. Also, more realistically magnetic field configurations for the study of the terrestrial magnetopause should be considered.

Acknowledgements

All the research activities related to my PhD thesis have been carried out at the *Institute of Space Science*, Magurele in close collaboration with Dr. Marius Echim. Part of the work presented in the first chapter has been performed in collaboration with Prof. Richard Marchand from the *University of Alberta* in Canada. The three-dimensional particle-in-cell simulations included in the third chapter of my thesis have been run at the *Belgian Institute of Space Aeronomy* in Brussels.

The work for my thesis has been financially supported by the following national and international research projects:

- Sectorial Operational Programme Human Resources Development (SOP HRD) financed from the European Social Fund and by the Romanian Government under the contract number SOP HRD/107/1.5/S/82514.
- European Community's Seventh Framework Programme (FP7/2007-2013) under grant agreement no. 313038/STORM.
- Romanian Ministry of National Education, CNCS – UEFISCDI, project number PN-II-ID-PCE-2012-4-0418/TIMESS.
- Bilateral project approved by the Wallonie-Bruxelles International through project GL/AS/CAS/SOR/2012/70032 and by the Romanian Ministry of Education and Research through the grant CAPACITATI-593/2012/OMMA.
- European Space Agency Plan for European Cooperating States (ESA PECS) project no. 98049/2007-2012/KEEV.

References

- [1] Alfvén, H.: *Cosmical Electrodynamics*, Oxford, The Clarendon Press, 1953.
- [2] Archer, M. O. and Horbury, T. S.: *Magnetosheath dynamic pressure enhancements: occurrence and typical properties*, *Ann. Geophys.*, 31, 319-331, 2013.
- [3] Ashour-Abdalla, M., L. M. Zelenyi, V. Perroomian, R. L. Richard: *Consequences of magnetotail ion dynamics*, *J. Geophys. Res.*, 99:14, 891–916, 1994.
- [4] Ashour-Abdalla, M., J. N. Leboeuf, D. Schriver, J.-M. Bosqued, N. Cornilleau-Wehrlin, V. Sotnikov, A. Marchaudon, and A. N. Fazakerley, *J. Geophys. Res.* 111, A10223, 2006.
- [5] Birdsall, C. K. and Langdon, A. B.: *Plasma Physics via Computer Simulation*, Taylor and Francis, 1991.
- [6] Birn, J., J. Raeder, Y. Wang, R. Wolf, and M. Hesse, *Ann. Geophys.* 22, 1773, 2004.
- [7] Bostick, W. H.: *Experimental study of ionized matter projected across a magnetic field*, *Physical Review*, 104, 292, 1956.
- [8] Bosqued, J. M., J. A. Sauvaud, D. Delcourt, and R. A. Kovrazhkin: *Precipitation of suprathermal ionospheric ions accelerated in the conjugate hemisphere*, *J. Geophys. Res.* 91, 7006-7018, 1986.
- [9] Buneman, O.: *TRISTAN – The 3D electromagnetic particle code*, in *Computer Space Plasma Physics: Simulation Techniques and Software*, edited by Matsumoto, H. and Omura, Y., Terra Scientific Publishing Company, Tokyo, 1993.
- [10] Cai, D., Li, Y., Nishikawa, K.-I., Xiao, C., Yan, X, and Pu., Z: *Parallel 3-D electromagnetic particle code using High Performance Fortran: Parallel TRISTAN*, in *Space Plasma Simulation*, Lecture Notes in Physics, vol. 615, pp. 25-53, Springer, 2003.
- [11] Cargill, P. J.: *Hybrid simulations of tangential discontinuities*, *Geophysical Research Letters*, 17, 1037-1040, 1990.
- [12] Cargill, P. J. și Eastman, T. E.: *The structure of tangential discontinuities 1. Results of hybrid simulations*, *J. Geophys. Res.*, 96, 13763-13779, 1991.
- [13] Chen, F. F.: *Introduction to plasma physics*, Plenum Press, New York, 1974.
- [14] Curran, D. B., Goertz ,C. K., and Whelan, T. A.: *Ion Distributions in a Two-Dimensional Reconnection Field Geometry*, *Geophys. Res. Lett.*, 14, 99, 1987.

REFERENCES

- [15] Curran, D. B., Goertz, C. K.: *Particle Distributions in a Two-Dimensional Reconnection Field Geometry*, J. Geophys. Res., 94, 272, 1989.
- [16] De Keyser, J. and Roth, M.: *Equilibrium conditions for the tangential discontinuity magnetopause*, Journal of Geophysical Research: Space Physics, Volume 102, Issue A5, pages 9513–9530, 1997.
- [17] Delcourt, D. C., Martin, R. F. Jr., and Alem, F.: *A simple model of magnetic moment scattering in a field reversal*, Geophys. Res. Lett., 21, 1543, 1994.
- [18] Delcourt, D. C., Sauvaud, J. A., Martin, R. F., Moore, T. E.: *Gyrophase effects in the centrifugal impulse model of particle motion in the magnetotail*, J. Geophys. Res., 100, 17211, 1995.
- [19] Delcourt, D. C., Sauvaud, J.-A., Martin, R. F., Moore, T. E.: *On the non-adiabatic precipitation of ions from the near-Earth plasma sheet*, J. Geophys. Res., 101, 17409, 1996.
- [20] Delcroix, J. L. and Bers, A.: *Physique des plasmas*, Tome 2, Savoirs Actuels-InterÉditions, CNRS Éditions, Paris, 1994.
- [21] Demidenko, I. I., Lomino, N. S., Padalka, V. G., Safronov, B. G. and Sinelnikov, K. D.: *Motion of a Plasmoid in a Nonuniform Transverse Magnetic Field*, Soviet Physics-Technical Phys., 11, 1354, 1967.
- [22] Demidenko, I. I., Lomino, N. S., Padalka, V. G., Safronov, B. G. and Sinelnikov, K. D.: *Plasma stream in an inhomogeneous transverse magnetic field*, Soviet Physics-Technical Phys., 14, 16, 1969.
- [23] Demidenko, I. I., Lomino, N. S. and Padalka, V. G.: *Plasma Flow in a Strong Transversal Magnetic Field*, Soviet Physics-Technical Phys., 16, 1096, 1972.
- [24] Echim, M. M. and Lemaire, J. F.: *Laboratory and numerical simulations of the impulsive penetration mechanism*, Space Science Reviews, 92, 565, 2000.
- [25] Echim, M. M. and Lemaire, J.: *Advances in the kinetic treatment of the solar wind magnetosphere interaction: the impulsive penetration mechanism*, AGU Geophysical Monograph 133 Earth's Low Latitude Boundary Layer, Washington, 2003.
- [26] Echim, M. M.: *Kinetic investigation of the impulsive penetration mechanism of 2D plasma elements into the Earth's magnetosphere*, PhD thesis, Bruxelles, 2004.
- [27] Echim, M. M., Lemaire, J. and Roth, M.: *Self-consistent solution for a collisionless plasma slab in motion across a magnetic field*, Phys. Plasmas, 12, 072904, 2005.
- [28] Echim, M. M. and Lemaire, J.: *Two-dimensional Vlasov solution for a collisionless plasma jet across transverse magnetic field lines with a sheared bulk velocity*, Physical Review E, vol. 72, Issue 3, 2005.

- [29] Echim, M., Maggiolo, R., De Keyser, J., Zhang, T. L., Voitcu, G., Barabash, S., Lundin, R.: *Comparative investigation of the terrestrial and venusian magnetopause: Kinetic modeling and experimental observations by Cluster and Venus Express*, Planetary and Space Science, 59, 10, 1028-1038, 2011.
- [30] Escoubet, C. P. , C. T. Russell, and R. Schmidt: *The Cluster and Phoenix missions*, Kluwer Academic Publishers, Dordrecht, 1997.
- [31] Frank, L. A., W. R. Paterson, and M. G. Kivelson, J. Geophys. Res. 99, 14877, 1994.
- [32] Galvez, M.: *Computer simulation of a plasma streaming across a magnetic field*, Physics of fluids, 30, 2729, 1987.
- [33] Galvez, M., Gary, S. P., Barnes, C., Winske, D.: *Computer simulations of plasma expansion across a magnetic field*, Phys. Fluids 31, 6, 1988.
- [34] Galvez, M. and Borovsky, J. E.: *The expansion of polarization charge layers into a magnetized vacuum: theory and computer simulations*, Phys. Fluids B 3(8), 1991.
- [35] Grigorenko, E. E., A. Fedorovand, and L. M. Zelenyi, Ann. Geophys. 20, 329, 2002.
- [36] Gunell, H., Walker, J. J., Koepke, M. E., Hurtig, T., Brenning, N., Nilsson, H.: *Numerical experiments on plasmoids entering a transverse magnetic field*, Physics of Plasmas, 16 (11), 8, 2009.
- [37] Horbury, T. S., Burgess, D., și Franz, M.: *Three spacecraft observations of solar wind discontinuities*, Geophys. Res. Lett., 28, 677-680, 2001.
- [38] Hurtig, T., Brenning, N., Raadu, M. A.: *Three-dimensional electrostatic particle-in-cell simulation with open boundaries applied to a plasma beam entering a curved magnetic field*, Physics of Plasmas, 10 (11), 4291-4305, 2003.
- [39] Karlsson, T., N. Brenning, H. Nilsson, J.-G. Trotignon, X. Vallières, and G. Facsko: *Localized density enhancements in the magnetosheath: Three-dimensional morphology and possible importance for impulsive penetration*, J. Geophys. Res., 117, A03227, 2012.
- [40] Keiling, A., H. Reme, I. Dandouras, J. M. Bosqued, V. Sergeev, J.-A. Sauvaud, C. Jacquy, B. Lavraud, P. Louarn, T. Moreau, C. Vallat, C. P. Escoubet, G. K. Parks, M. McCarthy, E. Mobius, E. Amata, B. Klecker, A. Korth, R. Lundin, P. Daly, and Q.-G. Zong, J. Geophys. Res. 109, A05215, 2004a.
- [41] Keiling, A., H. Reme, I. Dandouras, J. M. Bosqued, G. K. Parks, M. McCarthy, L. Kistler, E. Amata, B. Klecker, A. Korth, and R. Lundin, Geophys. Res. Lett. 31, L12804, 2004b.
- [42] Keiling, A., G. K. Parks, H. Reme, I. Dandouras, M. Wilber, L. Kistler, C. Owen, A. N. Fazakerley, E. Lucek, M. Maksimovic, and N. Cornilleau-Wehrin, Ann. Geophys. 24, 2685, 2006.

REFERENCES

- [43] Knetter, T., Neubauer, F. M., Horbury, T., și Balogh, A.: *Discontinuity observations with Cluster*, Adv. Space Res., 32, 543–548, 2003.
- [44] Knetter, T., Neubauer, F. M., Horbury, T., și Balogh, A.: *Four-point discontinuity observations using Cluster magnetic field data: A statistical survey*, J. Geophys. Res., 109, A06102, 2004.
- [45] Langdon, A. B. and Birdsall, C. K.: *Theory of Plasma Simulation Using Finite-Size Particles*, The Physics of Fluids, 13, 2115–2122, 1970.
- [46] Lee, E., Wilber, M., Parks, G. K., Min, K. W., Lee, D. Y.: *Modeling of remote sensing of thin current sheet*, Geophys. Res. Lett., 31, L21806, 2004.
- [47] Lemaire, J. and Burlaga, L. F.: *Diamagnetic boundary layers: a kinetic theory*, Astrophys. Space Sci., 45, 303, 1976.
- [48] Lemaire, J.: *Impulsive penetration of filamentary plasma elements into the magnetospheres of the Earth and Jupiter*, Planet. Space Sci., 25, 887, 1977.
- [49] Lemaire, J.: *Plasmoid motion across a tangential discontinuity (with applications to the magnetopause)*, J. Plasma Phys., 33, 425-436, 1985.
- [50] Liu, W. W., J. Geophys. Res., 106, 289, 2001.
- [51] Livesey, W. A., Pritchett, P. L.: *Two-dimensional simulations of a charge-neutral plasma beam injected into a transverse magnetic-field*, Phys. Fluids B - Plasma Physics, 1, 914-922, 1989.
- [52] Lu, G., Onsager, T. G., Le, G., Russell, C. T.: *Ion injections and magnetic field oscillations near the high-latitude magnetopause associated with solar wind dynamic pressure enhancement*, Journal of Geophysical Research, 109, 2004.
- [53] Lundin, R., Yamauchi, M., Sauvaud, J.-A., and Balogh, A.: *Magnetospheric plasma boundaries: a test of the frozen-in magnetic field theorem*, Annales Geophysicae, 23, 2565-2578, 2005.
- [54] Mackay, F., Marchand, R., Kabin, K., Lu, J. Y.: *Test kinetic modelling of collisionless perpendicular shocks*, J. Plasma Physics, 74, 301, 2008.
- [55] Marchand, R., Mackay, F., Lu, J. Y., Kabin, K.: *Consistency check of a global MHD simulation using the test-kinetic approach*, Plasma Phys. Control. Fusion, 50, 074007, 2008.
- [56] Marchand, R.: *Test-particle simulation of space plasma*, Commun. Comput. Phys., 8, 2010.
- [57] Matsumoto, H. and Omura, Y.: *Particle Simulation of Electromagnetic Waves and its Application to Space Plasmas*, in *Computer Simulation of Space Plasmas*, edited by H. Matsumoto and T. Sato, pp. 43-102, Terra Scientific Publishing Company, Tokyo, 1984.

- [58] Meziane, K., M. Wilber, R. P. Lin, and G. K. Parks, *Geophys. Res. Lett.*, 30, 2049, 2003.
- [59] Nakamura, M., G. Paschmann, W. Baumjohann, and W. Sckopke, *J. Geophys. Res.* 96, 5631, 1991.
- [60] Nakamura, M., G. Paschmann, W. Baumjohann, and W. Sckopke, *J. Geophys. Res.* 97, 1449, 1992.
- [61] Neubert, T., Miller, R. H., Buneman, O., Nishikawa, K. I.: *The dynamics of low-beta plasma clouds as simulated by a 3-dimensional, electromagnetic particle code*, *Journal of Geophysical Research - Space Physics*, 97, 12057-12072, 1992.
- [62] Neugebauer, M., Clay, D. R., Goldstein, B. E., Tsurutani, B. T.: *A reexamination of rotational and tangential discontinuities in the solar wind*, *Journal of Geophysical Research*, 89, 5395-5408, 1984.
- [63] Northrop, T. G.: *The adiabatic motion of charged particles*, Interscience Publishers, New York, 1963.
- [64] Olsson, A., P. Janhunen, and W. Peterson, *Ann. Geophys.* 22, 2115, 2004.
- [65] Omura, Y. and Matsumoto, H.: *KEMPO1*, in *Computer Space Plasma Physics: Simulation Techniques and Software*, edited by H. Matsumoto and Y. Omura, pp. 21-65, Terra Scientific Publishing Company, Tokyo, 1993.
- [66] Omura, Y.: *One-dimensional Electromagnetic Particle Code: KEMPO1 A Tutorial on Microphysics in Space Plasmas*, in *Advanced Methods for Space Simulations*, edited by H. Usui and Y. Omura, pp. 1-21, TERRAPUB, Tokyo, 2007.
- [67] Papamastorakis, I., Paschmann, G., Sckopke, N., Bame, S. J., și Berchem, J.: *The magnetopause as a tangential discontinuity for large field rotation angles*, *J. Geophys. Res.*, 89, 127-135, 1984.
- [68] Plaschke, F., Hietala, H. and Angelopoulos, V.: *Anti-sunward high-speed jets in the subsolar magnetosheath*, *Ann. Geophys.*, 31, 1877-1889, 2013.
- [69] Pritchett, P. L. and F. V. Coroniti, *J. Geophys. Res.* 104, 12289, 1999.
- [70] Reme, H., J.-M. Bosqued, J.-A. Sauvaud, A. Cros, I. Dandouras, C. Aoustin, J. Bouyssou, T. Camus, J. Cuvilo, C. Martz, J.-L. Medale, H. Perrier, D. Romefort, J. Rouzaud, D. d'Uston, E. Mobius, K. N. Crocker, M. Granoff, L. M. Kistler, M.A. Popecki, D. Hovestadt, B. Klecker, G. Paschmann, M. Scholer, C. W. Carlson, D. W. Curtis, R. P. Lin, J. P. McFadden, V. Formisano, E. Amata, M.-B. Bavassano-Cattaneo, P. Baldetti, G. Belluci, R. Bruno, G. Chionchio, A. M. DiLellis, E. G. Shelley, A. G. Ghielmetti, W. Lennartsson, A. Korth, U. Rosenbauer, R.N.Lundin, S. Olsen, G. K. Parks, M.P. McCarthy, H. Balsiger, *Space Science Reviews* 79, 303, 1997.

REFERENCES

- [71] Richard, R.L., R.J.Walker, and M. Ashour-Abdalla: *The population of the magnetosphere by solar winds ions when the interplanetary magnetic field is northward*, Geophys. Res. Lett., 21:2455–8, 1994.
- [72] Roth, M.: *The plasmopause as a plasmasheath: a minimum thickness*, J. Atmospheric Terrest. Phys., 38, 1065, 1976.
- [73] Roth, M., DeKeyser, J., and Kuznetsova, M. M.: *Vlasov theory of the equilibrium structure of tangential discontinuities in space plasmas*, Space Science Reviews, 76, 251, 1996.
- [74] Rothwell, P. L., Silevitch, M. B., Block, L. P., Fälthammar, C.-G.: *Particle dynamics in a spatially varying electric field*, J. Geophys. Res., 100, 14875, 1995.
- [75] Saito, Y., T. Mukai, M. Hirahara, S. Machida, A. Nishida, T. Terasawa, S. Kokubun, and T. Yamamoto, Geophys. Res. Lett. 21, 2999, 1994.
- [76] Sauvaud, J.-A. and R. A. Kovrazhkin, J. Geophys. Res. 109, A12213, 2004.
- [77] Schmidt, G: *Plasma motions across magnetic fields*, The Physics of Fluids, 3, 961-965, 1960.
- [78] Scholer, M., Ipavich, F. M., Gloeckler, G., Hovestadt, D., and Klecker, B.: *Leakage of magnetospheric ions into the magnetosheath along reconnected field lines at the dayside magnetopause*, Journal of Geophysical Research, 86, 1299, 1981.
- [79] Sestero, A.: *Structure of plasma sheaths*, Phys. Fluids, 7, 44, 1964.
- [80] Sestero, A., Phys. Fluids 9, 2006, 1966.
- [81] Speiser, T. W., Williams, D. J., and Garcia, H. A.: *Magnetospherically trapped ions as a source of magnetosheath energetic ions*, J. Geophys. Res, 86, 723, 1981.
- [82] Villasenor, J. and Buneman, O.: *Rigorous charge conservation for local electromagnetic field solvers*, Computer Physics Communications, vol. 69, 1992.
- [83] Voitcu, G. and Echim, M.: *Ring-shaped velocity distribution functions in energy-dispersed structures formed at the boundaries of a proton stream injected into a transverse magnetic field: test-kinetic results*, Phys. Plasmas, 19, 022903, 2012.
- [84] Voitcu, G., Echim, M. and Marchand, R.: *Comparative study of forward and backward test-kinetic simulation approaches*, Comput. Phys. Commun., 2561-2569, 2012.
- [85] West, H. I. and Buck, R. M.: *Observations of >100-keV protons in the Earth's magnetosheath*, Journal of Geophysical Research, 81, 569, 1976.
- [86] Wetstone, D. M., Ehrlich, M. P., and Finkelstein, D.: *Experiments on plasmoids motion along magnetic fields*, Physics of Fluids, 3, 617, 1960.

- [87] Wilber, M. et al.: *Cluster observations of velocity space-restricted ion distributions near the plasma sheet*, Geophys. Res. Lett., 31, L24802, 2004.
- [88] Woch, J. and Lundin, R.: *Signatures of transient boundary layer processes observed with Viking*, Journal of Geophysical Research, 97, 1431, 1992.
- [89] Yamauchi, M., Woch, J., Lundin, R., Shapshak, M., and Elphinstone, R.: *A new type of ion injection event observed by Viking*, Geophysical Research Letters, 20, 795, 1993.
- [90] Yee, K. S.: *Numerical solution of initial boundary value problems involving Maxwell's equations in isotropic media*, IEEE Transactions on Antennas and Propagation, vol. AP-14, no. 3, pp. 302-307, 1966.
- [91] Zelenyi, L. M., R. A. Kovrazkhin, and J. M. Bosqued, J. Geophys. Res. 95, 12119, 1990.

Appendix A

TRISTAN code

In TRISTAN code (Buneman, 1993) the self-consistent electric and magnetic fields are computed from Ampère and Faraday's laws. In normalized units (see Appendix B for details) the two Maxwell's equations take the following form:

$$\begin{aligned}\frac{\partial \vec{e}}{\partial t} &= c \nabla \times \vec{b} - \vec{J} \\ \frac{\partial \vec{b}}{\partial t} &= -c \nabla \times \vec{e}\end{aligned}\tag{A.1}$$

where \vec{e} is the electric field intensity and \vec{b} is a notation for $c\vec{B}$, with \vec{B} the magnetic field induction and c the speed of light in vacuum; \vec{J} is the current density. The two equations (A.1) take the following form when written for each component of the fields:

$$\begin{aligned}\frac{\partial e_x}{\partial t} &= c \left(\frac{\partial b_z}{\partial y} - \frac{\partial b_y}{\partial z} \right) - J_x \\ \frac{\partial e_y}{\partial t} &= c \left(\frac{\partial b_x}{\partial z} - \frac{\partial b_z}{\partial x} \right) - J_y \\ \frac{\partial e_z}{\partial t} &= c \left(\frac{\partial b_y}{\partial x} - \frac{\partial b_x}{\partial y} \right) - J_z \\ \frac{\partial b_x}{\partial t} &= -c \left(\frac{\partial e_z}{\partial y} - \frac{\partial e_y}{\partial z} \right) \\ \frac{\partial b_y}{\partial t} &= -c \left(\frac{\partial e_x}{\partial z} - \frac{\partial e_z}{\partial x} \right) \\ \frac{\partial b_z}{\partial t} &= -c \left(\frac{\partial e_y}{\partial x} - \frac{\partial e_x}{\partial y} \right)\end{aligned}\tag{A.2}$$

where e_x, e_y, e_z are the components of the electric field and b_x, b_y, b_z are the components of the magnetic field. The three components of the total current density are denoted by J_x, J_y, J_z . Note that throughout the TRISTAN code all units are normalized.

Equations (A.2) are solved numerically using the finite-differences method with a centered-difference scheme on a three-dimensional staggered-grid system known as the Yee lattice (Yee, 1966). The space and time discretization of equations (A.2) is given in (A.3) where i, j, k indexes the number of grid points inside the simulation domain along the Ox, Oy and Oz axes. In TRISTAN the grid sizes along all the three coordinate axes are

equal, i.e. $\Delta x = \Delta y = \Delta z = 1$. Also, the time-step $\Delta t = 1$. More details about the normalization scheme used are given in Appendix B.

$$\begin{aligned}
 & e_x^{n+1}(i+1/2, j, k) - e_x^n(i+1/2, j, k) \\
 & = c \left[b_z^{n+1/2}(i+1/2, j+1/2, k) - b_z^{n+1/2}(i+1/2, j-1/2, k) \right. \\
 & \quad \left. - b_y^{n+1/2}(i+1/2, j, k+1/2) + b_y^{n+1/2}(i+1/2, j, k-1/2) \right] - J_x^{n+1/2}(i+1/2, j, k) \\
 & e_y^{n+1}(i, j+1/2, k) - e_y^n(i, j+1/2, k) \\
 & = c \left[b_x^{n+1/2}(i, j+1/2, k+1/2) - b_x^{n+1/2}(i, j+1/2, k-1/2) - \right. \\
 & \quad \left. - b_z^{n+1/2}(i+1/2, j+1/2, k) + b_z^{n+1/2}(i-1/2, j+1/2, k) \right] - J_y^{n+1/2}(i, j+1/2, k) \\
 & e_z^{n+1}(i, j, k+1/2) - e_z^n(i, j, k+1/2) \\
 & = c \left[b_y^{n+1/2}(i+1/2, j, k+1/2) - b_y^{n+1/2}(i-1/2, j, k+1/2) \right. \\
 & \quad \left. - b_x^{n+1/2}(i, j+1/2, k+1/2) + b_x^{n+1/2}(i, j-1/2, k+1/2) \right] - J_z^{n+1/2}(i, j, k+1/2)
 \end{aligned} \tag{A.3}$$

$$\begin{aligned}
 & b_x^{n+1/2}(i, j+1/2, k+1/2) - b_x^{n-1/2}(i, j+1/2, k+1/2) \\
 & = -c \left[e_z^n(i, j+1, k+1/2) - e_z^n(i, j, k+1/2) \right. \\
 & \quad \left. - e_y^n(i, j+1/2, k+1) + e_y^n(i, j+1/2, k) \right]
 \end{aligned}$$

$$\begin{aligned}
 & b_y^{n+1/2}(i+1/2, j, k+1/2) - b_y^{n-1/2}(i+1/2, j, k+1/2) \\
 & = -c \left[e_x^n(i+1/2, j, k+1) - e_x^n(i+1/2, j, k) \right. \\
 & \quad \left. - e_z^n(i+1, j, k+1/2) + e_z^n(i, j, k+1/2) \right]
 \end{aligned}$$

$$\begin{aligned}
 & b_z^{n+1/2}(i+1/2, j+1/2, k) - b_z^{n-1/2}(i+1/2, j+1/2, k) \\
 & = -c \left[e_y^n(i+1, j+1/2, k) - e_y^n(i, j+1/2, k) - \right. \\
 & \quad \left. - e_x^n(i+1/2, j+1, k) + e_x^n(i+1/2, j, k) \right]
 \end{aligned}$$

The electric charge of a finite-size superparticle is distributed among its eight neighboring grid points by using the volume weighting method, which is a first order interpolation scheme in all the three spatial coordinates:

$$q(i, j, k) = w(i, j, k) \cdot q_p \tag{A.4}$$

where $q(i, j, k)$ is the electric charge assigned to the grid point (i, j, k) , while $w(i, j, k)$ is its corresponding weight; q_p is the total charge of the superparticle. The weights w for all the eight neighboring grid points around a superparticle localized in (x_p, y_p, z_p) with:

$$i \leq x_p \leq i+1, \quad j \leq y_p \leq j+1, \quad k \leq z_p \leq k+1 \quad (\text{A.5})$$

are given in equation (A.6) where $\delta x = x_p - i$, $\delta y = y_p - j$, $\delta z = z_p - k$:

$$\begin{aligned} w(i, j, k) &= (1 - \delta x)(1 - \delta y)(1 - \delta z) \\ w(i, j, k+1) &= (1 - \delta x)(1 - \delta y)\delta z \\ w(i, j+1, k) &= (1 - \delta x)\delta y(1 - \delta z) \\ w(i, j+1, k+1) &= (1 - \delta x)\delta y\delta z \\ w(i+1, j, k) &= \delta x(1 - \delta y)(1 - \delta z) \\ w(i+1, j, k+1) &= \delta x(1 - \delta y)\delta z \\ w(i+1, j+1, k) &= \delta x\delta y(1 - \delta z) \\ w(i+1, j+1, k+1) &= \delta x\delta y\delta z \end{aligned} \quad (\text{A.6})$$

In order to compute the electric and magnetic fields in the actual positions of the particles, the volume weighting method (A.6) is applied again together with the same grid points that were used to distribute the charges over the grid:

$$\begin{aligned} \vec{e}(x_p, y_p, z_p) &= w(i, j, k) \cdot \vec{e}(i, j, k) + w(i, j, k+1) \cdot \vec{e}(i, j, k+1) \\ &+ w(i, j+1, k) \cdot \vec{e}(i, j+1, k) + w(i, j+1, k+1) \cdot \vec{e}(i, j+1, k+1) \\ &+ w(i+1, j, k) \cdot \vec{e}(i+1, j, k) + w(i+1, j, k+1) \cdot \vec{e}(i+1, j, k+1) \\ &+ w(i+1, j+1, k) \cdot \vec{e}(i+1, j+1, k) + w(i+1, j+1, k+1) \cdot \vec{e}(i+1, j+1, k+1) \end{aligned} \quad (\text{A.7})$$

Equation (A.7) is applied for all components of the electric and magnetic fields. As can be noticed, we need to know the fields in full-integer grid points and not in their actual positions computed from equation (A.3). Therefore, relocations are required:

$$\begin{aligned} e_x(i, j, k) &= \frac{1}{2} [e_x(i-1/2, j, k) + e_x(i+1/2, j, k)] \\ e_y(i, j, k) &= \frac{1}{2} [e_y(i, j-1/2, k) + e_y(i, j+1/2, k)] \\ e_z(i, j, k) &= \frac{1}{2} [e_z(i, j, k-1/2) + e_z(i, j, k+1/2)] \\ b_x(i, j, k) &= \frac{1}{4} [b_x(i, j-1/2, k-1/2) + b_x(i, j-1/2, k+1/2) \\ &\quad + b_x(i, j+1/2, k-1/2) + b_x(i, j+1/2, k+1/2)] \\ b_y(i, j, k) &= \frac{1}{4} [b_y(i-1/2, j, k-1/2) + b_y(i-1/2, j, k+1/2) \\ &\quad + b_y(i+1/2, j, k-1/2) + b_y(i+1/2, j, k+1/2)] \\ b_z(i, j, k) &= \frac{1}{4} [b_z(i-1/2, j-1/2, k) + b_z(i-1/2, j+1/2, k) \\ &\quad + b_z(i+1/2, j-1/2, k) + b_z(i+1/2, j+1/2, k)] \end{aligned} \quad (\text{A.8})$$

The total current density is obtained by using the current deposition of particles method (Villasenor and Buneman, 1992). All three components of the current density, for both electrons and ions, are calculated by effectively taking into account the amount of charge crossing the faces of the grid cells used to integrate the Maxwell's equations by finite-differences. The method used ensures the conservation of the electric charge at each time-step during the simulation. Each simulated particle will contribute to the total current density according to the following weights:

$$\begin{aligned}
 w_x(i+1/2, j, k) &= \Delta\xi(1-\bar{\eta})(1-\bar{\zeta}) + \Delta\xi\Delta\eta\Delta\zeta / 12 \\
 w_x(i+1/2, j, k+1) &= \Delta\xi(1-\bar{\eta})\bar{\zeta} - \Delta\xi\Delta\eta\Delta\zeta / 12 \\
 w_x(i+1/2, j+1, k) &= \Delta\xi\bar{\eta}(1-\bar{\zeta}) - \Delta\xi\Delta\eta\Delta\zeta / 12 \\
 w_x(i+1/2, j+1, k+1) &= \Delta\xi\bar{\eta}\bar{\zeta} + \Delta\xi\Delta\eta\Delta\zeta / 12 \\
 \\
 w_y(i, j+1/2, k) &= (1-\bar{\xi})\Delta\eta(1-\bar{\zeta}) + \Delta\xi\Delta\eta\Delta\zeta / 12 \\
 w_y(i, j+1/2, k+1) &= (1-\bar{\xi})\Delta\eta\bar{\zeta} - \Delta\xi\Delta\eta\Delta\zeta / 12 \\
 w_y(i+1, j+1/2, k) &= \bar{\xi}\Delta\eta(1-\bar{\zeta}) - \Delta\xi\Delta\eta\Delta\zeta / 12 \\
 w_y(i+1, j+1/2, k+1) &= \bar{\xi}\Delta\eta\bar{\zeta} + \Delta\xi\Delta\eta\Delta\zeta / 12 \\
 \\
 w_z(i, j, k+1/2) &= (1-\bar{\xi})(1-\bar{\eta})\Delta\zeta + \Delta\xi\Delta\eta\Delta\zeta / 12 \\
 w_z(i, j+1, k+1/2) &= (1-\bar{\xi})\bar{\eta}\Delta\zeta - \Delta\xi\Delta\eta\Delta\zeta / 12 \\
 w_z(i+1, j, k+1/2) &= \bar{\xi}(1-\bar{\eta})\Delta\zeta - \Delta\xi\Delta\eta\Delta\zeta / 12 \\
 w_z(i+1, j+1, k+1/2) &= \bar{\xi}\bar{\eta}\Delta\zeta + \Delta\xi\Delta\eta\Delta\zeta / 12
 \end{aligned} \tag{A.9}$$

where $\Delta\bar{\xi}=x_{p2}-x_{p1}$, $\Delta\bar{\eta}=y_{p2}-y_{p1}$, $\Delta\bar{\zeta}=z_{p2}-z_{p1}$ are the displacements of a particle along the Ox , Oy and Oz axes when is moving over a time-step from x_{p1} to x_{p2} , y_{p1} to y_{p2} and z_{p1} to z_{p2} . The three variables $\bar{\xi}$, $\bar{\eta}$, $\bar{\zeta}$ represent the average positions of the particle along Ox , Oy and Oz with respect to the nearest grid point (i, j, k) :

$$\begin{aligned}
 \bar{\xi} &= (x_{p1} + x_{p2}) / 2 - i \\
 \bar{\eta} &= (y_{p1} + y_{p2}) / 2 - j \\
 \bar{\zeta} &= (z_{p1} + z_{p2}) / 2 - k
 \end{aligned} \tag{A.10}$$

In obtaining equation (A.9) it was considered that x_{p1} and x_{p2} , y_{p1} and y_{p2} , z_{p1} and z_{p2} satisfy (A.5) conditions. Otherwise, if those restrictions are not fulfilled, the current will flow to more than 12 faces and the computation procedure gets more complicated. Nevertheless, the weights (A.9) can still be used if the motion of the particle is split in parts that all satisfy (A.5). Therefore, the effective contribution of each particle to the J_x , J_y , J_z components of the total current density is given by:

$$J_x = w_x q_p, \quad J_y = w_y q_p, \quad J_z = w_z q_p \tag{A.11}$$

where the weights w_x , w_y , w_z are taken from equation (A.9). A complete description of the current deposition of particles method is given by *Villasenor and Buneman (1992)*.

In TRSITAN code (*Buneman, 1993*) a smoothing procedure is taken into account in order to reduce the amplitude of the statistical noise generated by the small number of simulated particles compared to real plasmas and also to limit the possible unwanted effects of the aliasing that could arise due to the discretization of configuration space. The smoothing procedure is applied to all the current density components computed from equation (A.11) (*Birdsall and Langdon, 1991*):

$$\vec{J}_s(i, j, k) = \frac{M \cdot \vec{J}(i, j, k) + S \cdot S_{\text{terms}} + K \cdot K_{\text{terms}} + C \cdot C_{\text{terms}}}{M + 6S + 12K + 8C} \quad (\text{A.12})$$

where $M=8$, $S=4$, $K=2$, $C=1$ and:

$$S_{\text{terms}} = \vec{J}(i-1, j, k) + \vec{J}(i+1, j, k) + \vec{J}(i, j-1, k) + \vec{J}(i, j+1, k) + \vec{J}(i, j, k-1) + \vec{J}(i, j, k+1) \quad (\text{A.13})$$

$$K_{\text{terms}} = \vec{J}(i-1, j-1, k) + \vec{J}(i+1, j-1, k) + \vec{J}(i-1, j+1, k) + \vec{J}(i+1, j+1, k) + \vec{J}(i, j-1, k+1) + \vec{J}(i, j+1, k+1) + \vec{J}(i-1, j, k+1) + \vec{J}(i+1, j, k+1) + \vec{J}(i, j-1, k-1) + \vec{J}(i, j+1, k-1) + \vec{J}(i-1, j, k-1) + \vec{J}(i+1, j, k-1) \quad (\text{A.14})$$

$$C_{\text{terms}} = \vec{J}(i-1, j-1, k-1) + \vec{J}(i-1, j+1, k-1) + \vec{J}(i+1, j-1, k-1) + \vec{J}(i+1, j+1, k-1) + \vec{J}(i-1, j-1, k+1) + \vec{J}(i-1, j+1, k+1) + \vec{J}(i+1, j-1, k+1) + \vec{J}(i+1, j+1, k+1) \quad (\text{A.15})$$

Further, only the smoothed currents given by (A.12) are introduced in (A.3). It should be mentioned that the same smoothing procedure is also applied to compute the charge density and the number density when diagnostics are performed. A full description of the TRISTAN code is given in *Buneman (1991)* and *Cai et al. (2003)*.

When simulating the dynamics of a localized plasma cloud the most desirable boundary conditions would be the ones with the boundaries located at infinity, which of course is not possible. Therefore, over time, different sets of boundary conditions have been considered in the plasma-field interaction studies. For example, *Galvez and Borovsky (1991)* introduced a combination of periodic and conducting boundaries in their two-dimensional electrostatic PIC code. On the other hand, *Neubert et al. (1992)* considered periodic boundaries for particles and radiating ones for fields in their three-dimensional full-electromagnetic particle-in-cell code. In our simulations the boundary conditions are assumed to be periodic for both particles and fields. To reduce the possible influence of the boundaries on the plasma dynamics we keep the edges of the simulation domain as far as possible from the plasma cloud. Also, the simulations are stopped when the particles reach the boundaries of the domain.

In TRISTAN code (Buneman, 1993) the simulation domain is defined between $3 \leq x \leq mx-2$ along the x-axis, $3 \leq y \leq my-2$ along the y-axis and $3 \leq z \leq mz-2$ along the z-axis, where mx , my , mz are the number of grid cells along the Ox , Oy and Oz axes. Thus, two guard cells are kept at each boundary of the simulation domain along all three coordinate axes. Since we assumed periodic boundaries, the particles that leave the simulation domain will be relocated inside the domain as follows:

$$\begin{aligned}
 &\text{if } x_p < 3 \text{ then } x_p := x_p + L_x \\
 &\text{if } x_p > mx - 2 \text{ then } x_p := x_p - L_x \\
 &\text{if } y_p < 3 \text{ then } y_p := y_p + L_y \\
 &\text{if } y_p > my - 2 \text{ then } y_p := y_p - L_y \\
 &\text{if } z_p < 3 \text{ then } z_p := z_p + L_z \\
 &\text{if } z_p > mz - 2 \text{ then } z_p := z_p - L_z
 \end{aligned} \tag{A.16}$$

where (x_p, y_p, z_p) is the position of a particle at a given time, while $L_x = mx - 5$, $L_y = my - 5$, $L_z = mz - 5$ represent the length of the simulation domain along Ox , Oy , Oz . On the other hand, all the grid quantities will be updated at the boundaries of the simulation domain such that the following equalities to be satisfied at any given time during the simulation:

$$\begin{aligned}
 G(3, j, k) &= G(mx - 2, j, k) \\
 G(i, 3, k) &= G(i, my - 2, k) \\
 G(i, j, 3) &= G(i, j, mz - 2)
 \end{aligned} \tag{A.17}$$

where the grid quantity G can be the electric field, the magnetic field or the current density; i, j, k indexes the number of grid points inside the simulation domain along the Ox , Oy and Oz axes. The boundary conditions (A.16) and (A.17) are applied at each time-step during the simulation.

Appendix B

Normalization in TRISTAN code

TRISTAN code (*Buneman, 1993*) uses a particular normalization scheme that will be described further. Let Q be a physical quantity expressed in SI units and Q_N its corresponding normalization factor. The quantity Q is expressed in normalized units as:

$$Q^* = \frac{Q}{Q_N} \quad (\text{B.1})$$

where Q^* is a dimensionless quantity and Q_N has the same units as Q .

The normalization scheme used in the TRISTAN code (*Buneman, 1993*) takes into account the following four basic normalization factors for space x_N , time t_N , charge-to-mass ratio $(q/m)_N$ and electric permittivity ε_N :

$$x_N = \Delta x, \quad t_N = \Delta t, \quad (q/m)_N = e/m_e, \quad \varepsilon_N = \varepsilon_0 \quad (\text{B.2})$$

where Δx is the grid spacing, Δt is the time-step, e is the elementary charge, m_e is the electron mass and ε_0 is the electric permittivity of vacuum. Using the normalization factors given by equation (B.2), the following normalized quantities are obtained:

$$\Delta x^* = 1, \quad \Delta t^* = 1, \quad (e/m_e)^* = 1, \quad \varepsilon_0^* = 1 \quad (\text{B.3})$$

Based on the normalization scheme expressed by equations (B.1) and (B.2) we can provide the normalization factors for all the physical quantities of interest in our simulations. In Table B.1 we list the normalization factors for velocity, number density, charge density, current density, magnetic induction and electric field intensity.

Table B.1 – Normalization factors for different physical quantities of interest in our simulations.

| Physical quantity | Normalization factor |
|--------------------------|---|
| Velocity | $v_N = \frac{x_N}{t_N} = \frac{\Delta x}{\Delta t}$ |
| Number density | $n_N = \frac{1}{x_N^3} = \frac{1}{(\Delta x)^3}$ |
| Charge density | $\rho_N = q_N n_N = \frac{\varepsilon_0 m_e}{e(\Delta t)^2}$ |
| Current density | $J_N = \rho_N v_N = \frac{\varepsilon_0 m_e \Delta x}{e(\Delta t)^3}$ |
| Magnetic induction | $B_N = \frac{\omega_N}{(q/m)_N} = \frac{m_e}{e\Delta t}$ |
| Electric field intensity | $E_N = v_N B_N = \frac{m_e \Delta x}{e(\Delta t)^2}$ |

List of tables

Table 1.1 – Input parameters of the test-kinetic simulations: N_0 , $k_B T_0$, V_0 are the density, thermal energy and average velocity of the drifting Maxwellian (1.12); B_{1z} , B_{2z} are the asymptotic values of the magnetic field; L is the length scale of the TD; R_L is the Larmor radius of the thermal protons; T_L is the proton cyclotron period; $N_x \times N_y$ is the number of injection sources; n_p is the number of test-particles injected from each source; x_0 , y_0 are the coordinates of the first source; dx_0 , dy_0 are the separation distances between sources along Ox and Oy . _____ 16

Table 1.2 – Values of f obtained with both forward and backward approaches for three selected velocity bins centered at a , b and c . _____ 31

Table 2.1 – Plasma and field parameters for the three cases considered in the second chapter: N = number density, T = temperature, V_z = bulk velocity, B_y = magnetic induction and E_x = electric field intensity at $t=0$ for case A (see Figure 2.2), case B (see Figure 2.3) and case C (see Figure 2.4); indices “1” and “2” denote the values corresponding to the two plasma regions illustrated in the aforementioned figures. _____ 43

Table 2.2 – Simulation parameters for cases A, B and C: n_x = number of grid points, nt = number of time-steps, L = length of the simulation domain, r_L = Larmor radius, T = total simulation time, T_L = Larmor period, λ_D = Debye length, Δx = grid spacing, Δt = time-step, c = speed of light in vacuum; “e” and “i” indices designates the electrons and ions corresponding quantities. In case A the gyration radius and the cyclotron period are computed for the left population (see Figure 2.2). _____ 44

Table 2.3 – Input parameters for the test-simulations with a variable number of particles: N = number density, T = temperature, V_z = bulk velocity, B_y = magnetic induction, E_x = electric field intensity, n_x = number of grid points, nt = number of time-steps, Δx = grid spacing, Δt = time-step and ion-to-electron mass ratio m_i/m_e ; λ_D is the Debye length and c is speed of light in vacuum; “e” and “i” indices designates the electrons and ions corresponding quantities. _____ 44

Table 3.1 – Input parameters for all the simulations discussed in Chapter 3: m_i/m_e is the ion-to-electron mass ratio; T_e/T_i is the electron-to-ion temperature ratio; β_e is the plasma-beta parameter for electrons; ϵ is the dielectric constant of the plasma element; w_x , w_y , w_z are the widths of the plasma element along Ox , Oy , Oz axes; r_{Li} is the ion Larmor radius; Δx is the grid spacing; λ_D is the electron Debye length; Δt is the time-step; c is the speed of light in vacuum; N_c is the number of particles per grid-cell at $t=0$. _____ 60

Table 3.2 – Input parameters for the five cases and the three sub-cases shown in Chapter 3: V_0 is the initial plasma bulk velocity; V_{Ti} is the ion thermal speed; B_1 and B_2 are the asymptotic magnetic fields defined in equation (3.9); x_1 and x_2 define the non-uniform magnetic field region given by equation (3.9); r_{Li} is the ion Larmor radius; x_0 , y_0 , z_0 gives the starting position of the plasma element along the Ox , Oy , Oz axes; m_x , m_y , m_z are the number of grid points along the Ox , Oy , Oz axes; T is the total simulation time; T_{Li} is the ion Larmor period. _____ 60

List of figures

- Figure 1.1** – Schematic diagram of the forward Liouville approach; a positive time-step is used to integrate test-particle orbits in given electric and magnetic fields. _____ 9
- Figure 1.2** – Schematic diagram of the backward Liouville approach; a negative time-step is used to integrate test-particle orbits in given electric and magnetic fields. _____ 10
- Figure 1.3** – Schematic diagram of the source region defined in terms of guiding centers positions. The blue circles illustrate different orbits of the particles (green dots) that gyrate around their guiding centers (red dots). _____ 11
- Figure 1.4** – Schematic diagram of the simulation geometry. The source region (red rectangle) where the initial velocity distribution function is known is localized in the xOy plane perpendicular to the magnetic field, at the left hand side of the transition region. _____ 13
- Figure 1.5** – Example of ring-shaped and non-gyrotropic (crescent-like) ion VDFs observed by Cluster (C1) CIS instruments (Reme et al., 1997) at 09:25:40 UT (left panel), 09:36:32 UT (middle panel) and 09:46:11 UT (right panel) on 1st of October 2001. All panels illustrate sections in the velocity plane perpendicular to the local magnetic field; the units are km/s on both axes (from Lee et al., 2004). _____ 14
- Figure 1.6** – Left panel: magnetic field profile in the simulation domain; the B-field is unidirectional and changes orientation at $x=0$. Right panel: electric field profile in the simulation domain; E_y changes sign whenever B_z reverses sign. The simulation domain is limited by: $-40000 \text{ km} \leq x \leq +40000 \text{ km}$, $-30000 \text{ km} \leq y \leq +30000 \text{ km}$. _____ 15
- Figure 1.7** – Distribution of protons in the xOy plane after 120 seconds ($\sim 55T_L$) from injection in the electromagnetic field illustrated in Figure 1.6. The local value of the number density is color coded. The cloud moved in a region of virtually uniform electric and magnetic fields. The spatial mesh on which the VDF is reconstructed is also shown; each bin is identified by a combination of letters and numbers as shown on the left side and bottom side of the figure. _____ 18
- Figure 1.8** – Projection in the space of perpendicular velocities, for $v_z=0$, of the Liouville mapped velocity distribution functions of protons in the cloud at $t=120$ seconds. The spatial bins are defined in Figure 1.7. One notes the drifting Maxwellian VDF obtained in the central core of the cloud and non-gyrotropic VDFs at the edges of the cloud; the latter result from the large Larmor radius particles with gyro-centers inside the cloud. Note the different regions of the velocity space populated in bins C1–I1 compared to C5–I5. 18
- Figure 1.9** – Distribution of protons in the xOy plane after 225 seconds ($\sim 100T_L$) from injection in the electromagnetic field illustrated in Figure 1.6. The local value of the number density is color coded. The cloud has spent some time in the region of non-uniform fields and its shape is elongated into the +y-direction under the action of the gradient-B drift. The spatial mesh on which the VDF is reconstructed is also shown. _____ 19
- Figure 1.10** – Projection in the space of perpendicular velocities, for $v_z=0$, of the Liouville mapped velocity distribution functions of protons in the cloud at $t=225$ seconds. The spatial bins are defined in Figure 1.9. A drifting Maxwellian VDF is obtained in the core of the cloud, in bins D1–F1, D2–F2. Ring-shaped VDFs are obtained close to the edges of the cloud, bins D4–F4, E5–F5. Crescent-like VDF are obtained close to the trailing and leading edges, A2–A4, B4–B5, C4–C5, G4–G5, H4–H5, I4–I5. _____ 19

Figure 1.11 – Distribution of protons in the xOy plane after 275 seconds ($\sim 125T_L$) from injection in the electromagnetic field illustrated in Figure 1.6. This snapshot illustrates the initial stage of the interaction between the proton cloud and the region of the most rapid variation of B; some parts of the cloud intersected the plane $x=0$ where $B=0$. The local value of the number density is color coded. The spatial mesh on which the VDF is reconstructed is also shown. _____ 20

Figure 1.12 – Projection in the space of perpendicular velocities, for $v_z=0$, of the Liouville mapped velocity distribution functions of protons in the cloud at $\Delta t=275$ seconds. The spatial bins are defined in Figure 1.11. During this initial stage of the interaction of the cloud with the discontinuity one identifies the Maxwellian core of the cloud (bins B1–B2) and non-gyrotropic VDFs at the leading edge (e.g. bins D5–I5). _____ 20

Figure 1.13 – Distribution of protons in the xOy plane after 300 seconds ($\sim 135T_L$) from injection in the electromagnetic field illustrated in Figure 1.6. The local value of the number density is color coded. The spatial mesh on which the VDF is reconstructed is also shown. The figure illustrates a later stage of the interaction between the cloud and the central region of the discontinuity where the magnetic field vanishes. A significant number of protons moved in the region of positive B_z . _____ 21

Figure 1.14 – Projection in the space of perpendicular velocities, for $v_z=0$, of the Liouville mapped velocity distribution functions of protons at $\Delta t=300$ seconds. The spatial bins are defined in Figure 1.13. We note that in the region of positive B_z the VDFs of protons are ring-shaped (bins G4–I4, H5–I5) or crescent-like (bins G3–I3, E5–G5). _____ 21

Figure 1.15 – Distribution of protons in the xOy plane after 350 seconds ($\sim 160T_L$) from injection in the electromagnetic field illustrated in Figure 1.6. The local value of the number density is color coded. The spatial mesh on which the VDF is reconstructed is also shown. One notes the splitting of the cloud into two populations: population P1 that does not cross the surface where $B=0$ and remains trapped in some region on the left side of the discontinuity ($x<0$) and respectively population P2 that penetrates into the right side of the magnetic discontinuity. At later stages the two populations disconnect. In the reminder of the paper we follow only P2. _____ 22

Figure 1.16 – Projection in the space of perpendicular velocities, for $v_z=0$, of the Liouville mapped velocity distribution functions of protons in the cloud at $\Delta t=350$ seconds. The spatial bins are defined in Figure 1.15. Only VDFs of the P2 population are shown. Ring-shaped and crescent-like VDFs are observed in the large majority of spatial bins. _____ 22

Figure 1.17 – Distribution of protons of the population P2 in the xOy plane after 600 seconds ($\sim 270T_L$) from injection in the electromagnetic field illustrated in Figure 1.6. The local value of the number density is color coded. The spatial mesh on which the VDF is reconstructed is also shown. The protons move in a region of uniform magnetic and electric field, on the right side of the discontinuity. _____ 23

Figure 1.18 – Projection in the space of perpendicular velocities, for $v_z=0$, of the Liouville mapped velocity distribution functions of protons in the cloud at $\Delta t=600$ seconds. The spatial bins are defined in Figure 1.17. All the VDFs obtained for this stage of propagation are either ring-shaped or crescent-like, a signature of the interaction of the cloud with the region of magnetic field gradient. _____ 23

Figure 1.19 – Distribution of protons in the xOy plane after 360 seconds ($\sim 160T_L$) from injection on the left side in the case of a unidirectional, non-uniform, parallel magnetic field and a uniform electric field. The local value of the number density is color coded. The spatial mesh on which the VDF is reconstructed is also shown. The deformation of the shape of the cloud is due to the gradient-B drift. _____ 26

Figure 1.20 – Projection in the space of perpendicular velocities, for $v_z=0$, of the Liouville mapped velocity distribution functions of protons in the cloud at $\Delta t=600$ seconds for a parallel magnetic field and a uniform electric field. Spatial bins are defined in Figure 1.19. Note the formation of the central cavity due to the gradient-B drift in bins of the upper three rows; non-gyrotropic VDFs are obtained in bins from the column A, B, C, G, H and I. _____ 26

- Figure 1.21** – Proton density distribution in the xOy plane, perpendicular to the magnetic field, at $t=225s$ ($\sim 100T_L$) obtained with the forward approach. The local number density is color coded using a 2D mesh of 60×60 cells. The blue rectangles indicate the spatial bins used to compute the VDF shown in Figure 1.22. 27
- Figure 1.22** – Velocity distribution functions obtained at $t=225s$ ($\sim 100T_L$) using the forward approach in the spatial bins indicated by blue rectangles in Figure 1.21. The plots correspond to $v_z=0$ cross-sections. 27
- Figure 1.23** – VDFs obtained at $t=225s$ ($\sim 100T_L$) using the backward approach for the central points of the bins indicated by blue rectangles in Figure 1.21. $C1^*$ is the middle point between $C1$ and $C2$. 28
- Figure 1.24** – Velocity distribution functions obtained at $t=225s$ ($\sim 100T_L$) with the backward approach by averaging over the spatial bins indicated with blue rectangles in Figure 1.21. 29
- Figure 1.25** – Schematic diagram illustrating the sampling method used to compute the velocity distribution function with the forward Liouville approach. 32
- Figure 1.26** – Schematic diagram illustrating the averaging method used to compute the velocity distribution function with the backward Liouville approach. 32
- Figure 2.1** – A typical cycle in a one-dimensional particle-in-cell simulation code. The quantities computed in the position of each particle are indexed with p , while the grid quantities are indexed with i (adapted from Birdsall and Langdon, 1991). 41
- Figure 2.2** – Schematic diagram of the simulation geometry for case A: tangential discontinuity without velocity shear. In this case there is no asymptotic variation of the plasma bulk velocity across the discontinuity and the two plasma populations have different asymptotic densities and temperatures. 42
- Figure 2.3** – Schematic diagram of the simulation geometry for case B: tangential discontinuity with velocity shear. In this case the plasma bulk velocity varies in the perpendicular direction to the magnetic field, but the two populations have equal asymptotic densities and temperatures. 42
- Figure 2.4** – Schematic diagram of the simulation geometry for case C: plasma slab. In this case the central plasma population is streaming across a transverse magnetic field and a background stagnant plasma with equal densities and temperatures. 42
- Figure 2.5** – Space and time evolution of the E_x component of the electric field when 4096 particles per grid cell are loaded into the simulation domain. The simulation time covers 8 electron plasma periods. 46
- Figure 2.6** – Net charge density (left column) and electric field intensity (right column) obtained with 4096 particles per cell (top panels), 65536 particles per cell (middle panels) and 262144 particles per cell (bottom panels). The blue lines show the results obtained at the end of the simulations, while the red ones illustrate the time-averaged profiles. The total simulation time covers ~ 8 electron plasma periods. 46
- Figure 2.7** – Net charge density (left column) and electric field intensity (right column) obtained with 512 particles per cell for a total simulation time that covers ~ 1000 electron plasma periods or, equivalently, ~ 4 ion Larmor periods. The blue lines show the results obtained at the end of the simulations, while the red ones illustrate the time-averaged profiles. 47
- Figure 2.8** – Histograms of the net charge density (left panel) and electric field intensity (right panel) deviations from their time-averaged values, computed for the central region of the simulation domain ($x=202$ km). The red line illustrates the fitting curve of the histogram using a normal distribution. 47
- Figure 2.9** – Simulation results for a tangential discontinuity without velocity shear (case A). On the left column we show the time history for the electric field (first line), the magnetic field (second line), the electron number density (third line) and the net electrical charge (fourth line). The second column shows the time-averaged profiles, while on the last column we have the results of a theoretical kinetic model for a tangential discontinuity (Roth et al., 1996). 49

- Figure 2.10** – Histogram of the electric field deviation from average, $E_x(t) - \langle E_x(t) \rangle$, computed for the central region of the simulation domain ($x \approx 200$ km). The red line illustrates the fitting curve of the histogram using a normal distribution with mean $\mu \approx 0$ and standard deviation $\sigma \approx 600$ mV/m. _____ 49
- Figure 2.11** – Simulation results for a tangential discontinuity with velocity shear (case B). On the left column we show the time history for the electric field (first line), the magnetic field (second line), the electron number density (third line) and the net electrical charge (fourth line). The second column shows the time-averaged profiles, while on the last column we have the results of a theoretical kinetic model for a tangential discontinuity (Roth et al., 1996). _____ 50
- Figure 2.12** – The simulated profile of the ions bulk velocity for case B. The transition layer between the left asymptotic region ($V_z = 0$) and the right asymptotic region ($V_z = -1000$ km/s) has a width of approximately 3.5 ion Larmor radii. _____ 51
- Figure 2.13** – Simulation results for a plasma slab streaming across a transverse magnetic field (case C). On the left column we show the time history for the electric field (first line), the magnetic field (second line), the electron number density (third line) and the net electrical charge (fourth line), while on the right column we show the time-averaged profiles. _____ 52
- Figure 2.14** – The simulated profile of the ions bulk velocity for case C. Two asymmetric boundary layers are formed at the edges of the plasma slab. The left boundary layer has a width of approximately 7.6 ion Larmor radii, while the right boundary layer has a width of approximately 10.2 ion Larmor radii. _____ 53
- Figure 3.1** – Yee lattice (Yee, 1966) used to solve the Maxwell's equations using finite-differences method with a centered-difference scheme. The electric field is computed at the locations shown by blue dots, while the magnetic field is computed at the locations shown by red dots (adapted from Yee, 1966). ____ 56
- Figure 3.2** – Schematic diagram of a three-dimensional particle-in-cell simulation cycle. Each of the 8 steps illustrated above are performed iteratively until the end of the simulation. The time-step Δt must fulfill the Courant condition of numerical stability (adapted from Cai et al., 2003). _____ 58
- Figure 3.3** – Schematic diagram of the simulation setup. The three-dimensional plasma element/cloud (red rectangular box) is injected with a non-zero bulk velocity (blue arrow), in vacuum, across a transverse magnetic field (black arrow). _____ 59
- Figure 3.4** – Initial number density of electrons in the xOy (left panel) and xOz (right panel) sections of the simulation domain. The uniform background magnetic field is parallel to the z-axis. The ions and electrons are initialized with the same number density. At $t=0$ the three-dimensional plasma element has a rectangular shape and a uniform density. _____ 61
- Figure 3.5** – Initial velocity distribution function of electrons (left panel) and ions (right panel) in the $v_z=0$ section perpendicular to the background magnetic field. The VDFs are computed in the central region of the plasma element for $46 \leq x \leq 51$, $68.5 \leq y \leq 88.5$ and $3 \leq z \leq 303$. Note that the initial velocity distribution function of both electrons and ions is an isotropic Maxwellian with zero average velocity. _____ 61
- Figure 3.6** – Number densities of electrons n_e (top panels) and ions n_i (middle panels) and the electric charge separation computed as $n_i - n_e$ (bottom panels) at $t = T_{Le}/2$ (left column) and $t = 3T_{Le}$ (right column), where T_{Le} is the electron Larmor period; xOy central sections perpendicular to the background magnetic field are shown. _____ 63
- Figure 3.7** – Number densities of electrons n_e (top panels) and ions n_i (middle panels) and the charge separation computed as $n_i - n_e$ (bottom panels) at $t = T_{Le}/2$ (left column) and $t = 3T_{Le}$ (right column), where T_{Le} is the electron Larmor period; xOz central sections parallel to the ambiental magnetic field are shown. 64
- Figure 3.8** – E_x (top panels) and E_y (bottom panels) components of the electric field at $t = T_{Le}/2$ (left column) and $t = 3T_{Le}$ (right column), where T_{Le} is the electron Larmor period; xOy central sections perpendicular to the background magnetic field are shown. _____ 65

Figure 3.9 – E_z component of the electric field at $t=T_{Le}/2$ (left panel) and $t=3T_{Le}$ (right panel), where T_{Le} is the electron Larmor period; xOz central sections parallel to the background magnetic field are shown. 65

Figure 3.10 – The B_x (top panels), B_y (middle panels) and B_z (bottom panels) components of the magnetic field, at $t=T_{Le}/2$ (T_{Le} is the electron Larmor period), in the xOy plane (left column), xOz plane (middle column) and yOz plane (right panel) inside the simulation domain, for the cross-sections specified in the title of each of the nine plots. 66

Figure 3.11 – The B_x (top panels), B_y (middle panels) and B_z (bottom panels) components of the magnetic field, at $t=3T_{Le}$ (T_{Le} is the electron Larmor period), in the xOy plane (left column), xOz plane (middle column) and yOz plane (right panel) inside the simulation domain, for the cross-sections specified in the title of each of the nine plots. 66

Figure 3.12 – J_x (top panels) and J_y (bottom panels) components of the total current density at $t=T_{Le}/2$ (left column) and $t=3T_{Le}$ (right column), where T_{Le} is the electron Larmor period; xOy central sections perpendicular to the background magnetic field are shown. 68

Figure 3.13 – Variation with x of the J_x component of the current density for electrons (left panels) and ions (right panels) at $t=T_{Le}/4$ (top panels), $t=T_{Le}/2$ (middle-top panels), $t=2.5T_{Le}$ (middle-bottom panels) and $t=3T_{Le}$ (bottom panels), where T_{Le} is the electron Larmor period. The dependence $J_x=J_x(x)$ is shown for $y=78$ and $z=153$. 69

Figure 3.14 – Variation with y of the J_y component of the current density for electrons (left panels) and ions (right panels) at $t=T_{Le}/4$ (top panels), $t=T_{Le}/2$ (middle-top panels), $t=2.5T_{Le}$ (middle-bottom panels) and $t=3T_{Le}$ (bottom panels), where T_{Le} is the electron Larmor period. The dependence $J_y=J_y(y)$ is shown for $x=49$ and $z=153$. 70

Figure 3.15 – Number density of electrons at $t=3T_{Le}$, where T_{Le} is the electron Larmor period, in the xOy central section perpendicular to the background magnetic field. This is a zoom in the top-right panel of Figure 3.6. The five black rectangles mark the spatial bins used to compute the velocity distribution function for both electrons and ions. 71

Figure 3.16 – Velocity distribution function of electrons at $t=3T_{Le}$ in the $v_z=0$ section perpendicular to the background magnetic field; T_{Le} is the electron Larmor period. Each of the five (v_x, v_y) panels correspond to a certain spatial bin that covers the entire simulation domain along the z -axis. The bins locations in the xOy plane are shown with black rectangles in Figure 3.15. 72

Figure 3.17 – Velocity distribution function of ions at $t=3T_{Le}$ in the $v_z=0$ section perpendicular to the background magnetic field; T_{Le} is the electron Larmor period. Each of the five (v_x, v_y) panels correspond to a certain spatial bin that covers the entire simulation domain along the z -axis. The bins locations in the xOy plane are shown with black rectangles in Figure 3.15. 73

Figure 3.18 – Schematic diagram of the two space charge layers forming at the edges of a plasma beam injected across a transverse background magnetic field. Panel (a) illustrate the trajectories of the electrons and ions immediately after injection, while panel (b) shows the polarization electric field inside the quasineutral plasma core (adapted from Livesey and Pritchett, 1989). 74

Figure 3.19 – Variation along the y -axis of the net charge density (top panels) and of the E_y component of the electric field (bottom panels), at $t=T_{Le}/4$, for case I (left column) and case II (right column); T_{Le} is the electron Larmor period. The black line in the bottom-right panel marks the value of the polarization electric field given by equation (3.11), i.e. $E_y=V_0B_0$. 75

Figure 3.20 – Number density of electrons n_e (top panels) and ions n_i (middle panels) and the charge separation computed as n_i-n_e (bottom panels) in the xOy plane (left column), xOz plane (middle column) and yOz plane (right column), at $t=T_{Li}$ (T_{Li} is the ion Larmor period), for the cross-sections indicated in the title of each plot. 78

Figure 3.21 – Number density of electrons n_e (top panels) and ions n_i (middle panels) and the charge separation computed as $n_i - n_e$ (bottom panels) in the xOy plane (left column), xOz plane (middle column) and yOz plane (right column), at $t=2T_{Li}$ (T_{Li} is the ion Larmor period), for the cross-sections indicated in the title of each plot. _____ 78

Figure 3.22 – U_x (top panels), U_y (middle panels) and U_z (bottom panels) components of the plasma bulk velocity in the xOy plane (left column), xOz plane (middle column) and yOz plane (right column), at $t=T_{Li}$ (T_{Li} is the ion Larmor period), for the cross-sections indicated in the title of each plot. _____ 79

Figure 3.23 U_x (top panels), U_y (middle panels) and U_z (bottom panels) components of the plasma bulk velocity in the xOy plane (left column), xOz plane (middle column) and yOz plane (right column), at $t=2T_{Li}$ (T_{Li} is the ion Larmor period), for the cross-sections indicated in the title of each plot. _____ 79

Figure 3.24 – E_x (top panels), E_y (middle panels) and E_z (bottom panels) components of the electric field in the xOy plane (left column), xOz plane (middle column) and yOz plane (right column), at $t=T_{Li}$ (T_{Li} is the ion Larmor period), for the cross-sections indicated in the title of each plot. _____ 80

Figure 3.25 – E_x (top panels), E_y (middle panels) and E_z (bottom panels) components of the electric field in the xOy plane (left column), xOz plane (middle column) and yOz plane (right column), at $t=2T_{Li}$ (T_{Li} is the ion Larmor period), for the cross-sections indicated in the title of each plot. _____ 80

Figure 3.26 – Variation over time of the polarization electric field, E_y , along the y-axis between $t=T_{Li}$ and $t=2T_{Li}$, where T_{Li} is the ion Larmor period; the representation is made for $x=110$ and $z=153$. _____ 81

Figure 3.27 – B_x (top panels), B_y (middle panels) and B_z (bottom panels) components of the magnetic field in the xOy plane (left column), xOz plane (middle column) and yOz plane (right column), at $t=2T_{Li}$ (T_{Li} is the ion Larmor period), for the cross-sections indicated in the title of each plot. _____ 81

Figure 3.28 – Background magnetic field profile inside the simulation domain. The B-field is oriented along the positive z-axis and increases linearly with x-coordinate over a transition region having the width of $5r_{Li}$ (r_{Li} is ion Larmor radius in the left hand side of the transition region). _____ 82

Figure 3.29 – Initial number density of electrons in the xOy (left panel) and xOz (right panel) central sections of the simulation domain. The non-uniform background magnetic field is oriented along the positive direction of the z-axis. The two black lines mark the position of the transition region where the magnetic field increases linearly from B_1 up to $B_2=1.5B_1$. The ions and electrons are initialized with the same number density. At $t=0$ the three-dimensional plasma element has a rectangular shape and is localized on the left hand side of the transition region. _____ 83

Figure 3.30 – Number density of electrons (top panels) and ions (bottom panels) at $t=T_{Li}$ (left column), $t=2T_{Li}$ (middle-left column), $t=3T_{Li}$ (middle-right column) and $t=3.75T_{Li}$ (right column); T_{Li} is the ion Larmor period in the left hand side of the transition region. The two black lines mark the position of the transition region where the magnetic field is non-uniform. The xOy plane perpendicular to the background magnetic field is shown here, for $z=253$ cross-section. _____ 84

Figure 3.31 – Number density of electrons (top panels) and ions (bottom panels) at $t=T_{Li}$ (left column), $t=2T_{Li}$ (middle-left column), $t=3T_{Li}$ (middle-right column) and $t=3.75T_{Li}$ (right column); T_{Li} is the ion Larmor period in the left hand side of the transition region. The two black lines mark the position of the transition region where the magnetic field is non-uniform. The xOz plane perpendicular to the background magnetic field is shown here, for $y=128$ cross-section. _____ 84

Figure 3.32 – V_x (top panels) and V_y (bottom panels) components of the plasma bulk velocity at $t=T_{Li}$ (left column), $t=2T_{Li}$ (middle-left column), $t=3T_{Li}$ (middle-right column) and $t=3.75T_{Li}$ (right column); T_{Li} is the ion Larmor period in the left hand side of the transition region. The two black lines mark the position of the transition region where the B-field is non-uniform. The xOy plane perpendicular to the background magnetic field is shown here, for $z=253$ cross-section. _____ 85

Figure 3.33 – E_x component of the electric field (top panels) and $U_{E,y}$ component of the zero-order drift (bottom panels) in the xOy plane perpendicular to the ambient magnetic field, for $t=3T_{Li}$ (left column) and $t=3.75T_{Li}$ (right column); T_{Li} is the ion Larmor period in the left hand side of the transition region. The two black lines mark the position of the transition region where the magnetic field is non-uniform. The zero-order drift is computed only for those grid cells having a number density of at least 5% from its initial value, otherwise the value of $U_{E,y}$ is set to zero. _____ 87

Figure 3.34 – (Left panel) Net charge density in the xOy plane perpendicular to the ambient magnetic field at $t=3T_{Li}$; T_{Li} is the ion Larmor period at the left hand side of the transition region. The non-uniform magnetic field region is marked with the two black straight lines, while the initial position of the plasma cloud is shown by a black rectangle. The net charge in the core of the cloud has been artificially assigned to zero in order to remove the numerical noise and emphasize the effects in the lateral edges. (Right panel) Schematic diagram of the plasma polarization when it interacts with the increasing magnetic field. _____ 88

Figure 3.35 – Initial number density of electrons in the xOy (left panel) and xOz (right panel) sections of the simulation domain. The non-uniform background magnetic field is oriented along the positive direction of the z-axis. The two black lines mark the position of the transition region where the magnetic field increases linearly from B_1 up to $B_2=1.5B_1$. The ions and electrons are initialized with the same number density. At $t=0$ the three-dimensional plasma element has a rectangular shape and is localized on the left hand side of the transition region. _____ 90

Figure 3.36 – Number density of electrons (top panels) and ions (bottom panels) at $t=1.5T_{Li}$ (left column) and $t=3T_{Li}$ (right column); T_{Li} is the ion Larmor period in the left hand side of the transition region. The two black lines mark the position of the transition region where the magnetic field is non-uniform. The xOy plane perpendicular to the background magnetic field is shown here, for $z=203$. _____ 91

Figure 3.37 – V_x (top panels) and V_y (bottom panels) components of the plasma bulk velocity in the xOy plane perpendicular to the ambient magnetic field, for $t=1.5T_{Li}$ (left column) and $t=3T_{Li}$ (right column); T_{Li} is the ion Larmor period in the left hand side of the transition region. The two black lines mark the position of the transition region. The bulk velocity is computed only for those grid cells having a number density of at least 5% from its initial value, otherwise its value is set to zero. _____ 92

Figure 3.38 – Number density of electrons (top panels) and ions (bottom panels) in the xOy (left column) and xOz (right column) planes, at the end of the simulation, i.e for $t=3T_{Li}$; T_{Li} is the ion Larmor period at the left hand side of the transition region. The two black lines mark the position of the transition region where the magnetic field is non-uniform. _____ 93

Figure 3.39 – Plasma bulk velocity (the V_x component) in the xOy plane (left panel) and xOz plane (right panel) at $t=3T_{Li}$; T_{Li} is the ion Larmor period at the left hand side of the transition region. The two black lines mark the position of the transition region where the magnetic field is non-uniform. _____ 94

Figure 3.40 – Forward plasma bulk velocity as a function of the y-coordinate, $V_x=V_x(y)$, for $x=182$ and $z=203$. The black line corresponds to the average value of the plasma bulk velocity, while the red one represents the initial injection velocity. _____ 94

Figure 3.41 – Number density of electrons (first column) and ions (second column) and also the V_x (third column) and V_y (fourth column) components of the plasma bulk velocity, in the xOy plane perpendicular to the magnetic field, at $t=0.5T_{Li}$ (first line), $t=1T_{Li}$ (second line), $t=1.5T_{Li}$ (third line), $t=2T_{Li}$ (fourth line), $t=2.5T_{Li}$ (fifth line) and $t=3T_{Li}$ (sixth line); T_{Li} is the ion Larmor period in the left hand side of the transition region. The two black lines mark the position of the transition region where the magnetic field is non-uniform. The bulk velocity is computed only for those grid cells having a number density of at least 5% from its initial value, otherwise V_x and V_y are set to zero. _____ 95

LIST OF FIGURES

Figure 3.42 – Plasma convection velocity V_x as a function of the magnetic field strength B in the following representation, i.e. $(1-V_x/V_0)^2$ as a function of B/B_1-1 for seven pairs V_x-B obtained at the propagation front of the plasma element at different moments of the interaction with the magnetic discontinuity (blue dots). The red line shows the linear fitting of the simulation data with equation (3.22). The coefficient of determination R^2 for the linear fit is equal to 0.94. _____ 96

Figure 3.43 – Number density of electrons (top panels) and ions (bottom panels) at $t=0$ (left column), $t=0.65T_{Li}$ (middle-left column), $t=1.55T_{Li}$ (middle-right column) and $t=2T_{Li}$ (right column); T_{Li} is the ion Larmor period in the left hand side of the transition region. The two black lines mark the position of the transition region where the magnetic field is non-uniform. The xOy plane perpendicular to the background magnetic field is shown here, for $z=153$ cross-section. _____ 97

Figure 3.44 – V_x component of the plasma bulk velocity at $t=0.65T_{Li}$ (left column), $t=1.55T_{Li}$ (middle column) and $t=2T_{Li}$ (right column); T_{Li} is the ion Larmor period in the left hand side of the transition region. The two black lines mark the position of the transition region where the B-field is non-uniform. The xOy plane perpendicular to the background magnetic field is shown here, for $z=153$. _____ 98

Figure 3.45 – Variation along the x -axis, for $y=77$ and $z=153$, of the electron number density n_e (top panel), plasma convection velocity V_x (middle panel) and magnetic field B_z (bottom panel), at $t=1.55T_{Li}$. We illustrate here only the values corresponding to the central region of the plasma element, i.e. from $x=68$ to $x=104$. The grey rectangle indicates the transition region with a non-uniform magnetic field, while the red line on the middle panel mark the ion sound speed V_s . _____ 99

This page intentionally left blank.

This page intentionally left blank.